TECHNISCHE UNIVERSITÄT MÜNCHEN

WALTHER-MEISSNER-INSTITUT FÜR TIEFTEMPERATUR-FORSCHUNG

BAYERISCHE AKADEMIE DER WISSENSCHAFTEN

Growth optimization and magnetotransport properties of ferromagnetic insulating gadolinium nitride thin films

Master´s thesis in Physics

by

Raphael Hoepfl

Fakultät für Physik

TECHNISCHE UNIVERSITÄT MÜNCHEN

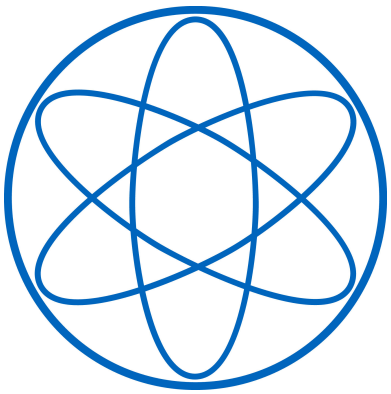

Supervisor: Prof. Dr. Rudolf Gross

Advisor: Dr. Matthias Althammer, M.Sc. Manuel Mueller

Garching – 30. Mai 2023

Contents

1 Introduction **1**

2 Theoretical background **3**
2.1 Spin currents 4
2.2 Spin Hall effect 5
2.3 Spin Hall Magnetoresistance 6
2.4 Weak localization (WL) and weak anti-localization (WAL) 9

3 Fabrication and manufacturing process of FM GdN thin films **11**
3.1 Reactive direct current (DC) magnetron sputtering 12
3.2 SUPERBOWL 14
3.3 Fabrication of gadolinium nitride (GdN) 16
3.4 Fabrication of Hall-bar (HB) patterned GdN thin films 19
3.5 Characterization of the GdN samples 20
3.5.1 X-ray diffraction (XRD)-scans 20

4 Experimental measurement techniques **23**
4.1 Electrical transport measurement 23
4.2 Van-der-Pauw-measurement method and *RRR*-ratio 25
4.3 Magnetotransport measurements 27
4.3.1 Field-dependent magnetoresistance (FDMR) measurements 27
4.3.2 Angle-dependent magnetoresistance (ADMR) measurements 28
4.4 SQUID magnetometry 30

5 Growth optimization of ferromagnetic GdN thin films **31**
5.1 Data analysis procedure 32
5.1.1 Extraction of the static magnetic parameters 32
5.1.2 Magnetic background correction 34
5.1.3 X-ray diffraction spectroscopy 35
5.2 N_2/Ar gas flow ratio variation series 37
5.2.1 Magnetic parameters of N_2/Ar gas flow ratio variation series 37
5.2.2 Lattice parameters of N_2/Ar gas flow ratio variation series 43
5.2.3 Summary of the N_2/Ar gas flow ratio series and comparison to literature 45
5.3 Deposition temperature T_{depo} variation series 48
5.3.1 Magnetic parameters of deposition temperature T_{depo} variation series . 49
5.3.2 Lattice parameters of deposition temperature T_{depo} variation series . . 54
5.3.3 Summary of the deposition temperature T_{depo} variation series and comparison to literature 56
5.4 Comparison of various sputtering configurations 60
5.4.1 N_2/Ar gas flow ratio variation series: tilt-in vs. face-to-face 61
5.4.2 Deposition power P_{depo} variation series: tilt-in vs. face-to-face 63
5.5 Reproducibility and growth on different substrate materials 65

6 Magnetotransport properties of GdN/TaN heterostructures **69**

6.1 Insulating properties of FM GdN 69
6.2 Magnetotransport experiments 73
6.2.1 Magnetic properties and temperature-dependent resistance $R(T)$ of a AlN/GdN/TaN/AlN heterostructure 73
6.2.2 Magnetic properties and temperature-dependent resistance R(T) of a AlN/GdN/AlN/TaN/AlN heterostructure 77
6.2.3 Temperature-dependent resistance $R(T)$ of a AlN/TaN/AlN heterostructure 81
6.2.4 Field-dependent magnetotransport properties of a AlN/GdN/TaN/AlN heterostructure 83
6.2.5 Field-dependent magnetotransport properties of a AlN/GdN/AlN/TaN/AlN heterostructure 88
6.2.6 Field-dependent magnetotransport properties of a AlN/TaN/AlN heterostructure 92
6.2.7 Angle-dependent magnetoresistance (ADMR) of GdN/TaN heterostructures 97
6.2.8 Study for the ADMR amplitude of the GdN/TaN heterostructures as a function of temperature T 101
6.2.9 Magnetic field dependence of the ADMR amplitude 109

7 Spin Hall magnetoresistance (SMR) analysis **113**

8 Summary **121**

9 Outlook **127**

A Appendix **131**
A.1 Tables of the N_2/Ar- and P_{depo}-variation series in the SUPERBOWL 131
A.2 Tables of the T_{depo}-variation series in the SUPERBOWL 132
A.3 Table of the N_2/Ar-variation series in the SUPERBOWL (ftf-config.) 133
A.4 Table of the P_{depo}-variation series in the SUPERBOWL (ftf-config.) 133
A.5 Table of parameters for simulating FDMR-data, recorded for AlN/GdN/TaN/AlN, with WAL model 134
A.6 Table of parameters for simulating FDMR-data, recorded for AlN/GdN/TaN/AlN, with WL model 134
A.7 Table of parameters for simulating FDMR-data, recorded for AlN/GdN/AlN/TaN/AlN, with WAL model 135
A.8 Table of parameters for simulating FDMR-data, recorded for AlN/GdN/AlN/TaN/AlN, with WL model 135
A.9 Table of parameters for simulating FDMR-data, recorded for AlN/TaN/AlN, with WAL model 136

1 Introduction

Recent scientific studies have identified rare-earth nitrides (REN) as interesting compounds for the development of spintronic-based applications, such as novel logic devices [1],[2] and spin-based data storage media [3],[4], which in turn find application in the further development of commercially usable quantum technologies such as quantum information processing and quantum computing [5],[6],[7],[8]. Among the various REN compounds, in particular the ferromagnetic semiconductor gadolinium nitride (GdN), which exhibits ferromagnetic and electrically highly resistive properties [12],[13], is a promising candidate for the development of high-quality REN-based materials for spintronic devices [1],[9],[10],[11]. To realize REN-based spintronic devices, one of the major challenges is the development of ferromagnetic semiconducting thin films, which enables an efficient induction of spin-polarized charge carriers and thus spin currents into adjacent semiconducting layers [1],[10]. Furthermore, magnetic insulators are the cornerstone of the emerging field of *spin insulatronics* (SI), where ferromagnetic insulating (FMI) (hybrid-) structures are appropriate materials for the generation, detection and the control of pure spin currents and excitations inside magnetic insulators (see work of *Arne Brataas et al.* [14]). Here, the combination of ferromagnetic insulating (FMI) thin films and normal metal (NM) layers, such as YIG (FMI)/Pt (NM) [15] or EuO (FMI)/W (NM) [16], used to study spin currents in the FMI/NM-interface, due to the spin Hall effect (SHE), as well as the investigation of spin injection in the NM layer via the spin Hall magnetoresistance (SMR) effect (see chapter 2.3). Moreover, in the ferromagnetic resonance (FMR) measurements, performed by *Y. Yao et al.* [17], they have investigated the magnetization dynamics of FMI GdN thin films sandwiched between a superconducting (SC) niobium nitride (NbN) top and bottom layer to investigate spin dynamics and thus spin currents in the SC NbN thin film via spin pumping effects from the adjacent FMI GdN thin film. These aspects motivated us to investigate the growth properties of GdN thin films via reactive sputter deposition and investigate their spin transport properties by performing magnetotransport experiments.

In the first main part of this master´s thesis, we optimize the growth process of ferromagnetic insulating (FMI) gadolinium nitride (GdN) thin films by performing reactive direct current (DC) magnetron sputtering processes in the sputtering system SUPERBOWL. Due to the oxophilicity of GdN, we deposite the GdN thin films (d=60 nm) between a protective bottom and capping layer of tantalum nitride (TaN) (d=20 nm) on a silicon (Si) substrate ($6 \times 10 \times 0.55$) mm^3 with a thermally oxidized SiO_2 (d=1 μm) top layer. For the development of an ideal deposition recipe of FMI GdN thin films, we sequentially optimize the growth parameters, such as the N_2/Ar gas mixture ratio [%], the sputtering power P_{depo} [W] and the growth temperature T_{depo} [°C], whereas the top and bottom TaN buffer layers were grown unchanged using a previously developed deposition recipe for normal conducting (NC) TaN derived from my bachelor´s thesis [18]. For all of the thin films grown in our optimization series, we perform SQUID magnetometry experiments to determine the static magnetic properties, such as the saturation magnetization $\mu_0 M_{\mathrm{s}}$ and the coercive field $\mu_0 H_{\mathrm{c}}$, and the ferromagnetic Curie temperature T_{C}, and thus to investigate the interplay between the growth parameters and the magnetic characteristics of our GdN thin films.

Afterwards, we perform XRD scans to analyze the crystalline quality of our GdN thin films grown with the optimized deposition- and magnetic-parameters on a Si/SiO_2 substrate. Finally, we test the optimized growth recipe of FM GdN thin films for its reproducibility on a second Si/SiO_2 substrate $(6 \times 10 \times 0.55)\,mm^3$ as well as on crystalline sapphire (Al_2O_3) substrate $(6 \times 10 \times 0.55)\,mm^3$ and compare the examined magnetic- and crystalline-properties with our FM GdN reference sample grown on Si/SiO_2.

The second main part of this master´s thesis discusses the results of the magnetotransport experiments performed for several GdN/TaN multilayer heterostructures fabricated with the dc magnetron sputtering process in the SUPERBOWL. Here, we first determine the insulating properties of a ferromagnetic insulating (FMI) AlN/GdN/AlN trilayer thin film, which we manufactured with the previously developed growth recipe for a FM GdN thin film, by performing an electrical transport measurement in a cryogenic environment. Next, we use the optimized growth recipe of our FMI AlN/GdN/AlN sample to fabricate several multilayer heterostructures deployed in our magnetotransport experiments performed in the *MORIA* cryostat. Here, we prepared three different samples, which we pattern into Hall-bar structures by using photolithography and argon ion milling, to investigate a potential spin Hall magnetoresistance (SMR) effect in the GdN/TaN interface. In detail, we manufactured a so-called *SMR test sample* with the stack sequence AlN/GdN/TaN/AlN, a *SMR reference sample* AlN/GdN/AlN/TaN/AlN and a AlN/TaN/AlN trilayer heterostructure and determine also the resistive- and magnetic-properties of all three multilayer samples by performing electrical transport- and SQUID magnetometry- measurements. As a next step we performed *field-dependent magnetoresistance* (FDMR) and *angle-dependent magnetoresistance* (ADMR) measurements to investigate the magnetotransport properties of our three multilayer heterostructures. In the FDMR experiments, we extract the symmetrized longitudinal magnetoresistance MR as a function of an applied external magnetic field $\mu_0 H_{\text{ext}}$ (-7 T to +7 T) at various fixed temperatures T=(7.5, 10, 12, 15, 18, 20) K in the three different field geometries oop ($\mathbf{h} \| \mathbf{n}$) and ip ($\mathbf{h} \| \mathbf{j}$ and $\mathbf{h} \| \mathbf{t}$). Afterwards, we discuss ADMR measurements of our multilayer heterostructures in three different rotation planes in-plane (ip), out-of-plane $\perp \mathbf{j}$ (oopj) and out-of-plane $\perp \mathbf{t}$ (oopt) in the T-range $5\,K \leq T \leq 25\,K$ at an applied external magnetic field $\mu_0 H_{\text{ext}}$=7 T. Furthermore, we analyze the T-dependent evolution of the ADMR amplitude in the entire measured T-range $7\,K \leq T \leq 50\,K$ at 7 T as well as the magnetic field dependence of the ADMR amplitude at various fixed temperatures T. In order to gain access to investigate the origin of our magnetotransport measurement results, we study and compare the FDMR- and the ADMR-data and verify their correspondence.

In the last chapter of this master´s thesis, we analyze the results from our magnetotransport experiments with regard to a possible SMR effect at the GdN/TaN interface and then compare our results with those of the SMR studies in a YIG (FMI)/Pt (NM)-interface (see work of *M. Althammer et al.* [15]) and EuO (FMI)/W (NM)-bilayer (see work of *P. Rosenberger et al.* [16]).

2 Theoretical background

In this chapter, we introduce the theoretical concepts of spin currents, which play an important role for the development of functional spintronic devices. Afterwards, for the generation and detection of spin currents, we discuss the spin Hall effect (SHE) and the inverse spin Hall effect (ISHE) as well as the combination of these two effects in the so-called spin Hall magnetoresistance (SMR), which represents an angle-dependent magnetoresistive effect generated in ferromagnetic insulator (FMI)/normal metal (NM) heterostructures. In the second part of this chapter, we discuss the basic principles of the quantum transport effects weak localization (WL) and weak anti-localization (WAL) in a disordered electron system.

2.1 Spin currents

As a first step, we introduce the so-called *two current model*, which considers two degrees of freedom: The *charge carrier degree of freedom*, due to the moving charges in an electrical current, as well as the *spin degree of freedom*, which originates from the flow of the intrinsic spin angular momentum of the electrons in an electrical current. Consequently, the *two current model* represents a combination of the charge current density $\mathbf{J}_c$ and the spin current desity $\mathbf{J}_s$. The charge current density is defined by [19],[20]

$$\mathbf{J}_c = (\mathbf{J}_\uparrow + \mathbf{J}_\downarrow), \tag{1}$$

where $\mathbf{J}_\uparrow$ and $\mathbf{J}_\downarrow$ represents the charge current density of the electrons with a spin polarization $\mathbf{s}$ pointing up ($\uparrow$) („spin $\uparrow$ electrons“) or ($\downarrow$) („spin $\downarrow$ electrons“). Eq. (1) describes a *pure charge current* (see Fig. 2.1 (a)) for an ensemble of electrons with an equal numbers of $\uparrow$ and $\downarrow$ spins and an equal flow direction. In another case, if there exist an unequal number of $\uparrow$ and $\downarrow$ spin electrons, with a preferred orientation of the spins, in a charge current, we also observe a spin current $\mathbf{J}_s$, described by [19],[20]

$$\mathbf{J}_s = -\frac{\hbar}{2e}(\mathbf{J}_\uparrow - \mathbf{J}_\downarrow), \tag{2}$$

as well as a charge current $\mathbf{J}_c \neq 0$ in the system of a *spin-polarized current* model (see Fig. 2.1 (b)). Finally, in a charge current with an euqal numbers of $\uparrow$ and $\downarrow$ spin electrons and an opposing flow direction ($\mathbf{J}_\uparrow = -\mathbf{J}_\downarrow$), we obtain a *pure spin current* with $\mathbf{J}_s \neq 0$ and therefore no charge current transport $\mathbf{J}_s = 0$ exist in this model (see Fig. 2.1 (c)).

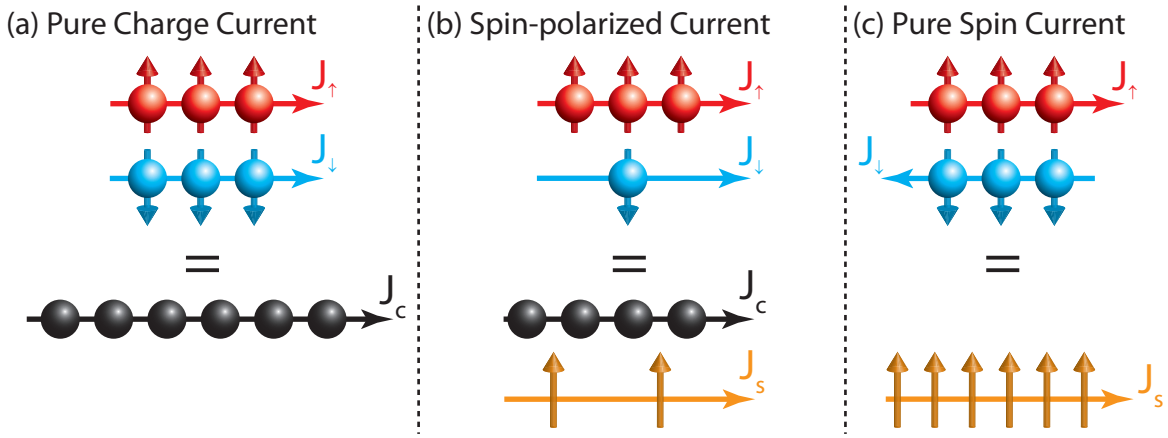

Fig. 2.1: Various current models in solids: (a) A *pure charge current* consists of an equal number of $\uparrow$ and $\downarrow$ electron spins and show an equal flow direction $\rightarrow$ only a charge current $\mathbf{J}_c \neq 0$ and no spin transport $\mathbf{J}_s = 0$ is mediated. (b) In a *spin-polarized current*, an unequal number of $\uparrow$ and $\downarrow$ electron spins with an equal flow direction is available $\rightarrow$ charge current $\mathbf{J}_c \neq 0$ and spin transport $\mathbf{J}_s \neq 0$ is mediated. (c) A *pure spin current* consists of an equal number of $\uparrow$ and $\downarrow$ electron spins, which flow in an opposing direction $\rightarrow$ only a spin current $\mathbf{J}_s \neq 0$ and no no charge current $\mathbf{J}_c = 0$ is mediated. Taken from Ref. [20].

2.2 Spin Hall effect

The generation of pure spin currents in metals is based on the physical principles of the spin Hall effect (SHE) (see Fig. 2.2 (a)). Moreover, the detection of pure spin curents are possible via the inverse effect spin Hall effect (ISHE) (see Fig. 2.2 (b)) [20].

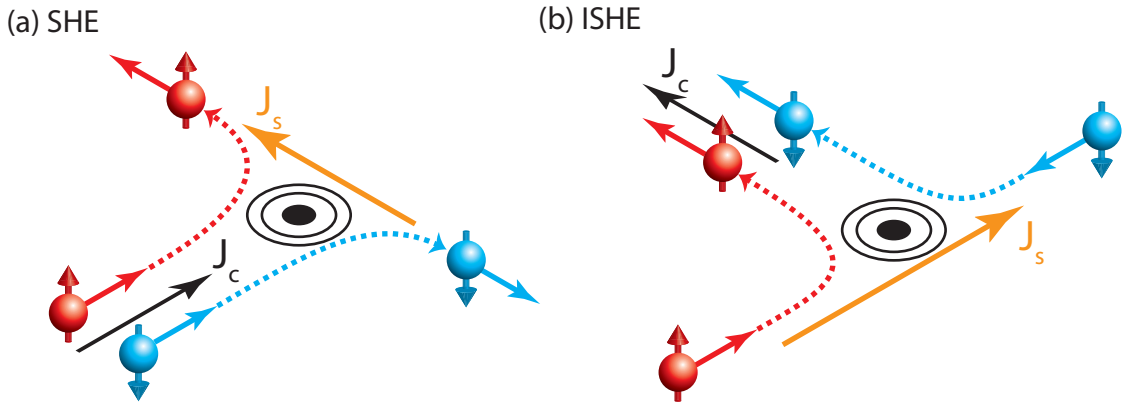

Fig. 2.2: Illustration of (a) the spin Hall effect (SHE), where a charge current $\mathbf{J}_c$ is converted into a transverse spin current $\mathbf{J}_s$. Figure (b) shows the inverse spin Hall effect (ISHE), where a spin current $\mathbf{J}_s$ is converted into a transverse charge current $\mathbf{J}_c$. In both effects, scattering effects due to the strong spin-orbit coupling (SOC) give rise to the interconversion of charge currents into spin currents and vice versa. Taken from Ref. [20].

In the spin Hall effect (SHE), the charge current $\mathbf{J}_c$ is converted to a perpendicular spin current $\mathbf{J}_s$ (see Fig. 2.2 (a)), which is defined by [21]

$$\mathbf{J}_c \overset{(\mathrm{SHE})}{\longrightarrow} \mathbf{J}_s = \theta_{\mathrm{SH}} \left(-\frac{\hbar}{2e}\right) \mathbf{J}_c \times \mathbf{s}, \tag{3}$$

due to spin-dependent scattering processes of the electron spins and their strong spin-orbit coupling (SOC) governed by the spin Hall angle θ_{SH}. Furthermore, we obtain in the opposite effect, the inverse spin Hall effect (ISHE), a transformation of the spin current $\mathbf{J}_s$ to a transversal charge current $\mathbf{J}_c$ (see Fig. 2.2 (b)) according to [22]

$$\mathbf{J}_s \overset{(\mathrm{ISHE})}{\longrightarrow} \mathbf{J}_c = \theta_{\mathrm{SH}} \left(-\frac{2e}{\hbar}\right) \mathbf{J}_s \times \mathbf{s}, \tag{4}$$

where the spin Hall angle θ_{SH} represents a ratio for the efficiency of the current interconversion process, governed by the intrinsic bandstructure mechanisms [23] and the extrinsic scattering effects on defects in the material [24],[25],[26], from spin to charge current (via ISHE) as well as charge to spin current (via SHE) [20],[27]. Therefore, we use heavy, paramagnetic metals (HM) like platinum (Pt) or tantalum (Ta), which exhibit a strong spin-orbit coupling $\propto Z^4$, to achieve a large spin Hall angle [20],[27]. In this master´s thesis, we use tantalum nitride (TaN), which shows a large spin Hall angle $\theta_{\mathrm{SH,TaN}}$=0.034 (see work of *P. W. Swatek et al.* [28]), for the creation of a spin Hall effect (SHE) and an inverse spin Hall effect (ISHE).

2.3 Spin Hall Magnetoresistance

In this section, we discuss the spin Hall Magnetoresistance (SMR) effect, which represents a magnetoresistive effect dependent on the magnetization orientation **m**, of a ferromagnetic insulator (FMI)/normal metal (NM) bilayer (see Fig. 2.3 (a)-(b)) [20].

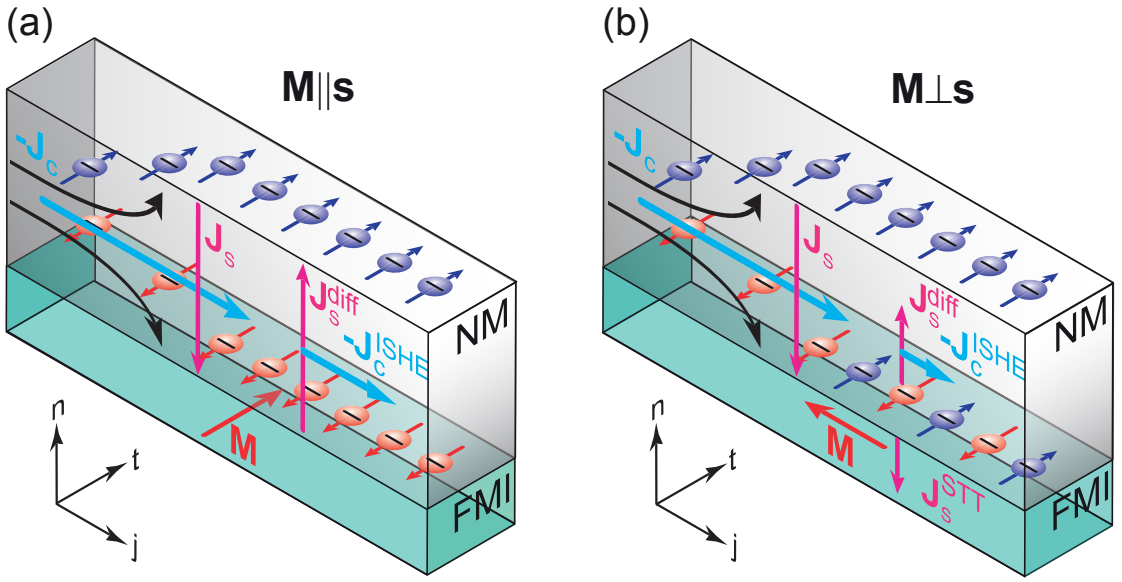

Fig. 2.3: Principle of the spin Hall magnetoresistance (SMR): The charge current $-\mathbf{J}_c$ is converted by the spin Hall effect (SHE) to a transverse pure spin current $\mathbf{J}_s$ and generates a spin accumulation $\boldsymbol{\mu}_s$ at the NM/FMI interface. (a) The spin current $\mathbf{J}_s$ is completely reflected, due to the parallel alignment of the magnetization $\mathbf{M}$ of the FMI and the spin polarization $\mathbf{s}$ of the electrons, at the interface and results in a diffusive spin current backflow $\mathbf{J}_s^{diff}$, which is in turn converted into a charge current $\mathbf{J}_c^{ISHE}$ via the inverse spin Hall efect (ISHE). For $\mathbf{M}\perp\mathbf{s}$, a fraction of $\mathbf{J}_s$ denoted $\mathbf{J}_s^{STT}$ is absorbed in the FMI due to the a spin transfer torque on the magnetization $\mathbf{M}$. Thus, the diffusive spin current backflow $\mathbf{J}_s^{diff}$ is smaller for $\mathbf{M}\perp\mathbf{s}$ than $\mathbf{M}\|\mathbf{s}$, which results in a lower charge current $\mathbf{J}_c^{ISHE}$ created by the ISHE effect and corresponds finally in an increase of the resistivity in the NM layer. Taken from Ref. [20]

The phenomenological mechanism of the spin Hall magnetoresistance is shown in Fig. 2.3 (a)-(b). As a first step, a charge current $-\mathbf{J}_c$ is driven through the normal metal (NM) in the **j**-direction and is converted by the spin Hall effect (SHE) (see Fig. 2.2 (a)) into a pure spin current $\mathbf{J}_s$ along the **-n**-direction, which is perpendicular to $-\mathbf{J}_c$ as well as to the FMI/NM interface. Therefore, the spin current $\mathbf{J}_s$, with its spin polarization **s** along **-t**, generates a spin accumulation $\boldsymbol{\mu}_s$ at the NM/FMI interface and we observe a diffusive spin current backflow $\mathbf{J}_s^{diff}$ with opposite direction to $\mathbf{J}_s$, which is converted to a charge current $-\mathbf{J}_c^{ISHE}$ parallel to $-\mathbf{J}_c$ via the inverse spin Hall effect (ISHE). Moreover, the spin accumulation at the FMI/NM interface generates a gradient $\nabla\boldsymbol{\mu}_s$ in the spin chemical potential $\boldsymbol{\mu}_s=\boldsymbol{\mu}_\uparrow-\boldsymbol{\mu}_\downarrow$ and we obtain the following expression for the spin diffusion current [20],[29]

$$\mathbf{J}_s^{diff} = \frac{\hbar\sigma}{2e^2}\nabla\boldsymbol{\mu}_s, \tag{5}$$

where $\sigma = 1/\rho$ defines the electrical conductivity. As a next step, the electron spin polarization **s**, which is accumulated at the FMI/NM interface, interacts with the magnetization $\mathbf{M}$ in the FMI in two different ways: For $\mathbf{M}\perp\mathbf{s}$ (see Fig. 2.3 (b)), we observe a partially absorbed

spin current $\mathbf{J}_s^{STT}$, and acts as a torque on the magnetization $\mathbf{M}$ of the FMI. This mechanism is described as the so called spin transfer torque (STT). Due to the partially converted spin current $\mathbf{J}_s$ to the charge current -$\mathbf{J}_c^{ISHE}$ via the ISHE, the net charge current -$\mathbf{J}_c$ is reduced and thus the resistance of the NM increases. In the other case no STT can manifest as $\mathbf{M}\|\mathbf{s}$ (see Fig. 2.3 (a)). Hence, the spin current $\mathbf{J}_s$ reflected at the FMI/NM interface and is transformed into charge current -$\mathbf{J}_c^{ISHE}$ via the ISHE. Consequently, the complete charge current -$\mathbf{J}_c$ increases and thus the resistance of the NM decreases. In summary, there exist only for $\mathbf{M}\perp\mathbf{s}$ (see Fig. 2.3 (b)) a spin current, which flows across the FMI/NM interface and can be described by the expression [20],[29]

$$\mathbf{J}_s^{STT} \propto G_{\uparrow\downarrow}\mathbf{m} \times (\mathbf{m} \times \boldsymbol{\mu}_s), \tag{6}$$

where $G_{\uparrow\downarrow}$ defines the so-called spin mixing conductance (see Eq. (43)) and represents the efficiency of the spin transport across the FMI/NM-interface [20]. Consequently, the spin accumulation $\boldsymbol{\mu}_s$ decreases at the NM/FMI interface, due spin current $\mathbf{J}_s^{STT}$ injected into the FMI, and thus the diffusive spin current backflow $\mathbf{J}_s^{diff}$ is also reduced. As already mentioned, the remaining spin diffusion current $\mathbf{J}_s^{diff}$ in the NM is converted to a charge current -$\mathbf{J}_c^{ISHE}$ via the inverse spin Hall effect (ISHE) and is part of the completely reduced transverse charge current -$\mathbf{J}_c$ and therefore responsible for the growing resistance in the NM layer. In summary, the spin current $\mathbf{J}_s^{STT}$ across the NM/FMI interface depends on the relative alignment of the magnetization $\mathbf{M}$ and the electron spin polarization $\mathbf{s}$. Therefore, the spin Hall magnetoresistance (SMR) represents a magnetization orientation $\mathbf{m}$ dependent magnetoresistive effect. We can describe the longitudinal resistivity of the NM as an angle-dependent resistance on the magnetization $\mathbf{M}$ of the FMI layer by the following expression [20],[27],[29]

$$\rho_{long}^{SMR} = \rho_0^{SMR} + \rho_1^{SMR}(1 - m_t^2), \tag{7}$$

where m_t defines the projection of the magnetization $\mathbf{m}$=$\mathbf{M}/M_s$ in the $\mathbf{t}$-direction, where M_s is the saturation magnetization. Furthermore, the contribution ρ_0^{SMR} is approximately equal to the resistivity of the sole NM and we obtain $\rho_0^{SMR} \approx \rho_0^{NM}$ (see work of *P. Schwenke* [27]). Furthermore, ρ_1^{SMR} represents the change in the resistivity, generated by the SMR effect, in the NM layer and we assume $\rho_1^{SMR} << \rho_0^{SMR}$ (see work of *Y.-T. Chen et al.* [29]). In this master´s thesis, we perform angle-dependent magnetoresistance (ADMR) measurements (see Sec. 6.2.7) to investigate a potential SMR effect in a ferromagnetic insulating (FMI) gadolinium nitride (GdN) / normally conducting (NM) tantalum nitride (TaN) interface (see chapter 7). To this end, we use three different rotation planes for the magnetic field direction $\mathbf{h}$ of an applied external magnetic field $\mu_0 H_{ext}$ (see top panels of Fig 2.4) to change the orientation of the magnetization $\mathbf{M}$ in the FMI layer and therefore to modulate the resistivity in the NM. Here, we expect in the in-plane (ip) rotation plane (see top panel (a) of Fig 2.4) a $\cos^2(\alpha)$-dependence for the resistivity according to the following expression

$$\rho_{long,ip}^{SMR} = \rho_0^{SMR} + \rho_1^{SMR}\cos^2(\alpha), \tag{8}$$

as well as a $\sin^2(\beta)$-signature in the out-of-plane $\perp$ $\mathbf{j}$ (oopj) field geometry (see top panel

(b) of Fig 2.4) according to

$$\rho_{\mathrm{long,oopj}}^{\mathrm{SMR}} = \rho_0^{\mathrm{SMR}} + \rho_1^{\mathrm{SMR}} \sin^2(\beta). \tag{9}$$

Due to m_{t}=0 in the **t**-direction, we expect in out-of-plane $\perp$ **t** (oopt) measurement geometry (see top panel (c) of Fig 2.4) a constant resistivity of

$$\rho_{\mathrm{long,oopt}}^{\mathrm{SMR}} = \rho_0^{\mathrm{SMR}} + \rho_1^{\mathrm{SMR}} \tag{10}$$

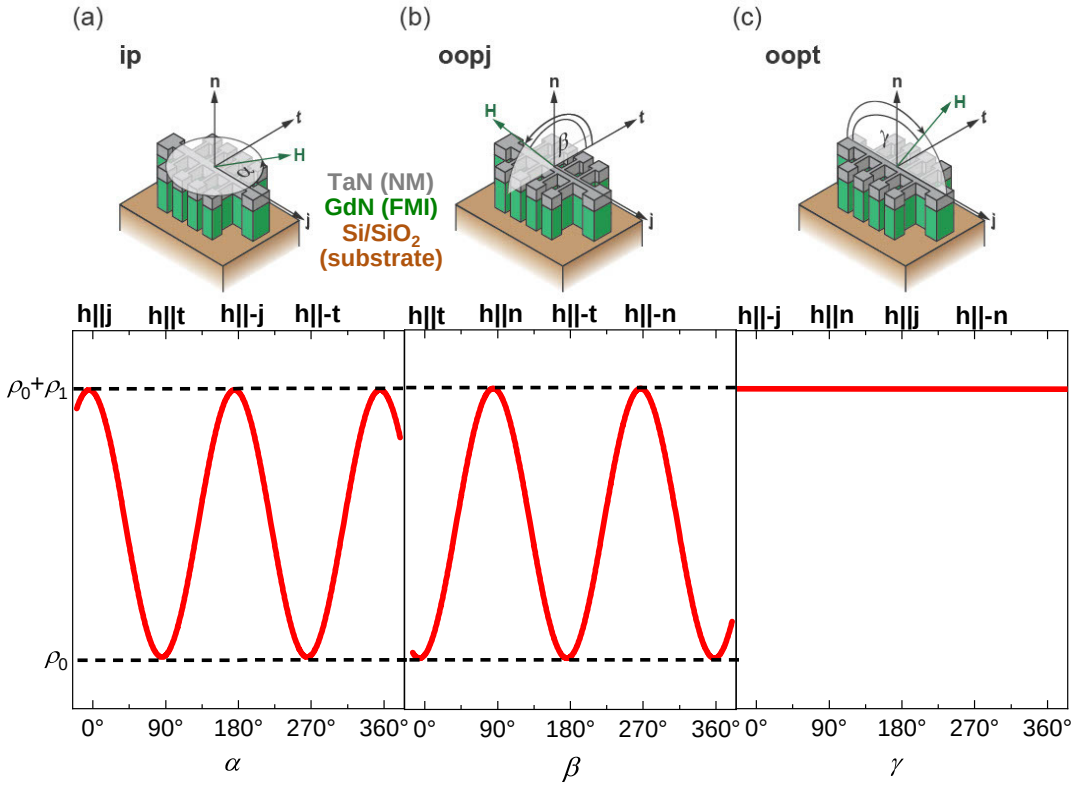

Fig. 2.4: Expected angle-dependence of the SMR-effect in a GdN (FMI)/TaN (NM) heterostructure grown on Si/SiO_2-substrate: Rotation of the magnetic field **H** in three different measurement geometries: (a) In the in-plane (ip) rotation plane, we expect a $\cos^2(\alpha)$-dependence for $\rho_{\mathrm{long,ip}}{}^{\mathrm{SMR}}$ (see Eq. (8)). (b) In the out-of-plane $\perp$ **j** (oopj) field geometry, we expect $\rho_{\mathrm{long,oopj}}{}^{\mathrm{SMR}} \propto \sin^2(\beta)$ (see Eq. (9)). (c) In the out-of-plane $\perp$ **t** (oopt) measurement geometry, no angle-dependence is expected for $\rho_{\mathrm{long,oopt}}{}^{\mathrm{SMR}}$ (see Eq. (10)). Adapted from Ref. [30].

Finally, the longitudinal SMR amplitude can be calculated by the following relationship [29]

$$\mathrm{SMR}_{\mathrm{long}} = \frac{\rho_1^{\mathrm{SMR}}}{\rho_0^{\mathrm{SMR}}} \approx \theta_{\mathrm{SH}}^2 \frac{\lambda_{\mathrm{sf}}}{t_{\mathrm{NM}}} \left[\frac{2\rho_{\mathrm{NM}}\lambda_{\mathrm{sf}}G_{\mathrm{r}} \tanh^2\left(\frac{t_{\mathrm{NM}}}{2\lambda_{\mathrm{sf}}}\right)}{1 + 2\rho_{\mathrm{NM}}\lambda_{\mathrm{sf}}G_{\mathrm{r}} \coth\left(\frac{t_{\mathrm{NM}}}{\lambda_{\mathrm{sf}}}\right)} \right], \tag{11}$$

where G_{r} represents the real part of the complex spin mixing conductance $G_{\uparrow\downarrow}$=G_{r}+iG_{i} and the parameters θ_{SH}, λ_{sf}, ρ_{NM}, t_{NM} defines the spin Hall angle (SHA), the spin diffusion length, the resistivity and the layer thickness of the normal metal (NM) i.e tantalum nitride (TaN) in our experiments.

2.4 Weak localization (WL) and weak anti-localization (WAL)

During the investigation of the resistive properties of transition metal oxides (e.g. ZnO [31] or MgZnO [32]), semiconductors (e.g. GaN [33]) or topological insulators (TI), in which a charge carrier transport exists on its surface, deposited on ferromagnetic insulators (FMI) (e.g. Bi_2Se_3 (TI)/EuS (FMI) [34],[35] or Bi_2Se_3 (TI)/GdN (FMI) [36] in magnetotransport experiments, a large number of non-trivial physical effects can manifest themselves [32]. A well-known effect in (multilayer) thin film heterostructures is the so-called *weak localization* (WL), which can be observed at very low temperatures and describes the charger carrier transport phenomena in a disordered electron system (see work of *P. A. Lee et al.* [37] and *B. L. Altshuler et al.* [38]) of e.g. (transition-) metals, semiconductors [39] or TI/FMI-hybrid structures [40]. In such disordered systems, the electrons do not move along a straight path, but rather in a random walk, due to their random scatterings by impurities [37]. Here, the transport phenomena can not be explained with classical physics and therefore the theoretical model by Drude [41] (see also Eq. (50)), which describes the movement of the electrons on a diffusive path deflected on static ions in the metal, is not valid. Consequently, the WL effect in a disordered electron system is a quantum mechanic (QM)-based effect, which describes the propagation of the electrons as a wave with a wavelength $\lambda{=}2\pi/k_\mathrm{F}$ larger than the mean free path length l, which defines the average distance of the movement of the electrons before its direction is changed by elastic scattering processes, in a crystal [37]. In the QM model for charge carrier transport, constructive interference occurs, which generally describes the positive change in amplitude when waves are superimposed according to the superposition principle, in the WL transport effect due to the coherent backscattered electronic wave functions [32],[31]. As described in the work of *E. M. Likovich et al.* [31] and *M. Lv et al.*[32], the backscattering leads to an increasing probability of electron localization, provided that the deflected electron again follows its initial path but in the inverse direction, in the disordered system. This phenomenon corresponds to a positive correction for the resistivity at zero applied external magnetic field ($\mu_0 H_\mathrm{ext}{=}0\,\mathrm{T}$), whereas for $\mu_0 H_\mathrm{ext}{>}0\,\mathrm{T}$, the constructive interference is reduced and the coherent superposition of the electron waves break down accompanied by a lower contribution to the resistivity and thus the system shows a negative magneto-resistivity [32],[31]. In summary, the contribution in the resistivity correction originates from WL transport phenomena due to the quantum interference effects of electron waves propagating on two self-intersecting scattering paths on a circle [37],[40],[42] (see Fig. 2.5).

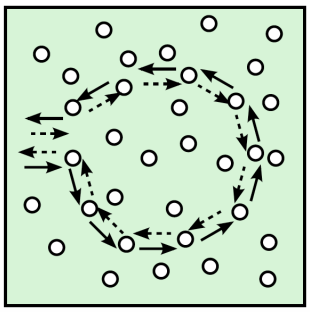

Fig. 2.5: Schematic illustration of the charge carrier transport in a disordered electron system. The white dots represent the impurities and the arrows defines the two opposite circular scattering paths of the electron. Taken from Ref. [40].

A further transport effect in a disordered electron system is the so-called *weak anti-localization* (WAL) effect, which exists considering the spin–orbit coupling (SOC) [43] due to the interaction between the intrinsic angular momentum (spin) of the charge carriers and their momentum [44],[45],[46]. Here, the rotation direction of the spins are inverse to the two different wave propagation directions on the cirle, which results in destructive interference effects of the electron waves and finally a reduced net resistivity at zero magnetic field is observed in magnetotransport experiments [44],[45],[46]. In a two-dimensional systems, we can calculate the change in the conductivity, due to WL and WAL, with the expression

$$\Delta G = G(B) - G(0), \tag{12}$$

which originates from the work of *P. J. Newton et al.* [47] and is connected to the theoretical model of *Hikami-Larkin-Nagaoka* (HLN) [44]

$$\Delta G(B)_{\mathrm{HLN}}^{\mathrm{WL}} = \alpha \cdot \rho_0 \cdot \frac{e^2}{2\pi^2\hbar} \cdot \left[\psi\left(\frac{1}{2} + \frac{B_\phi}{B}\right) - \ln\left(\frac{B_\phi}{B}\right)\right]. \tag{13}$$

In the case of WL transport effects, we add a quadratic background term, which originates from the quadratic background from the Lorentz force the recorded resistivity data, to Eq. (13) and we obtain the final expression for the fitting-function [47]:

$$\Delta G(B)_{\mathrm{FIT}}^{\mathrm{WL}} = \Delta G(B)_{\mathrm{HLN}}^{\mathrm{WL}} + CB^2. \tag{14}$$

As already mentioned, in WAL the spin–orbit coupling (SOC) cannot be neglected and we get the following expression for the change in the conductivity based on the HLN model [47],[44]

$$\begin{aligned}\Delta G(B)_{\mathrm{HlN}}^{\mathrm{WAL}} = \alpha \cdot \rho_0 \cdot \frac{e^2}{2\pi^2\hbar} \cdot \Bigg[&\psi\left(\frac{1}{2} + \frac{B_\phi}{B}\right) - \ln\left(\frac{B_\phi}{B}\right) - 2\psi\left(\frac{1}{2} + \frac{B_\phi + B_{\mathrm{SO}}}{B}\right) \\ &+2\ln\left(\frac{B_\phi + B_{\mathrm{SO}}}{B}\right) - \psi\left(\frac{1}{2} + \frac{B_\phi + 2B_{\mathrm{SO}}}{B}\right) + \ln\left(\frac{B_\phi + 2B_{\mathrm{SO}}}{B}\right)\Bigg]\end{aligned} \tag{15}$$

and we linear background term to Eq. (15) and we obtain the following fitting-function:

$$\Delta G(B)_{\mathrm{FIT}}^{\mathrm{WAL}} = \Delta G(B)_{\mathrm{HLN}}^{\mathrm{WAL}} + F|B|. \tag{16}$$

In Eqs. (13)−(16), α=1 (WL) or -1/2 (WAL) is a constant, ρ_0 is the resistivity of the sample at zero field, e the positive electron charge, $\hbar$ is the reduced Planck constant, C and F are T-dependent constants and $\psi(x)$ is the so-called the Digamma function [47]. Furthermore, the Eqs. (13) and (15) contain two characteristic magnetic fields: $B_\phi = \frac{\hbar}{4eL_\phi{}^2}$ defined by the electron wave phase coherence length L_ϕ, which measures the average distance of an existing phase coherence of a propagating electron wave [40][48], and $B_{\mathrm{SO}} = \frac{\hbar}{4eL_{\mathrm{SO}}{}^2}$ represented by the spin-orbit length L_{SO}. In section 6.2.4,6.2.5,6.2.6, we discuss the *field-dependent magnetoresistance* (FDMR) measurement results of several mutlilayer heterostructures in terms of the manifestation of weak localization (WL) and weak anti-localization (WAL) transport phenomena.

3 Fabrication and manufacturing process of FM GdN thin films

In this master´s thesis, we fabricate ferromagnetic (FM) gadolinium nitride (GdN) thin films using the reactive DC magnetron sputtering process in an ultra-high vacuum (UHV) chamber. After fabricating the GdN thin films, we determine the magnetic parameters, such as the saturation magnetization $\mu_0 M_s$, the coercive field $\mu_0 H_c$ and the ferromagnetic Curie temperature T_C, of our GdN thin films by performing a SQUID magnetometry (see Sec. 4.4). The basic principles of the reactive DC magnetron sputtering process are detailed in many publications (e.g. work of *A. Anders* [49]) and theses at WMI [50, 51]. In the following section we describe the fabrication steps in our UHV-deposition system.

3.1 Reactive direct current (DC) magnetron sputtering

In the reactive sputtering process, we inject argon gas into the main chamber via the target gas inlet and the chamber pressure is set to (10^{-2}-10^{-3}) mbar by the control valve in front of the turbomolecular pump [50, 51]. To ignite the plasma near the target by impact ionization of the gas atoms, we apply a direct voltage of several hundred volts to the cathode (target material) and to the anode cylinder around the target material. Thereby, we generate accelerated electrons, which collide with the argon atoms and ionize them if the kinetic energy of the electrons is sufficient. Due to a high density of argon atoms between the anode and cathode, one electron is able to ionize several gas atoms before recombination. The probability of an impact ionization is increased by a magnetic field generated by a permanent magnet underneath the magnetron which forces the electrons on helical paths and thereby increases the path, they traverse before impacting on the target surface. In this way, further ionization processes take place in avalanche processes and a plasma of positive charged Ar^+ ions and negative charged electrons is created. The external electric field accelerates the argon ions towards the target and the ions collide with the target atoms. Depending on the kinetic energy of the ion, it can collide with many traget atoms and thereby transfers its momentum, while surface target atoms are removed and can deposit on the substrate [50, 51]. This so-called collision cascade process is shown in Fig 3.1.

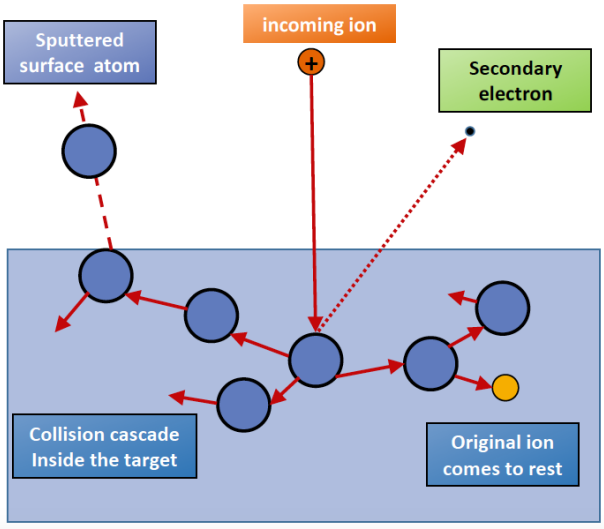

Fig. 3.1: Principle of cathode sputtering and collision cascade in the target material. Taken from Ref.[49],[52].

Figure 3.1 shows a collision cascade where multiple atoms and more complex compounds are released from the target surface and then reach the substrate with high enough kinetic energy to coat it. The sputtering rate R, which indicates how many particles arrive the substrate, is an essential process parameter and can be adjusted via several deposition parameters, such as the distance between substrate and target. A high deposition rate R can be achieved at low ambient pressure in the system, because the released target particles scatter less with other particles in the chamber. Furthermore, the power level of the voltage source has a substantial influence on the rate, whereby an increasing sputtering or deposition power P_{depo} is corresponding to an increase in kinetic energy of the individual argon ions and deposition rate [50, 51].

Therefore, when the ions collide with the target atoms, there is a higher energy transfer and it is possible for an argon ion to release several atoms or molecules from the target. In order to ensure the stability of the plasma even at low pressures, we use an electrically conductive target as well as a magnetron, which are shown in Figure 3.2 (a)-(b), in our sputtering process.

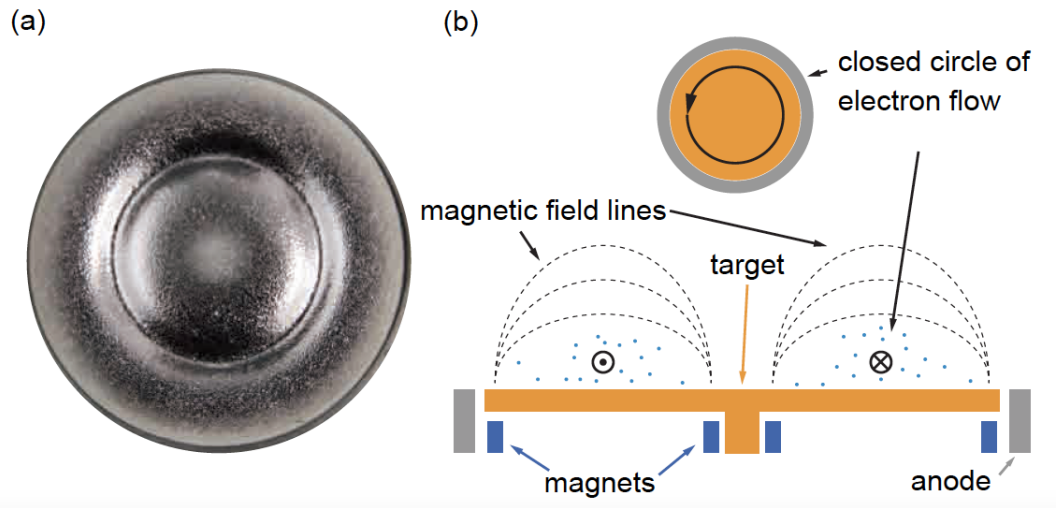

Fig. 3.2: (a) The gadolinium (Gd) target used for the magnetron sputtering process. (b) The electrons are kept on a ring-shaped orbit by the magnetic field of the magnets below the Gd target. Adapted from Ref. [51].

Figure 3.2 (b) shows the magnetron consisting of several magnets installed under the target material (see Fig. 3.2 (b)). This arrangement creates a ring-shaped magnetic field and leads to a circular wear of the gadolinium target (see Fig. 3.2 (a)). The magnetic field constricts the electrons in a ring-shaped path around the target. Hence, significantly more argon atoms can be ionized in this case and a higher deposition and sputtering rate R is obtained than with direct voltage (DC) sputtering. In the reactive cathode sputtering, we add a reactive gas (e.g. oxygen or nitrogen) to the pure inert gas (e.g. argon) [50, 51]. In order to produce gadolinium nitride thin films, we add nitrogen as a reactive gas to the argon inert gas. The reactive gas first nitrates the surface of the target material and forms radicals in the plasma, which react with the released target particles. Hence, in our deposition process the plasma consists of positive charged Ar^+ ions, negative electrons and positive and negative nitrogen ions. Here, the negative nitrogen ions are accelerated in the direction of the substrate because the magnetic field generated by the magnetron does not completely enclose them. It is important to note, that the physical properties of the substrate or target surface are influenced in the reactive sputtering process. Consequently, another process parameter to be optimized is the ratio of argon inert gas to nitrogen reactive gas, the so-called N_2/Ar gas flow ratio [50, 51].

3.2 SUPERBOWL

In this master´s thesis, we fabricate gadolinium nitride (GdN) thin films in the sputtering system SUPERBOWL (SB). In the two-chamber deposition system, we coat substrates in an ultra-high vacuum (UHV) at a base pressure of $\approx 10^{-9}$ mbar. Figure 3.3 shows the overall schematic of the sputtering system with the two separately operated vacuum chambers SP2 (non-ferromagnetic or superconducting targets) and SP4 (ferromagnetic targets).

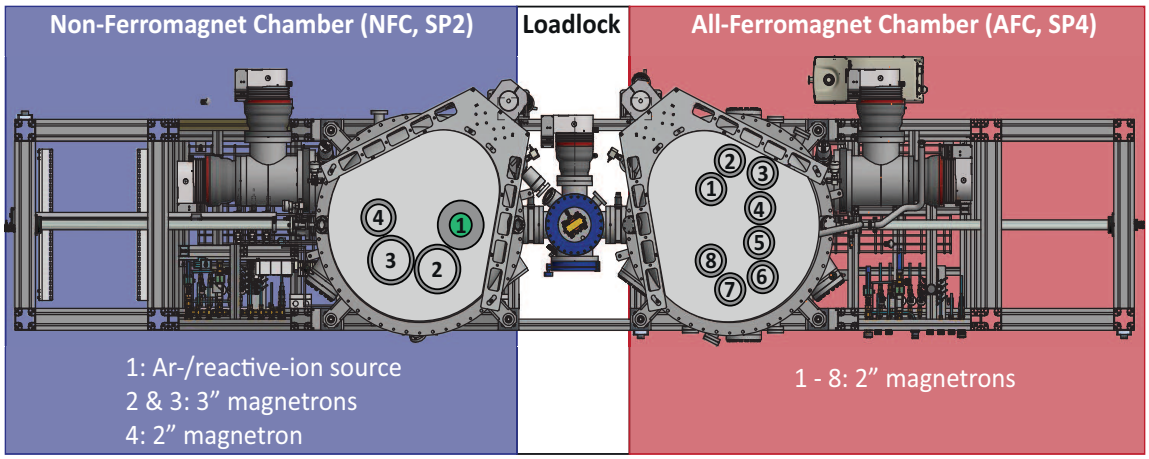

Fig. 3.3: Setup of the two-chamber cathode sputtering system SUPERBOWL. Taken from Ref. [51].

The sputtering chamber SP4 contains two clusters each with four 2 inch sources and in the chamber SP2 two 3 inch sources and one 2 inch source are installed [50, 51]. Furthermore, all sources are equipped with a magnetron [50, 51]. Both sputtering chambers are connected to each other via a loading lock, which can hold up to six sample holders. The substrates mounted on a sample holder are transfered via the load lock, which is completely shielded from the two chambers SP2 and SP4 via a gate valve and an independent vacuum system, into the sputtering system [50, 51]. In this way, a simultaneous deposition in both sputtering chambers is possible. The substrate holder is transferred manually with a transfer arm from the load lock into the vacuum chamber. Afterwards, the substrate to be coated is placed on the substrate stage and heated to a temperature of up to $\approx 850\,^{\circ}\mathrm{C}$ by using a ceramic radiant heater with a heating power of 1.5 kW [50, 51]. The substrate temperature has a significant influence on the crystalline growth of the layers, because it governs the kinetic energy of the target particles, deposited on the sample surface. At high kinetic energies, they can rearrange and form crystalline lattices on the substrate surface. Therefore, the deposition temperature T_{depo} is another process parameter to be optimized [50, 51]. In addition, the sputtering pressure p_{depo} during the deposition process has an impact on the quality of the deposited film because the pressure in the vacuum chamber affects the mean free path of the sputtered particles and ultimately the size of the particle complexes arriving on the substrate.

In several variation series with regard to the optimization of the deposition parameters, we fabriacte the GdN thin films in the „confocal“/„tilt-in“ sputtering configuration (see Fig. 3.4 (b)) in the SP4 chamber (see chapter 5). Figure 3.4 (b) shows the „confocal“ and „face-to-face“ sputtering configurations of the magnetrons and the substrate to be coated in the SP4 used for the manufacturing process. The „confocal“ or „tilt-in“ arrangement of the three magnetrons of the sputtering chamber SP2 is shown in image 3.4 (a).

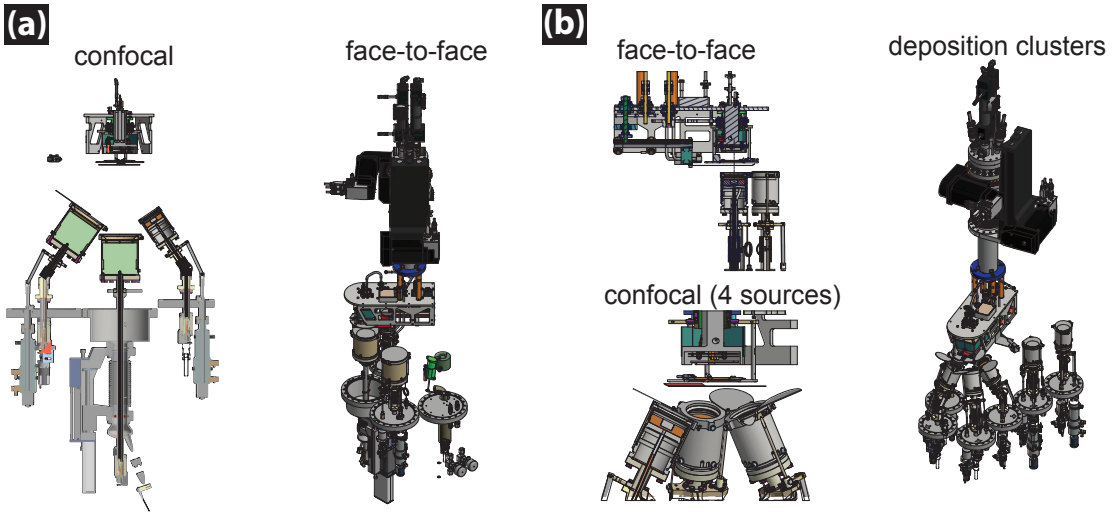

Fig. 3.4: Arrangements of the magnetrons of the SUPERBOWLS: (a) Arrangement of the three magnetrons of the SP2 and (b) Arrangement of the eight magnetrons of the SP4. Taken from Ref. [52].

After the substrate has been heated, the nitrogen-argon gas mixture is inserted into the evacuated chamber and a plasma is ignited using a DC voltage source with a maximum output power of 1 kW [50, 51]. Here, the N_2/Ar gas flow ratio has a major influence on the deposition process, because in addition to the argon inert gas, the additionally supplied reactive nitrogen gas reacts with both the sputtered tantalum particles and the target itself and nitrates it. As a result of the nitration of the target, there is a change in its chemical composition and thus the electrical conductivity is influenced [50]. Furthermore, the deposition rate R changes, when we vary the N_2/Ar gas flow ratio. After the insertion of the reactive gas mixture, the reactive direct current (DC) magnetron sputtering process (see Sec. 3.1) takes place. After the deposition process, the sample, which has cooled down to room temperature, is lifted off the substrate plate and transferred to the load lock by using the transfer arm. Finally, we vent the LL to remove the GdN sample from the sputtering system.

3.3 Fabrication of gadolinium nitride (GdN)

Gadolinium nitride (GdN) is a gadolinium-nitrogen compound. The chemical element gadolinium (Gd) is part of the lanthanide series in the periodic table and is one of the so-called rare earth (RE) metals. Furthermore, Gd is a silvery-white ductil metal that crystallizes in a hexagonal close packed (hcp) structure. Regarding its magnetic properties, Gd exhibits a Curie temperature T_C=292.5 K [53] and above this temperature it is paramagnetic. In this master´s thesis, we study the ferromagnetic insulator (FMI) gadolinium nitride (GdN), which exhibits a Curie temperature varying greatly between different publications ranging from 20 K to 70 K [54],[55],[56],[57],[58] and is considered as a suitable FMI candidate for the implementation of spintronic devices [17],[14]. Therefore, we fabricate GdN thin films in a reactive direct current (DC) magnetron sputtering process. As published in Ref. [54],[59],[60], GdN crystallized in a sodium chloride (NaCl) structure with a face-centered-cubic (fcc) unit cell and a lattice constant of a_{lattice}=4.98 Å (see. Fig. 3.5).

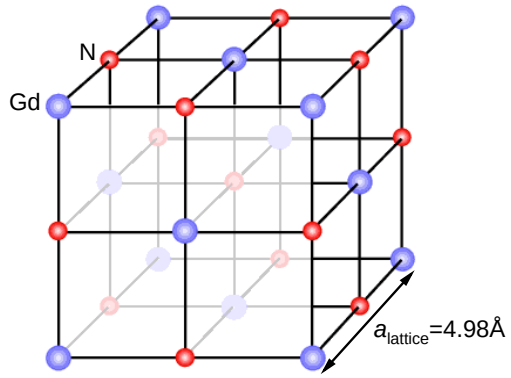

Fig. 3.5: Gadolinium nitride (GdN) in a sodium chloride (NaCl) structure with a face-centered-cubic (fcc) unit cell and a lattice constant of a_{lattice}=4.98 Å. Taken from Ref. [61].

As a next step, we discuss the magnetic ordering mechanisms in GdN depicted in Fig. 3.6.

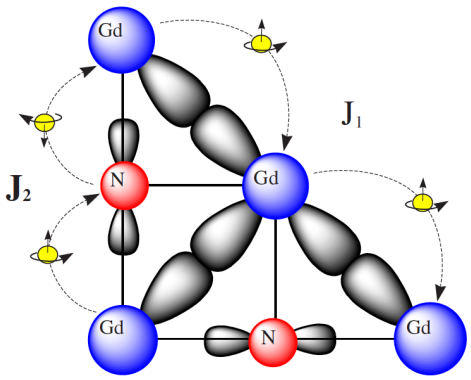

Fig. 3.6: Magnetic odering mechanisms of GdN: Direct ferromagnetic (FM) exchange interaction J_1 between the nearest-neighbor Gd ions generated by the direct overlap of the 5d-t_{2g} orbitals and a indirect antiferromagnetic (AFM) exchange interaction J_2 between the next-nearest neighbor Gd ions conveyed by a superexchange of the 5d-e_g and the N 2p orbitals. Taken from Ref. [62].

Fig. 3.6 illustrates the magnetic ordering mechanisms of GdN. As discussed in the PhD-thesis of *F. Leuenberger* [62], the magnetic coupling in rare earth (RE) metals can be explained with the theoretical model of Ruderman-Kittel-Kasuya-Yosida (RKKY) [63],[64],[65]. In a RE metal, there is a RKKY exchange via the conduction electrons in the s, p, d bands [62]. The mechanism of magnetic exchange interaction in a RE semiconductor such as GdN is discussed in the work of *S. Methfessel* [66] and *F. Leuenberger* [62] and can be simplified in a localized Heisenberg picture (see Fig. 3.6) as published in [67],[68],[69],[70]. Here, the magnetic characteristics of GdN is explained by a direct ferromagnetic (FM) exchange interaction J_1 between the nearest-neighbor Gd ions and a indirect antiferromagnetic (AFM) exchange interaction J_2 between the next-nearest neighbor Gd ions via the N orbitals [62]. The FM coupling J_1 originates from the direct overlap of the 5d-t_{2g} orbitals and the indirect AFM coupling J_2 resultes from the so-called superexchange of the 5d-e_g and the N 2p orbitals [59],[62],[67].

Following this model, GdN has a dual phase in terms of its magnetic ordering mechanisms, which has been experimentally investigated by *K. Senapati et al.* [54]. They studied the relationship between the magnetic properties, such as the saturation magnetization $\mu_0 M_s$ and the ferromagnetic Curie temperature T_C, of GdN and its magnetic ordering mechanisms depending on the varying growth parameters of the thin films (see Fig. 5(a) in [54]). For a Curie temperature up to T_C=60 K, GdN thin films are grown in the so-called N-rich zone (Zone 1) with a ferromagnetic (FM) ordering [54]. In Zone 2 (60 K<T_C<120 K), a nitrogen deficiency manifests in the GdN thin film giving rise to a secondary phase of GdN (GdN-II) with an antiferromagnetic (AFM) behavior governed by N vacancies as they increase the effective a_{lattice} (see. Fig. 3.7) and thereby reduced the direct exchange coupling mechanism and thus lowering the magnitude of J_1 [54]. Within this vacancy region, J_2 becomes the dominant contribution and the Gd moments order in antiparallel fashion. Consequently, there is an exchange bias in Zone 2, which is caused by the coupling of a FM and an AFM ordering mechanism of GdN [54].

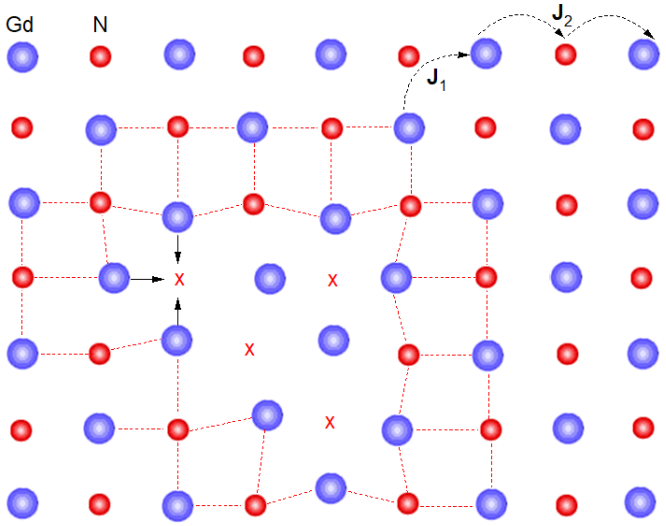

Fig. 3.7: Two-dimensional face-centered-cubic (fcc) lattice of GdN: Nitrogen (N) vaccancies (red crosses) are responsible for the lattice distortion which generates a secondary phase in GdN (GdN II, red dashed lines) with an AFM ordering. Taken from Ref. [54].

Figure 3.7 illustrates the local lattice distortion (see red dashed lines) in a two-dimensional face-centered-cubic (fcc) lattice caused by nitrogen vacancies, which are mainly responsible for the AFM behavior in GdN [54]. In chapter 5, we optimize the growth of GdN thin films with regards to their magnetic properties, such as the saturation magnetization $\mu_0 M_\mathrm{s}$, the coercive field $\mu_0 H_\mathrm{c}$ and the ferromagnetic Curie temperature T_C. As a fist step, we here discuss suitable substrates for the deposition of gadolinium nitride (GdN) thin films. Here, the substrate materials have a significant impact on the growth process of the sputtered material and ultimately determines the quality of fabricated the thin films. Due to the successful experiments of *K. Senapati et al.* [54], we deposite the GdN thin films on a $(6 \times 10 \times 0.55)\,\mathrm{mm}^3$ silicon (Si) substrate with a thermally oxidized SiO_2 (d=1 μm) top layer. In order to avoid GdN from oxidation [12],[54] and to investigate the magnetotransport properties (see chapter 6) in a ferromagnetic insulating (FMI)/normal conducting (NC) bilayer, we deposite the GdN thin film (d=60 nm) between a top and bottom buffer layer of normal conducting (NC) tantalum nitride (TaN) (d=20 nm) on the Si/SiO_2 substrate with a [100]-orientation. For the fabrication of NC TaN in the „face-to-face“ sputtering configuration (see Fig. 3.4 (a)) in the chamber SP4, we use the growth recipe (N_2/Ar=10 %, T_depo=500 °C, P_depo=30 W, $p_\mathrm{depo}=5 \times 10^{-3}$ mbar) which was developed in my bachelor´s thesis *Growth optimization of superconducting tantalum nitride (TaN) thin films for advanced spin electronics* [18]. To verify the optimized growth recipe of FM TaN/GdN/TaN thin films on its reproducibility, we investigate the growth of the trilayer on a crystalline sapphire (Al_2O_3) substrate as well as on further Si/SiO_2 substrates. Furthermore, in Chapter 4, we examine its resistive properties (see orange curve in Fig. 4.2) by performing electrical transport measurements (see Sec. 4.1) in the Van-der Pauw geometry (see Sec. 4.2).

3.4 Fabrication of Hall-bar (HB) patterned GdN thin films

This section deals with the description of the structuring process of Hall-bars from the GdN/TaN multilayer heterostructures (see Sec. 6.2.1, 6.2.2 and 6.2.3) which we use to perform the field-dependent magnetotransport- (see Sec. 6.2.4, 6.2.5, 6.2.6) and the angle-dependent magnetoresistance (ADMR) (see Sec. 6.2.7) experiments. Our GdN/TaN multilayer thin films are patterned into Hallbar (HB) structures by using high resolution photolithography, which involves the following steps: First, we cover the sample surface with an optical resist layer (AZ MIR 701 from *MicroChemicals*). Thereafter, we pattern up to 6 HB pairs into the resist by using the laserwriting system *PicoMaster200*, which works with a UV laser power of around 100 μW and a focus-sum-voltage between 3 V and 4 V, see also Ref. [27]. After UV exposure, the exposed resist is removed using the developer AZ 726 MIF from *MicroChemicals* for 60s. As a next step, we perform an etching process with the use of an Argon ion milling gun at an etching rate of ≈4 nm/min. The operation principle and the technical properties as well as the fundamental physics of ion beam etching (IBE) and milling with inert gases are described in Ref. [71] by *Oxford Instruments*. Afterwards, we remove the protective layer from of the sample using the resist stripper P1331 from *Micro-Chemicals*. Here, the removal process takes place in a timeframe of approximately 10 min bath of P1331 at a processing temperature of T=80 °C.

Figure 3.8 illustrates the resulting Hall-bar structures in an optical microscope image. Here, we observe a Hall-bar pair rotated by 90° patterned on a GdN/TaN multilayer thin film and the geometrical dimension of one Hall-Bar is defined by the width w_{HB}=76 μm and the length l_{HB}=622 μm.

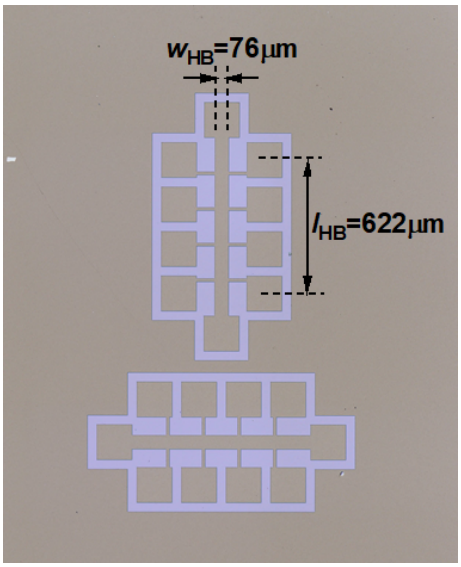

Fig. 3.8: Depiction of the finalized Hallbars patterned into our GdN/TaN heterostructures: Hall-bar pair rotated by 90° patterned on a GdN/TaN multilayer thin film by using photolithography. The geometrical dimension of one HB is defined by w_{HB}=76 μm and l_{HB}=622 μm.

To perform the magnetotransport experiments, we glue the HB patterned sample onto a chip carrier by using low temperature GE varnish and then we contact the HB-arms to the Cu pads of the chip carrier frame by thin-wire bonding with an Al wire (see Fig. 4.3 (b)).

3.5 Characterization of the GdN samples

In this section, we describe the experimental procedure for the investigation of the structural properties of our GdN thin films in particular the crystal structure by performing X-ray diffraction (XRD) spectroscopy. The principles of XRD spectroscopy have already been described in great detail in several works and thesies at WMI [50],[51]. We here only briefly summarize the main principles of these experimental techniques.

3.5.1 X-ray diffraction (XRD)-scans

To analyze the structural properties of our GdN thin films, we use two different measurement methods: The layer thickness of the deposited thin films and their surface roughness are determined by performing reflectometry measurements. Furthermore, we study the crystalline properties of GdN by using X-ray diffraction (XRD) measurements. In both cases, the sample is installed in a 4-axis X-ray diffractometer and we use the wavelength λ=1.54 Å of the copper $K_{\alpha 1}$ line [50]. The detailed functionality and the physical principles of X-ray diffractometry (XRD) are described for example in the work of *A. A. Bunaciu et al.* [72].

We investigate the crystalline structure of our GdN samples using X-ray diffraction (XRD)-scans. For greater detailed informations on the principles of X-ray reflections at crystals, see the work of *W. H. Bragg et al.* [73] and *A. M. Glazer* [74]. Basically, in this analysis method, the condition for constructive interference of the incident and reflected X-rays - reflected from the lattice planes of a crystal - is given by the so-called Bragg condition

$$2d_{hkl}sin(\omega) = \lambda, \tag{17}$$

where the diffracted X-rays interfere constructively under the angle of incidence ω. Here, d_{hkl} represents the distance of the lattice planes and h,k,l defines the Miller indices. Considering of GdN owns a cubic crystall system- / crystallized in sodium chloride (NaCl) structure with a face-centered-cubic (fcc) unit cell (see Sec. 3.3), we find for the distance of the lattice planes d_{hkl} the following equation

$$d_{hkl} = \frac{a}{\sqrt{h^2 + k^2 + l^2}}, \tag{18}$$

where a defines the lattice constant of the deposited GdN thin film [50].

Figure 3.9 represents the rotational degrees of freedom in our 4-axis X-ray diffractometer. To record a coupled 2θ-ω scan to identify crystalline phases, we align the system to a substrate reflection and utilize the extracted sample misalignment with respect to the XRD coordinate system. Afgter the alignment procedure, full range 2θ-ω scans can be conducted to check for crystalline film reflections [50]. Characteristic XRD spectra are shown in Fig. 5.3, 5.7 (a)-(c), 5.13 (a)-(c) and 5.18 for the deposition of our TaN/GdN/TaN thin films on different substrates like Si/SiO_2 or Al_2O_3.

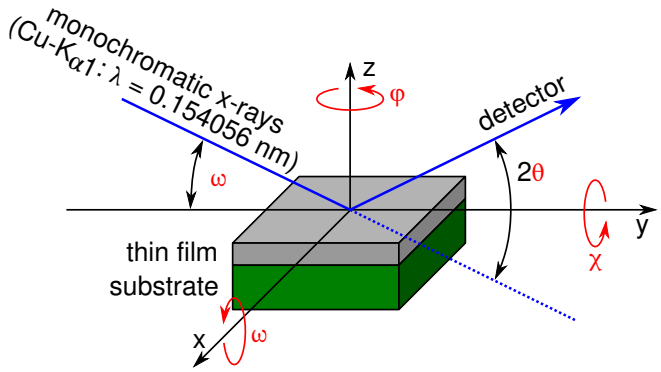

Fig. 3.9: Principle of 2θ-ω-scans: Relationship of the different angles of incidence. Taken from [50].

4 Experimental measurement techniques

This chapter deals with the description of the experimental measurement methods to determine the electrical transport properties as well as the magnetotransport characteristics of various GdN thin films. The principles of the transport measurement methods have already been described detailed in several works and thesis at WMI ([50],[51]). Furthermore, we detail the operation principles of the SQUID magnetometer, which we use to investigate the magnetic properties of our GdN thin films.

4.1 Electrical transport measurement

To investigate the electrical transport properties of our GdN thin films, we perform electrical transport experiments on unpatterned thin films in the Van-der-Pauw geometry [75], as described for example in the work of *M. Reichert* [50] and *A. Faltermeier* [51]. This measurement method allows us to investigate the normal conducting (NC) or insulating (I) properties of our GdN thin films. Before we measure the GdN samples, we first cleave the unpatterned samples, such as the optimized ferromagnetic (FM) TaN/GdN/TaN reference sample (see Fig. 4.2 and Tab. 5.2) as well as the ferromagnetic insulating (FMI) AlN/GdN/AlN heterostructure (see Sec. 6.1 and Tab. 6.1), into smaller pieces with a diamond tip and then glue the smaller pieces onto a chip carrier by using low temperature GE varnish. As a next step, we contact the samples to the chip frame by thin-wire bonding with an aluminum wire. Afterwards, we start a so-called four-point measurement for measuring the resistivity ρ [$\mu\Omega$·cm] of the thin film [50, 51]. To control the sample temperature during the measuring procedure, we placed the sample on a dipstick, which is installed in a liquid helium cryostat, namely the so-called *MORIA* cryostat. Here, we are able to perform transport measurements in a temperature range of (2-300) K and a magnetic field range of (0-7) T. Figure 4.1 shows the fundamental operation principle of the four-point measurement / four-wire measurement in a cryostat.

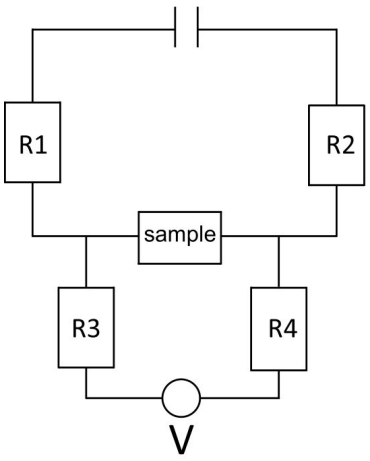

Fig. 4.1: Functionality of the four-point measurement / four-wire measurement in a T-adjustable cryostat. Taken from Ref. [50].

In Fig. 4.1, the resistances R1 and R2 represent the wire resistances of the measurement dipstick in the cryostat. The resistances R3 and R4 are the summation of the line resistances and the input resistances of the voltmeters [50].

Accounting for the high input resistance of the voltmeter as compared to sample resistance, the measured voltage is given by the sample [51]. In addition, we use a *current reversal method* in which the polarity of the applied direct current is swept during the measurement. Here, we obtain the odd in current polarity contribution, which we refer to as the ohmic contribution, by [51]

$$V = \frac{V_+ - V_-}{2}. \tag{19}$$

In Eq. (19), $V_\pm$ defines the measured voltage values for positive or negative current polarity [50]. Using the current reversal method, the electrical transport measurement runs in the following steps: The samples, first cooled to a temperature of $T<T_\mathrm{C}$, are slowly heated up to room temperature at a rate of about 5 K/min to study the evolution of the resistivity ρ of our samples as a function of the temperature T [51]. Finally, we calculate the resistance of a GdN thin film from the measured voltage values by using Ohm's law

$$R = \frac{U}{I}. \tag{20}$$

4.2 Van-der-Pauw-measurement method and *RRR*-ratio

To calculate the resistivity ρ [$\mu\Omega$·cm] from the measured ohmic resistance R [Ω] of the unpatterned GdN thin films, we use the so-called Van-der-Pauw (VdP)-measurement method [75] which is given by

$$\rho = \frac{\pi d}{\ln(2)} \cdot R \simeq 4.532 \cdot d \cdot R. \tag{21}$$

In Eq. (21), d defines the layer thickness of the thin film and R represents the measured resistance between the contacts [50]. For the longitudinal and transversal resistivity ρ of our Hall-bar (HB), we calculate ρ_{long} and ρ_{trans} from the measured ohmic resistance R and the geometric dimensions of the Hall-bar using Eq. (22) and (23) from Ref. [30], w_{HB} and l_{HB} defines the width and the length of the Hall-bar (see Fig. 3.8) and d represents the layer thickness the conductive TaN layer

$$\rho_{\mathrm{long}} = R_{\mathrm{long}} \cdot \frac{A}{l_{\mathrm{HB}}} = R_{\mathrm{long}} \cdot \frac{w_{\mathrm{HB}} \cdot d}{l_{\mathrm{HB}}}, \tag{22}$$

$$\rho_{\mathrm{trans}} = R_{\mathrm{trans}} \cdot \frac{A}{w_{\mathrm{HB}}} = R_{\mathrm{trans}} \cdot \frac{w_{\mathrm{HB}} \cdot d}{w_{\mathrm{HB}}} = R_{\mathrm{trans}} \cdot d. \tag{23}$$

Figure 4.2 shows the results of the electrical transport measurement with the VdP method of the optimized TaN/GdN/TaN reference sample (see Sec.5.2 and 5.3 and Tab. 5.2) measured in a zero field $\mu_0 H_{\mathrm{ext}}$ at I_{meas}=30 μA.

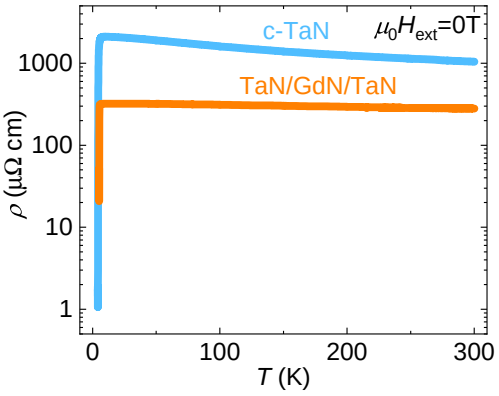

Fig. 4.2: Electrical resistivity ρ of our samples as function of temperature T recorded using the the Van-der-Pauw method: The sample TaN/GdN/TaN (see orange curve) exhibits a nearly constant electrical resistance of R≈17 Ω in the T-region 10 K<T<300 K as well as a partially superconducting (SC) transition in the area of low temperatures. For the sample c-TaN (see blue curve) is an average resistance of R≈55 Ω in 10 K<T<300 K and a slight increase of ρ with a SC transition close by low temperatures visible.

Figure 4.2 illustrates the electrical resistivity ρ on a logarithmic scale as a function of the temperature T by performing the electrical transport measurement (see Sec. 4.1) in the VdP geometry (see Sec. 4.2). Here, we observe for the TaN/GdN/TaN sample (see orange curve in Fig. 4.2) and almost constant electrical resistance of R≈17 Ω in the T-range 10 K<T<300 K and a superconducting (SC) transition for TaN at low temperatures.

The blue curve in Fig. 4.2 represents the reference sample TaN-09 (d=60 nm), called c-TaN, in the cubic-phase which was measured in my bachelor´s thesis ([18]). Here, we extract a SC temperature of T_C=5.05 K and we observe an average electrical resistance of R≈55 Ω in the T-range 10 K<T<300 K as well as a slight increase of the resistivity ρ towards to low temperatures.

As a next step, we calculate the so-called *RRR*-ratio (Residual Resistance Ratio), see Eq. (24) [50], to investigate the electrical transport properties of TaN thin film

$$RRR = \frac{R_{20}}{R_{300}} = \frac{\rho_{20}}{\rho_{300}}. \tag{24}$$

In Eq. (24), the *RRR*-ratio is defined as the quotient of the resistance R_{20} at a temperature of T=20 K and the resistance R_{300} at T=300 K [50]. To prevent the TaN layers of our TaN/GdN/TaN thin films from growing in an *N-rich-compounds-phase* and with the intention that the TaN layers would be deposited with normal conducting properties in the *N-deficient-phase*, we fabricated the samples at a N_2/Ar gas flow ratio of 10 %. However, we observe for our TaN/GdN/TaN sample (see orange curve in Fig. 4.2) a superconducting (SC) transition at a temperature of T_{SC}≈5 K, which we associated with a N-diffusion from the GdN thin film into the TaN top (20 nm) and bottom (20 nm) buffer layer due to the nitrogen (N) lability of the gadolinium nitrogen (GdN) compound (see Sec. 3.3). Afterwards, we calculated with Eq. (24) a *RRR*-ratio=1.21 for the TaN/GdN/TaN sample (see orange curve in Fig. 4.2), which indicates that our sample grew nearly in a transition phase between the *N-deficient-phase* (*RRR*<1.25) with normal conducting (NC) characteristics and the *cubic-phase* (1.25<*RRR*-ratio<2.69) with also partially superconducting (SC) properties, see Ref. [18]. In comparison with the results of my bachelor´s thesis [18], the SC temperature T_{SC} and the *RRR*-ratio of the TaN/GdN/TaN sample (see orange curve in Fig. 4.2) are comparable with T_C=5.05 K and *RRR*=1.82 of the reference sample c-TaN (see blue curve in Fig. 4.2). In this master´s thesis we are mainly interested in the growth optimization of FM GdN thin films as well as on the investigation of the magnetotransport properties of GdN/TaN multilayer heterostructures. Therefore, it is sufficient to estimate the SC temperature T_{SC} of the samples from the $\rho(T)$-plot. For an exact determination of T_{SC} and the transition width ΔT_{SC}, see Sec. 3.3 in my bachelor´s thesis [18].

4.3 Magnetotransport measurements

To study the field-dependent magnetotransport properties (see Sec. 6.2.4, 6.2.5, 6.2.6) and the angle-dependent magnetoresistance (ADMR) (see Sec. 6.2.7) of several Hall-bar (HB) patterned GdN/TaN multilayer heterostructures (see Sec. 6.2.1, 6.2.2 and 6.2.3), we perform magnetotransport experiments in the cryostat *MORIA*. Figure 4.3 shows exemplary a Hall-bar (HB) patterned from a GdN/TaN thin film grown on a Si/SiO_2 substrate.

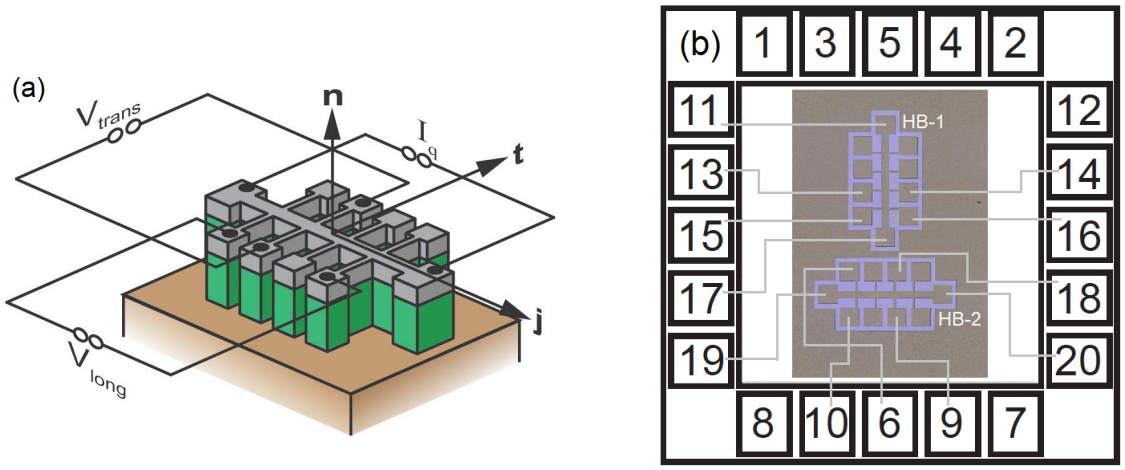

Fig. 4.3: (a) Measurement geometry of the Hall-bar (HB) patterned GdN (green layer)/TaN (grey layer) bilayer on a Si/SiO_2 substrate (brown layer) in a **n**, **j**, **t** coordinate system. Taken from Ref. [30]. (b) Hall-bar pair rotated by 90° patterned on a GdN/TaN multilayer thin film: Bonding scheme and pin assignment on the Cu pads of the chip carrier frame.

Figure 4.3 (a) shows the measurement geometry of the Hall-bar (HB) patterned GdN/TaN heterostructure in a **n**, **j**, **t** coordinate system, where **n** represents the normal vector perpendicular to the sample plane, **j** defines the vector parallel to the applied current I_q and **t** is perpendicular to it. To study the magnetoresistive properties of our GdN/TaN multilayer heterostructures, we glue the HB patterned sample as a whole piece onto a chip carrier and then we contact the HB-arms to the Cu pads of the chip frame by thin-wire bonding with an aluminum wire (see Fig. 4.3 (b)). Afterwards, we measure the voltage drop along V_{long} as well as perpendicular V_{trans} to the applied current I_q=200 μA by performing electrical transport experiments with the current reversal method (see Sec. 4.1).

4.3.1 Field-dependent magnetoresistance (FDMR) measurements

For our *field-dependent magnetotransport experiments* (see Sec. 6.2.4, 6.2.5, 6.2.6), we analyze the resistance R of several HB patterned GdN/TaN multilayer samples, which are mounted on the chip carrier in the cryostat, under varying external magnetic fields $\mu_0 H_{ext}$ and at different fixed temperatures T. Here, we apply an external magnetic field $\mu_0 H_{ext}$ which is varied from -7 T to +7 T in 0.2 T steps and measure the resistance R of the sample at each of the individual magnetic fields. Afterwards, we calcualte the longitudinal symmetric as well as the transversal antisymmetric component of the magnetotransport signal by using the expression [76]

$$\rho_{long}^{symm}(H) = \frac{\rho_{long}(H\downarrow) + \rho_{long}(-H\uparrow)}{2} \tag{25}$$

and [76]

$$\rho_{\mathrm{trans}}^{\mathrm{antisymm}}(H) = \frac{\rho_{\mathrm{trans}}(H\downarrow) - \rho_{\mathrm{trans}}(-H\uparrow)}{2}, \tag{26}$$

where $H\downarrow$ represents the down-sweep ($\downarrow$) resulting from the fieldsweep from $+H_{\mathrm{max}}$ to $-H_{\mathrm{max}}$ and $H\uparrow$ defines the up-sweep ($\uparrow$) originating from the fieldsweep from $-H_{\mathrm{max}}$ to $+H_{\mathrm{max}}$ in the entire field-range [76]. The magnetotransport measurements are performed at an external magnetic in-plane (ip) field (field lines **h** perpendicular to the normal vector **n** of the thin film) and at an external out-of-plane (oop) magnetic field (field lines **h** parallel to the normal vector **n** of the sample). To investigate the field-dependent magnetoresistance of various HB patterned GdN/TaN multilayer thin films in the three field geometries such as in-plane (ip) (**h**$\|$**j**) and (**h**$\|$**t**) as well as out-of-plane (oop) (**h**$\|$**n**) in two measurement runs, we have patterned two Hall-bars rotated by 90° on the sample and bonded them to the Cu contacts on the chip frame (see Fig. 4.3 (b)).

4.3.2 Angle-dependent magnetoresistance (ADMR) measurements

For our *angle-dependent magnetoresistance* (ADMR) *experiments* (see Sec. 6.2.7), we use the basic principles of the electrical transport measurement (see Sec. 4.1) and determine the resistance R of several Hall-bar (HB) patterned GdN/TaN multilayer heterostructures at I_{q}=50 μA. Here, we perform T-sweeps from 5 K to 50 K in 1.5 K steps at a fixed magnetic field of $\mu_0 H_{\mathrm{ext}}$=7 T (see Sec. 6.2.8) as well as H-sweeps from 0.5 T to 7 T in 0.5 T steps at several fixed temperatures T (see Sec. 6.2.9). To determine the ADMR, we perform the H- and T-sweep series by rotating the measurement dipstick from 0° to 360° in 5°-steps in the *MORIA* cryostat using a stepper motor. Here, we measure also two Hall-bars rotated by 90° (see Fig. 4.3 (b)) patterned on the GdN/TaN multilayer thin films to investigate the ADMR in the three different field geometries (see. Fig. 4.4 (a)-(c)) by performing two separate measurements. The orientation of the magnetic field **H** in the **n**, **j**, **t** coordinate system under the varying angle α, β, γ in the field geometry in-plane (ip) (**H** rotates in the **j**-**t** plane $\perp$ to **n**, see Fig. 4.4 (a)), out-of-plane-j (oopj) (**H** rotates in the **n**-**t** plane $\perp$ to **j**, see Fig. 4.4 (b)) and out-of-plane-t (oopt) (**H** rotates in the **n**-**j** plane $\perp$ to **t**, see Fig. 4.4 (c)) are shown in Figure 4.4 (a)-(c) as well as in Table 4.1.

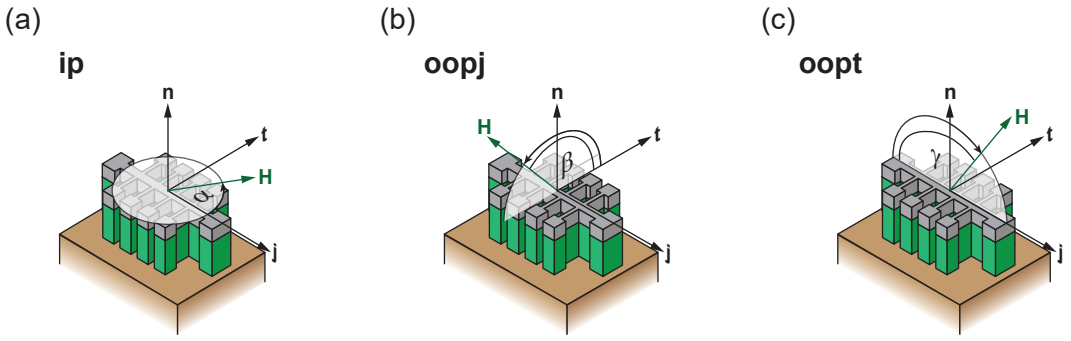

Fig. 4.4: Field geometries of the ADMR measurements: (a) in-plane (ip) (**H** rotates in the **j**-**t** plane $\perp$ to **n**). (b) out-of-plane-j (oopj) (**H** rotates in the **n**-**t** plane $\perp$ to **j**). (c) out-of-plane-t (oopt) (**H** rotates in the **n**-**j** plane $\perp$ to **t**). Adapted from Ref. [30].

	0°	90°	180°	270°	360°
ip (α=$\sphericalangle_{\mathbf{j},\,\mathbf{t}}$)	**H**$\|$**j**	**H**$\|$**t**	**H**$\|$**-j**	**H**$\|$**-t**	**H**$\|$**j**
oopj (β=$\sphericalangle_{\mathbf{n},\,\mathbf{t}}$)	**H**$\|$**t**	**H**$\|$**n**	**H**$\|$**-t**	**H**$\|$**-n**	**H**$\|$**t**
oopt (γ=$\sphericalangle_{\mathbf{n},\,\mathbf{j}}$)	**H**$\|$**-j**	**H**$\|$**n**	**H**$\|$**j**	**H**$\|$**-n**	**H**$\|$**-j**

Tab. 4.1: Orientation of the magnetic field **H** in the ADMR measurement geometries in-plane (ip), out-of-plane-j (oopj) and out-of-plane-t (oopt) under rotating the angles α, β, γ.

4.4 SQUID magnetometry

To investigate the static magnetic properties, such as the saturation magnetization $\mu_0 M_s$, the coercive field $\mu_0 H_c$ and the ferromagnetic Curie temperature T_C, of the GdN thin films, we use a SQUID (superconducting quantum interference device) magnetometer, which is an established method for precision measurements of extremely small magnetic moments. For the operation principle and the fundamental physics of a SQUID, see the work of S. A. Pranav [77]. The extraction methods of the magnetic parameters of our GdN thin films are discussed in section 5.1.1. Here, we recorded the magnetic hysteresis loops $M(H)$ and the magnetization as a function of the temperature T, the so-called $M(T)$-curves, with a SQUID magnetometer from the manufacturer *Quantum Design* (see Ref. [78]), which operates in a magnetic field range from -7 T to +7 T and at temperatures T between 1.8 K and 400 K. Figure 4.5 shows the experimental setup and the basic operation principle of the SQUID magnetometer.

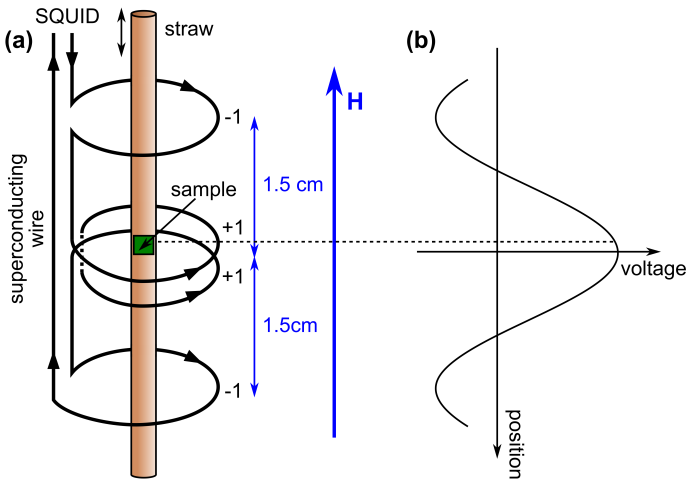

Fig. 4.5: (a) Setup of the SQUID magnetometer (*second order gradiometer*) consiting of two outer SC coils (clockwise wounded (-1)) and a middle SC coil (counterclockwise double wounded (+1)) and an applied external magnetic field $H \parallel$ to the GdN sample fixed in the straw. (b) Voltage, converted from the induced current due to the sample movement between the SC coils in the external magnetic field H, as a function of the sample position. Taken from Ref. [79].

In the SQUID measurement setup shown in Fig. 4.5 (a), we fix the GdN sample in the middle of a straw (see brown rod in Fig. 4.5 (a)) and place it between helium cooled superconducting (SC) detection coils where the top and bottom coil consits of a single twisted wire (clockwise wounded (-1)) and the intermediate coil is fabricated of a double twisted wire (counterclockwise wounded (+1)) [79]. The detection setup with the SC coils (see Fig. 4.5 (a)) represents a so-called *second order gradiometer*. During the measurement, the straw with the fixed GdN sample is moving up and down between the SC coils at an applied external magnetic in-plane (ip) field (**H** perpendicular to the normal vector **n** of the thin film) [79]. Due to the sinusoidal movement of the sample, a current is induced in the SC loops which is converted into a voltage by using a radio frequency (RF) SQUID [79]. Figure 4.5 (b) shows the extracted voltage, fitted by a software developed by *Quantum Design*, as a function of the sample position [79]. Afterwards, the magnetic moment m of the GdN thin film is calculated automatically by the *Quantum Design* software (see *F. M. Schade* [79]).

5 Growth optimization of ferromagnetic GdN thin films

In the following chapter, we present the results of the growth optimization for the growth of the ferromagnetic insulator (FMI) gadolinium nitride (GdN) on thermally oxidized Si substrates in the SUPERBOWL with regards to their magnetic properties and Curie temperature T_C. To this end, in individual deposition series we sequentially optimized the deposition parameters such as the N_2/Ar gas mixture ratio [%], the deposition rate R [Å/s] controlled by the sputtering power P_{depo} [W], and the growth temperature T_{depo} [°C]. In order to investigate the correlation between the optimized growth parameters and the crystalline quality and lattice constants of our GdN thin films, we also performed XRD. As a next step, we compare GdN samples grown in the tilt-in (tin) and face-to-face (ftf) sputtering configuration. Finally, we provide insights into the reproducibility of the optimized growth recipe and investigate the growth of a GdN thin film on a crystalline sapphire (Al_2O_3) substrate.

5.1 Data analysis procedure

5.1.1 Extraction of the static magnetic parameters

First, we discuss the determination of the static magnetic parameters, such as the saturation magnetization $\mu_0 M_s$, the coercive field $\mu_0 H_c$ and the ferromagnetic Curie temperature T_C, of the GdN thin films by using SQUID magnetometry (see Sec. 4.4). Exemplary data showing the data analysis procedure to extract the magnetic properties of our GdN thin films are shown in Figure 5.1.

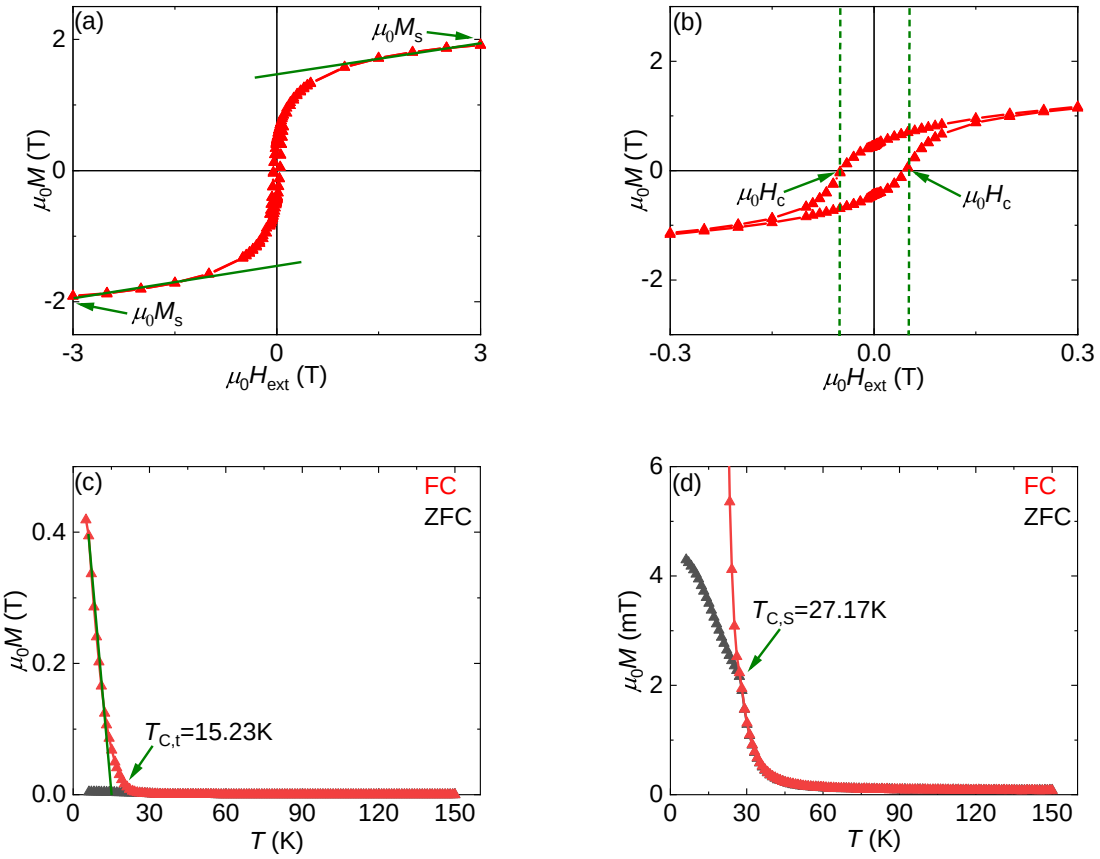

Fig. 5.1: (a) Hysteresis curve $M(H)$ recorded at $T = 5\,\mathrm{K}$ for a GdN thin film grown on a thermally oxidized Si substrate. The saturation magnetization $\mu_0 M_s$ is extracted from tangents to the hysteresis loops in saturation. (b) Zoomed in view of the hysteresis in panel (a) to highlight the magnetic hysteresis . The coercive field $\mu_0 H_c$ is extracted from the x-axis intercepts of $M(H)$. (c) and (d) Magnetization $\mu_0 M$ of the GdN thin film measured as function of temperature up to T=150 K and $M(H)$ curve recorded by cooling down the GdN sample to T=5 K in an applied external magnetic field $\mu_0 H_{ext}$=7 T (field cooled=FC) and at zero magnetic field (zero field cooled=ZFC). (c) Extraction of the Curie temperature $T_{C,t}$ by apply a tangent to the steepest decay of the FC curve and forming the intersection of the tangent with the x-axis. (d) Zoomed in view of the $M(T)$-measruement in panel (c) to highlight the extraction of the Curie temperature $T_{C,S}$ by determining the intersect of the FC and the ZFC curve.

Fig. 5.1 (a)-(d) show the $M(H)$ and $M(T)$ curves recorded by SQUID magnetometry (see Sec. 4.4). Here, the sample under investigation is a GdN thin film wich was grown using the deposition parameters N_2/Ar=20 %, T_{depo}=500 °C, P_{depo}=45W and p_{depo}= 5×10^{-3} mbar.

Panels 5.1 (a) and (b) show the results of the $M(H)$-measurement recorded in the range $\mu_0 H_{\mathrm{ext}}$=-3 T to +3 T at a temperature T=5 K. The observed magnetic hysteresis loop is characteristic for ferromagnetic materials. We determine a saturation magnetization $\mu_0 M_{\mathrm{s}}$=1.91T from the intersection of the tangent to $M(H)$ in the saturated state with the y-axis as shown in panel 5.1 (a). A coercive field $\mu_0 H_{\mathrm{c}}$=46 mT is obtained from the intersection of the magnetic hysteresis with the x-axis (see Fig. 5.1 (b)). The extraction method for these two magnetic parameter as well as the extracted values are comparable to the work of *K. Senapati et al.* [54] and *K. Khazen et al.* [55].

To extract the ferromagnetic Curie temperature T_{C}, we plot the magnetization $\mu_0 M$ of the GdN thin film as a function of the temperature T in Fig. 5.1 (c) and (d). Here, we perform two sequential measurements for $M(T)$. The sample is cooled down to T=5 K both in an applied external magnetic field $\mu_0 H_{\mathrm{ext}}$=7 T (field cooled=FC) and at zero magnetic field (zero field cooled=ZFC) and then the magnetization $\mu_0 M$ of the thin film is measured as function of temperature up to T=150 K. To extract the Curie temperature T_{C}, we apply a tangent to the steepest decay of the FC $M(T)$-curve (see Fig. 5.1 (c)) (see work of *A. Shaib et al.* [56]). The intersection with the x-axis then yields a Curie temperature of $T_{\mathrm{C,t}}$=15.23 K. Another established method to determine the T_{C} of a FM material is to define it as the point, where the FC and ZFC curve of the $M(T)$-measurement intersect (see Fig. 5.1 (d)). This so called intersect method, see work of *K. Senapati et al.* [54], provides a $T_{\mathrm{C,S}}$=27.17 K. To compare both methods, we define ΔT_{C}=$T_{\mathrm{C,S}}$−$T_{\mathrm{C,t}}$ and obtain ΔT_{C}=11.94 K. This value will be discussed in detail in section 5.2.1 and 5.3.1.

It should be noted that the static magnetic paramters, such as the saturation magnetization $\mu_0 M_{\mathrm{s}}$ and the coercive field $\mu_0 H_{\mathrm{c}}$, as well as the ferromagnetic Curie temperature $T_{\mathrm{C,t}}$ and $T_{\mathrm{C,S}}$ of our GdN thin films are determined manually from the $M(H)$- and $M(T)$-curves and not by a fitting function (see Fig. 5.1 (a)-(d)). For this reason, we will not add any error bars to the extracted magnetic parameters in the $\mu_0 M_{\mathrm{s}}(\mathrm{N_2/Ar})-$, $\mu_0 H_{\mathrm{c}}(\mathrm{N_2/Ar})-$ and $T_{\mathrm{C}}(\mathrm{N_2/Ar})-$plots (see Sec. 5.2.1) as well as in the $\mu_0 M_{\mathrm{s}}(T_{\mathrm{depo}})-$, $\mu_0 H_{\mathrm{c}}(T_{\mathrm{depo}})-$ and $T_{\mathrm{C}}(T_{\mathrm{depo}})-$diagramms (see Sec. 5.3.1).

5.1.2 Magnetic background correction

In this section, the magnetic background of a GdN thin film grown at N_2/Ar=20 %, T_{depo}=500 °C, P_{depo}=45 W and p_{depo}= 5×10^{-3} mbar on a thermally oxidized Si substrate is exemplary analyzed. To characterize the background of the substrate and the GdN thin film, a magnetic background calibration at T_{meas}=150 K is performed. The results of the magnetic background correction are shown in Fig. 5.2.

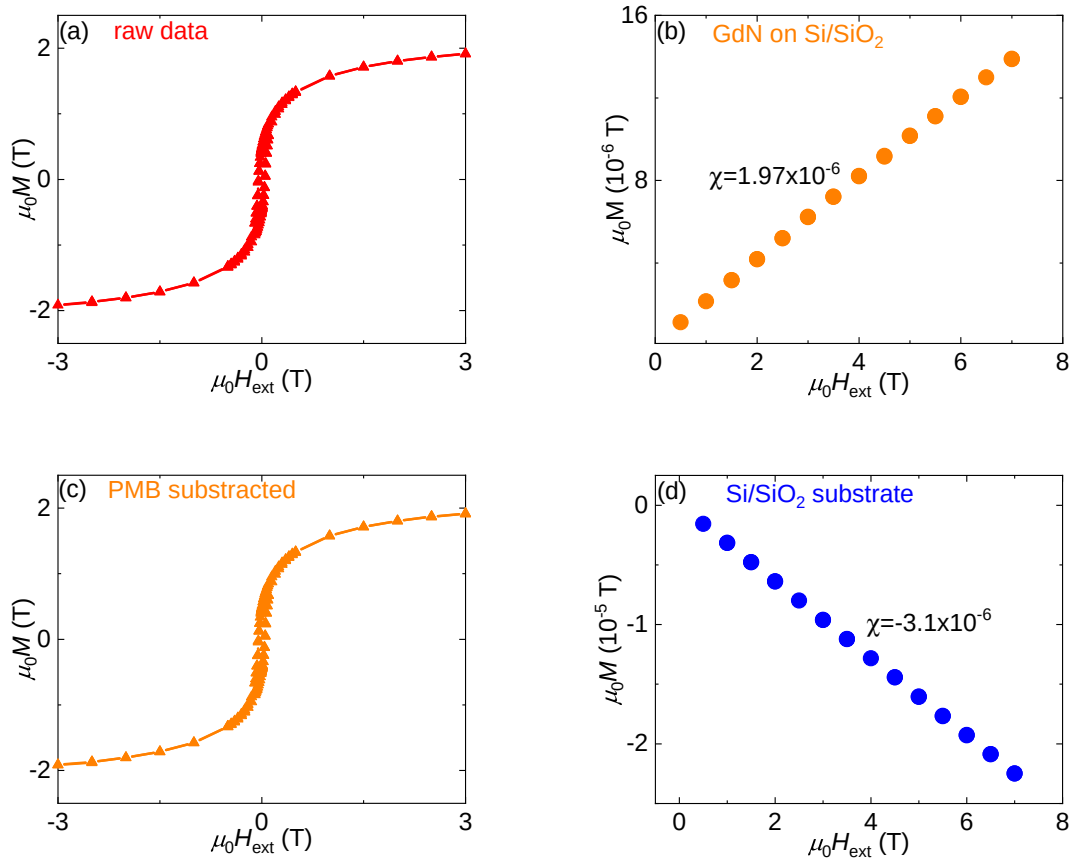

Fig. 5.2: Results of the magnetic background correction: (a) Magnetic hysteresis loop without background correction. (b) The slope of $M(H)$ for a GdN thin film in the saturated state shows a paramagnetic response induced by paramagnetic Gd impurities. (c) Magnetic hysterese loop after subtracting the background contribution of the substrate. (d) $M(H)$ of a bare thermally oxidized Si substrate indicates a diamagnetic response.

Figure 5.2 (a) illustrates the magnetic hysteresis loop, recorded at T=5 K, of a FM GdN thin film grown on a thermally oxidized Si substrate without a magnetic background correction. The slope of $M(H)$ for a GdN thin film in the saturated state is shown in the figure 5.2 (b). Here, we measured the magnetiziation $\mu_0 M$ as a function of an external magnetic field $\mu_0 H_{\mathrm{ext}}$ at T_{meas}=150 K. The recorded $M(H_{\mathrm{ext}})$ results in a linear relationship, which corresponds to a magnetic susceptibility of χ=1.97×10^{-6}, which we attribute to a paramagnetic response of the Gd impurities. Finally, we subtract the slope of this curve (see Fig. 5.2 (b)) as the paramagnetic background (PMB) from the $M(H_{\mathrm{ext}})$ raw data, as shown in Fig. 5.2 (c). In Fig. 5.2 (d), we show the negative slope in $M(H)$ of an uncoated thermally oxidized Si substrate, which corresponds to a diamagnetic response and a magnetic susceptibility

χ=-3.12×10^{-6}. Due to the paramagnetic response of Gd, the diamagnetic response from the substrate is not visible in Fig.5.2 (b). As described in section 3.3, we deposit GdN on $(6 \,\mathrm{x}\, 10 \,\mathrm{x}\, 0.55)\,\mathrm{mm}^3$ silicon (Si) substrates with a thermally oxidized SiO_2 (d=1 μm) top layer. For the magnetic susceptibility of Si, we find the value χ_{Si}=-4.2×10^{-6} published in the work of *F. M. Martínez Santiesteban et al.* [80], which is comparable with our measured value of χ=-3.12×10^{-6}. In summary: In our magnetic background correction performed at T=150 K, the Si/SiO_2-substrate provides a T-independent larmor-contribution. To separate the $M(H)$-measurement data from the larmor-contribution of the substrate, we subtract it from our raw data measured at T=5 K. Here are still paramagnetic moments present, but they originate from the sample.

5.1.3 X-ray diffraction spectroscopy

To examine the crystalline growth of our GdN thin films, we perform X-ray diffraction (XRD) spectroscopy (see Sec. 3.5.1). For this purpose we perform 2θ-ω scans, as discussed in section 3.5.1. Figure 5.3 shows an exemplary XRD-scan result of a GdN sample grown at N_2/Ar=10 %, T_{depo}=500 °C, P_{depo}=45 W and p_{depo}= 5×10^{-3} mbar between a protective top and bottom buffer layer of TaN (d=20 nm) on a thermally oxidized Si substrate (see Sec. 3.3).

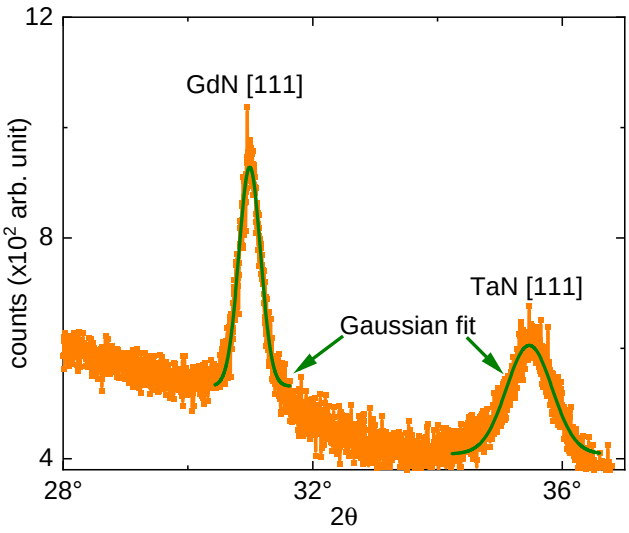

Fig. 5.3: 2θ-ω scan of a FM GdN thin film: Reflections from the [111] direction of GdN and TaN are visible. A Gaussian fit (green lines) enables to extract the peak amplitude A, position x_c and width w.

As picture 5.3 illustrates, we observe two crystalline reflections at 2θ=30.99 ° and 2θ=35.47 °, which we attribute to the crystalline reflections of GdN and TaN in the [111] direction. For both reflections, we perform a Gaussian fit

$$y = y_0 + \frac{A}{w\sqrt{\pi/2}} \cdot e^{-2\frac{(x-x_c)^2}{w^2}} \tag{27}$$

to the raw data of the 2θ-ω scan of our GdN sample.

From the fit of our raw data with Eq. (27), we can extract the position x_c, the amplitude A and the width w=FWHM/$\sqrt{ln(4)}$ of the crystalline reflections. This method allowed us to assign the peak positions at 30.99 ° and 35.47 ° to the GdN with NaCl structure and cubic TaN both with a texture in crystalline reflections [111] direction. These values are comparable with the work of *B. Downs et al.* [81] and *T. Hashizume et al.* [82].

As a next step, we introduce the Bragg relation

$$2d_{hkl}sin(\theta) = \lambda, \tag{28}$$

and the distance d_{hkl} of the lattice planes

$$d_{hkl} = \frac{a}{\sqrt{h^2 + k^2 + l^2}}, \tag{29}$$

to compute the lattice constant

$$a_{\text{lattice}} = \frac{\lambda}{2sin(\theta/2)}\sqrt{h^2 + k^2 + l^2} \tag{30}$$

of GdN and TaN, where h,k,l=1 defines the Miller indices and $\lambda_{K\alpha 1}$=1.54 Å (see Sec. 3.5.1). Table 5.1 displays the results of the Gaussian fit and the calculation of the lattice constant a_{lattice} for the GdN and TaN layer with a texture in [111] direction.

	x_c [°]	A [arb. unit]	w [°]	a_{lattice} [Å]
GdN [111]	30.99±0.0021	173.31±3.57	0.35±0.0058	4.99
TaN [111]	35.47±0.0057	180.01±5.51	0.73±0.017	4.38

Tab. 5.1: Guassian fit parameters x_c, A, w=FWHM/$\sqrt{ln(4)}$ and calculated lattice constant a_{lattice} of a GdN thin film.

As listed in Tab. 5.1, we get a lattice constant of $a_{\text{lattice,GdN}}$=4.99 Å for GdN and a value of $a_{\text{lattice,TaN}}$=4.38 Å for TaN with [111] texturing, which is in agreement with the results of *K. Senapati et al.* [54] and *N. Terao et al.* [83]. In section 5.2.2 and 5.3.2, we discuss the relationship between the lattice constant a_{lattice} and the growth parameters of our GdN thin films.

5.2 N_2/Ar gas flow ratio variation series

In the optimization series of the N_2/Ar gas flow ratios, GdN thin films were deposited using three different deposition powers (P_{depo}=15 W, 45 W, 75 W) under varying N_2/Ar gas flow ratio and at a fixed deposition temperature of T_{depo}=500 °C with a layer thickness of 60 nm on thermally oxidized Si substrates. The N_2/Ar gas flow series was performed for different powers to study the evolution of the optimal gas flow ratio with P_{depo}. Here, we investigate the impact of the different growth parameters on the magnetic properties $\mu_0 M_s$, $\mu_0 H_c$ and T_C of GdN. To this end, the starting value of the N_2/Ar gas flow ratio was 10 % and was varied in 10 %-steps for GdN thin films which were prepared using a deposition power of P_{depo}=45 W. For GdN samples fabricated at P_{depo}=15 W and 75 W, we select N_2/Ar-gas flow ratios with a comparable N_2/Ar·P_{depo}/45 W-ratio as starting points of the N_2/Ar gas flow ratio and its variation stepsize. In this way, we are able to compare the gas flow series performed at different powers. Finally, we study the crystalline growth of our GdN thin films under variation of the N_2/Ar gas flow ratio.

5.2.1 Magnetic parameters of N_2/Ar gas flow ratio variation series

In this section, we investigate the behavior of the static magnetic parameters $\mu_0 M_s$ and $\mu_0 H_c$, extracted by using the methods discussed in 5.1.1, of the GdN thin films fabricated at T_{depo}=500 °C with varied N_2/Ar gas flow ratio and a fixed sputtering power P_{depo}. Fig. 5.4 (a)-(f) shows the magnetic hysteresis loops (see $M(H)$-measurements 5.1.1) of GdN thin films prepared under varying N_2/Ar gas flow ratios and using the three different deposition powers P_{depo}=15 W, 45 W, and 75 W.

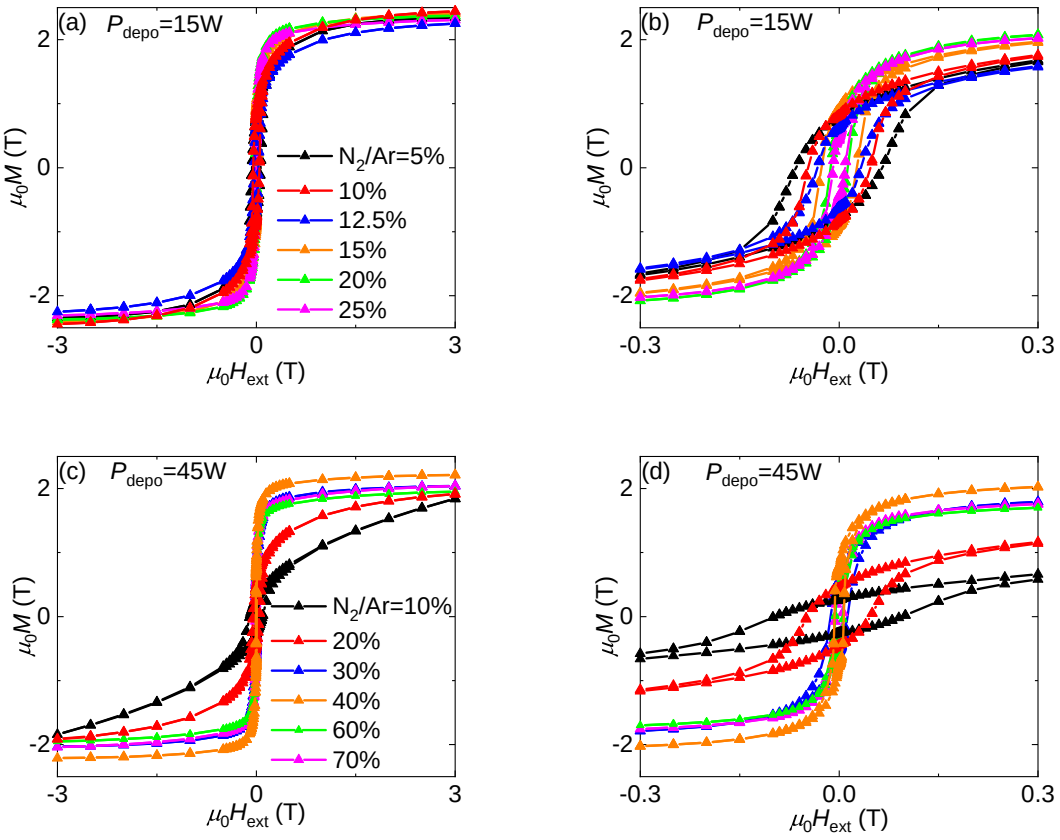

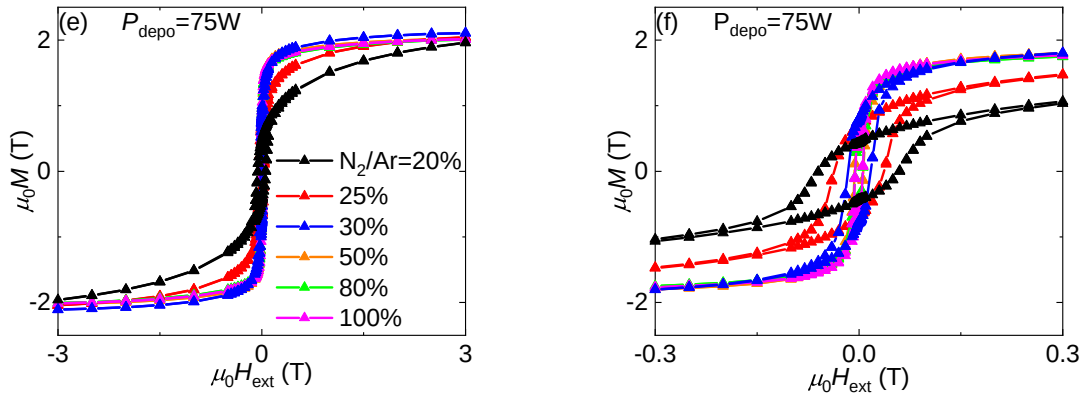

Fig. 5.4: (a)-(f) Hysteresis loops $M(H)$ recorded at T=5 K for GdN thin films grown under varying N_2/Ar gas flow ratio and fixed P_{depo}: (a) The hysteresis loops are all very similar in shape for P_{depo}=15 W and a saturation magnetization of $\mu_0 M_s$>2.2 T is observed in all magnetic curves. (c), (e) An increasing N_2/Ar gas flow ratio corresponds to an increasing $\mu_0 M_s$ and a maximum $\mu_0 M_{s,max}$=2.21 T at N_2/Ar=40 % / P_{depo}=45 W (see orange curve) and $\mu_0 M_{s,max}$=2.11 T at N_2/Ar=30 % / P_{depo}=75 W (see blue curve) is visible. Higher N_2/Ar gas flow ratios provide a sloping behavior of the hysteresis loops and therefore a decrease of $\mu_0 M_s$. (b), (d) and (f): Zoomed in view of the hystersis loops to highlight the width of the magnetic curves and to extract the coercive field $\mu_0 H_c$. We find, that in all variation series, $\mu_0 H_c$ decreases with an increasing N_2/Ar.

The Panels (a) and (b) of Fig. 5.4 shows the hysteresis loops of GdN thin films fabricated with a varying N_2/Ar gas flow ratio and a deposition power of P_{depo}=15 W. Here, we extract (see 5.1.1) for all hysteresis loops a saturation magnetization $\mu_0 M_s$>2.2 T and the magnetic curves are all comparable in shape. The GdN films produced under varying N_2/Ar gas ratio and with fixed P_{depo}=45 W in Fig. 5.4 (c) and (d) show an increasing N_2/Ar gas flow ratio corresponding to an increasing saturation magnetization $\mu_0 M_s$ and then a maximum $\mu_0 M_{s,max}$=2.21 T is observed at N_2/Ar=40 % (see orange curve). A similar trend is observed for GdN samples deposited with P_{depo}=75 W (see Fig. 5.4 (e) and (f)). Here, an increasing N_2/Ar gas flow ratio correspondes to an increasing saturation magnetization $\mu_0 M_s$ and we find a maximum value of $\mu_0 M_{s,max}$=2.11 T at N_2/Ar=30 % (see blue curve). Higher N_2/Ar gas flow ratios cause a decreasing height of the hysteresis loops and therefore a decrease of the saturation magnetization $\mu_0 M_s$. To highlight the width of the magnetic curves, a zoomed in view of the hysteresis loops is shown in Fig. 5.4 (b), (d) and (f). Here, in all variation series the coercive field $\mu_0 H_c$ decreases with an increasing N_2/Ar gas flow ratio.

To investigate the static magnetic parameters $\mu_0 M_s$ and $\mu_0 H_c$, extracted from hysteresis loops (see 5.2.1), grown at varying N_2/Ar gas flow ratios, we plot the saturation magnetization $\mu_0 M_s$ as a function of N_2/Ar (see Fig. 5.5 (a)) and the coercive field $\mu_0 H_c$ (see Fig. 5.5 (b)) depending on N_2/Ar of GdN thin films produced at P_{depo}=15 W (blue data points), 45 W (red data points) and 75 W (green data points) (see also Tabs. A.1,A.2).

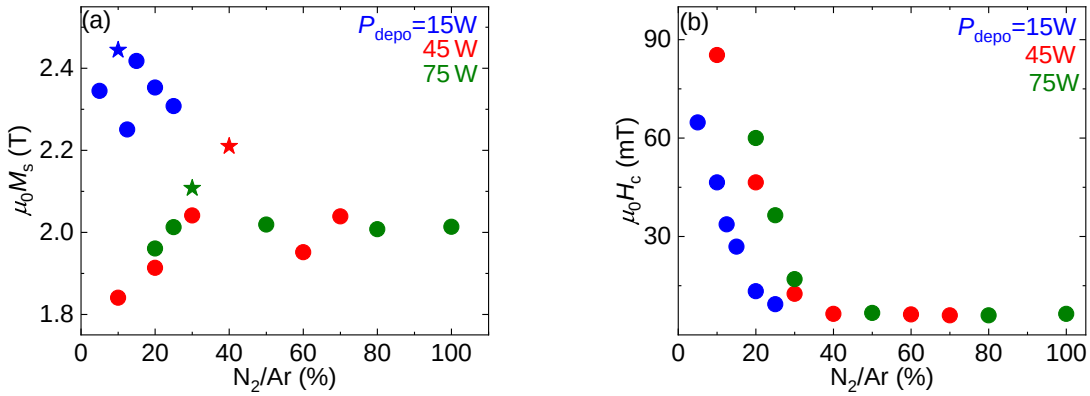

Fig. 5.5: Extracted static magnetic parameters $\mu_0 M_s$ and $\mu_0 H_c$ of GdN thin films grown under varying N_2/Ar gas flow ratio and fixed P_{depo}: (a) $\mu_0 M_s(N_2/Ar)$-plot shows an increasing N_2/Ar gas flow ratio corresponding to an increased $\mu_0 M_s$ and then results a maximum $\mu_0 M_{s,max}$=2.44 T at N_2/Ar=10 % / P_{depo}=15 W (see blue star), $\mu_0 M_{s,max}$=2.21 T at N_2/Ar=40 % / P_{depo}=45 W (see red star) and $\mu_0 M_{s,max}$=2.11 T at N_2/Ar=30 % / P_{depo}=75 W (see green star). Thereafter, with an increasing N_2/Ar we observe a decreasing behavior of $\mu_0 M_s$ in all P_{depo}-series and then only in the 75 W-series a saturation of $\mu_0 M_s$. (b) $\mu_0 H_c(N_2/Ar)$-plot shows an increasing N_2/Ar gas flow ratio provides a decreasing coercive field $\mu_0 H_c$ in all variation series and then from N_2/Ar=40 % a saturation of $\mu_0 H_c$ in the 45 W- and 75 W-series.

Figure 5.5 (a) shows the evolution of the saturation magnetization $\mu_0 M_s$ of GdN thin films grown under varying N_2/Ar gas flow ratio and fixed deposition powers P_{depo}=15 W, 45 W and 75 W. In the 15 W-series (see blue data points in Fig. 5.5 (a)), an increasing N_2/Ar gas flow ratio causes first an increase of the saturation magnetization $\mu_0 M_s$ and a maximum $\mu_0 M_{s,max}$=2.44 T is observed at N_2/Ar=10 % (see blue star). A comparable behavior is observed in the 45 W- (see red data points in Fig. 5.5 (a)) and 75 W-series (see green data points in Fig. 5.5 (a)). Here, we identify a maximum $\mu_0 M_{s,max}$=2.21 T at N_2/Ar=40 % for P_{depo}=45 W (see red star) and $\mu_0 M_{s,max}$=2.11 T at N_2/Ar=30 % for P_{depo}=75 W (see green star). Thereafter, with increasing N_2/Ar gas flow ratio we observe in all P_{depo}-series a decrease of $\mu_0 M_s$ and then only in the 75 W-series a saturation of $\mu_0 M_s$. We attribute this reduction in $\mu_0 M_s$ for higher N_2/Ar gas flow ratios to the growth of nitrogen rich $GdN_{1\pm x}$ compounds.

We compare our results to those of *K. Senapati et al.* [54], where in their Fig. 2(a) [54] shows the saturation magnetization M_s as a function of the sputtering power P. Here in various N_2-series, GdN films sputtered with a areal power density of 0.49 W/cm^2 show for decreasing N_2 partial pressures an increasing M_s close to $\approx 3\,\mu_B$/Gd, which is associated with FM GdN in the N-rich zone (discussion for our GdN thin films see 5.2.3). Further, GdN samples fabricated with 0.96 W/cm^2 show for an increasing N_2 partial pressures an increasing M_s close to $\approx 7\,\mu_B$/Gd. A maximum value of M_s and thereafter a decreasing M_s

for higher N_2 is shown in the intermediate P-regime ($\approx 0.76\,W/cm^2$ - $0.84\,W/cm^2$), which is comparable with our observation in Fig. 5.5 (a).

Panel 5.5 (b) shows the coercive field $\mu_0 H_c$ as a function of the N_2/Ar gas flow ratio of GdN thin films are grown under varying N_2/Ar gas flow ratio and fixed deposition power P_{depo}=15 W, 45 W and 75 W. In all P_{depo}-series, we observe that $\mu_0 H_c$ decreases with an increasing N_2/Ar ratio and starting from N_2/Ar=40 % the coercive field $\mu_0 H_c$ saturates at low magnetic field values. *K. Senapati et al.* [54] explains the enhancement of H_c for low N_2 partial pressures with a secondary phase of GdN (GdN-II) in a so-called N-deficient zone. A more detailed discussion of the magnetic ordering mechanisms of GdN (see Sec. 3.3 for more fundamental details) and the relationship between the static magnetic parameter $\mu_0 M_s$ and the lattice constant $a_{lattice}$ (see Sec. 5.2.2) of our GdN thin films is presented in section 5.2.3.

As a next step, we investigate the Curie temperature T_C, extracted with two different methods from $M(T)$-measurements (see Sec. 5.1.1), of GdN thin films fabricated at varied N_2/Ar gas flow ratio and fixed deposition power P_{depo}=45 W and 75 W. Due to oxidation (see Sec. 3.3) and the short lifetime τ of GdN films produced at P_{depo}=15 W ($\tau \approx 4$ weeks), we were not able to perform suitable $M(T)$-measurements for this growth series. Fig. 5.6 (a) shows the Curie temperature $T_{C,t}$, determined by using the tangent method (see Sec. 5.1.1), as a function of the N_2/Ar gas flow ratio and Fig. 5.6 (b) illustrates the Curie temperature $T_{C,S}$, extracted by the intersection of the FC and ZFC curve of $M(T)$-measurement (see 5.1.1), versus the N_2/Ar gas flow ratio. The difference value ΔT_C, between the two T_C-extraction methods, depending on varying N_2/Ar is shown in Fig. 5.6 (c) (see also Tabs. A.1,A.2).

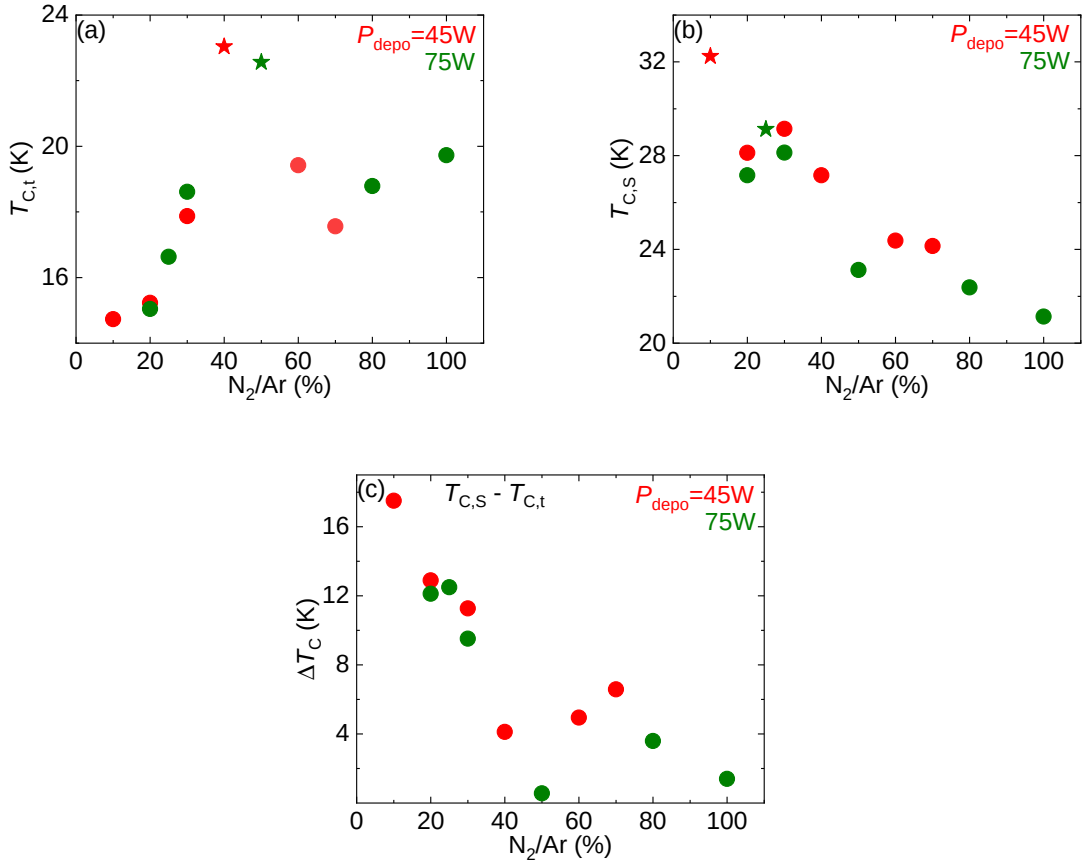

Fig. 5.6: Extracted Curie temperature T_C of GdN thin films grown under varying N_2/Ar gas flow ratio and fixed P_{depo}: (a) $T_{C,t}$, extracted with the tangent method, depending on N_2/Ar results in a maximum $T_{C,t,max}$=23.04 K at N_2/Ar=40 % / P_{depo}=45 W (highlighted with a red star) and $T_{C,t,max}$=22.56 K at N_2/Ar=50 % / P_{depo}=75 W (highlighted with a green star). (b) $T_{C,S}$, extracted with the intersection method, plotted as function of the N_2/Ar gas flow ratio shows a maximum value of $T_{C,S,max}$=32.24 K at N_2/Ar=10 % / P_{depo}=45 W (represented by a red star) and $T_{C,S,max}$=29.13 K at N_2/Ar=25 % / P_{depo}=75 W (represented by a green star). Starting from $T_{C,S,max}$, an increasing N_2/Ar causes a decrease of $T_{C,S}$ in both variation series. (c) The difference value of the two T_C-extraction methods $\Delta T_C = T_{C,S} - T_{C,t}$ shows a decreasing behavior for an increasing N_2/Ar gas flow ratio in both P_{depo}-series throughout the entire N_2/Ar gas flow regime.

Figure 5.5 (a) displays the Curie temperature $T_{C,t}$, extracted by using the tangent method (see Sec. 5.1.1), of GdN thin films as a function of the N_2/Ar gas flow ratio. Here, an increasing N_2/Ar gas flow ratio and fixed P_{depo}=45 W (see red data points in Fig. 5.5 (a)) corresponds to an increasing Curie temperature $T_{C,t}$ and we obtain a maximum value of $T_{C,t,max}$=23.04 K at N_2/Ar=40 % (see red star). A similar trend is shown in the P_{depo}=75 W-series (see green data points in Fig. 5.5 (a)). Here a maximum value of $T_{C,t,max}$=22.56 K is observed at N_2/Ar=50 % (see green star). Finally, we observe for higher N_2/Ar gas flow ratio a decrease of $T_{C,t}$ and then a saturation of the Curie temperature. A fundamentally different behavior for the Curie temperature $T_{C,S}$, determined by using the intersection method (see 5.1.1), as a function of the N_2/Ar gas flow ratio is shown in Fig. 5.5 (b). Here, starting from $T_{C,S,max}$=32.24 K at N_2/Ar=10 %, 45 W (see red star) and $T_{C,S,max}$=29.13 K at N_2/Ar=25 %, 75 W (see red star), $T_{C,S}$ decreases throughout the entire N_2/Ar-region. This clear discrepancy of T_C, determined from the two different T_C-extraction methods, indicates the presence of paramagnetic Gd vacancies in our GdN thin films, as will be discussed in greater detail in section 5.2.3.

A comparable trend is shown in the work of *K. Senapati et al.* [54], where their Fig. 2(c) [54] displays the Curie temperature T_C depending on the sputtering power P. Here in various N_2-series, an increasing sputtering power P together with a decreasing N_2 partial pressure corresponds to an increasing T_C. The enhancement of T_C is associated with N vacancies and an antiferromagnetic (AFM) ordering mechanism (T_C>60 K) of GdN (see Sec. 3.3).

In Figure 5.5 (c), the difference value $\Delta T_C = T_{C,S} - T_{C,t}$, computed from the Curie temperature of the two extraction methods, mostly shows a decreasing behavior for an increasing N_2/Ar gas flow ratio. The width of the transition temperature range and the difference in T_C indicates Gd vacancies in our GdN thin films. The correlation between the static magnetic parameter $\mu_0 M_s$, the Curie temperature $T_{C,S}$ and the lattice constant $a_{lattice}$ (see Sec. 5.2.2) of our GdN thin films is discussed in section 5.2.3.

5.2.2 Lattice parameters of N_2/Ar gas flow ratio variation series

This section deals with the study of the crystalline growth of GdN thin films, prepared under varying deposition parameters, by using X-ray diffraction (XRD) spectroscopy (see Sec. 3.5.1). As described in section 3.3, we deposited our GdN thin film between a protective top and bottom buffer layer of TaN (d=20 nm) on a thermally oxidized Si substrate. Figure 5.7 (a)-(c) shows the results of the 2θ-ω scans (see Sec. 3.5.1) of GdN thin films grown at T_{depo}=500 °C and varied N_2/Ar gas flow ratios as well as fixed deposition powers P_{depo}=15 W, 45 W and 75 W.

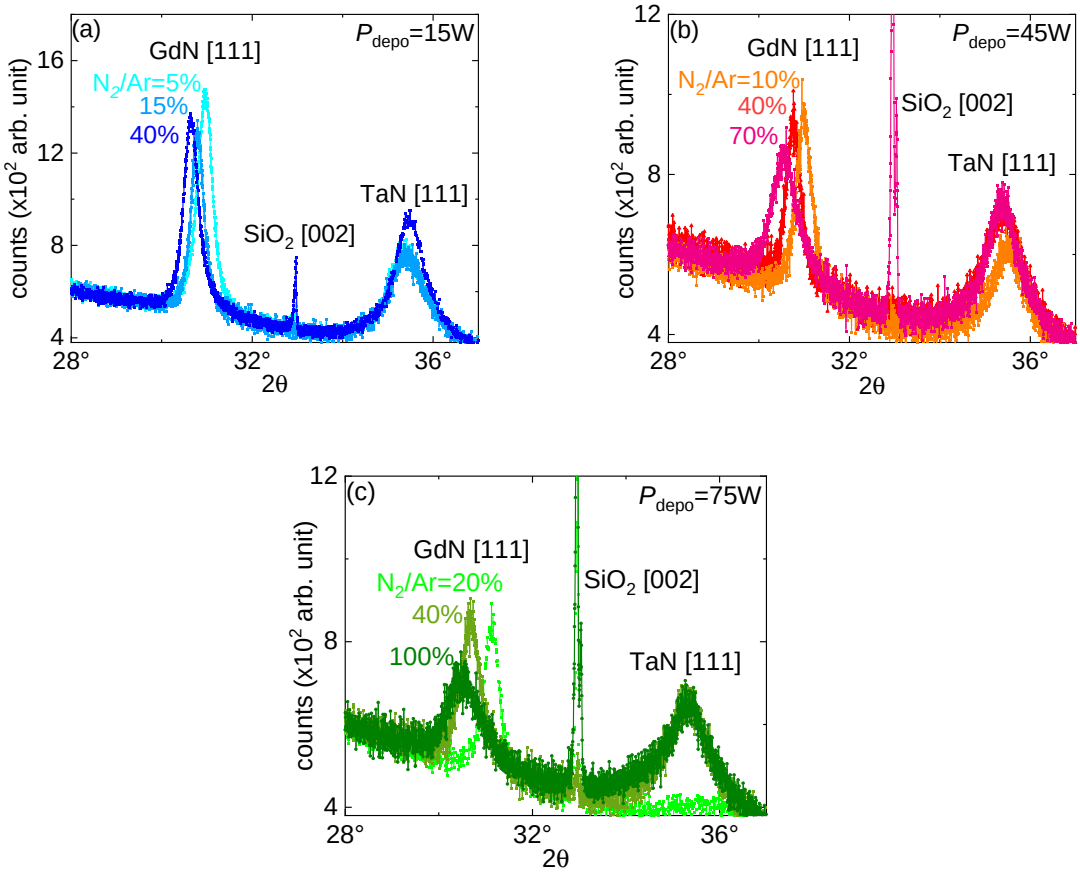

Fig. 5.7: 2θ-ω scans of our GdN samples deposited on a TaN buffer layer under varied N_2/Ar gas flow ratios at fixed P_{depo}: (a)-(c) Reflections from the [111]-direction of GdN ($2\theta \approx 31\,°$) and TaN ($2\theta \approx 35.5\,°$) as well as SiO_2 ($2\theta \approx 32.24\,°$) with [002]-texturing are visible. In all P_{depo}-series, an increasing N_2/Ar corresponds to a shift of the peak of GdN with [111]-texturing to lower 2θ. Furthermore, the amplitude A mostly decreases and the width w of the curves increases for higher N_2/Ar gas flow ratios. For TaN [111], we calculate a lattice constant $a_{\mathrm{lattice,TaN}}$=4.38 Å for the unchanged growth parameters.

Fig. 5.7 (a)-(c) show the results of the 2θ-ω scans for GdN thin films grown at different N_2/Ar gas flow ratios and fixed deposition powers P_{depo}=15 W, 45 W and 75 W. Here, we observe crystalline reflections at 2θ≈31 ° and 2θ≈35.5 ° and also a weak reflection of SiO_2 at 2θ≈32.9 ° in the [002]-direction. As described in Sec. 5.1.3, we assign the peak positions at 2θ≈31 ° and 2θ≈35.5 ° to the crystalline reflections of GdN and TaN in the [111]-direction.

In all P_{depo}-series, an increasing N_2/Ar gas flow ratios cause a shift to lower angles for the [111] GdN peak of GdN with [111]-texturing. Furthermore, the amplitude A decreases and the width w of the curves increases for an increasing N_2/Ar gas ratio and for higher deposition powers P_{depo}. For the crystalline reflections of TaN in the [111]-direction, we observe no significant modification of the peak position of the [111]-reflection in all P_{depo}-series. Finally, we compute with formula (30) a lattice constant of $a_{\text{lattice,TaN}}$=4.38 Å which is comparable to the results of *N. Terao et al.* [83].

Next, we investigate the extracted 2θ angle and the calculated lattice constant a_{lattice} (see Sec. 5.1.3) of our GdN films. Figure 5.8 (a) shows the crystalline reflection 2θ as a function of the N_2/Ar gas flow ratio and Fig. 5.8 (b) illustrates the lattice constant a_{lattice} of GdN thin films depending on the N_2/Ar gas flow ratio.

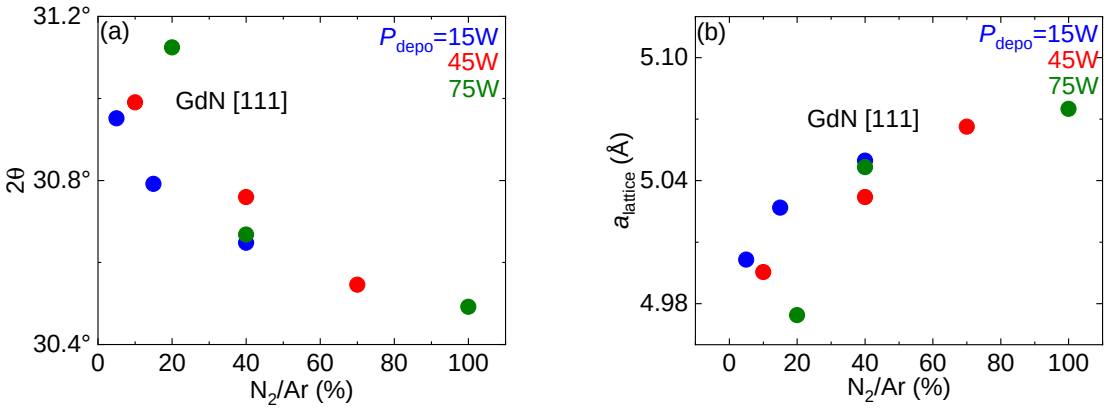

Fig. 5.8: Extracted 2θ angle and calculated lattice constant a_{lattice} of our GdN samples deposited on TaN under varying N_2/Ar gas flow ratio and fixed P_{depo}: (a) $2\theta(N_2/\text{Ar})$-plot shows an increasing N_2/Ar gas flow ratio leads to a decreasing 2θ for GdN [111]. (b) $a_{\text{lattice}}(N_2/\text{Ar})$-plot shows an increasing N_2/Ar gas flow ratio corresponds to an increasing a_{lattice} and a value of ≈(4.97-5.07) Å for GdN [111] is visible.

Fig. 5.8 (a) illustrates the 2θ angle as a function of the N_2/Ar gas flow ratio for a various sputtering powers (P_{depo}=15 W, 45 W and 75 W). Here, the 2θ angle, which we associate with the crystalline reflection of GdN in the [111]-direction, decreases with an increasing N_2/Ar gas flow ratio. Fig. 5.8 (b) shows the lattice constant a_{lattice} of our GdN thin films, calculated with formula (30), depending on the N_2/Ar gas flow ratio. In the entire N_2/Ar gas flow ratio range, an increasing gas flow ratio corresponds to an increasing lattice constant a_{lattice} of GdN with [111]-texturing and we extracted the value $a_{\text{lattice,GdN}}$≈(4.97-5.07) Å, which is comparable with *K. Senapati et al.* [54]. Compared to the work of *F. Leuenberger* [62] and *H. Holleck et al.* [84], an increase of $a_{\text{lattice,GdN}}$ is associate with a nitrogen deficiency or oxygen impurities. In contrast, for our N_2/Ar gas flow ratio variation series, we observe in Fig. 5.8 (b) an increase in a_{lattice} for higher N_2/Ar values. Here, we assume that an increasing N_2/Ar gas flow ratio at a constant deposition power P_{depo} corresponds to a prefered growth of nitrogen rich $GdN_{1\pm x}$ phases with an increased lattice constant $a_{\text{lattice,GdN}}$ due to the storage of N-interstitials in the lattice.

5.2.3 Summary of the N_2/Ar gas flow ratio series and comparison to literature

In section 5.2, we have optimized the N_2/Ar gas flow ratio of 60 nm GdN thin films, fabricated at a growth temperature of T_{depo}=500 °C, on on thermally oxidized Si substrates. Here, we have investigated in three growth series, at the different sputtering powers P_{depo}=15 W, 45 W and 75 W, the impact of varied N_2/Ar gas flow ratio on the magnetic parameters $\mu_0 M_{\mathrm{s}}$, $\mu_0 H_{\mathrm{c}}$ and T_{C}. First, the evolution of the magnetic hysteresis loops (see Fig. 5.4 (a)-(f)) of our $M(H)$-measurements (see 5.1.1 and 5.2.1) shows in all P_{depo}-series a similar signature: At first, an increasing N_2/Ar gas flow ratio and fixed P_{depo} results in an increasing saturation magnetization $\mu_0 M_{\mathrm{s}}$ reaching a maximum value $\mu_0 M_{\mathrm{s,max}}$ at a specific N_2/Ar gas flow ratio (see Fig. 5.5 (a)). Thereafter, we observed a decrease of $\mu_0 M_{\mathrm{s}}$ with increasing N_2/Ar gas flow ratio. A comparable trend is shown in the work of *K. Senapati et al.* [54] in the intermediate P-range ($\approx 0.76\,\mathrm{W/cm^2}$ - $0.84\,\mathrm{W/cm^2}$) of the $M_{\mathrm{s}}(P)$-plot (see Fig. 2(a) in [54]). In our $M(H)$-measurements, the coercive field $\mu_0 H_{\mathrm{c}}$ decreases with an increasing N_2/Ar gas flow ratio and starting from N_2/Ar=40 % the $\mu_0 H_{\mathrm{c}}$ saturates close to the zero value (see Fig. 5.5 (b)) for higher N_2/Ar. For P_{depo}=15 W we were able to fabricate GdN thin films with a saturation magnetization $\mu_0 M_{\mathrm{s}}$>2.2 T, which is larger compared to the $\mu_0 M_{\mathrm{s}}$ of the GdN samples prepared with P_{depo}=45 W ($\mu_0 M_{\mathrm{s,max}}$=2.21 T) and 75 W ($\mu_0 M_{\mathrm{s,max}}$=2.11 T). Furthermore, we have observed a saturation of $\mu_0 H_{\mathrm{c}}$ at high N_2/Ar-values and 45 W and 75 W. The lifetime τ of the GdN thin films produced with P_{depo}=15 W ($\tau\approx$4 weeks) was limited compared to the lifetime τ of the GdN samples fabricated with 45 W and 75 W ($\tau\approx$6 month).

Next, we examined the Curie temperature T_{C} of our GdN thin films fabricated under varied N_2/Ar gas flow ratio and a deposition power of P_{depo}=45 W and 75 W. Based on the results of the $M(T)$-measurements (see Sec. 5.1.1), we determined T_{C} with two different extraction methods and observed for each method an individual evolution of T_{C} as a function of varied N_2/Ar gas flow ratio (see Fig. 5.5 (a)-(b)). First, the $T_{\mathrm{C,t}}$, extracted by using the tangent method (see Sec. 5.1.1), increased for an increasing N_2/Ar gas flow ratio and P_{depo}= 45 W and then a maximum of $T_{\mathrm{C,t,max}}$=23.04 K has been observed at N_2/Ar=40 % (see Fig. 5.5 (a)). A similar trend was observed in the 75 W-series, where a maximum $T_{\mathrm{C,t,max}}$=22.56 K has been found at N_2/Ar=50 % (see Fig. 5.5 (b)). The Curie temperature $T_{\mathrm{C,S}}$, determined by using the intersection method (see 5.1.1), exhibits a maximum value of $T_{\mathrm{C,S,max}}$=32.24 K at N_2/Ar=10 %, (45 W) and $T_{\mathrm{C,S,max}}$=29.13 K at N_2/Ar=25 %, (75 W) (see Fig. 5.5 (b)). Starting from $T_{\mathrm{C,S,max}}$, a decreasing behavior of $T_{\mathrm{C,S}}$ throughout the entire N_2/Ar-range has been observed. In the work of *K. Senapati et al.* [54], they identified a comparable trend of T_{C} depending on the sputtering power P (see Fig. 2(c) in [54]). Here, the enhancement of T_{C} is explained by N vacancies, which results in a lattice destortion and a antiferomagnetic (AFM) behavior of GdN (see 3.3). However, the GdN thin films in [54] were fabricated at room temperature and lower sputtering powers compared to our GdN samples. In comparison to our N_2/Ar variation series, significantly smaller N_2 partial pressures (4 % - 10 %) and N_2 variation steps of 2 % were selected in the work of *K. Senapati et al.* [54]. Finally, we calculated the difference value ΔT_{C}=$T_{\mathrm{C,S}}$−$T_{\mathrm{C,t}}$ of the two extraction methods and observed a decreasing behavior of ΔT_{C} in the entire N_2/Ar-range (see 5.5 (c)). The signature of the ΔT_{C}(N_2/Ar)-plot indicates Gd vacancies in our GdN films, because paramagnetic impuri-

ties derived from Gd broaden the phase transition in the FC $M(T)$-curve, at low N_2/Ar-gas flow values. Consequently, the intersection method of the FC and ZFC $M(T)$-curves used for the determination of T_C will yield higher T_C-values compared to the tangent method and thereby give rise to a large ΔT_C. To investigate the crystalline growth of GdN thin films, at varying deposition parameters, we used X-ray diffraction (XRD) spectroscopy (see Sec. 3.5.1). Here, the results of the 2θ-ω scans (see Sec. 3.5.1) of GdN thin films grown at T_{depo}=500 °C and varied N_2/Ar gas flow ratios and fixed deposition power P_{depo}=15 W, 45 W and 75 W revealed crystalline reflections at $2\theta \approx 31$ ° and $2\theta \approx 35.5$ °. By performing a Gaussian fit (see 5.1.3), we assigned the peak positions to the crystalline reflections of GdN and TaN in the [111]-direction (see Fig. 5.7 (a)-(c)). In all P_{depo}-series, we observed for an increasing N_2/Ar gas ratio a decreasing 2θ angle (see Fig. 5.8 (a)) and the peak of GdN with [111]-texturing shifted to lower angles (see Fig. 5.7 (a)-(c)). Furthermore, the amplitude A decreased and the width w of the curves increased for higher N_2/Ar gas ratio. Moreover, we calculated (see formula (30)) the lattice constant $a_{lattice}$ of GdN and TaN with [111]-texturing. In the entire N_2/Ar-area, we observed an increasing N_2/Ar corresponds to an increasing $a_{lattice}$ and then a slight saturation of $a_{lattice}$ caused by higher N_2/Ar gas flow ratio and sputtering power P_{depo} (see Fig. 5.8 (b)). We extracted $a_{lattice,GdN} \approx 5.00$ Å for GdN in [111]-direction, which is comparable with *K. Senapati et al.* [54]. The crystalline reflection and the computed lattice constant $a_{lattice,TaN}$=4.38 Å of TaN in the [111]-direction [83] was almost constant for its unmodified growth parameters in all P_{depo}-series (see Fig. 5.7 (a)-(c)).

Finally, we investigate the relationship of the extracted saturation magnetization $\mu_0 M_s$ and the Curie temperature $T_{C,S}$ as well as the calculated lattice constant $a_{lattice}$ of our GdN thin films. For this purpose, we plot the saturation magnetization $\mu_0 M_s$ as a function of the Curie temperature $T_{C,S}$ (see Fig. 5.9 (a)). Furthermore, we plot the lattice constant $a_{lattice}$ depending on $T_{C,S}$ (see Fig. 5.9 (b)) of GdN films, which were fabricated under varied N_2/Ar gas flow ratio and fixed deposition power P_{depo}=15 W, 45 W and 75 W.

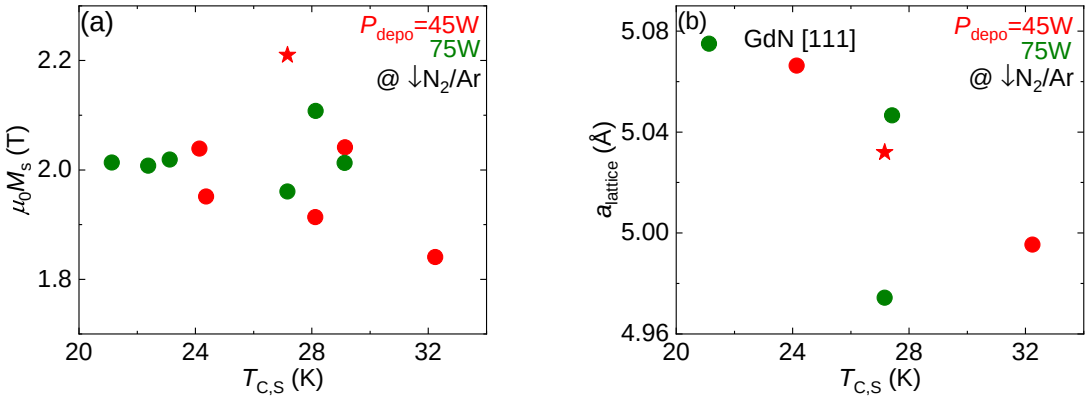

Fig. 5.9: Comparison of the extracted magnetic parameters $\mu_0 M_s$ and $T_{C,S}$ and the calculated lattice constant $a_{lattice}$ of GdN thin films fabricated at varying N_2/Ar gas flow ratios and fixed P_{depo}: (a) $\mu_0 M_s(T_{C,S})$-plot shows an almost constant value of $\mu_0 M_s \approx 2$ T and no clear relationship between $\mu_0 M_s$ and $T_{C,S}$ in the entire $T_{C,S}$-area. A maximum value of $\mu_0 M_{s,max}$=2.21 T at $T_{C,S}$=27.16 K is shown for a GdN thin film grown at N_2/Ar=40 % and P_{depo}=45 W (see red star). (b) $a_{lattice}(T_{C,S})$-plot shows a decreasing $a_{lattice}$ with increasing $T_{C,S}$ and a value of 5.03 Å at $T_{C,S}$=27.16 K (see red star).

In Fig. 5.9 (a), no clear relationship between $\mu_0 M_s$ and $T_{C,S}$ is visible. Instead, we observe an almost constant value of $\mu_0 M_s \approx 2$ T throughout the entire $T_{C,S}$-range. A maximum value of $\mu_0 M_{s,max}$=2.21 T at $T_{C,S}$=27.16 K is shown for a GdN thin film grown at N_2/Ar=40 % and P_{depo}=45 W (see red star in Fig. 5.9 (a)). Fig. 5.9 (b)) shows the lattice constant $a_{lattice}$ of our GdN films depending on the Curie temperature $T_{C,S}$. We consider for the increase of $T_{C,S}$ a decrease of $a_{lattice}$, which is associated with a stronger FM exchange interaction in our GdN thin films. At $T_{C,S}$=27.16 K (see red star in Fig. 5.9 (b)), the GdN thin films exhibit $a_{lattice}$=5.03 Å.

Comparing our results to the work of *K. Senapati et al.* [54], we observe a comparable trend in the $M_s(T_C)$-plot and $a(T_C)$-plot (see Fig. 5(a) in [54]). In their work, an increasing Curie temperature T_C corresponds to an increasing saturation magnetization M_s and simultaneously a decreasing lattice constant $a_{lattice}$. Further, the $M_s(T_C)$-area up to T_C=60 K is the so called N-rich zone (Zone 1), where GdN thin films, fabricated at high N_2 pressures and low sputtering power P, are grown with a ferromagnetic (FM) ordering. In Zone 2 (60 K<T_C<120 K), a nitrogen deficiency manifests in the GdN thin film giving rise to a secondary phase of GdN (GdN-II) with an antiferromagnetic (AFM) behavior controlled by N vacancies.

In this section, we have optimized the N_2/Ar gas flow ratio as well as the sputtering power P_{depo} at a fixed growth temperature of T_{depo}=500 °C. Here, we observed for the growth of a FM GdN thin film fabricated at N_2/Ar=40 %, T_{depo}=500 °C and P_{depo}=45 W a maximum saturation magnetization $\mu_0 M_s$=2.21 T, a low coercive field $\mu_0 H_c$=6.4 mT, a high Curie temperature $T_{C,S}$=27.16 K and a low lattice constant $a_{lattice}$ =5.03 Å (see red star in Fig. 5.9 (a) and (b)). Based on the discussion of our results in section 5.2 and the comparison with the work of *K. Senapati et al.* [54], we conclude that only GdN thin films ($T_{C,S,max}$=32.24 K, $a_{lattice,max}$ =5.075 Å) with FM ordering mechanism and no dual-phase GdN samples with an exchange bias effect (see Sec. 3.3) have been grown in our N_2/Ar gas flow ratio variation series. In the following section 5.3 we optimize the growth temperature T_{depo} utilizing the FM GdN sample prepared at T_{depo}=500 °C, N_2/Ar=40 % and P_{depo}=45 W as a starting point.

5.3 Deposition temperature $T_{\mathbf{depo}}$ variation series

In the optimization series of the deposition temperatures T_{depo}, GdN thin films, between a protective top and bottom buffer layer of TaN (d=20 nm) (see Sec. 3.3), were deposited under varying deposition temperatures T_{depo} at a N_2/Ar gas flow ratio of 40% and a depostion power P_{depo}=45 W with a layer thickness of 60 nm on thermally oxidized Si substrates. Here, we investigate the impact of deposition temperature T_{depo} on the magnetic properties $\mu_0 M_{\mathrm{s}}$, $\mu_0 H_{\mathrm{c}}$ and T_{C} of GdN. Considering to the results of the N_2/Ar gas flow ratio variation series (see Sec. 5.2), we optimize the growth temperature T_{depo} in 100 °C-steps around the FM GdN thin film fabricated at T_{depo}=500 °C, N_2/Ar=40 % and P_{depo}=45 W. For this reference GdN sample, we observe a maximum saturation magnetization $\mu_0 M_{\mathrm{s}}$=2.21 T, a low coercive field $\mu_0 H_{\mathrm{c}}$=6.4 mT and a high Curie temperature $T_{\mathrm{C,S}}$=27.16 K. Thereafter, we study the crystalline growth of our GdN thin films under variation of the growth temperature T_{depo}.

5.3.1 Magnetic parameters of deposition temperature T_{depo} variation series

In this section, we investigate the behavior of the static magnetic parameters $\mu_0 M_{\mathrm{s}}$ and $\mu_0 H_{\mathrm{c}}$, extracted by using the methods discussed in 5.1.1, of GdN thin films grown with varying deposition temperatures T_{depo} at fixed N_2/Ar gas flow ratio and a defined deposition power P_{depo}. The figures 5.10 (a)-(d) show the magnetic hysteresis loops (see $M(H)$-measurements 5.1.1) of GdN thin films prepared under varied growth temperatures T_{depo} at a N_2/Ar gas flow ratio of 40 % and a fixed sputtering power of P_{depo}=45 W.

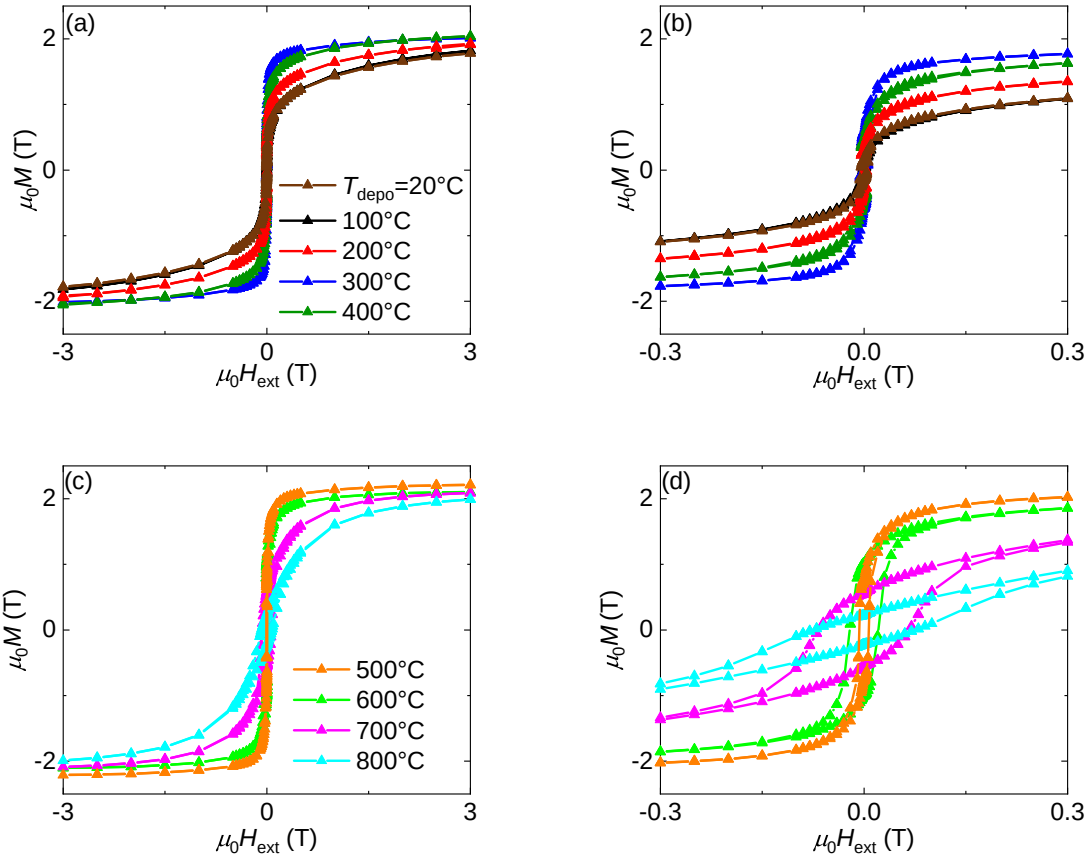

Fig. 5.10: (a)-(f) Hysteresis loops $M(H)$ recorded at T=5 K for GdN thin films grown under varying deposition temperatures T_{depo} at N_2/Ar=40 % and P_{depo}=45 W: (a) An increasing T_{depo} corresponds to an increasing $\mu_0 M_{\mathrm{s}}$ and then results in a maximum $\mu_0 M_{\mathrm{s,max}}$=2.04 T at T_{depo}=400 °C. (b) Zoomed in view of the hystersis loops to highlight the width of the magnetic curves and to extract the coercive field $\mu_0 H_{\mathrm{c}}$. Here, in the T_{depo}-area 20 °C≤T_{depo}≤500 °C the coercive field $\mu_0 H_{\mathrm{c}}$ remains small. (c) Maximum saturation magnetization $\mu_0 M_{\mathrm{s,max}}$=2.21 T at T_{depo}=500 °C and a decreasing behavior of $\mu_0 M_{\mathrm{s}}$ is visible for high T_{depo}. (d) For T_{depo}>500 °C, the coercive field $\mu_0 H_{\mathrm{c}}$ increases and reaches a maximum at T_{depo}=800 °C.

Figure 5.10 (a)-(d) depicts the magnetic hysteresis loops of GdN thin films fabricated at varying deposition temperatures T_{depo} at N_2/Ar=40 % and P_{depo}=45 W. Panel 5.10 (a) shows the evolution of $M(H)$ with an increasing growth temperature T_{depo} in the range from T_{depo}=20 °C to T_{depo}=400 °C. Magnetic hysteresis loops recorded for GdN thin films fabricated at higher T_{depo} are presented in Fig. 5.10 (c). Here, the maximum saturation magnetization $\mu_0 M_{\mathrm{s,max}}$=2.21 T of the variation series is shown at T_{depo}=500 °C.

Furthermore, an increasing T_{depo} gives rise to a decreasing $\mu_0 M_s$ decreasing to $\mu_0 M_s$=1.98 T at T_{depo}=800 °C. To highlight the width of the magnetic curves, a zoomed in view of the hysteresis loops is shown in Fig. 5.10 (b), and (d). Here, in the T_{depo}-area 20 °C≤T_{depo}≤500 °C the coercive field $\mu_0 H_c$ is saturated close to zero. For higher T_{depo}, the coercive field $\mu_0 H_c$ increases and reaches a maximum value of $\mu_0 H_{c,max}$=74.67 mT at T_{depo}=800 °C.

To investigate the static magnetic parameters $\mu_0 M_s$ and $\mu_0 H_c$, extracted from hysteresis loops (see 5.2.1), under varying deposition Temperature T_{depo}, we plot the saturation magnetization $\mu_0 M_s$ as a function of T_{depo} (see Fig. 5.11 (a)) and the coercive field $\mu_0 H_c$ depending on T_{depo} (see. Fig. 5.11 (b)) of GdN thin films produced at N_2/Ar=40 % and P_{depo}=45 W (see also Tabs. A.3,A.4).

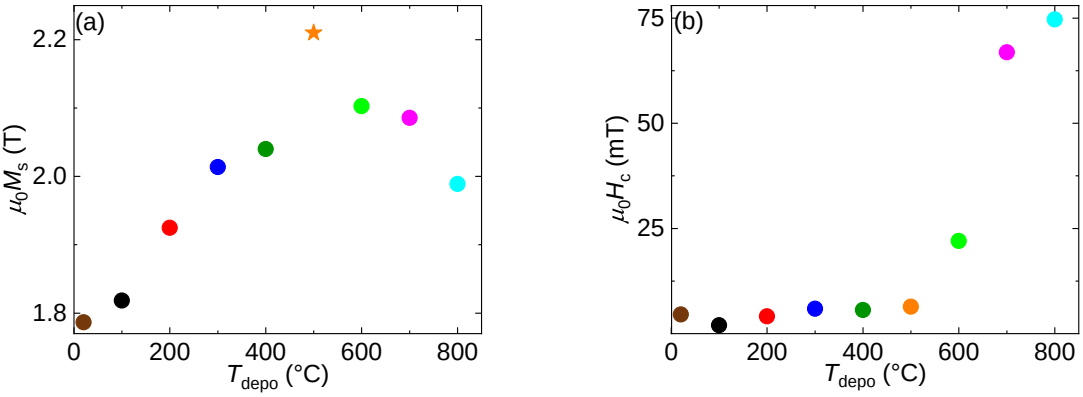

Fig. 5.11: Extracted static magnetic parameters $\mu_0 M_s$ and $\mu_0 H_c$ of GdN thin films grown under varying deposition temperatures T_{depo} at N_2/Ar=40 % and P_{depo}=45 W: (a) $\mu_0 M_s(T_{depo})$-plot shows an increasing N_2/Ar gas flow ratio corresponds to an increasing $\mu_0 M_s$ and a maximum $\mu_0 M_{s,max}$=2.21 T at T_{depo}=500 °C (see orange star). Thereafter, with an increasing T_{depo} we observe a decreasing behavior of $\mu_0 M_s$ reducing down to a value of $\mu_0 M_s$=1.98 T at T_{depo}=800 °C. (b) $\mu_0 H_C(T_{depo})$-plot shows in 20 °C≤T_{depo}≤500 °C a low coercive field $\mu_0 H_c$ close to the zero value. Thereafter, from $\mu_0 H_C$=6.4 mT at T_{depo}=500 °C (see orange data point) an increasing T_{depo} corresponds to an increasing $\mu_0 H_C$ and a maximum value at T_{depo}=800 °C.

Figure 5.11 (a) shows the evolution of the saturation magnetization $\mu_0 M_s$ of GdN thin films are grown under varied deposition temperature T_{depo} at N_2/Ar=40 % and a deposition power of P_{depo}=45 W. Here, an increasing T_{depo} corresponds to an increasing saturation magnetization $\mu_0 M_s$ and then a maximum $\mu_0 M_{s,max}$=2.21 T is observed at T_{depo}=500 °C (see orange star in Fig. 5.12 (a)). Starting from this maximum value, an increasing T_{depo} provides a decreasing $\mu_0 M_s$ reducing down to $\mu_0 M_s$=1.98 T at T_{depo}=800 °C. The coercive field $\mu_0 H_c$ as a function of the deposition temperature T_{depo} of GdN thin films fabricated under varied T_{depo} at N_2/Ar=40 % and P_{depo}=45 W is illustrated in Fig. 5.11 (b).

In the T_{depo}-area 20 °C≤T_{depo}≤500 °C, we observe a low and approximately constant coercive field $\mu_0 H_c$. Starting from $\mu_0 H_c$=6.4 mT at T_{depo}=500 °C (see orange data point in Fig. 5.12 (b)), an increasing T_{depo} corresponds to an increasing $\mu_0 H_c$ and then a maximum value of $\mu_0 H_{c,max}$=74.67 mT results at T_{depo}=800 °C.

The sharp drop of $\mu_0 M_\mathrm{s}$ (see Fig. 5.11 (a)) and the strong increase of $\mu_0 H_\mathrm{c}$ (see Fig. 5.11 (b)) at growth temperatures T_depo>500 °C suggests the thermally induced generation of paramagnetic Gd vacancies in our GdN thin films. Furthermore, *K. Senapati et al.* [54] associated the enhancement of H_c with N deficiency coupled to a secondary phase of GdN (GdN-II). A detailed investigation of the magnetic ordering of GdN (see Sec. 3.3) and the relationship between the static magnetic parameter $\mu_0 M_\mathrm{s}$ and the lattice constant a_lattice (see Sec. 5.3.2) of our GdN thin films is discussed in section 5.14.

As a next step, we investigate the Curie temperature T_C, extracted with two different methods from $M(T)$-measurements (see Sec. 5.1.1), of GdN thin films fabricated under varying deposition temperature T_{depo} at a fixed N_2/Ar gas flow ratio of 40 % as well as a sputtering power P_{depo}=45 W. Fig. 5.12 (a) shows the Curie temperature $T_{C,t}$, determined by using the tangent method (see 5.1.1), as a function of the deposition temperature T_{depo} and Fig. 5.6 (b) illustrates the Curie temperature $T_{C,S}$, examined by the intersection of the FC and ZFC curve of $M(T)$-measurement (see Sec. 5.1.1), depending on T_{depo}. The difference value ΔT_C, defined as the difference of the transition temperatures for the two T_C-extraction methods, is shown in Fig. 5.12 (c) (see also Tabs. A.3,A.4).

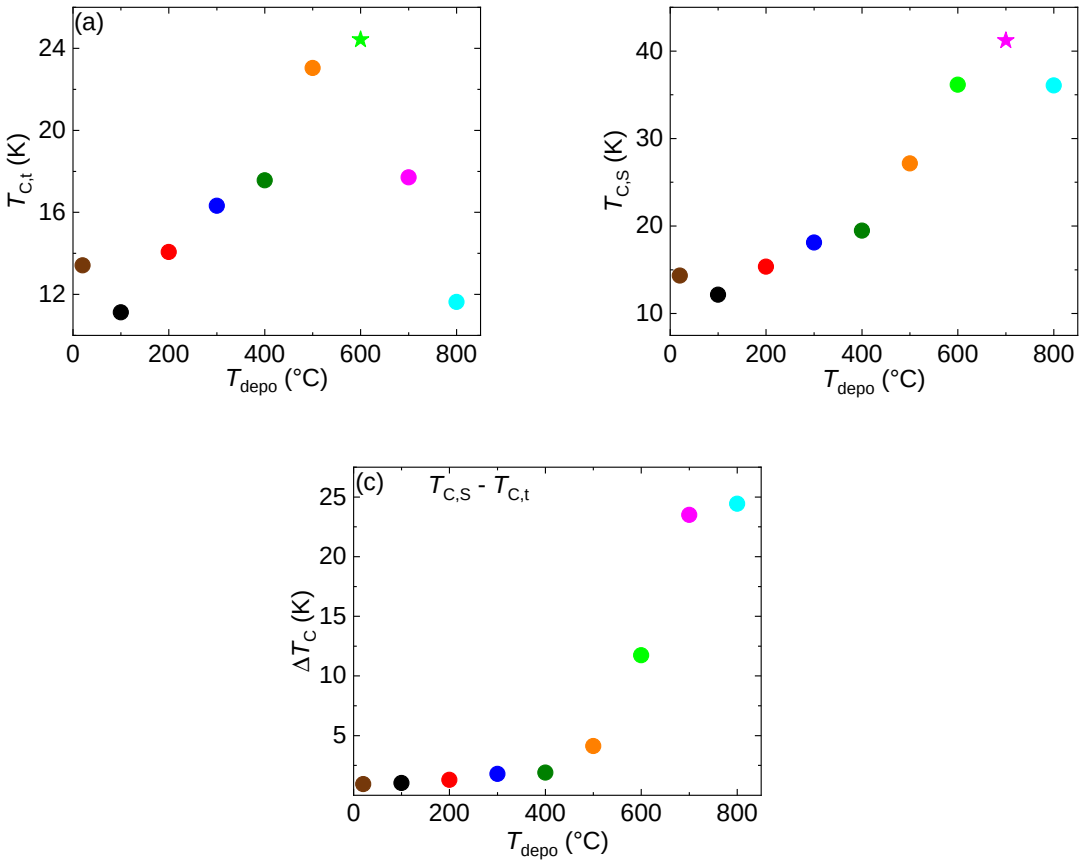

Fig. 5.12: Extracted Curie temperatures T_C of GdN thin films grown under varying deposition temperature T_{depo} at N_2/Ar=40 % and P_{depo}=45 W: (a) $T_{C,t}$, extracted with tangent method, depending on T_{depo} shows an increasing T_{depo} corresponds to an increasing $T_{C,t}$ and then results in a maximum $T_{C,t,max}$=24.42 K at T_{depo}=600 °C (see light-green star). Thereafter, with an increasing T_{depo} we observe a decreasing behavior of $T_{C,t}$ with a minimum $T_{C,t,min}$=11.63 K at T_{depo}=800 °C (see light-blue data point). (b) $T_{C,S}$, extracted with intersection method, depending on T_{depo} shows an increasing T_{depo} corresponding to an increasing $T_{C,S}$ and then results a maximum $T_{C,S,max}$=41.21 K at T_{depo}=700 °C (see magenta star). (c) The difference value $\Delta T_C = T_{C,S} - T_{C,t}$ shows in 20 °C$\leq T_{depo} \leq$400 °C a saturation of ΔT_C close to the zero value and then from ΔT_C=500 °C an increasing behavior of ΔT_C for an increasing T_{depo} and a maximum $\Delta T_{C,max}$=24.44 K is observed at T_{depo}=800 °C.

Figure 5.12 (a) shows the Curie temperature $T_{\mathrm{C,t}}$, extracted by using the tangent method (see 5.1.1), of GdN thin films as a function of the deposition temperature T_{depo}. Here, an increasing deposition temperature T_{depo} corresponds to an increasing Curie temperature $T_{\mathrm{C,t}}$ and we get a maximum value of $T_{\mathrm{C,t,max}}$=24.42 K at T_{depo}=600 °C (see light-green star). For higher T_{depo}, we observe a decrease of $T_{\mathrm{C,t}}$ and then a minimum $T_{\mathrm{C,t,min}}$=11.63 K at T_{depo}=800 °C (see light-blue data point). A similar trend is shown in Fig. 5.12 (b), which presents the Curie temperature $T_{\mathrm{C,S}}$, determined by using the intersection method (see 5.1.1), as a function of the deposition temperature T_{depo}. Here, we observe that an increasing deposition temperature T_{depo} gives rise to an increase in the Curie temperature $T_{\mathrm{C,S}}$ and we find a maximum value of $T_{\mathrm{C,S,max}}$=41.21 K at T_{depo}=700 °C (see magenta star). Thereafter, at higher T_{depo}, we observe a decrease of $T_{\mathrm{C,S}}$ with a minimum of $T_{\mathrm{C,S}}$=36.07 K at T_{depo}=800 °C.

Finally, the difference between the two T_{C}-determination methods is calculated by ΔT_{C}=$T_{\mathrm{C,S}}$-$T_{\mathrm{C,t}}$ and presented in Fig. 5.12 (c). In 20 °C≤T_{depo}≤500 °C, only low values for ΔT_{C} occur. Starting from ΔT_{C}=4.12 K at T_{depo}=400 °C (see orange data point in Fig. 5.12 (c)), an increasing T_{depo} corresponds to an increasing ΔT_{C} and then a maximum value of $\Delta T_{\mathrm{C,max}}$=24.44 K is observed at T_{depo}=800 °C. The sharp drop of $T_{\mathrm{C,t}}$ (see Fig. 5.12 (a)) and the strong increase of ΔT_{C} (see Fig. 5.12 (c)) at growth temperatures T_{depo}>500 °C also indicates the thermally induced generation of paramagnetic Gd vacancies in our GdN thin films. The relationship between the static magnetic parameter $\mu_0 M_{\mathrm{s}}$, the Curie temperature $T_{\mathrm{C,S}}$ and the lattice constant a_{lattice} (see Sec. 5.3.2) of our GdN thin films is discussed in section 5.3.3.

5.3.2 Lattice parameters of deposition temperature T_{depo} variation series

This section deals with the study of the crystalline growth of GdN thin films. prepared under varying deposition parameters, by using X-ray diffraction (XRD) spectroscopy (see Sec. 3.5.1). As described in Sec. 3.3, we deposited our GdN thin films between a protective top and bottom buffer layer of TaN (d=20 nm) on a thermally oxidized Si substrate. Figure 5.13 (a)-(c) shows the results of the 2θ-ω scans (see Sec. 3.5.1) of GdN thin films grown with varied deposition temperature T_{depo} at a fixed N_2/Ar gas flow ratios of 40 % and a deposition power P_{depo}=45 W.

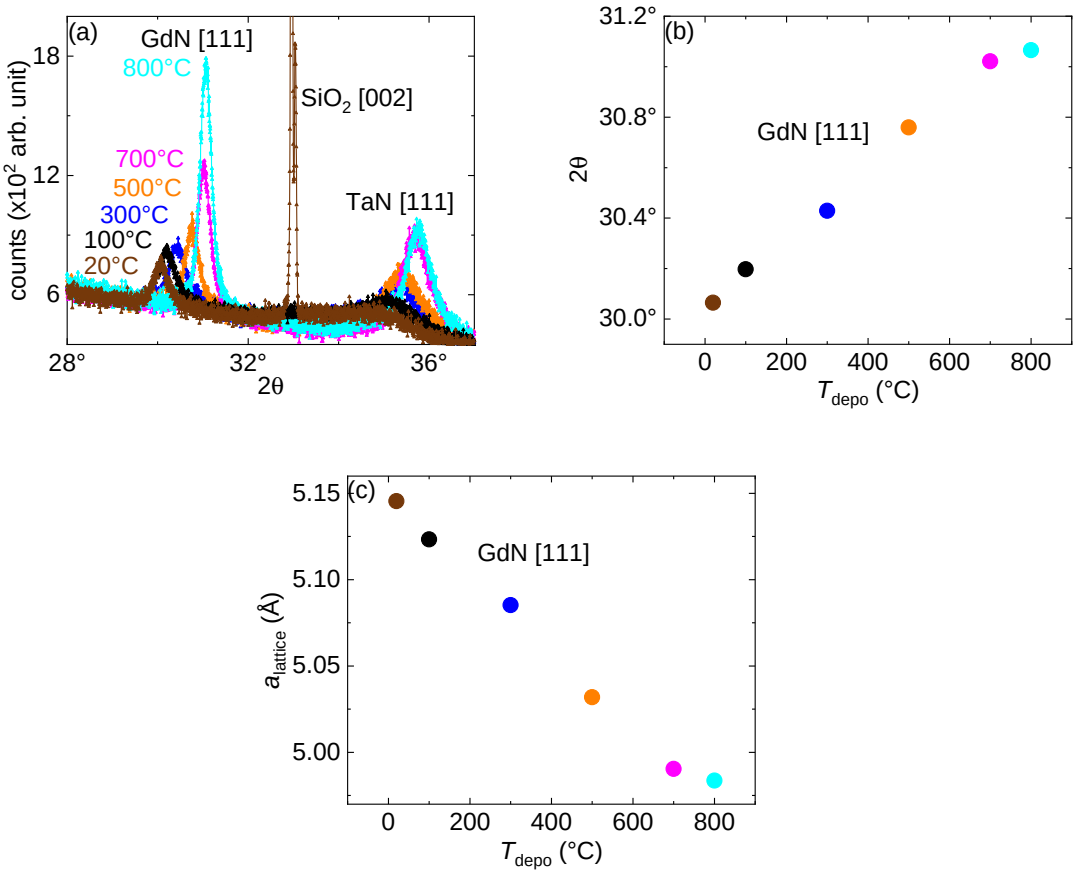

Fig. 5.13: 2θ-ω scans of our GdN thin films deposited on TaN under varying deposition temperatures T_{depo} at N_2/Ar=40 % and P_{depo}=45 W: (a) Reflections from the [111]-direction of GdN (2θ≈31 °) and TaN (2θ≈35.5 °) as well as SiO_2 (2θ≈32.24 °) with [002]-texturing are visible. In the entire T_{depo}-series, an increasing growth temperature T_{depo} corresponds to an increasing 2θ angle and the peak of GdN and TaN with [111]-texturing shift to higher angles. Furthermore, the amplitude A increases and the width w of the curves decreases for higher T_{depo}. (b) $2\theta(T_{\mathrm{depo}})$-plot shows an increasing T_{depo} provides an increasing 2θ for GdN [111]. (c) $a_{\mathrm{lattice}}(T_{\mathrm{depo}})$-plot shows an increasing T_{depo} corresponds to a decreasing a_{lattice} and provides a value of (4.98-5.14) Å for GdN [111].

Figure 5.13 (a) shows the reults of 2θ-ω scans for GdN thin films grown at various deposition temperatures T_{depo} and N_2/Ar=40 % as well as a deposition power P_{depo}=45 W. Here, we observe crystalline reflections at 2θ≈31 ° and 2θ≈35.5 ° and also a weak reflection of SiO_2 at 2θ≈32.9 ° in the [002]-direction.

As described in 5.1.3, we assign the peak positions at $2\theta{\approx}31\,^{\circ}$ and $2\theta{\approx}35.5\,^{\circ}$ to the crystalline reflections of GdN and TaN in the [111]-direction. In the entire T_{depo}-series, we observe that an increasing T_{depo} induces a shift to higher angles for the peak of GdN with [111]-texturing. Furthermore, the amplitude A increases and the width w of the curves decreases for an increasing deposition temperature T_{depo}. Due to annealing effects during the sputtering process of the TaN/GdN/TaN trilayer in the UHV chamber (see Sec. 3.2 and 3.3), we also identify a shift to higher angles for the peak of TaN in the [111]-direction for its fixed growth temperature T_{depo}=500 °C. Therefore, a growth of the amplitude A and a reducing width w of the curves of TaN [111] is visible throughout the entire T_{depo}-series.

Next, we investigate the extracted 2θ angle and the calculated lattice constant a_{lattice} of our GdN films. For this purpose, we plot the crystalline reflection 2θ as a function of the deposition temperature T_{depo} (see Fig. 5.13 (b)). Here, the 2θ angle, which we associated with the crystalline reflection of GdN in [111]-direction, increases with an increasing T_{depo} and then a slight saturation of 2θ is visible at T_{depo}=(700-800) °C. Fig. 5.13 (c) shows the lattice constant a_{lattice} of our GdN thin films, calculated with formula (30), depending on T_{depo}. Here, we observe an increasing T_{depo} corresponding to a decreasing lattice constant a_{lattice} of GdN with [111]-texturing which is also shown in the PhD-thesis of *F. Leuenberger* [62] (see Fig. 4.3). In the work of *K. Senapati et al.* [54], a decrease of the lattice constant $a_{\mathrm{lattice,GdN}}$ is visible in the N-rich zone (Zone 1) coupled to a ferromagnetic (FM) ordering mechanism of GdN (see Fig. 5(a)). Compared to the observed a_{lattice} values in the N_2/Ar gas flow ratio variation series (see Sec. 5.2.2), we obtain an equal value $a_{\mathrm{lattice,GdN}}$=4.99 Å for GdN in [111]-direction [54] and a similar lattice constant $a_{\mathrm{lattice,TaN}}$=4.38 Å of TaN with [111]-texturing [83] in the T_{depo} variation series.

5.3.3 Summary of the deposition temperature T_{depo} variation series and comparison to literature

In section 5.3, we have optimized the deposition temperature T_{depo} of 60 nm GdN thin films, fabricated at a N_2/Ar gas flow ratio of 40 % and a deposition power P_{depo}=45 W, on thermally oxidized Si substrates. From the results of the N_2/Ar gas flow ratio variation series (see Sec. 5.2), we have optimized the growth temperature T_{depo} in 100 °C-steps around the FM GdN thin film fabricated at T_{depo}=500 °C, N_2/Ar=40 % and P_{depo}=45 W. This GdN film exhibited a maximum saturation magnetization $\mu_0 M_{\mathrm{s}}$=2.21 T, a low coercive field $\mu_0 H_{\mathrm{c}}$=6.4 mT and a high Curie temperature $T_{\mathrm{C,S}}$=27.16 K. Based on this reference sample, we have studied in a growth series the impact of varied deposition temperature T_{depo} on the magnetic parameters $\mu_0 M_{\mathrm{s}}$, $\mu_0 H_{\mathrm{c}}$ and T_{C} of GdN. First, the evolution of the magnetic hysteresis loops (see Fig. 5.10 (a)-(d)) of our $M(H)$-measurements (see Sec. 5.1.1 and 5.3.1) show in the T_{depo} variation series the following signature: An increasing deposition temperatrue T_{depo} and fixed N_2/Ar gas flow ratio as well as a defined deposition power P_{depo} corresponds to an increasing saturation magnetization $\mu_0 M_{\mathrm{s}}$ and then a maximum $\mu_0 M_{\mathrm{s,max}}$=2.21 T is found at at T_{depo}=500 °C (see Fig. 5.11 (a)). Thereafter, we have observed a decrease of $\mu_0 M_{\mathrm{s}}$ with increasing T_{depo}. The coercive field $\mu_0 H_{\mathrm{c}}$ saturated close to the zero value in the T_{depo}-area 20 °C$\leq T_{\mathrm{depo}} \leq$500 °C (see Fig. 5.11 (b)) and higher T_{depo} caused an increase of $\mu_0 H_{\mathrm{c}}$ and then a maximum value of $\mu_0 H_{\mathrm{c,max}}$=74.67 mT resulted at T_{depo}=800 °C. The enhancement of H_{c} is described by *K. Senapati et al.* [54] with N deficiency coupled to a secondary phase of GdN (GdN-II). Moreover, we have observed a lifetime $\tau \approx$6 months of GdN thin films produced with varied T_{depo}. This result is compatible with the lifetime τ of the GdN samples fabricated in the N_2/Ar gas flow ratio variation series.

Next, we examine the Curie temperature T_{C} of our GdN thin films fabricated under varied deposition temperature T_{depo} at N_2/Ar=40 % P_{depo}=45 W. From the results of the $M(T)$-measurements (see Sec. 5.1.1), we have determined T_{C} with two different extraction methods and observed for both methods a comparable evolution of T_{C} as a function of varied T_{depo} (see Fig. 5.12 (a)-(b)). First, the Curie temperature $T_{\mathrm{C,t}}$, extracted by using the tangent method (see Sec. 5.1.1), increases for an increasing deposition temperature T_{depo} and then a maximum value of $T_{\mathrm{C,t,max}}$=24.42 K is observed at T_{depo}=600 °C (see Fig. 5.12 (a)). For higher T_{depo}, we observe a decrease of $T_{\mathrm{C,t}}$ and then a minimum $T_{\mathrm{C,t,min}}$=11.63 K at T_{depo}=800 °C. A similar trend revealed for the Curie temperature $T_{\mathrm{C,S}}$, determined by using the intersection method (see Sec. 5.1.1), as a function of the deposition temperature T_{depo}. Here, we have observed an increasing deposition temperature T_{depo} gives rise to an increase in the Curie temperature $T_{\mathrm{C,S}}$ and we observe a maximum value of $T_{\mathrm{C,S,max}}$=41.21 K at T_{depo}=700 °C. Thereafter, a higher T_{depo} leads to a decrease of $T_{\mathrm{C,S}}$ and then a lower value of $T_{\mathrm{C,S}}$=36.07 K resultes at T_{depo}=800 °C. The enhancement of T_{C} describes *K. Senapati et al.* [54] with N vacancies and a resulting lattice distortion coupled to an antiferomagnetic (AFM) behavior of GdN (see Sec. 3.3). However, the GdN thin films in *K. Senapati et al.* [54] were fabricated at room temperature and lower sputtering powers as well as lower gas flow ratios compared to our GdN samples (see Sec. 5.2.3).

As a last step, we have calculated the difference value $\Delta T_{\mathrm{C}}=T_{\mathrm{C,S}}-T_{\mathrm{C,t}}$ of the two extraction methods and observe an increasing behavior of ΔT_{C} started from ΔT_{C}=4.12 K at T_{depo}=400 °C and then a maximum value of $\Delta T_{\mathrm{C,max}}$=24.44 K resulted at T_{depo}=800 °C (see Fig. 5.12 (c)). Therefore, we associated the sharp drop of $T_{\mathrm{C,t}}$ at ΔT_{C}=600 °C (see Fig. 5.12 (a)) and the strong increase of ΔT_{C} (see Fig. 5.12 (c)) at growth temperatures T_{depo}>500 °C to thermally induced Gd vacancies, due to paramagnetic impurities originating from Gd, in our GdN thin films.

To investigate the crystalline growth of GdN thin films at varying deposition parameters, we used X-ray diffraction (XRD) spectroscopy (see Sec. 3.5.1). Here, the results of the 2θ-ω scans (see Sec. 3.5.1) of GdN thin films grown under varied deposition temperature T_{depo} at N_2/Ar=40 % and a deposition power of P_{depo}=45 W revealed crystalline reflections at $2\theta\approx31\,^\circ$ and $2\theta\approx35.5\,^\circ$. By performing a Gaussian fit (see Sec. 5.1.3), we assigned the peak positions to the crystalline reflections of GdN and TaN in the [111]-direction (see Fig. 5.13 (a)). In the entire T_{depo} variation series, we observe, that an increasing deposition temperature T_{depo} accompies an increasing 2θ angle (see Fig. 5.13 (b)) for the x-ray peak of GdN and TaN along the [111]-direction (see Fig. 5.13 (a)). Furthermore, the amplitude A increased and the width w of the curves decreased for higher T_{depo}. Moreover, we calculated (see Eq. 30) the lattice constant a_{lattice} of GdN and TaN with [111]-texturing. Here, we observed that an increasing T_{depo} accompies a decreasing a_{lattice} (see Fig. 5.13 (c)). *K. Senapati et al.* [54] associates the decrease of the lattice constant a_{lattice} of GdN thin films with a nitrogen richness and a ferromagnetic (FM) behavior of GdN in Zone 1 (20 K<T_{C}<60 K). Finally, we extract for GdN in [111]-direction a lattice constant of $a_{\mathrm{lattice,GdN}}\approx5.00$ Å, which is comparable with *K. Senapati et al.* [54]. Furthermore, the computed lattice constant of TaN with [111]-texturing $a_{\mathrm{lattice,TaN}}$=4.38 Å is compatible with the results of *N. Terao et al.* [83]. The values of $a_{\mathrm{lattice,GdN}}$ and $a_{\mathrm{lattice,TaN}}$ are compatible to the results obtained in the N_2/Ar gas flow ratio variation series (see Sec. 5.2.2).

Finally, we investigate the relationship of the extracted saturation magnetization $\mu_0 M_s$ and the Curie temperature $T_{C,S}$ as well as the calculated lattice constant $a_{lattice}$ of our GdN thin films. For this purpose, we plot the saturation magnetization $\mu_0 M_s$ as a function of the Curie temperature $T_{C,S}$ (see Fig. 5.14 (a)). Furthermore, we plot the lattice constant $a_{lattice}$ depending on $T_{C,S}$ (see Fig. 5.14 (b)) of GdN films, which were fabricated under varied deposition temperature T_{depo} at a N_2/Ar gas flow ratio of 40 % and a deposition power of P_{depo}=45 W.

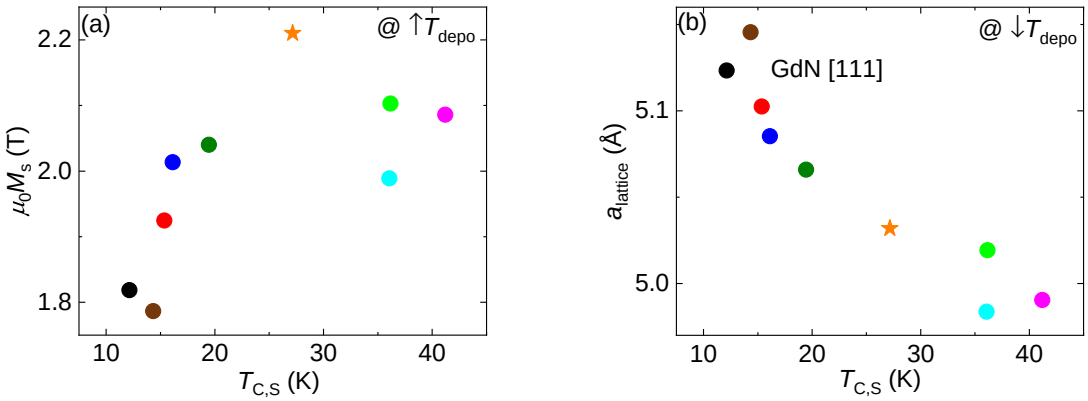

Fig. 5.14: Comparison of the extracted magnetic parameters $\mu_0 M_s$ and $T_{C,S}$ and the calculated lattice constant $a_{lattice}$ of GdN thin films fabricated under varying deposition temperature T_{depo} at N_2/Ar=40 % and P_{depo}=45 W: (a) $\mu_0 M_s(T_{C,S})$-plot shows an increasing Curie temperature $T_{C,S}$ corresponding to an increasing $\mu_0 M_s$ and then a maximum $\mu_0 M_{s,max}$=2.21 T results at $T_{C,S}$=27.16 K (see orange star). For higher temperatures, a decreasing behavior of $\mu_0 M_{s,max}$ is found for $T_{C,S}$>500 °C. (b) $a_{lattice}(T_{C,S})$-plots show an increasing $T_{C,S}$ with decreasing $a_{lattice}$ and a value of 5.03 Å at $T_{C,S}$=27.16 K (see orange star) is visible.

Figure 5.14 (a) shows the evolution of the extracted saturation magnetization $\mu_0 M_s$ as a function of the determined Curie temperature $T_{C,S}$. Here, we observe an increasing $T_{C,S}$ corresponding to an increasing $\mu_0 M_s$ with a maximum $\mu_0 M_{s,max}$=2.21 T at $T_{C,S}$=27.16 K (see orange star in Fig. 5.14 (a)). This GdN thin film represents our reference sample prepared at T_{depo}=500 °C, N_2/Ar=40 % and P_{depo}=45 W. Furthermore, a decreasing behavior of $\mu_0 M_{s,max}$ is found for $T_{C,S}$>500 °C. Fig. 5.14 (b) shows the lattice constant $a_{lattice}$ of our GdN films depending on the Curie temperature $T_{C,S}$. We find with increasing $T_{C,S}$ a decrease of $a_{lattice}$ and only a minor difference in the magnitudes of $a_{lattice}$. At $T_{C,S}$=27.16 K (see orange star in Fig. 5.14 (b)), the GdN thin films exhibit a $a_{lattice}$=5.03 Å.

Compared to the work of *K. Senapati et al.* [54], we observe a comparable trend in the $M_s(T_C)$-plot and $a(T_C)$-plot (see Fig. 5(a) in [54]). Here, an increasing Curie temperature T_C accompies an increasing saturation magnetization M_s and simultaneously a decreasing lattice constant a is shown in Zone 1 (20 K<T_C<60 K). This area is the so called N-rich zone (Zone 1), where GdN shows a ferromagnetic (FM) behavior. In Zone 2 (60 K<T_C<120 K) occurs GdN in a N deficient secondary phase (GdN-II) manifests with an antiferromagnetic (AFM) ordering controlled by N vacancies. Here, nitrogen vacancies are responsible for an increase in the lattice constant a coupled to a lattice distortion.

In this section, we have optimized the deposition temperature T_{depo} at a defined N_2/Ar gas flow ratio of 40% and a fixed sputtering power of P_{depo}=45 W. We have observed for the growth of a FM GdN thin film prepared at T_{depo}=500 °C, N_2/Ar=40 % and P_{depo}=45 W a maximum saturation magnetization $\mu_0 M_{\mathrm{s}}$=2.21 T, a low coercive field $\mu_0 H_{\mathrm{c}}$=6.4 mT, a high Curie temperature $T_{\mathrm{C,S}}$=27.16 K and a low lattice constant a_{lattice}=5.03 Å (see orange star in Fig. 5.14 (a) and (b)). Based on the discussion of our data in section 5.3 and 5.2 as well as the comparison with the work of *K. Senapati et al.* [54], we conclude that only ferromagnetic (FM) GdN thin films ($T_{\mathrm{C,S,max}}$=41.21 K, $a_{\mathrm{lattice,max}}$ =5.14 Å) and no dual-phase GdN samples with an antiferromagnetic (AFM) behavior grew in our deposition temperature T_{depo} variation series.

Table 5.2 shows the growth recipe, which was developed in the N_2/Ar gas flow ratio variation series (see Sec. 5.2) as well as in the deposition temperature T_{depo} variation series (see Sec. 5.3), and the magnetic properties of a FM GdN thin film with a layer thickness of 60 nm. As described in section 3.3), we deposited the GdN thin film between a protective top and bottom buffer layer of TaN (d=20 nm) on a thermally oxidized Si substrate. For the growth of the TaN layers, we use the deposition parameters N_2/Ar=10 %, T_{depo}=500 °C, P_{depo}=30 W and p_{depo}=5 × 10^{-3} mbar.

Growth recipe of FM GdN				
Growth parameters	N_2/Ar [%]	T_{depo} [°C]	P_{depo} [W]	p_{depo} [mbar]
	40	500	45	5×10^{-3}
Magnetic properties	$\mu_0 M_{\mathrm{s}}$ [T]	$\mu_0 H_{\mathrm{c}}$ [mT]	$T_{\mathrm{C,t}}$ [K]	$T_{\mathrm{C,S}}$ [K]
	2.21	6.41	23.04	27.16

Tab. 5.2: Growth parameters and magnetic properties of a FM GdN thin film with a layer thickness of 60 nm fabricated on a thermally oxidized Si substrate.

In the following section 5.4, we use the growth recipe to compare FM GdN thin films fabricated in the tilt-in (tin) and face-to-face (ftf) sputtering configuration. Finally, we test in section 5.5 the optimized growth recipe for its reproducibility and investigate the growth of a GdN thin film on a crystalline sapphire (Al_2O_3) substrate.

5.4 Comparison of various sputtering configurations

In this section we compare the growth of GdN thin films fabricated in two different sputtering configurations in the SUPERBOWL. For the development of an ideal growth recipe for FM GdN thin films (see Sec. 5.2 and 5.3), we prepared our samples in the tilt-in (tin) sputtering configuration, i.e. in a confocal alignment of magnetron and substrate (see Sec. 3.2). Here, in individual variation series we optimized the N_2/Ar gas flow ratio and the sputtering power P_{depo} (see Sec. 5.2) as well as the growth temperature T_{depo} (see Sec. 5.3). In a further optimization series, we test the growth recipe for fabricating GdN thin films in the face-to-face (ftf) sputtering configuration (see Sec. 3.2). Finally, we investigate the magnetic parameters $\mu_0 M_{\mathrm{s}}$, $\mu_0 H_{\mathrm{c}}$ and T_{C} depending on the growth parameters of the GdN samples resulting from the two sputtering configurations.

5.4.1 N_2/Ar gas flow ratio variation series: tilt-in vs. face-to-face

First, we compare the growth of FM GdN thin films, fabricated at varying N_2/Ar gas flow ratios and a fixed deposition temperature of T_{depo}=500 °C as well as a fixed sputtering power of P_{depo}=45 W, in the tilt-in (tin) and face-to-face (ftf) sputtering configuration. Figure 5.15 (a)-(d) shows the extracted magnetic parameters $\mu_0 M_s$, $\mu_0 H_c$ and T_C (see Sec. 5.1.1) as a function of the N_2/Ar gas flow ratio of GdN thin films fabricated in different sputtering configurations (see also Tab. A.5).

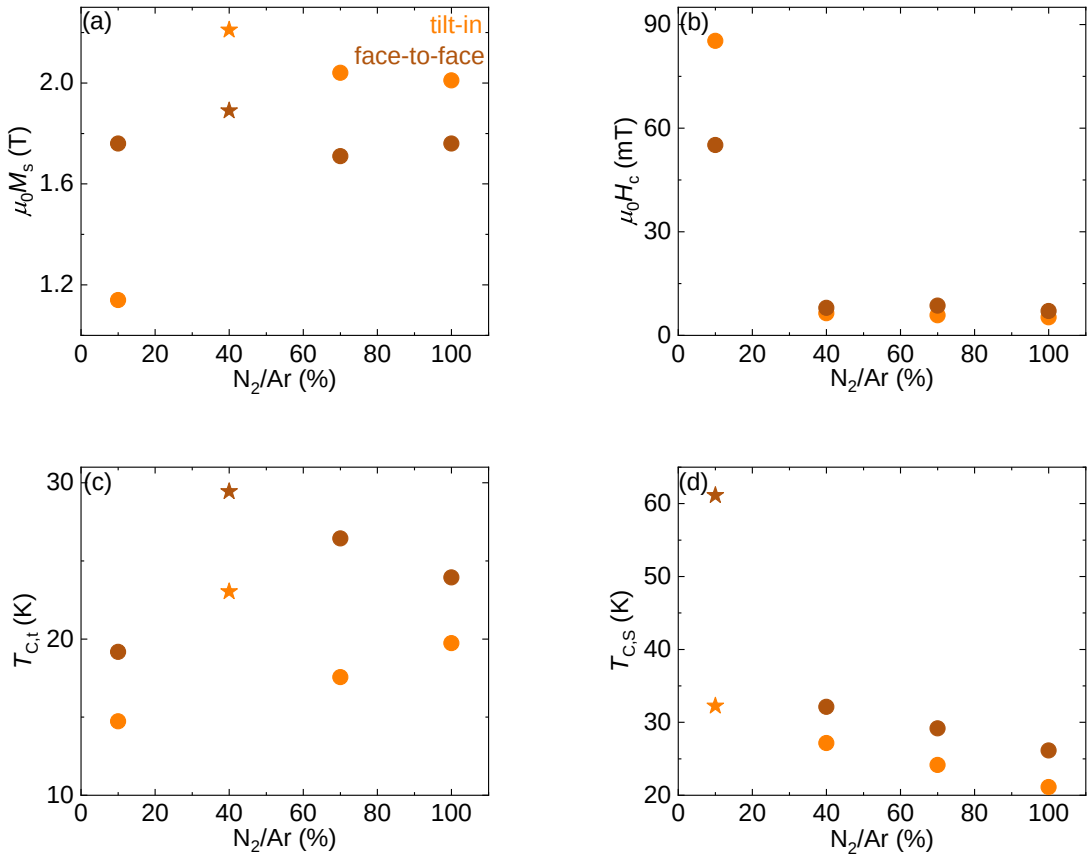

Fig. 5.15: Comparison of GdN thin films grown at varying N_2/Ar gas flow ratios and fixed deposition power P_{depo} in the tilt-in (tin) and face-to-face (ftf) sputtering configuration: (a) $\mu_0 M_s$(N_2/Ar)-plot shows in face-to-face an approximately constant saturation magnetization $\mu_0 M_s$ and a maximum $\mu_0 M_{s,max}$=1.89 T at N_2/Ar=40 % (see brown star). In tilt-in we observe a non-monotonic behavior of $\mu_0 M_{s,max}$ and a maximum $\mu_0 M_{s,max}$=2.21 T at N_2/Ar=40 % (see orange star). (b) $\mu_0 H_c$(N_2/Ar)-plot illustrates in both sputtering configurations a reduction of the corecive field $\mu_0 H_c$ by an increasing N_2/Ar gas flow ratio. (c) $T_{C,t}$(N_2/Ar)-plot shows in tilt-in and in face-to-face a similar trend for the evolution of the Curie temperature $T_{C,t}$. Here, a maximum $T_{C,t,max}$=23.04 K (see orange star) and $T_{C,t,max}$=29.44 K (see brown star) is found at N_2/Ar=40 %. (d) $T_{C,S}$(N_2/Ar)-plot shows in both sputtering configurations a decrease for $T_{C,S}$ and we observe a maximum $T_{C,S,max}$=32.24 K (see orange star) and $T_{C,S,max}$=61.12 K (see brown star) at N_2/Ar=10 %.

Panel 5.15 (a) shows the saturation magnetization $\mu_0 M_s$ depending on the N_2/Ar gas flow ratio. Here, we observe in face-to-face (see brown data points in Fig. 5.15 (a)) an almost constant saturation magnetization $\mu_0 M_s$ throughout the entire N_2/Ar gas flow range and a slight maximum $\mu_0 M_{s,max}$=1.89 T at N_2/Ar=40 % (see brown star).

In tilt-in (see orange data points in Fig. 5.15 (a)), we observe the in section 5.2.1 discussed behavior of $\mu_0 M_s$ and a maximum $\mu_0 M_{s,max}$=2.21 T at N_2/Ar=40 % (see orange star). Figure 5.15 (b) illustrates the coercive field $\mu_0 H_c$ as a function of the N_2/Ar gas flow ratio. In the entire N_2/Ar gas flow range, we notice a similar trend for $\mu_0 H_c$ in both sputtering configurations. Here, an increasing N_2/Ar gas flow ratio corresponds to a decreasing corecive field $\mu_0 H_c$ and then starting from N_2/Ar=40 % a saturation of $\mu_0 H_c$ is visible. Except of $\mu_0 H_c$ at N_2/Ar=10 %, we observe in both sputtering configurations almost equal magnitudes of $\mu_0 H_c$.

Figure 5.15 (c) and (d) present the Curie temperature T_C, determined by using tow different extraction methods (see Sec. 5.1.1), as a function of the N_2/Ar gas flow ratio. Here, we identify for the evolution of $T_{C,t}$ and $T_{C,S}$ a comparable trend in both sputtering configurations, however the values of $T_{C,t}$ and $T_{C,S}$ tend to be higher in face-to-face (see brown data points in Fig. 5.15 (c) and (d)) than in tilt-in (see orange data points in Fig. 5.15 (c) and (d)). Here, we observe in tilt-in a maximum $T_{C,t,max}$=23.04 K (see orange star at N_2/Ar=40 % in Fig. 5.15 (c)) and $T_{C,S,max}$=32.24 K (see orange star at N_2/Ar=10 % in Fig. 5.15 (d)) as well as in face-to-face a maximum $T_{C,t,max}$=29.44 K (see brown star at N_2/Ar=40 % in Fig. 5.15 (c)) and $T_{C,S,max}$=61.12 K (see brown star at N_2/Ar=10 % in Fig. 5.15 (d)). Due to the unequal behavior of $T_{C,t}$ and $T_{C,S}$ at varying N_2/Ar gas flow ratios, we assume that paramagnetic Gd vacancies also exist in our FM GdN thin films fabricated in the face-to-face sputtering configuration.

5.4.2 Deposition power P_{depo} variation series: tilt-in vs. face-to-face

Next, we compare the growth of FM GdN thin films, produced with various sputtering powers P_{depo} at a fixed N_2/Ar gas flow ratio of 40 % and a fixed growth temperature T_{depo}=500 °C, in the tilt-in (tin) and face-to-face (ftf) sputtering configuration. Figure 5.16 (a)-(d) shows the extracted magnetic parameters $\mu_0 M_{\mathrm{s}}$, $\mu_0 H_{\mathrm{c}}$ and T_{C} (see Sec. 5.1.1) as a function of the deposition power P_{depo} of GdN thin films fabricated in different sputtering configurations (see also Tab. A.6).

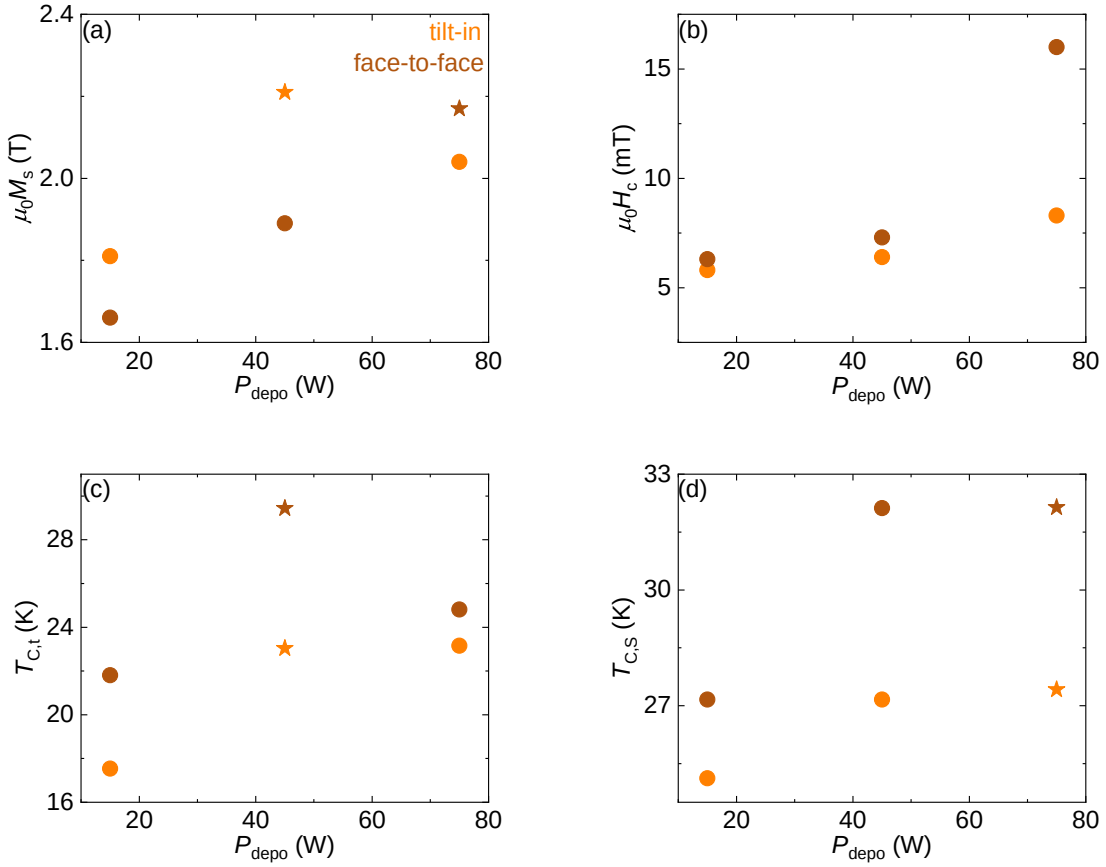

Fig. 5.16: Comparison of GdN thin films grown at varying deposition powers P_{depo} and fixed N_2/Ar gas flow ratio in the tilt-in (tin) and face-to-face (ftf) sputtering configuration: (a) $\mu_0 M_{\mathrm{s}}(P_{\mathrm{depo}})$-plot shows a linear progression in face-to-face and a maximum saturation magnetization $\mu_0 M_{\mathrm{s,max}}$=2.17 T at P_{depo}=75 W (see brown star). In tilt-in no clear trend is visible and we get a maximum $\mu_0 M_{\mathrm{s,max}}$=2.21 T at P_{depo}=45 W (see orange star). (b) $\mu_0 H_{\mathrm{c}}(P_{\mathrm{depo}})$-plot shows in tilt in a linear slope and in face-to-face an noticeable increased coercive field $\mu_0 H_{\mathrm{c}}$ at P_{depo}=75 W. (c) $T_{\mathrm{C,t}}(P_{\mathrm{depo}})$-plot illustrates in tilt-in and in face-to-face an approximately equal evolution of the Curie temperature $T_{\mathrm{C,t}}$. Here, we observe a maximum $T_{\mathrm{C,t,max}}$=23.04 K (see orange star) and $T_{\mathrm{C,t,max}}$=29.44 K (see brown star) at P_{depo}=45 W. (d) $T_{\mathrm{C,S}}(N_2/\mathrm{Ar})$-plot shows in both sputtering configurations an increasing P_{depo} is corresponding to an increasing $T_{\mathrm{C,S}}$ and a maximum $T_{\mathrm{C,S,max}}$=27.42 K (see orange star) and $T_{\mathrm{C,S,max}}$=31.14 K (see brown star) is visible at P_{depo}=75 W.

Figure 5.16 (a) shows the saturation magnetization $\mu_0 M_{\mathrm{s}}$ as a function of the sputtering power P_{depo}. Here, we observe in face-to-face (see brown data points in Fig. 5.16 (a)) a linear relationship between $\mu_0 M_{\mathrm{s}}$ and P_{depo} and a maximum $\mu_0 M_{\mathrm{s,max}}$=2.17 T at P_{depo}=75 W (see brown star).

In the face-to-face sputtering configuration, we observe a non-monotonic evolution of $\mu_0 M_s$ with a maximum $\mu_0 M_{s,max}$=2.21 T at P_{depo}=45W (see orange star) as discussed in section 5.2.1. The coercive field $\mu_0 H_c$ depending on the deposition power P_{depo} is presented in Figure 5.16 (b). Here, in the entire P_{depo}-range, we find in the tilt-in sputtering configuration an almost linear relationship between $\mu_0 H_c$ and P_{depo}. In face-to-face, we observe only in the P_{depo}-region 15 W$\leq P_{depo} \leq$45 W a comparable trend to the tilt-in configuration. Increased values for $\mu_0 H_c$ are visible at P_{depo}=75 W in both sputtering configurations.

Pictures 5.15 (c) and (d) illustrate the Curie temperature T_C, determined by using our two extraction procedures (see Sec. 5.1.1), as a function of the deposition power P_{depo}. Here, we observe in both sputtering configurations a comparable trend for the evolution of $T_{C,t}$ and $T_{C,S}$, however the values of the Curie temperatures are higher in face-to-face (see brown data points in Fig. 5.16 (c) and (d)) than in tilt-in configuration (see orange data points in Fig. 5.16 (c) and (d)). Here, we observe in tilt-in a maximum $T_{C,t,max}$=23.04 K (see orange star at P_{depo}=45 W in Fig. 5.16 (c)) and $T_{C,S,max}$=27.42 K (see orange star at P_{depo}=75 W in Fig. 5.16 (d)) as well as in face-to-face a maximum $T_{C,t,max}$=29.44 K (see brown star at P_{depo}=45 W in Fig. 5.16 (c)) and $T_{C,S,max}$=32.14 K (see brown star at P_{depo}=75 W in Fig. 5.16 (d)). Because of the comparable evolution of $T_{C,t}$ and $T_{C,S}$ at varying P_{depo}, we assume that fewer paramagnetic, metallic Gd defects are generated in our FM GdN thin films prepared in the face-to-face sputtering configuration.

Finally, we observe in the N_2/Ar gas flow ratio variation series and in the optimization series of the sputtering Power P_{depo} a higher saturation magnetization $\mu_0 M_s$, an approximately equal coercive field $\mu_0 H_c$ and a lower Curie temperature $T_{C,t}$ and $T_{C,S}$ for our GdN samples fabricated in the tilt-in conficuration as compared to the face-to-face sputtering configuration. Thus, we assume that the tilt-in configuration provides optimal results. We test in the following section 5.5 the optimized tilt-in growth recipe (N_2/Ar=40 %, T_{depo}=500 °C and P_{depo}=45 W) and the resulting magnetic properties ($\mu_0 M_s$=2.21 T, $\mu_0 H_c$=6.4 mT, $T_{C,S}$=27.16 K) of FM GdN for its reproducibility on a thermally oxidized Si substrate. Furthermore, we investigate the growth of a GdN thin film on a crystalline sapphire (Al_2O_3) substrate by using the developed tilt-in growth recipe.

5.5 Reproducibility and growth on different substrate materials

In the last section of this chapter, we analyse the optimized growth recipe and the resulting magnetic properties (see Tab. 5.2) of FM GdN thin films with a layer thickness of 60 nm for its reproducibility on a thermally oxidized Si substrate $(6 \times 10 \times 0.55)\,\mathrm{mm}^3$. Afterwards, we investigate the growth of a GdN thin film on a crystalline sapphire (Al_2O_3) substrate by using the developed tilt-in growth recipe, which is listed in Tab. 5.2. Figure 5.17 (a)-(d) shows the results of the SQUID magnetometry measurements (see Sec. 3.3) by using the optimized growth parameters of GdN thin films deposited on various substrate materials.

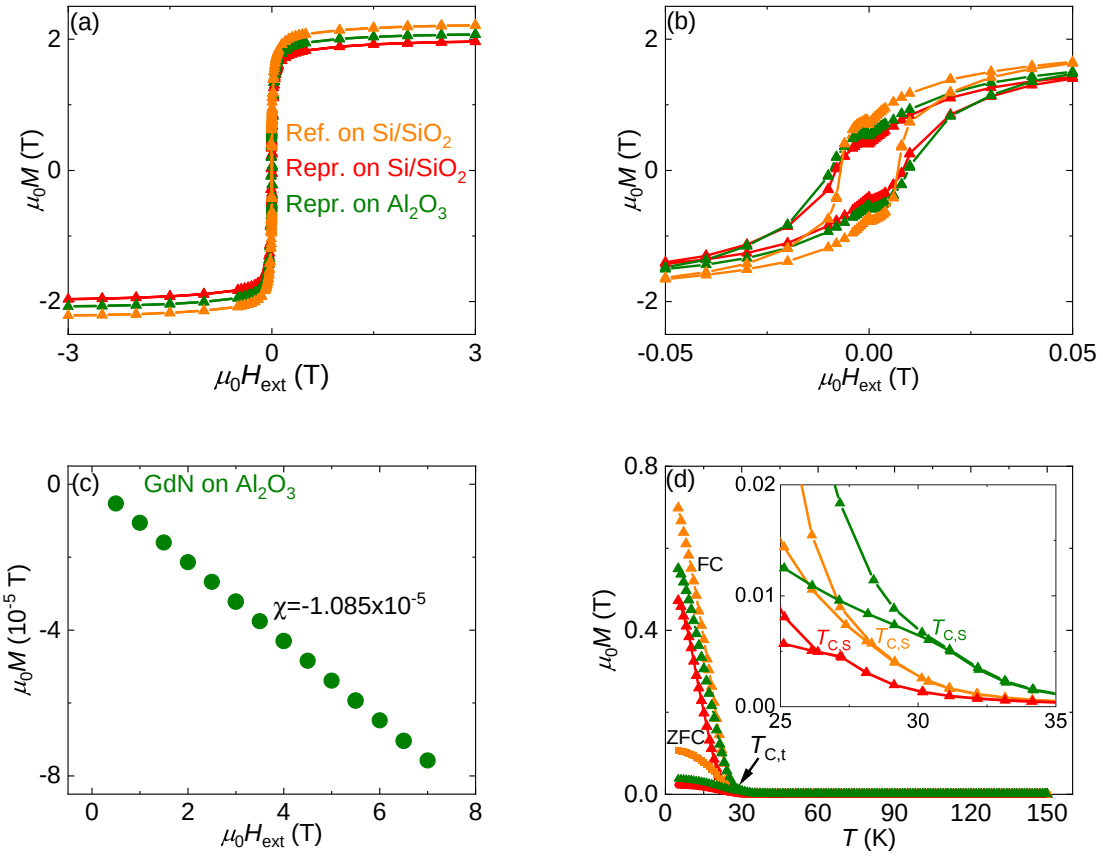

Fig. 5.17: Comparison of GdN thin films grown on different substrate materials by using the optimized growth recipe: (a) Hysteresis loops $M(H)$ recorded at T=5 K for GdN thin films grown on various substrate materials: A maximum saturation magnetization $\mu_0 M_{\mathrm{s,max}}$=2.21 T is shown for the GdN reference sample grown on SiO_2 (orange curve) and a slight reduced $\mu_0 M_{\mathrm{s}}$ of 1.96 T is visible for the reproduced GdN film on SiO_2 (red curve). The reproduced GdN thin film grown on Al_2O_3 (green curve) shows a slight reduced $\mu_0 M_{\mathrm{s}}$ of 2.07 T. (b) Zoomed in view of the hysteresis loops to extract the coercive field $\mu_0 H_{\mathrm{c}}$: Considering the magnitude of $\mu_0 H_{\mathrm{c}}$, no significant modification of the coercive field is observed for GdN thin films prepared on different substrates. (c) Result of the magnetic background correction of the reproduced GdN thin film grown on a sapphire (Al_2O_3) substrate at T_{meas}=150 K: The negative slope of $M(H)$ in the saturated state shows a diamagnetic response and we extract a magnetic susceptibility of $\chi = -1.085 \times 10^{-5}$. (d) Results of the $M(T)$-measurements: The Curie temperature $T_{\mathrm{C,t}}$, extracted with the tangent method, shows no siginificant alteration for GdN thin films deposited on different substrates. Zoomed in image from (d) illustrates the determination of the Curie temperature $T_{\mathrm{C,S}}$ by determining the intersection of field cooled (FC) and zero field cooled (ZFC) curve of various substrates: A higher $T_{\mathrm{C,S}}$ for GdN on Al_2O_3 (green curve) compared to GdN on SiO_2 (red and orange curve) is visible.

Figure 5.17 (a) and (b) shows the magnetic hysteresis loops of our optimized GdN reference sample on a thermally oxidized Si substrate (see Sec. 5.2 and 5.3) as well as reproducibility tests using GdN sample on Si/SiO_2 and Al_2O_3 fabricated with the optimized deposition recipe (see Tab. 5.2). Here, we observe fo the reference sample a maximum saturation magnetization of $\mu_0 M_{s,max}$=2.21 T and a minimum coercive field $\mu_0 H_{c,min}$=6.41 mT (see orange hysteresis loop in Fig 5.17 (a) and (b)) throghout the entire reproducibility series. However, the $M(H)$-curve of the reproduced GdN on Si/SiO_2 shows a slight reduction in its saturation magnetization and an increased width. For this reproduced sample, we extract a lower saturation magnetization $\mu_0 M_s$=1.96 T and a higher coercive field $\mu_0 H_c$=8.11 mT (see red hysteresis loop in Fig 5.17 (a) and (b)). The GdN thin film deposited on a crystalline sapphire (Al_2O_3) substrate shows a slight reduced saturation magnetization $\mu_0 M_{s,max}$=2.07 T as well as noticeable increased coercive field $\mu_0 H_{c,min}$=9.21 mT (see green hysteresis loop in Fig 5.17 (a) and (b)) compared to the static magnetic properties of our GdN reference sample on Si/SiO_2. We attribute the slightly worse magnetic properties of this sample to a slow degradation of the used Gd sputtering target.

The magnetic background correction (see Sec. 5.2) performed at T_{meas}=5 K for a GdN thin film grown on a Al_2O_3 substrate is illustrated in Fig. 5.17 (c). Here, the recorded $M(H_{ext})$ results in a negative slope, which corresponds to a diamagnetic response and a magnetic susceptibility of $\chi = -1.085 \times 10^{-5}$. The extracted magnetic susceptibility is compatible with the value $\chi_{Al_2O_3} \approx -1.86 \times 10^{-5}$ published in the work of *K. Gas et al.* [85] and is already subtracted from the $M(H_{ext})$ raw data in Fig 5.17 (a) and (b). As described in Sec. 5.2, the background correction of GdN on a thermally oxidized Si substrate provides a magnetic susceptibility of $\chi = 1.97 \times 10^{-6}$. This paramagnetic background is already subtracted from with the $M(H_{ext})$ raw data and plotted as corrected hysteresis loops of GdN on Si/SiO_2 (see Fig. 5.17 (a) and (b)).

Figure 5.17 (d) shows the results of the $M(T)$-measurements (see Sec. 5.1.1) for our GdN reference sample on a thermally oxidized Si substrate as well as a reproducibility GdN thin film on Si/SiO_2 and Al_2O_3. Here, we observed for the reproducibility GdN sample a Curie temperature of $T_{C,t}$=22.33 K extracted by using the tangent method (see Sec. 5.1.1). This value is slightly lower than the Curie temperature $T_{C,t}$=23.04 K of our GdN reference sample. However, the GdN thin film on Al_2O_3 shows a noticeable inceased Curie temperature of $T_{C,t}$=27.92 K. The zoomed in view of the $M(T)$-measurements in Fig. 5.17 (d) presents the Curie temperatures $T_{C,S}$ by performing the intersection method. Here, we observe for GdN thin films sputtered on various substrate materials the following evolution of $T_{C,S}$: For the reproducibility GdN thin film on Si/SiO_2 we obtain a Curie temperature of $T_{C,S}$=26.36 K which is slightly lower than $T_{C,S}$=27.16 K of our GdN reference sample. However, the GdN thin film on Al_2O_3 shows a clearly increased Curie temperature of $T_{C,S}$=31.17 K.

Finally, we analyze the crystalline growth of our FM GdN thin films deposited on different substrate materials by performing X-ray diffraction (XRD) spectroscopy (see Sec. 3.5.1). Figure 5.18 (d) shows the results of the 2θ-ω scans (see Sec. 3.5.1) of GdN thin films grown on a thermally oxidized Sisubstrates and on crystalline sapphire (Al_2O_3) by using the optimized growth recipe (see table 5.2).

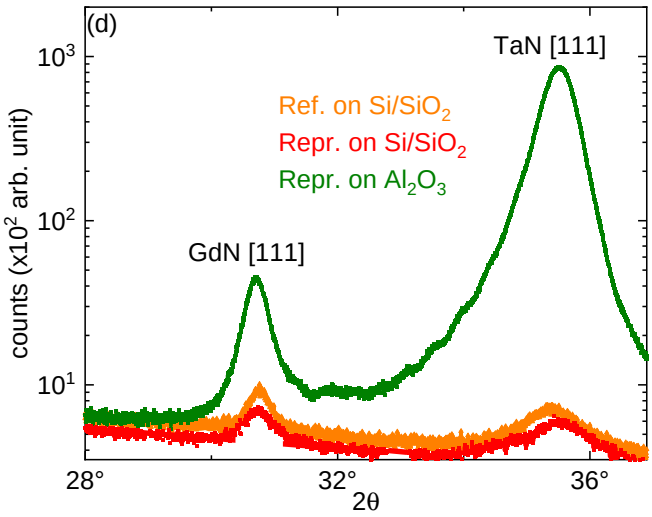

Fig. 5.18: 2θ-ω scans of GdN thin films deposited on different substrate materials by using the optimized growth recipe: Reflections from the [111]-direction of GdN ($2\theta \approx 31\,°$) and TaN ($2\theta \approx 35.5\,°$) are visible. The reproducibility GdN film on Si/SiO_2 (see red curve) shows no significant modification in its crystalline growth compared to the GdN reference sample on Si/SiO_2 (see orange curve). For the reproduced GdN thin film grown on a crystalline sapphire (Al_2O_3) substrate is an improved crystalline quality visible.

Image 5.18 (d) illustrates the results of the XRD spectroscopy measurements of the GdN reference and reproduced GdN thin films deposited on a Si/SiO_2- (see orange and red curve) as well as on a Al_2O_3-substrate (see green curve) by using the optimized growth parameters. Here, we observe crystalline reflections at $2\theta \approx 31\,°$ and $2\theta \approx 35.5\,°$, which we assign to the crystalline reflections of GdN and TaN in the [111]-direction (see 5.1.3). Regarding to the peak position 2θ, the amplitude A and the width w of the recorded XRD reflectometry curves, no significant modification for the reproduced GdN sample (see red curve) is visible compared to the GdN reference sample on Si/SiO_2 (see orange curve). However, we observe for the reproduced GdN thin film deposited on a crystalline Al_2O_3 substrate an noticeable increased peak at $2\theta \approx 31\,°$ for GdN [111] as well as a considerable higher peak at $2\theta \approx 35.5\,°$ for TaN with [111]-texturing which indicates an improved crystalline growth of our TaN/GdN/TaN trilayer on Al_2O_3. This result demonstrates, that the crystalline growth of GdN gives rise to films with a higher T_C. In my bachelor´s thesis [18] 2020, we also observed at 35.4 ° the pronounced peak for TaN [111] on a crystalline Al_2O_3 substrate, which is comparable to the results published by *T. Hashizume et al.* [82]). For all GdN samples in the reproducibility series, we calculate with formula (30) a lattice constant of $a_{\text{lattice,GdN[111]}} \approx 5.032$ Å (comparable with *K. Senapati et al.* [54]) and $a_{\text{lattice,TaN[111]}} \approx 4.38$ Å (comparable with *N. Terao et al.* [83]), see Tab. 5.4.

The results of the reproducibility of our optimized GdN growth recipe are summarized in the following tables. The magnetic parameters of GdN deposited on different substrate materials are listed in Tab. 5.3.

Magnetic properties of FM GdN on Si/SiO_2 and Al_2O_3				
	$\mu_0 M_s$ [T]	$\mu_0 H_c$ [mT]	$T_{C,t}$ [K]	$T_{C,S}$ [K]
Ref. on Si/SiO_2	2.21	6.41	23.04	27.16
Repr. on Si/SiO_2	1.96	8.11	22.33	26.36
Repr. on Al_2O_3	2.07	9.21	27.92	31.17

Tab. 5.3: Magnetic properties of FM GdN thin films with a layer thickness of 60 nm deposited on thermally oxidized Si and Al_2O_3 substrates.

Tab. 5.4 contains the Gaussian fit parameters of the 2θ-ω scans of GdN thin films grown on thermally oxidized Si and a crystalline sapphire (Al_2O_3) substrate.

Lattice parameters of FM GdN on Si/SiO_2 and Al_2O_3					
	Reflection	x_c [°]	A [arb. unit]	w [°]	$a_{lattice}$ [Å]
Ref. on Si/SiO_2	GdN [111]	30.76 ± 0.0021	1129.42 ± 4.034	0.29 ± 0.0068	5.028
	TaN [111]	35.37 ± 0.0041	262.31 ± 6.0025	0.79 ± 0.013	4.39
Repr. on Si/SiO_2	GdN [111]	30.74 ± 0.0048	119.56 ± 4.086	0.43 ± 0.012	5.032
	TaN [111]	35.47 ± 0.0079	183.35 ± 6.61	0.79 ± 0.013	4.38
Ref. on Al_2O_3	GdN [111]	30.71 ± 0.0011	1533.35 ± 11.51	0.36 ± 0.0025	5.036
	TaN [111]	35.49 ± 0.0011	54603.43 ± 246.095	0.55 ± 0.0024	4.37

Tab. 5.4: Guassian fit parameters x_c, A, w=FWHM/$\sqrt{ln(4)}$ and calculated lattice constant $a_{lattice}$ of GdN thin films deposited on thermally oxidized Si and Al_2O_3 substrates.

In this section we have verified the reproducibility of our optimized growth recipe of FM GdN thin films on various substrate materials such as thermally oxidized Si and Al_2O_3. Due to the good static magnetic properties $\mu_0 M_s$ and $\mu_0 H_c$ and the low Curie temperature T_C as well as a reasonable crystalline quality of GdN on Si/SiO_2, we use in the following chapter 6 for the fabrication of a ferromagnetic insulating (FMI) GdN thin film (see Sec. 6.1) and the magnetotransport measurements of GdN multilayer systems (see Sec. 6.2.1, 6.2.2 and 6.2.3) the optimized growth recipe for a FM GdN thin film on a thermally oxidized Si substrate (see Tab. 5.2).

6 Magnetotransport properties of GdN/TaN heterostructures

In the following chapter, we investigate the magnetotransport properties of several GdN/TaN multilayer thin films. For this purpose, we first verify the magnetic and insulating characteristics of our ferromagnetic insulating (FMI) GdN thin films prepared by using the optimized growth recipe of a FM GdN thin film (see Tab. 5.2). As a next step, we apply the developed growth recipe of a FMI GdN thin film to deposite various FMI GdN/TaN multilayer heterostructures on thermally oxidized Si substrates. Our multilayer thin films are patterned into Hallbar structures by using photolithography and argon ion milling (see Sec. 3.4). In order to investigate the spin Hall magnetoresistance (SMR) in a ferromagnetic insulating (FMI)/normal metal (NM) interface (see Sec. 2.3), we fabricate a so-called *SMR test sample* with the stack sequence AlN/GdN/TaN/AlN. To verify the manifestation of said SMR effect in our test sample, we prepare also a *SMR reference sample* consisting of the layers AlN/GdN/AlN/TaN/AlN. Here, the intermediate AlN layer serves to interrupt the FMI/NM interface and hence to suppress the SMR effect. In addition, we also investigate the transport in a pure TaN thin film of a AlN/TaN/AlN trilayer. Afterwards, we study the magnetic and resistive properties of our GdN multilayer systems by performing SQUID magnetometry experiments as well as electrical transport measurements. In the main part of this chapter, we investigate the *field-dependent magnetotransport properties* and the *angle-dependent magnetoresistance* (ADMR) of our FMI GdN multilayer stacks by performing magnetotransport experiments in a cryogenic environment. Finally, we analyse the results of the magnetotransport experiments with respect to the spin Hall magnetoresistance (SMR).

6.1 Insulating properties of FM GdN

This section deals with the investigation of the insulating properties of the FM GdN thin films which we have optimized in Chapter 5. To this end, we deposited an aluminium nitride (AlN)/GdN/AlN heterostructure on a thermally oxidized Si substrate $(6 \times 10 \times 0.55)\,\mathrm{mm}^3$ by using the optimized growth recipe of a FM TaN/GdN/TaN thin film (see Tab. 5.2). Figure 6.1 shows the stack sequence of the FMI AlN/GdN/AlN heterostructure thin film.

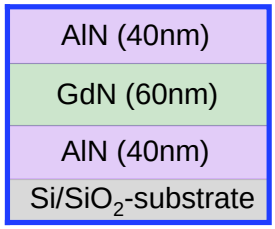

Fig. 6.1: Stack sequence of a FMI AlN/GdN/AlN heterostructure on a Si/SiO_2 substrate.

In the FMI trilayer system shown in Fig. 6.1, we have replaced the protective TaN buffer layers (d=20 nm) with insulating AlN top and bottom layers (d=40 nm) which likewise protects the intermediate GdN thin film from oxidation (see Sec. 3.3). The growth of AlN has already been optimized by *G. Terrasanta et al.* [86] and we use for the fabrication of

our AlN layers the growth parameters N_2/Ar=35 %, T_{depo}=20 °C, P_{depo}=70 W and p_{depo}= 5×10^{-3} mbar (see Tab. 6.1). As described in section 3.2, we fabricate the GdN thin film (d=60 nm) in the tilt-in sputtering configuration in the chamber SP4 and for the deposition of AlN, we use the face-to-face configuration in the sputter chamber SP2 of the SB.

As a first step, we verify the unchanged static magnetic properties $\mu_0 M_s$, $\mu_0 H_c$ and the Curie temperature T_C of the FMI AlN/GdN/AlN thin film. Fig. 6.2 (a)-(c) shows the magnetic hysteresis curve $M(H_{ext})$ for this sample recorded in the SQUID magnetometry measurements (see Sec. 4.4).

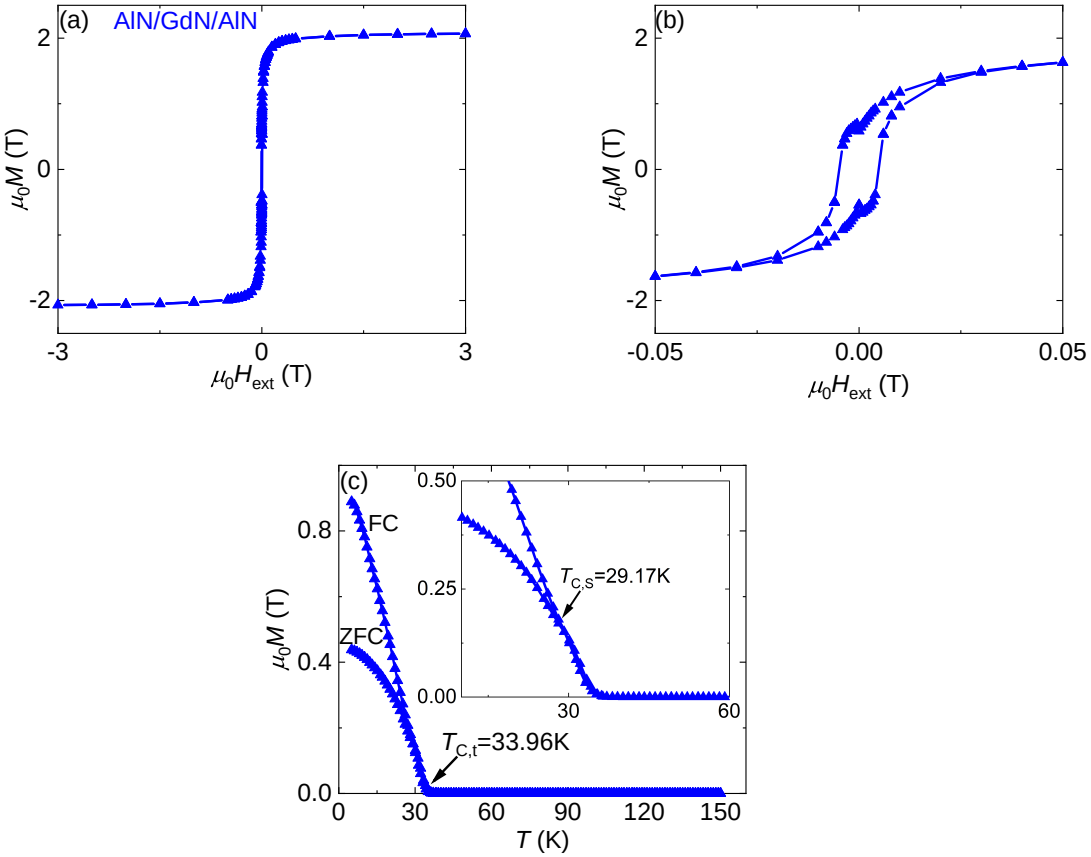

Fig. 6.2: Magnetic properties of the FMI AlN/GdN/AlN thin film: (a) Magnetic hysteresis loop recorded at T=5 K. A saturation magnetization of $\mu_0 M_s$=2.01 T is observed. (b) Zoomed in view of the hysteresis loop from (a) to extract a coercive field of $\mu_0 H_c$=4.47 mT. (c) Result of the $M(T)$-measurement: Curie temperatures of $T_{C,t}$=33.96 K and $T_{C,S}$=29.17 K (see zoomed in view of (c)) are determined with the two different extraction methods.

Figure 6.2 (a) shows the magnetic hysteresis loop of the AlN/GdN/AlN heterostructure by performing SQUID magnetometry at T=5 K. Here, we observe a saturation magnetization of $\mu_0 M_s$=2.01 T which is slightly reduced compared to $\mu_0 M_s$=2.21 T of our TaN/GdN/TaN reference sample. We associate the reduction of the effective saturation magnetization $\mu_0 M_{eff}$ with a formation of a thin $Al_xGd_{1-x}N$-phase at the interface, as described in the publications by *Y. Chen et al.* [87] and *C. A. Ekstrum et al.* [88]. The zoomed in view of the magnetic hysteresis loop (see Fig. 6.2 (b)) shows a slightly lower coercive field $\mu_0 H_c$=4.47 mT in contrast to the coercive field $\mu_0 H_c$=6.41 mT of the optimized GdN thin film.

Panel 6.2 (c) presents the results of the $M(T)$-measurements (see Sec. 5.1.1) of our AlN/GdN/AlN thin film. Here, we observe a Curie temperature of $T_{C,t}$=33.96 K extracted by using the tangent method (see Sec. 5.1.1) which is approximately 10 K higher than the Curie temperature of our optimized TaN/GdN/TaN thin film. The extracted T_C is comparable to the result published in the work of *R. Vidyasagar et al.* [12]. For the Curie temperature $T_{C,S}$ by performing the intersection method (see zoomed in view in Fig. 6.2 (c)), we extracted a slight increased value of $T_{C,S}$=29.17 K compared to $T_{C,S}$=27.16 K of our GdN reference sample. The clear difference between $T_{C,t}$ and $T_{C,S}$ indicates the presence of metallic, paramagnetic Gd vacancies also in our AlN/GdN/AlN heterostructure.

Next, we investigate the insulating properties of the AlN/GdN/AlN thin film by performing an electrical transport measurement (see Sec. 4.1) using the Van-der-Pauw method (see Sec. 4.2) in a cryogenic environment. Fig. 6.3 (a)-(b) illustrates the results of the transport experiments of the unpatterned (6 x 10) mm^2 AlN/GdN/AlN heterostructure measured in zero field $\mu_0 H_{ext}$=0 T.

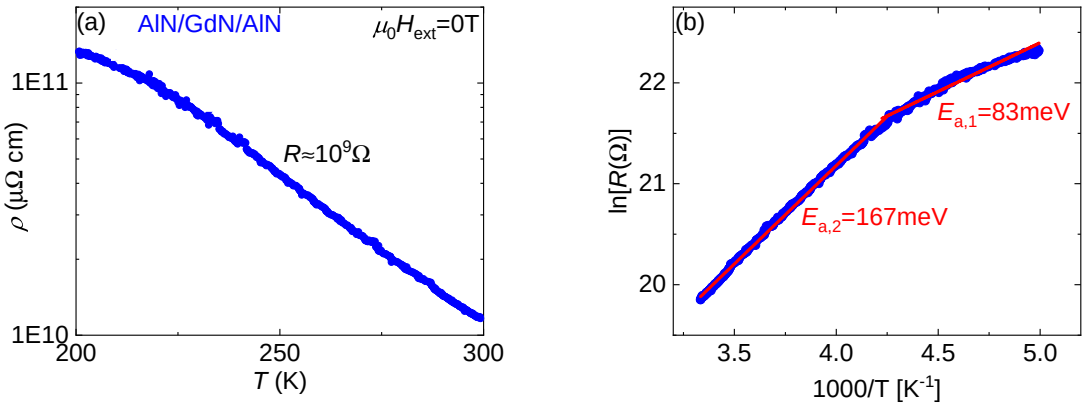

Fig. 6.3: Resistive characteristics of the FMI AlN/GdN/AlN thin film: (a) $\rho(T)$ recorded at $\mu_0 H_{ext}$=0 T. In the T-area 200 K<T<300 K is an average electrical resistance of R≈10^9 Ω observable and a maximum value ρ_{max}≈1.33 × 10^{11} μΩ cm of the electrical resistivity is visible at T=200 K. (b) Arrhenius plot to determine the activation energy E_a of the FMI AlN/GdN/AlN: $E_{a,1}$=83 meV (225 K<T<200 K) and $E_{a,2}$=167 meV (300 K<T<230 K).

The insulating properties of the FMI GdN thin film are shown in Fig. 6.2 (a), where the electrical resistivity ρ is plotted in a logarithmic scale as a function of the temperature T. Here, we observe an increasing resistivity ρ with a decreasing temperature T and a maximum value of ρ_{max}≈1.33 × 10^{11} μΩ cm (R_{max}≈4.89 × 10^9 Ω) is visble at T=200 K. In the entire T-range 200 K<T<300 K, we find an electrical resistance of R≈10^9 Ω which suggests good insulating properties of our FMI AlN/GdN/AlN thin film. The high electrical resistive properties of our trilayer thin film is comparable to the value of ρ≈1 MΩcm observed at T≈300 K for Gd-doped GaN thin films (d=400−700 nm) in the work of *S. Dhar et al.* [13]. Finally, we determine the activation energy E_a of our FMI trilayer heterostructure by performing an Arrhenius plot of the raw data measured in the transport experiment. For this purpose, we introduce the Arrhenius function [89]

$$\rho = \rho_0 \cdot e^{\frac{E_a}{k_B \cdot T}}, \tag{31}$$

where k_B is the Boltzmann constant and T presents the absolute temperature. Fig. 6.2 (b) shows the Arrhenius plot. Here, we plot the natural logarithm of the electrical resistance R as a function of the reciprocal temperature T. To determine the activation energy, $E_{a,1}$ we perform in two T-regions a linear regression on our Arrhenius plot (see Fig. 6.2 (b)). Afterwards, we calculate the activation energy by using the value of the extracted slope m and we obatin the relationship $E_a = m \cdot k_B$. For $225\,K < T < 200\,K$ we extract an activation $E_{a,1} = (83 \pm 1.082)\,meV$ as well as a value of $E_{a,2} = (167 \pm 0.368)\,meV$ in $300\,K < T < 230\,K$, by using the method illustrated in Fig. 5 in the work of *S. Balaji et al.* [89]. In Fig. 6.3 (b), we observe that the electrical resistance falls slowly in the low T-area $225\,K < T < 200\,K$ by an activation energy of $E_{a,1} = (83 \pm 1.082)\,meV$. However, in the T-area $300\,K < T < 230\,K$, the electrical resistance decreases rapidly, accompanied with an activation energy of $E_{a,2} = (167 \pm 0.368)\,meV$, and reaches its minimum near room temperature $T = 300\,K$. Furthermore, we observe an intersection of the two activation energies $E_{a,1,2}$ at $T \approx 220\,K$. Finally, we associate the two different activation energies with two temperature regimes in our FMI semiconductor. Here, we assume that the conductivity is governed by defect transport from paramagnetic, metallic Gd impurities in the range $300\,K < T < 230\,K$ and thus a lower electrical resistance R is visible in this T-range. Table 6.1 shows the growth recipe and the magnetic properties of the FMI AlN/GdN/AlN thin film on a $(6 \times 10 \times 0{,}55)\,mm^3$ Si/SiO_2 substrate.

Growth recipe of FMI GdN ($R \approx 10^9\,\Omega$)				
Stack sequence	N_2/Ar [%]	T_{depo} [°C]	P_{depo} [W]	p_{depo} [mbar]
AlN (40nm)	35	20	70	5×10^{-3}
GdN (60nm)	40	500	45	5×10^{-3}
AlN (40nm)	35	20	70	5×10^{-3}
Magnetic properties	$\mu_0 M_s$ [T]	$\mu_0 H_c$ [mT]	$T_{C,t}$ [K]	$T_{C,S}$ [K]
	2.01	4.47	33.96	29.17

Tab. 6.1: Growth parameters and magnetic properties of a FMI AlN/GdN/AlN heterostructure.

6.2 Magnetotransport experiments

Regarding to the study of the spin Hall magnetoresistance (SMR) (see chapter 7), we investigate the *field-dependent magnetotransport properties* (see Sec. 6.2.4, 6.2.5, 6.2.6) the *angle-dependent magnetoresistance* (ADMR) (see Sec. 6.2.7) of various Hall-bar (HB) structures patterned (see Sec. 3.4) into ferromagnetic insulating (FMI) GdN multilayers by performing magnetotransport experiments. To verify a SMR effect in a ferromagnetic insulating (FMI)/normal metal (NM) bilayer (see Sec. 2.3), we prepare a FMI GdN/TaN thin film as well as a GdN/AlN/TaN sample in which we interrupt the FMI/NM interface with an intermediate AlN layer. Furthermore, we also investigate the magnetotransport properties in a pure TaN layer of a AlN/TaN/AlN heterostructure. Moreover, we examine with a SQUID magnetometer (see Sec. 4.4) the magnetic parameters $\mu_0 M_s$, $\mu_0 H_c$, T_C and investigate the resistive properties of the multilayer heterostructures by performing electrical transport measurements in a cryogenic experimental setup (see Sec. 4.1).

6.2.1 Magnetic properties and temperature-dependent resistance $R(T)$ of a AlN/GdN/TaN/AlN heterostructure

As a first step, we fabricate a FMI GdN/TaN multilayer heterostructure on a thermally oxidized Si substrate $(6 \times 10 \times 0.55)\,\mathrm{mm}^3$ by using the optimized growth recipe of a FMI AlN/GdN/AlN thin film (see Tab. 6.1). Figure 6.4 illustrates the stack sequence of the GdN mulitlayer heterostructure.

Fig. 6.4: *SMR test sample*: FMI AlN/GdN/TaN/AlN heterostructure on a Si/SiO_2 substrate.

In the FMI multilayer heterostructure (see Fig. 6.4), we deposited a FMI/normal metal (NM) bilayer, consisting of GdN (d=60 nm)/TaN (d=10 nm), between two insulating AlN (d=40 nm) top and bottom layers. For the fabrication of the TaN layer, we use the growth parameters N_2/Ar=35 %, T_{depo}=500 °C, P_{depo}=30 W and p_{depo}= 5×10^{-3} mbar (see Tab. 6.2). This so-called *SMR test sample* enables the investigation of a potentiall spin Hall magnetoresistance (SMR) created in the FMI/NM interface (see Sec. 2.3) by analyzing the data of the magnetotransport experiments (see chapter 7). We first determine the magnetic properties $\mu_0 M_s$, $\mu_0 H_c$, T_C (see Fig. 6.5 (a)-(c)) and investigate the characteristics of the temperature-dependent resistance (see Fig. 6.6 (a) and (b)) of the GdN/TaN multilayer system.

Figure 6.5 (a)-(c) illustrates the results of the SQUID magnetometry experiments (see Sec. 4.4) of the unpatterned $(6 \times 10)\,\mathrm{mm}^2$ AlN/GdN/TaN/AlN heterostructure.

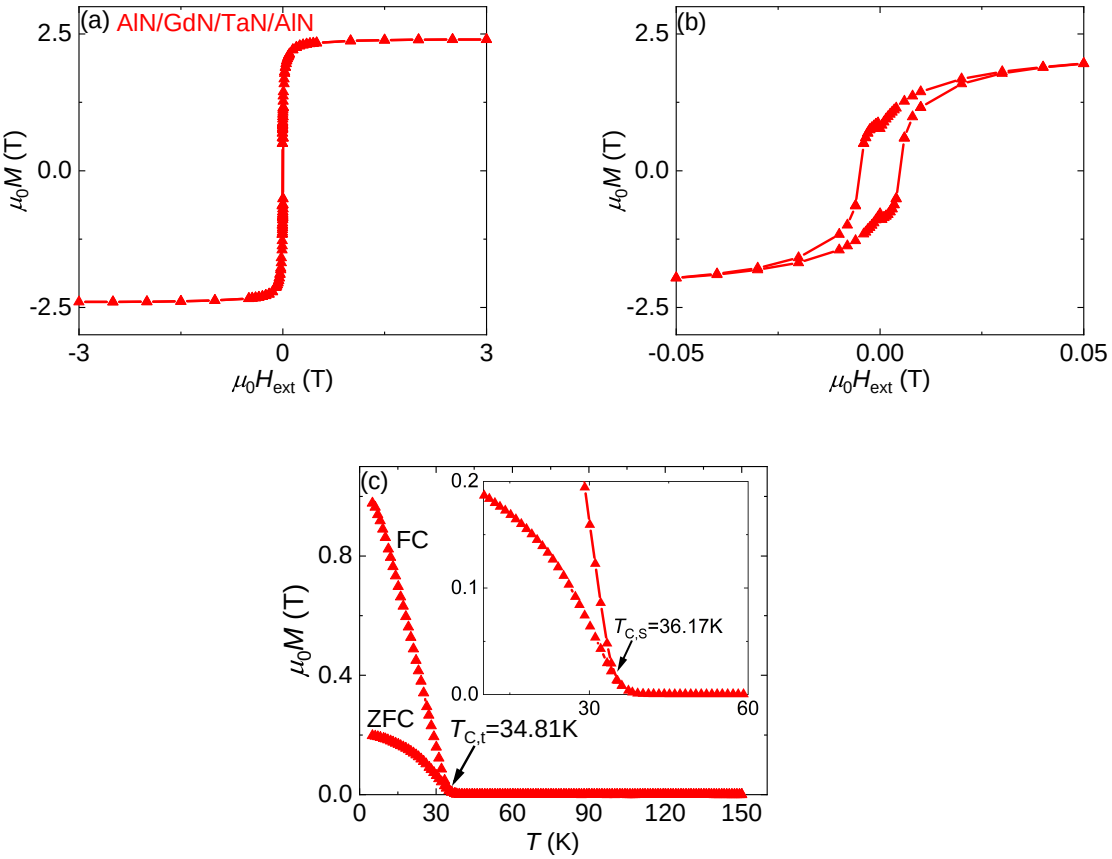

Fig. 6.5: Magnetic properties of the *SMR test sample*: (a) Magnetic hysteresis loop recorded at T=5 K. A saturation magnetization of $\mu_0 M_s$=2.39 T is visible. (b) Zoomed in view of the hysteresis loop from (a) to extract a coercive field of $\mu_0 H_c$=4.85 mT. (c) Result of the $M(T)$-measurement: Curie temperatures of $T_{C,t}$=34.81 K and $T_{C,S}$=36.17 K (see zoomed in view of (c)) are determined with the two different extraction methods.

In Fig 6.5 (a), we extract a saturation magnetization of $\mu_0 M_s$=2.39 T from the hysteresis loop (see Sec. 5.1.1) of our *SMR test sample*. The value is noticeably increased compared to the saturation magnetization $\mu_0 M_s$=2.01 T of the FMI AlN/GdN/AlN thin film (see Tab. 6.1). Figure 6.5 (b) shows a zoomed in view of the hysteresis loop from Fig 6.5 (a). Here, we observe a coercive field of $\mu_0 H_c$=4.85 mT which is comparable to the coercive field $\mu_0 H_c$=4.74 mT of the AlN/GdN/AlN sample (see Tab. 6.1). The results of the $M(T)$-measurements of the AlN/GdN/TaN/AlN heterostructure are shown in Fig 6.5 (c). Here, we determine a Curie temperature of $T_{C,t}$=34.81 K by performing the tangent method (see Sec. 5.1.1). The extracted Curie temperature is approximately equal to $T_{C,t}$=33.96 K of the FMI AlN/GdN/AlN thin film (see Tab. 6.1). The zoomed in view of Fig 6.5 (c) shows the extraction of the Curie temperature $T_{C,S}$=36.17 K by forming the intersection of the FC- and ZFC-curve (see Sec. 5.1.1). This value is substantially increased in contrast to $T_{C,S}$=29.17 K of the ferromagnetic insulating AlN/GdN/AlN sample (see Tab. 6.1). The small difference between $T_{C,t}$ and $T_{C,S}$ of the AlN/GdN/TaN/AlN heterostructure indicates a low amount of metallic paramagnetic Gd in our *SMR test sample*.

Figure 6.6 (a)-(b) shows the electrical resistance R evolution with temperature of the Hall-bar patterned AlN/GdN/TaN/AlN multilayer thin film (*SMR test sample*) derived from the electrical transport measurements (see Sec. 4.1).

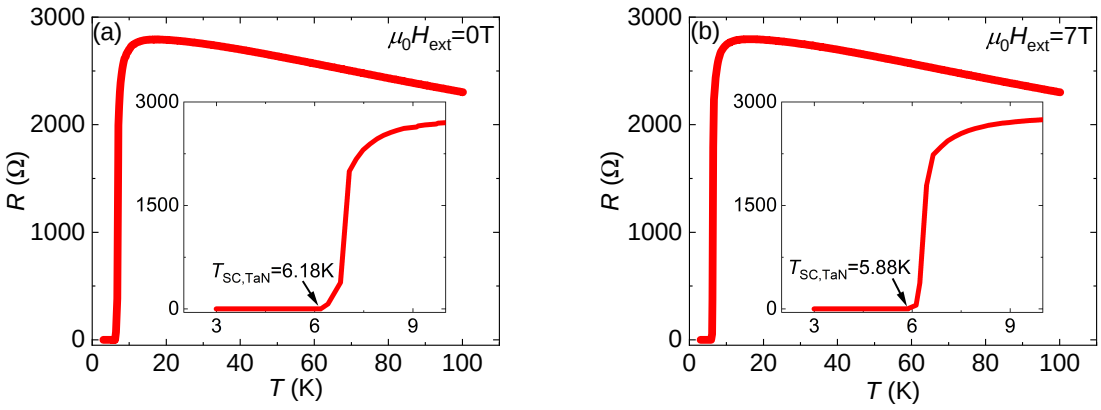

Fig. 6.6: Resistive properties of the *SMR test sample*: $R(T)$ recorded at $\mu_0 H_{ext}$=0 T (a) and at $\mu_0 H_{ext}$=7 T (b). For both measurements is in the T-area 10 K<T<100 K an average electrical resistance of R≈2.5 kΩ is found and a maximum value of R≈2.8 kΩ is visible at T≈10 K. The zoomed in view in (a) and (b) shows a superconducting (SC) transition temperature in the T-area 3 K<T<10 K. For $\mu_0 H_{ext}$=0 T a SC temperature of $T_{SC,\,TaN}$=6.18 K is visible and for $\mu_0 H_{ext}$=7 T a value of $T_{SC,\,TaN}$=5.88 K is extracted.

Panel 6.6 (a) and (b) illustrates the electrical resistance R as a function of the temperature T measured in the so-called in-plane (ip) direction (H-field is applied in the sample plane) and at I_{meas}=50 μA. For to the magnetotransport experiments (see Sec. 6.2.4), we recorded $R(T)$ at zero field $\mu_0 H_{ext}$=0 T (see Fig. 6.6 (a)) and at $\mu_0 H_{ext}$=7 T (see Fig. 6.6 (b)). In the T-range 10 K<T<100 K, we observe an average electrical resistance of R≈2.5 kΩ for both measurements. Furthermore, we observe in this T-range a decreasing temperature T is corresponding to an increasing resistance R and a maximum value of R≈2.8 kΩ is visible at T≈10 K. The zoomed in view in Fig. 6.6 (a) and (b) shows the behavior of the electrical resistance R in the T-area 3 K<T<10 K. Here, we observe zero electrical resistance in the T-range 3 K<T<6 K which we associate with the superconductivity (SC) of the TaN layer (d=10 nm) in our FMI GdN multilayer heterostructure. In the zero field measurement $\mu_0 H_{ext}$=0 T, we identify a superconducting (SC) temperature of $T_{SC,\,TaN}$=6.18 K and for $\mu_0 H_{ext}$=7 T we extract the SC temperature $T_{SC,\,TaN}$=5.88 K which demonstrates, that TaN does become superconducting even for an applied in-plane field up to 7 T in our magnetotransport experiments.

A comparable SC temperature of TaN is published in the work of *P. W. Swatek et al.* [28] and we observe a SC temperature of $T_{SC,\,TaN}$=5.6 K measured at $\mu_0 H_{ext}$=0 T which is associated with δ-TaN (d=10 nm). Furthermore, we observe in [28] a maximum electrical resistance of R≈130 Ω at T≈10 K which is substantially lower compared to the electrical resistance R of our *SMR test sample* with the direct GdN (FMI)/TaN (SC) interface. In my BA thesis 2020, we assign T_{SC}≈5.5 K to c-TaN with a cubic crystal structure. The relationship between the SC TaN layer and the FMI GdN thin film is discussed in the results of the magnetotransport experiments (see Sec. 6.2.4).

Table 6.2 shows the growth recipe, the magnetic-, the superconducting (SC)- and the resistive-properties of the *SMR test sample* on a Si/SiO_2 substrate $(6\,\mathrm{x}\,10\,\mathrm{x}\,0.55)\,\mathrm{mm}^3$.

Growth recipe of the *SMR test sample*				
Stack sequence	N_2/Ar [%]	T_{depo} [°C]	P_{depo} [W]	p_{depo} [mbar]
AlN (40nm)	35	20	70	5×10^{-3}
TaN (10nm)	35	500	30	5×10^{-3}
GdN (60nm)	40	500	45	5×10^{-3}
AlN (40nm)	35	20	70	5×10^{-3}
Magnetic properties	$\mu_0 M_{\mathrm{s}}$ [T]	$\mu_0 H_{\mathrm{c}}$ [mT]	$T_{\mathrm{C,t}}$ [K]	$T_{\mathrm{C,S}}$ [K]
	2.39	4.85	34.81	36.17
SC- / resistive-properties	$T_{\mathrm{SC,TaN(0\,T)}}$ [K]	$R_{(0\,\mathrm{T})}$ [Ω]	$T_{\mathrm{SC,TaN(7\,T)}}$ [K]	$R_{(7\,\mathrm{T})}$ [Ω]
	6.18	2500	5.88	2500

Tab. 6.2: Growth parameters, magnetic-, superconducting (SC)- and resistive-properties of a FMI AlN/GdN/TaN/AlN heterostructure.

6.2.2 Magnetic properties and temperature-dependent resistance R(T) of a AlN/GdN/AlN/TaN/AlN heterostructure

As a next step, we prepare a FMI AlN/GdN/AlN/TaN/AlN heterostructure on a thermally oxidized Si substrate $(6 \times 10 \times 0.55)\,\mathrm{mm}^3$ by modifying the FMI/NM interface of the *SMR test sample* (see Sec. 6.2.1). Figure 6.7 illustrates the stack sequence of the GdN mulitlayer heterostructure.

Fig. 6.7: *SMR reference sample*: FMI AlN/GdN/AlN/TaN/AlN heterostructure on a Si/SiO_2 substrate.

The FMI multilayer heterostructure shown in Fig. 6.7 is the so-called *SMR reference sample*. Here, we prevent a possible SMR effect, created in the FMI/NM interface, by depositing an insulating AlN thin film (d=20 nm) between the GdN/TaN bilayer. The intermediate AlN layer is grown with the deposition parameters N_2/Ar=35 %, T_{depo}=20 °C, P_{depo}=70 W and $p_{\mathrm{depo}} = 5 \times 10^{-3}$ mbar (see Tab. 6.3). As a next step, we extract the magnetic properties $\mu_0 M_{\mathrm{s}}$, $\mu_0 H_{\mathrm{c}}$, T_{C} (see Fig. 6.8 (a)-(c)) of our multilayer thin film and then we analyze the temperature-dependent resistance (see Fig. 6.9 (a) and (b)) of the GdN/AlN/TaN multilayer system.

Figure 6.8 (a)-(c) shows the magnetic hysteresis loops $M(H)$ and the $M(T)$-curve recorded in the SQUID magnetometry measurements (see Sec. 4.4) of the unpatterned $(6 \times 10)\,\mathrm{mm}^2$ AlN/GdN/AlN/TaN/AlN multilayer heterostructure.

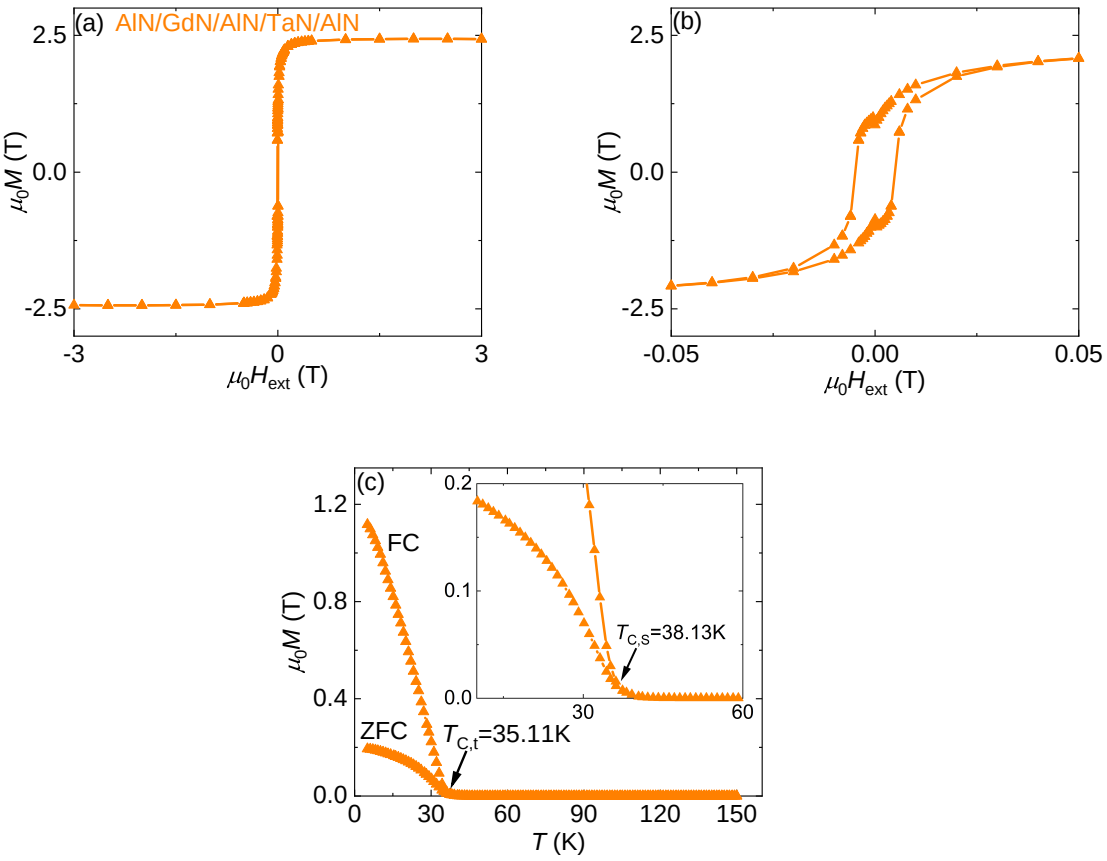

Fig. 6.8: Magnetic properties of the *SMR reference sample*: (a) Magnetic hysteresis loop recorded at T=5 K. A saturation magnetization of $\mu_0 M_s$=2.43 T is visible. (b) Zoomed in view of the hysteresis loop from (a) to extract a coercive field of $\mu_0 H_c$=5.12 mT. (c) Result of the $M(T)$-measurement: Curie temperatures of $T_{C,t}$=35.11 K and $T_{C,S}$=38.13 K (see zoomed in view of (c)) are determined with the two different extraction methods.

Panel 6.8 (a) shows a saturation magnetization of $\mu_0 M_s$=2.43 T for our *SMR reference sample*, which is slightly increased compared to the saturation magnetization $\mu_0 M_s$=2.39 T of the *SMR test sample* (see. Tab. 6.2). Fig. 6.8 (b) shows a zoomed in view of the magnetic hysteresis loop from Fig. 6.8 (a) and a coercive field of $\mu_0 H_c$=5.12 mT is observed. Regarding the magnitude of $\mu_0 H_c$, the extracted coercive field $\mu_0 H_c$ is approximately equal to the value of the *SMR test sample* (see. Tab. 6.2). Figure 6.8 (c) illustrates the magnetization M as a function of the temperature T of the AlN/GdN/AlN/TaN/AlN heterostructure. The result of the $M(T)$-measurement enables us to extract a Curie temperature of $T_{C,t}$=35.11 K by performing the tangent method (see Sec. 5.1.1). Using the intersection method (see Sec. 5.1.1), we determine a value of $T_{C,S}$=38.13 K. Both extracted Curie temperatures a comparable to the values of the *SMR test sample* with the stack sequence AlN/GdN/TaN/AlN (see. Tab. 6.2). In the *SMR reference sample*, we also expect a minor amount of metlallic, paramagnetic Gd because of the low difference value $\Delta T_C = T_{C,t} - T_{C,S}$.

The results of the electrical transport measurements (see Sec. 4.1) of the Hall-bar patterned AlN/GdN/AlN/TaN/AlN multilayer thin film (*SMR reference sample*) are shown in Figure 6.9 (a) and (b).

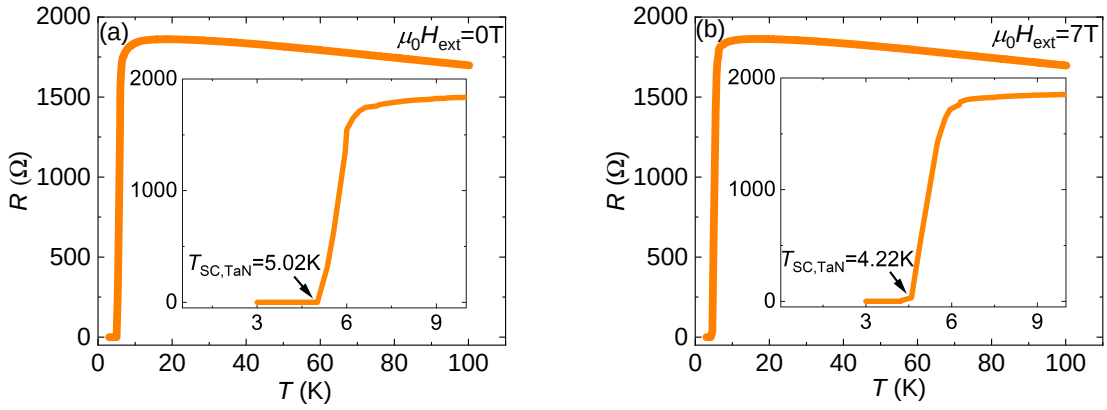

Fig. 6.9: Resistive properties of the *SMR reference sample*: $R(T)$ recorded at $\mu_0 H_{ext}$=0 T (a) and at $\mu_0 H_{ext}$=7 T (b). For both measurements is in the T-area 10 K<T<100 K an average electrical resistance of R≈1.78 kΩ is observed and a maximum value of R≈1.85 kΩ is visible at T≈10 K. The zoomed in view in (a) and (b) shows a superconducting (SC) transition temperature in the T-area 3 K<T<10 K. For $\mu_0 H_{ext}$=0 T a SC temperature of $T_{SC,\ TaN}$=5.02 K is visible and for $\mu_0 H_{ext}$=7 T a value of $T_{SC,\ TaN}$=4.22 K is extracted.

Figure 6.9 (a) and (b) shows the $R(T)$-curves recorded in the in-plane (ip) direction at zero field $\mu_0 H_{ext}$=0 T (see Fig. 6.9 (a)) and at $\mu_0 H_{ext}$=7 T (see Fig. 6.9 (b)) in a cryogenic experimental setup (I_{meas}=50 μA). For both measurements, we observe in the T-range 10 K<T<100 K an average electrical resistance of R≈1.78 kΩ. In the described T-region, we observe for decreasing temperature T an increase resistance R and a maximum value of R≈1.85 kΩ results at T≈10 K. Compared to the electrical resistance R≈2.8 kΩ of the *SMR test sample* (see. Fig. 6.6 (a) and (b)), we measure for the *SMR reference sample* an approximatley 1 kΩ lower electrical resistance R (see Fig. 6.9 (a) and (b)), which we associate with a various N content in the TaN thin film due to the intermediate AlN layer, which thus contributes to the transport, in the GdN/TaN-interface. The behavior of the electrical resistance R in the T-area 3 K<T<10 K is visible in the zoomed in view in Fig. 6.9 (a) and (b). In this T-region, we observe a superconducting (SC) temperature transition at T_{SC}≈5 K in our *SMR reference sample*. We assign the SC temperature to the TaN thin film (d=10 nm) in our multilayer heterostructure.

We identify a noticeably higher SC temperature $T_{SC,\ TaN}$ for the *SMR test sample* with the direct GdN/TaN interface as compared to the SC temperature of the *SMR reference sample* with the GdN/AlN/TaN layer sequence. This differnce in T_{SC} may be explained with a differnce in N content for the TaN films, which would also explain the reduced resistance. The influence of the intermediate AlN layer in the GdN (FMI)/TaN (SC) bilayer to its magnetotransport properties is discussed in section 6.2.5).

The growth recipe and the magnetic-, the superconducting (SC)- as well as the resistive-properties of the *SMR reference sample* on a Si/SiO_2 substrate $(6\,\mathrm{x}\,10\,\mathrm{x}\,0.55)\,\mathrm{mm}^3$ are shown in Tab. 6.3.

Growth recipe of the *SMR reference sample*				
Stack sequence	N_2/Ar [%]	T_{depo} [°C]	P_{depo} [W]	p_{depo} [mbar]
AlN (40nm)	35	20	70	5×10^{-3}
TaN (10nm)	35	500	30	5×10^{-3}
AlN (20nm)	35	20	70	5×10^{-3}
GdN (60nm)	40	500	45	5×10^{-3}
AlN (40nm)	35	20	70	5×10^{-3}
Magnetic properties	$\mu_0 M_{\mathrm{s}}$ [T]	$\mu_0 H_{\mathrm{c}}$ [mT]	$T_{\mathrm{C,t}}$ [K]	$T_{\mathrm{C,S}}$ [K]
	2.43	5.12	35.11	38.13
SC- / resistive-properties	$T_{\mathrm{SC,TaN(0\,T)}}$ [K]	$R_{(0\,\mathrm{T})}$ [Ω]	$T_{\mathrm{SC,TaN(7\,T)}}$ [K]	$R_{(7\,\mathrm{T})}$ [Ω]
	5.02	1780	4.22	1780

Tab. 6.3: Growth parameters, magnetic-, superconducting (SC)- and resistive-properties of a FMI AlN/GdN/AlN/TaN/AlN heterostructure.

6.2.3 Temperature-dependent resistance $R(T)$ of a AlN/TaN/AlN heterostructure

Finally, we fabricate a AlN/TaN/AlN heterostructure on a thermally oxidized Si substrate $(6\,\mathrm{x}\,10\,\mathrm{x}\,0{,}55)\,\mathrm{mm}^3$. The stack sequence of the TaN trilayer thin film is shwon in Fig. 6.10.

Fig. 6.10: Stack sequence of a AlN/TaN/AlN heterostructure on a Si/SiO_2 substrate.

The previous section 6.2.2 deals with the investigation of the *SMR reference sample* consisting of a AlN/TaN bilayer on top of the FMI AlN/GdN/AlN stack (see Fig. 6.7). To investigate the electrical resistive properties and the angle-dependent- as well as the field-dependent magnetotransport properties of the AlN/TaN/AlN heterostructure, we deposite the trilayer stack on a thermally oxidized Si substrate (see Fig. 6.10).

The results of the electrical transport experiments of the Hall-bar patterned AlN/TaN/AlN thin film measured in a cryostat at I_{meas}=50 μA (see Sec. 4.1) are shown in Figure 6.11 (a) and (b).

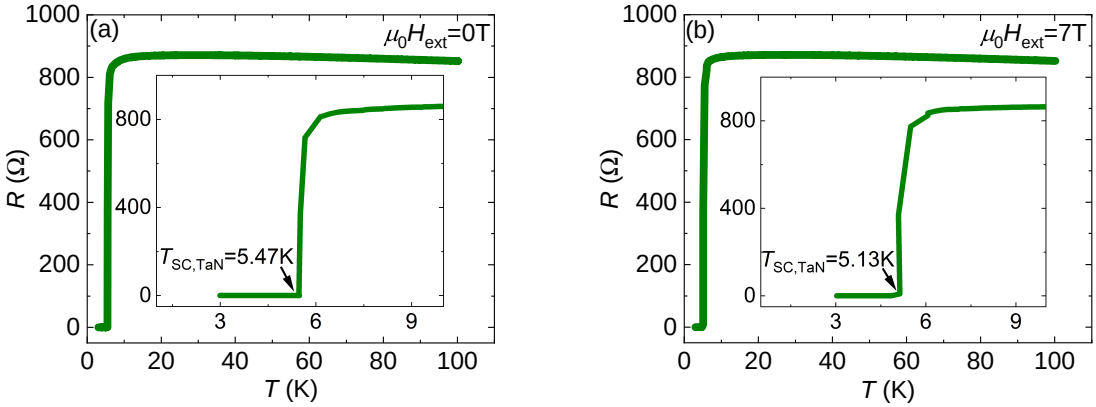

Fig. 6.11: Resistive properties of the insulating AlN/TaN/AlN heterostructure: $R(T)$ recorded at $\mu_0 H_{\mathrm{ext}}$=0 T (a) and at $\mu_0 H_{\mathrm{ext}}$=7 T (b). For both measurements is in the T-area 10 K<T<100 K an almost constant electrical resistance of R≈850 Ω visible. The zoomed in view in (a) and (b) shows a superconducting (SC) transition temperature in the T-area 3 K<T<10 K. For $\mu_0 H_{\mathrm{ext}}$=0 T a SC temperature of $T_{\mathrm{SC,\ TaN}}$=5.47 K is visible and for $\mu_0 H_{\mathrm{ext}}$=7 T a value of $T_{\mathrm{SC,\ TaN}}$=5.13 K is extracted.

Figure 6.11 (a) and (b) illustrate the electrical resistance R depending on the temperature T measured in the in-plane (ip) direction at zero field $\mu_0 H_{\mathrm{ext}}$=0 T (see Fig. 6.11 (a)) and at $\mu_0 H_{\mathrm{ext}}$=7 T (see Fig. 6.11 (b)). Here, we observe for both measurements an almost constant electrical resistance R≈850 Ω in the T-area 10 K<T<100 K.

Compared to the transport properties of the *SMR test sample* (see. Fig. 6.6 (a) and (b)) and the *SMR reference sample* (see. Fig. 6.9 (a) and (b)), we observe a reduced electrical resistance R for our AlN/TaN/AlN heterostructure. This makes us assume, that the direct interface of GdN (FMI)/TaN (SC) is responsible for the increased electrical resistance R. In the zoomed in view in Fig. 6.11 (a) and (b), we observe for the TaN layer (d=10 nm) a superconducting (SC) transition temperature at $T_{\mathrm{SC,\ TaN}}\approx$5.5 K. For the zero field-measurement ($\mu_0 H_{\mathrm{ext}}$=0 T), we extract the SC temperature $T_{\mathrm{SC,\ TaN}}$=5.47 K and for $\mu_0 H_{\mathrm{ext}}$=7 T we determine the value $T_{\mathrm{SC,\ TaN}}$=5.13 K. We assume that the direct GdN (FMI)/TaN (SC) interface in the *SMR test sample* (see. Fig. 6.6 (a) and (b)) causes a higher superconducting (SC) temperature in the TaN layer. In section 6.2.6, we analyze the magnetotransport properties of our AlN/TaN/AlN heterostructure. Table 6.4 lists the growth recipe as well as the superconducting (SC)- and resistive-properties of an insulating AlN/TaN/AlN heterostructure deposited on a Si/SiO_2 substrate $(6\,\mathrm{x}\,10\,\mathrm{x}\,0.55)\,\mathrm{mm}^3$.

Growth recipe of insulating AlN/TaN/AlN				
Stack sequence	N_2/Ar [%]	T_{depo} [°C]	P_{depo} [W]	p_{depo} [mbar]
AlN (40nm)	35	20	70	5×10^{-3}
TaN (10nm)	35	500	30	5×10^{-3}
AlN (40nm)	35	20	70	5×10^{-3}
SC- / resistive-properties	$T_{\mathrm{SC,TaN(0\,T)}}$ [K]	$R_{(0\,\mathrm{T})}$ [Ω]	$T_{\mathrm{SC,TaN(7\,T)}}$ [K]	$R_{(7\,\mathrm{T})}$ [Ω]
	5.47	850	5.13	850

Tab. 6.4: Growth parameters, superconducting (SC)- and resistive-properties of an insulating AlN/TaN/AlN heterostructure.

6.2.4 Field-dependent magnetotransport properties of a AlN/GdN/TaN/AlN heterostructure

This section discusses the field-dependent magnetotransport properties of our *SMR test sample* with the stack sequence AlN/GdN/TaN/AlN (see Fig. 6.4) for which we have performed magnetotransport measurements in a cryogenic environment (see section section 4.3.1 of chapter 4).

Figure 6.12 (a)-(f) shows the symmetric component of the magnetotransport signal MR_{symm} (see Eq. (25)) of our GdN/TaN multilayer heterostructure under varying external magnetic fields $\mu_0 H_{ext}$ and at various fixed temperatures T.

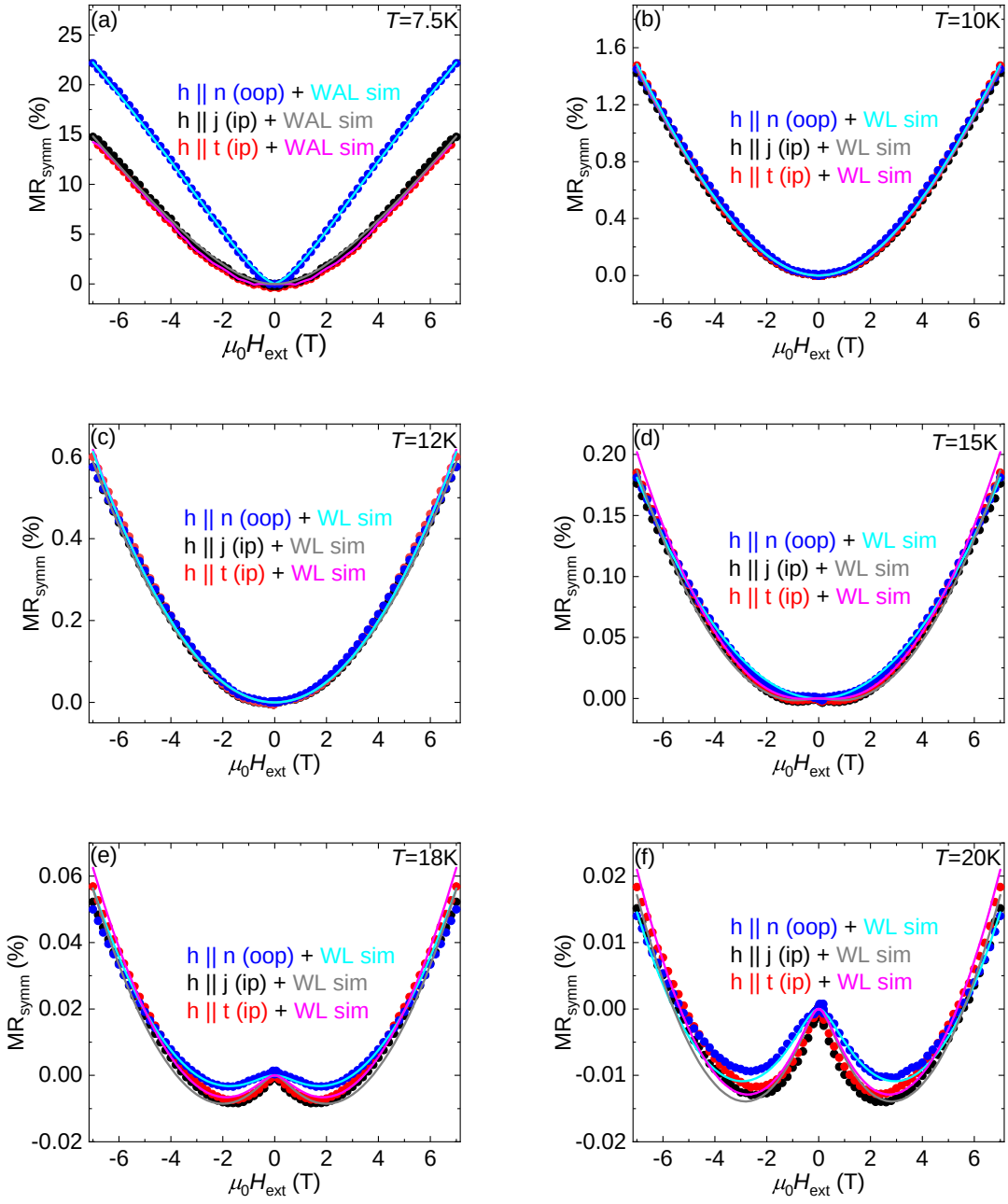

Fig. 6.12: Results of the FDMR measurements (-7 T to +7 T) of our AlN/GdN/TaN/AlN heterostructure at different fixed temperatures T: (a)-(f) The magnitude of the symmetrized longitudinal magnetoresistance MR decreases in all field geometries (see colored circles) with an increasing temperature T. (a) An almost linear behavior of MR is visible in out-of-plane (oop) ($\mathbf{h}\|\mathbf{n}$) and the FDMR curves recorded in in-plane (ip) ($\mathbf{h}\|\mathbf{j}$ and $\mathbf{h}\|\mathbf{t}$) show a parabolic signature at 7.5 K. (b)-(d) The MR shows a parabolic behavior in all field geometries at higher T and for $T \geq 15$ K, the space between the FDMR curves increases and the manifestation of a slight dip below the zero line of MR_{symm} is visible at T=15 K. (e)-(f) An increasing negative contribution of the MR at an increasing T is visible and the dip reaches a maximum at 20 K. The colored lines in (a)-(f) represent the simulation curves by assuming weak anti-localization (WAL) (Eq. (33)) (T=7.5 K) and weak localization (WL) (Eq. (34)) (T=10−20 K) transport in TaN.

Figure 6.12 (a) illustrates the symmetrized longitudinal magnetoresistance MR as a function of the applied external magnetic field $\mu_0 H_{\text{ext}}$ (-7 T to +7 T) measured at T=7.5 K, which is close to the superconducting (SC) transition temperature T_{SC}≈5.5 K of TaN (see Fig. 6.6 (a)-(b)). In Fig. 6.12 (a), we observe in the out-of-plane (oop) ($\mathbf{h}\|\mathbf{n}$) field geometry (see blue dots) an approximatey linear behavior of the field-dependent magnetoresistance (FDMR) and a maximum value of MR_{max}≈22 % ($R_{B=7\,\text{T}}$≈2.4 kΩ) is visible at 7 T. Furthermore, we observe in both in-plane (ip) ($\mathbf{h}\|\mathbf{j}$ and $\mathbf{h}\|\mathbf{t}$) geometries (see black and red dots in Fig. 6.12 (a)) a parabolic signature of the FDMR curve with a slight outward curvature and a maximum MR_{max}≈15 % ($R_{B=7\,\text{T}}$≈2.4 kΩ) at 7 T. Comparable signatures of FDMR measurement curves are shown in the work of *A. H. Al-Tawhid et al.* [90] and *G. Xu et al.* [91]. Here, they have associated their FDMR results with so-called weak anti-localization (WAL) effects near the SC transition temperature of a $TiO_x/KTaO_3$ (111) interface [90] as well as in the SC semimetal LuPdBi [91]. Therefore, we assume a WAL transport (see Sec. 2.4) in the TaN thin film of our multilayer heterostructure and we use the theoretical model of *Hikami-Larkin-Nagaoka* (HLN) [44] (see Eq. (2) and (4) and Fig. 4 of *P. J. Newton et al.* [47]), which describes WAL transport phenomena, for simulating our FDMR measurement results with the expression [47]

$$\begin{aligned}\text{MR}(\%)_{\text{HLN}} \propto \alpha \cdot \rho_0 \cdot \frac{e^2}{2\pi^2\hbar} \cdot \Bigg[\psi\left(\frac{1}{2}+\frac{B_\phi}{B}\right) - \ln\left(\frac{B_\phi}{B}\right) - 2\psi\left(\frac{1}{2}+\frac{B_\phi+B_{\text{SO}}}{B}\right) \\ +2\ln\left(\frac{B_\phi+B_{\text{SO}}}{B}\right) - \psi\left(\frac{1}{2}+\frac{B_\phi+2B_{\text{SO}}}{B}\right) + \ln\left(\frac{B_\phi+2B_{\text{SO}}}{B}\right)\Bigg],\end{aligned} \tag{32}$$

where α=-1/2 is a constant due to the Dirac cone (see work of *G. M. Stephen et al.* [92]), ρ_0 is the resistivity of the multilayer at zero field, e the electron charge, $\hbar$ is the reduced Planck constant and $\psi(x)$ is the so-called the Digamma function of a physical variable x (*P. J. Newton et al.* [47]). Furthermore, Eq. (32) contains two characteristic magnetic fields: $B_\phi = \frac{\hbar}{4eL_\phi{}^2}$ defined by the electron wave phase coherence length L_ϕ and $B_{\text{SO}} = \frac{\hbar}{4eL_{\text{SO}}{}^2}$ represented by the spin-orbit length L_{SO}. To simulate our FDMR data recorded at T=7.5 K, we add a linear term $F|B|$ to Eq. (32) in agreement to Ref.[47], where F defines a temperature dependent constant, which yields the final equation [47]

$$\text{MR}(\%)_{\text{fit}} = \text{MR}(\%)_{\text{HLN}} + F|B|. \tag{33}$$

In Figure 6.12 (a), we observe that the simulation curves (light blue line for $\mathbf{h}\|\mathbf{n}$, grey line for $\mathbf{h}\|\mathbf{j}$, magenta line for $\mathbf{h}\|\mathbf{t}$), which were generated with Eq. (33), are compatible with our FDMR data by using the adjusted parameter L_ϕ and L_{SO} shown in Tab. A.7. Due to the iteration process by using the HLN model [44] and Eq. (33), we assume weak anti-localization (WAL) effects in the TaN layer measured at T=7.5 K.

Panel 6.12 (b)-(d) shows also a parabolic behavior of the FDMR and all curves, measured in the three field geometries $\mathbf{h}\|\mathbf{n}$, $\mathbf{h}\|\mathbf{j}$, $\mathbf{h}\|\mathbf{t}$, are very close to each other. Furthermore, we observe an increasing measurement temperature T is corresponding to a decreasing symmetrized longitudinal MR as well as an increasing width of the FDMR curves. In Fig. 6.12 (e)-(f), we observe two negative minima of the MR at negative and

positive magnetic fields. The occurrence of such minimas is already slightly visible in the 15 K measurement (see Fig. 6.12(d)). For temperatures above 15 K, the separation between the FDMR curves measured in different geometries increases with rising T and the negative contribution of the MR increases with increasing measurement temperature T. We observe the largest negative MR at T=20 K, which is close the ferromagnetic Curie temperature T_C≈25 K of GdN (see Tab. 5.2). The minma are located around +/- 5 T with a negative MR of -0.015 % for **h**‖**j**. This may indicate that the GdN layer plays a role in the measured magnetoresistance effect. Moreover, we find that the overall positive magnetoresistance effect is reduced with increasing temperature and at T=20 K we find MR_{max}≈0.018 % ($R_{B=7\,T}$≈2.7 kΩ) at 7 T. The work of *C. Ghezzi et al.* [93], *R. G. Mani et al.* [94] and *Y. Wang et al.* [95], report a comparable evolution of FDMR measurement cuves and they are associated their results with so-called weak localization (WL) effects (see Sec. 2.4). The theoretical model of *Hikami-Larkin-Nagaoka* (HLN) [44] works also to describe WL effects (see Eq. (1) and (3) and Fig. 3 in the work of *P. J. Newton et al.* [47]), but does not provide satisfactory simulation curves for our FDMR data measured between 10 K and 20 K. Therefore, we instead use the theoretical model of *A. Kawabata* [96],[97], which describes a negative magnetoresistance in a three-dimensional system and the weak localization (WL) [37] correction to the resistivity is given by the following expression [93],[94]

$$\mathrm{MR}(\%) = -\alpha \cdot \rho_0 \cdot \frac{e^2}{2\pi^2\hbar} \cdot \sqrt{\frac{eB}{\hbar}} \cdot F(x) + \beta \cdot B^2, \tag{34}$$

where α=0.35 is a fitting parameter, which we use as a fixed value in all our simulations, due to the Coulomb screening, ρ_0 is the resistivity of the multilayer at zero field, e the electron charge, $\hbar$ is the reduced Planck constant, $\beta \cdot B^2$ is the quadratic contribution in the MR effect and $F(x)$ is the Hurwitz zeta function [95], which is shown as

$$F(x) = \sum_{i=0}^{\infty} \left[2\left(n+1+\frac{1}{x}\right)^{\frac{1}{2}} - 2\left(n+\frac{1}{x}\right)^{\frac{1}{2}} - \left(n+\frac{1}{2}+\frac{1}{x}\right)^{\frac{1}{2}} \right]. \tag{35}$$

In Eq. (35), x represents a dimensionless quantity which is defined by [93],[94]

$$x = \frac{4e{L_\phi}^2}{\hbar} B, \tag{36}$$

where L_ϕ is the electron wave phase coherence length.

As a next step, we simulate our FDMR data measured between T=10 K and 20 K (see Fig. 6.12 (b)-(f)) by using Eq. (34). To this end, we set suitable values for L_ϕ and β that the weak localization contribution $\sim\sqrt{B}$ and the quadratic part B^2 in Eq. (34) are compatible with our FDMR curves measured in the three field geometries **h**‖**n**, **h**‖**j** and **h**‖**t** in the T-range 10 K<T<20 K (see Tab. A.8). This iteration method allows us, to define a suitable electron wave phase coherence length L_ϕ which describes potentially the weak localization transport in the TaN thin film of our multilayer heterostructure.

Figure 6.13 shows the phase coherence length L_ϕ depending on the measurement temperature T.

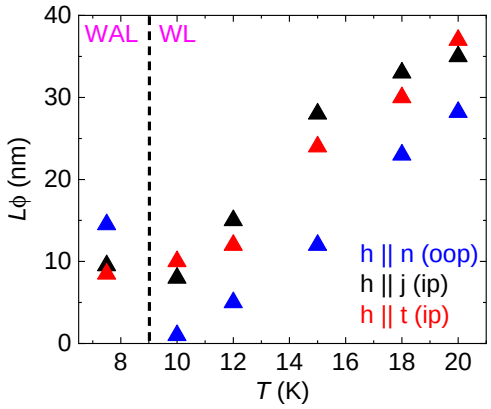

Fig. 6.13: Electron wave phase coherence length L_ϕ, applied to simulate the FDMR data with WAL (T=7.5 K) (see Eq. (33)) and WL (10 K<T<20 K) (see Eq. (34)) transport phenomena in TaN for the *SMR test sample*, as a function of the temperature T: L_ϕ increases with increasing T and reaches a maximum at 20 K in all field geometries.

Figure 6.13 illustrates the phase coherence length L_ϕ as a function of the measurement temperature T in the magnetotransport experiment determined from our simulations. We find a similar magnitude compared to the work of *Y. Wang et al.* [95] (see Fig. 5(b) in [95]). However, we observe in the T-range 10 K<T<20 K an increasing phase coherence length L_ϕ with increasing temperature T and an almost linear behavior in the three field geometries $\mathbf{h}\|\mathbf{n}$, $\mathbf{h}\|\mathbf{j}$ and $\mathbf{h}\|\mathbf{t}$. Typically one would expect a decrease of the phase coherence length with increasing temperature due to the increase in electron scattering rate. We suggest that the decrease of L_ϕ at decreasing T correlates with the ferromagnetic ordering and magnetic domain formation in GdN. Dipolar exchange effects between the magnetic domain structures, especially the domain walls in GdN and the TaN will influence electronic scattering and could lead to changes in the apparent phase coherence length L_ϕ in the weak localization (WL) model. Finally, we note that the temperature-dependent crossover from WAL to WL transport with increasing temperatures, observed in this sample, has already been observed in the work of *P. J. Newton et al.* [47], *X. Zhang et al.* [98] and *W. Stefanowicz et al.* [33] as well as theoretical described by *HZ. Lu et al.* [40].

6.2.5 Field-dependent magnetotransport properties of a AlN/GdN/AlN/TaN/AlN heterostructure

To better understand, if the observed magnetoresistance effects in the SMR refereence sample require a direct interface between GdN and TaN, we analyze the field-dependent magnetotransport properties of our *SMR reference sample* (see Fig. 6.7) using the experimental measurement techniques described in section 4.3.1 of chapter 4.

Figure 6.14 (a)-(f) illustrates the symmetric component of the magnetotransport signal MR_{symm} (see Eq. (25)) of our GdN/AlN/TaN multilayer heterostructure under varying external magnetic fields $\mu_0 H_{ext}$ and at different fixed temperatures T.

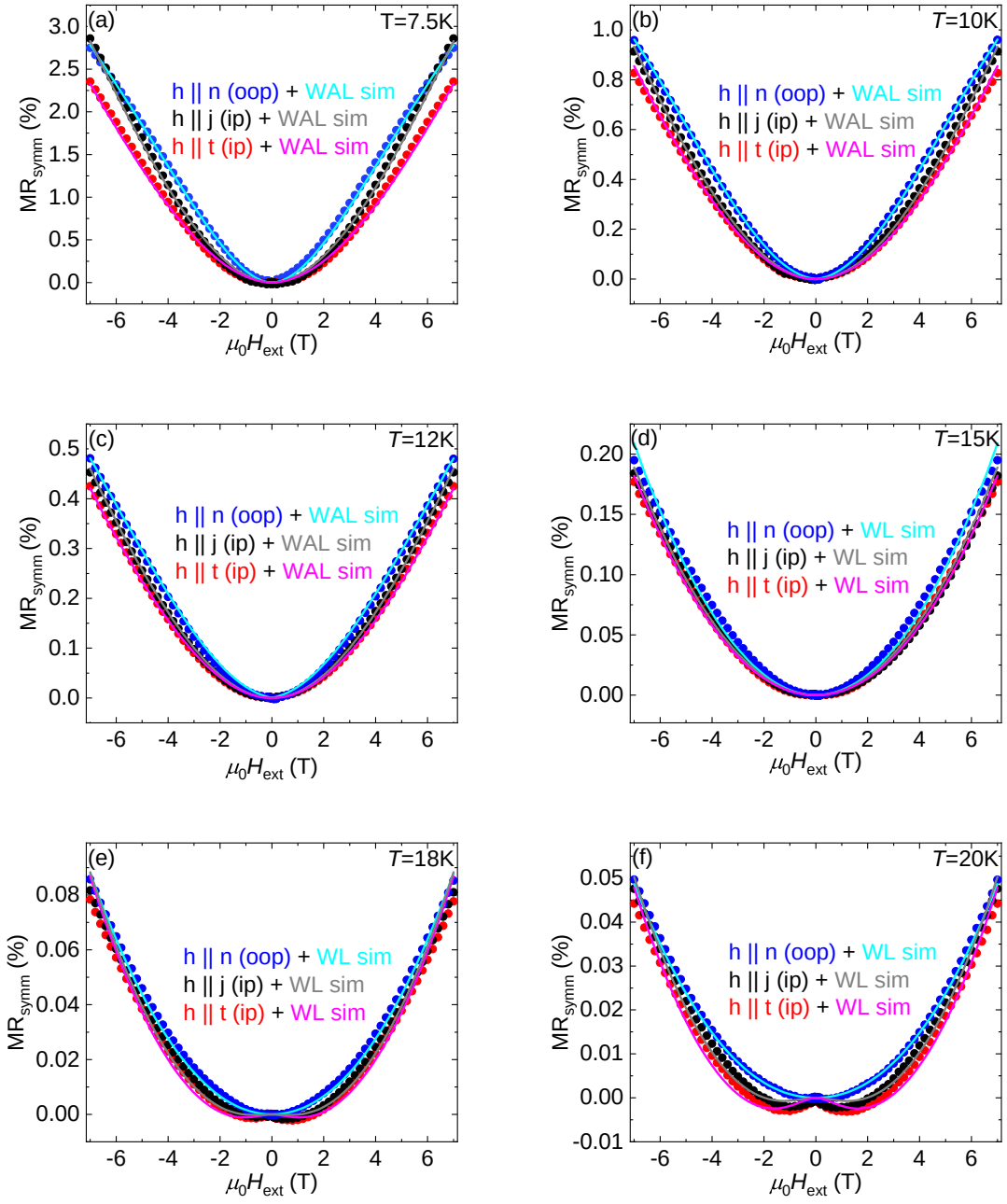

Fig. 6.14: Results of the field-dependent magnetotransport (FDMR) measurements (-7 T to +7 T) of our AlN/GdN/AlN/TaN/AlN heterostructure at different fixed temperatures T: (a)-(f) The symmetrized longitudinal magnetoresistance MR decreases in all field geometries (**h**||**n**, **h**||**j** and **h**||**t**) with an increasing temperature T (see colored circles). (a)-(c) An almost parabolic behavior of MR and a slight cusp-shape outwards of the FDMR curves is visible in all field geometries and the magnitudes of the curves increasingly conincide with each other with increasing T. (d) Starting from T=15 K the space between the FDMR curves increases and at T=18 K the generation of a slight dip below the zero line is visible. (e)-(f) An increasing negative contribution of the MR at increasing T is visible and the dip reaches its maximum at 20 K. The colored lines in (a)-(f) represent the simulation curves by assuming weak anti-localization (WAL) (Eq. (33)) (T=7.5−12 K) and weak localization (WL) (Eq. (34)) (T=15−20 K) transport in TaN.

In Fig. 6.14 (a)-(c), we observe for an increasing temperature T a decreasing field-dependent magnetoresistance (FDMR) as well as a decreasing space between the FDMR curves measured in the three field geometries $\mathbf{h}\|\mathbf{n}$, $\mathbf{h}\|\mathbf{j}$ and $\mathbf{h}\|\mathbf{t}$. In comparison with the FDMR curves of our *SMR test sample* measured at 7.5 K (see Fig. 6.12 (a)), we observe a substantially reduced $\mathrm{MR_{max}}\approx 3\,\%$ ($R_{B=7\,\mathrm{T}}\approx 1.8\,\mathrm{k\Omega}$) for our *SMR reference sample* (see Fig. 6.14 (a)) and no sharp linear behavior of the FDMR curve in out-of-plane (oop) ($\mathbf{h}\|\mathbf{n}$) is visible. This difference could be connected to the observed reduction in the superconducting transition temperature in the *SMR reference sample*. Thus, it is plausible that the observed magnetoresistance effect may be caused by resistance variations due to superconducting islands/grains in the sample, which become normal conducting by applying an external magnetic field (see further discussion in Sec. 6.2.6). Furthermore, the data recorded at T=10 K and 12 K are comparable to the MR values of our *SMR test sample* (see Fig. 6.12 (b)-(c)). Due to the sharp linear increase of the FDMR curves recorded at T=7.5 K, 10 K and 12 K and the slight curvature outwards (see Fig. 6.14 (a)-(c)), we use the theory of *Hikami-Larkin-Nagaoka* (HLN) [44] (see work of *P. J. Newton et al.* [47]), which describes WAL transport, for modeling our FDMR data by intserting suitable parameters L_ϕ and L_{SO}, which are listed in Tab. A.9, in Eq. (33).

The simulation curves are shown in Fig. 6.14 (a)-(c) (light blue line for $\mathbf{h}\|\mathbf{n}$, grey line for $\mathbf{h}\|\mathbf{j}$, magenta line for $\mathbf{h}\|\mathbf{t}$) and we find reasonable agreement between our FDMR data with the simulation curves. Consequently, one can describe the MR by weak anti-localization (WAL) effects in the TaN layer measured at T=7.5 K, 10 K and 12 K. In comparison to the simulation parameters of the *SMR test sample* (see Tab. A.7), we utilize similar values for our *SMR reference sample* (see Tab. A.9).

For the FDMR data recorded at T=15 K, 18 K and 20 K (see Fig. 6.14 (d)-(f)), we observe a similar evolution of the FDMR curves compared to the data of our *SMR test sample* (see Fig. 6.12 (d)-(f)). Fig. 6.14 (d)-(f) shows that an increasing temperature T is corresponding to a decreasing MR and an increasing width of the FDMR curves with a growing separation between the different magnetic field geometries is visible. Furthermore, we observe at and above 18 K the manifestation of a minima with negative MR values. The largest negative MR is observed at T=20 K (see. Fig. 6.14 (f)), but less pronounced as compared to the minima in MR at T=20 K of our GdN/TaN multilayer system (see. Fig. 6.12 (f)). Similar as in the *SMR test sample*, the positive MR at 7 T decreases with increasing temperature and we find $\mathrm{MR_{max}}\approx 0.05\,\%$ ($R_{B=7\,\mathrm{T}}\approx 1.8\,\mathrm{k\Omega}$) at 7 T (see. Fig. 6.14 (f)). Afterwards, we use the theory of *A. Kawabata* [96],[97], which describes the weak localization (WL) transport in a three-dimensional system, for simulating our FDM data by an iteration procedure of inserting suitable parameters L_ϕ and β (see Tab. A.10) in Eq. (34).

The results of the simulation are shown in Figure 6.14 (d)-(f). Here, the modeling curves (light blue line for $\mathbf{h}\|\mathbf{n}$, grey line for $\mathbf{h}\|\mathbf{j}$, magenta line for $\mathbf{h}\|\mathbf{t}$) agree well with our measured FDMR data, which indicates weak localization (WL) transport phenomena in the TaN thin film of our GdN/AlN/TaN multilayer heterostructure.

Finally, we plot the phase coherence length L_ϕ, which we use to simulate our FDMR data measured in the field geometries $\mathbf{h}\|\mathbf{n}$, $\mathbf{h}\|\mathbf{j}$ and $\mathbf{h}\|\mathbf{t}$, as a function of the measurement temperature T set in the magnetotransport experiment (see Fig. 6.15).

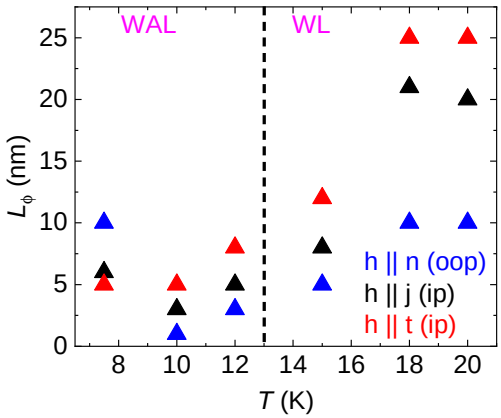

Fig. 6.15: Electron wave phase coherence length L_ϕ, applied to simulate the FDMR data with WAL (7.5 K$<T<$12 K) (see Eq. (33)) and WL (15 K$<T<$20 K) (see Eq. (34)) transport phenomena in TaN for the *SMR reference sample*, as a function of the temperature T: L_ϕ increases with increasing T and saturates in all field geometries at about 18 K / 20 K.

In Fig. 6.15, we observe an increase in the phase coherence length L_ϕ with increasing T and an almost linear temperature-dependence in the T-range 10 K$<T<$15 K followed by a sharp decrease as well as a slight saturation of L_ϕ at high T. In comparison to the phase coherence length L_ϕ of our *SMR test sample* (see Fig. 6.13), we observe for our *SMR reference sample* a magnitude of L_ϕ reduced by approximately half throughout the entire T-range (see Fig. 6.15). We associate this effect and the signature of the L_ϕ(T)-curves to the insertion of the AlN layer between GdN and TaN in our multilayer heterostructure (see Fig. 6.7). Assuming a closed AlN layer, the interaction between the magnetic moments in the GdN and the conduction electrons in the TaN are now only mediated by dipolar stray fields. Such that one expects a weaker MR effect originating from the interaction from GdN and TaN. This is indeed observed in our *SMR reference sample* (see Fig. 6.14 (e)-(f)). Therefore, we could attribute the shorter phase coherence length L_ϕ as compred to the *SMR test sample* to the missing direct interface between GdN and TaN. Moreover, the FDMR data of our GdN/AlN/TaN multilayer thin film can be simulated with the weak anti-localization (WAL) theory (see Fig. 6.14 (a)-(c)), i.e. a larger temperature range as compared to our multilayer stack with the direct GdN/TaN interface (see Fig. 6.12 (a)). These temperatures T are further away from the superconducting (SC) transition temperature ($T_{\mathrm{SC,TaN}}\approx$5 K) in the *SMR reference sample* (see Fig. 6.9 (a)-(b)) as compared to the *SMR test sample*.

6.2.6 Field-dependent magnetotransport properties of a AlN/TaN/AlN heterostructure

To better understand the role of GdN, we finally, we study the field-dependent magnetotransport characteristics of our AlN/TaN/AlN heterostructure (see Fig. 6.10) for which we have used the low-temperature transport measurement methods explained in section 4.3.1 of chapter 4.

Figure 6.16 (a)-(f) represents the symmetric component of the magnetotransport signal MR_{symm} (see Eq. (25)) of our AlN/TaN/AlN trilayer thin film under varying external magnetic fields $\mu_0 H_{ext}$ and at several fixed temperatures T.

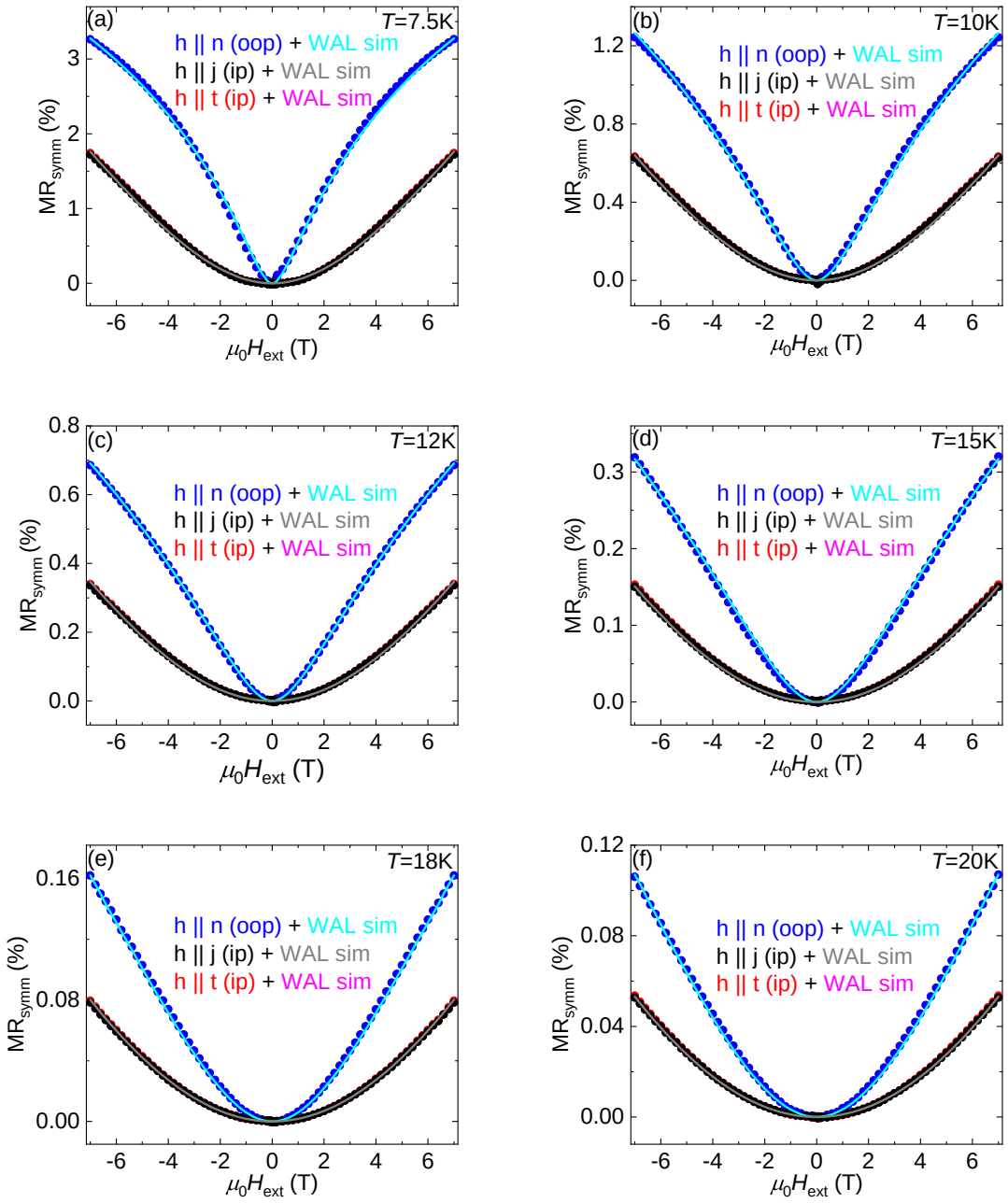

Fig. 6.16: Results of the field-dependent magnetotransport (FDMR) measurements (-7 T to +7 T) of our AlN/TaN/AlN heterostructure at different fixed temperatures T: (a)-(f) The symmetrized longitudinal magnetoresistance MR decreases in all field geometries (see colored circles) with an increasing temperature T and the outer curvature of the FDMR curves recorded in out-of-plane (oop) ($\mathbf{h}\|\mathbf{n}$) decreases and an almost parabolic behavior is visible for $T \geq 15$ K. The parabolic FDMR curves measured in the both in-plane (ip) ($\mathbf{h}\|\mathbf{j}$ and $\mathbf{h}\|\mathbf{t}$) geometries are similar in shape in the entire T-regime. The colored lines in (a)-(f) represent the simulation curves by assuming weak anti-localization (WAL) (Eq. (33)) (T=7.5−20 K) transport in the TaN layer of our trilayer heterostructure.

In Figure 6.16 (a)-(f), we observe for an increasing temperature T a decreasing field-dependent magnetoresistance (FDMR) measured in all field geometries and a decreasing outer curvature of the FDMR curves recorded in the out-of-plane (oop) ($\mathbf{h}\|\mathbf{n}$) configuration (see blue dots in Fig. 6.16 (a)-(f)) is visible. Furthermore, an almost parabolic behavior of the FDMR curves measured in oop is visible at $T\geq$15 K. For the FDMR data measured in the in-plane (ip) geometries ($\mathbf{h}\|\mathbf{j}$ and $\mathbf{h}\|\mathbf{t}$) (see black and red dots in Fig. 6.16 (a)-(f)), we observe a similar shape of the FDMR curves and no significant alteration in their quadratic field dependence is visible for an increasing temperature T. In comparison to the measurement data of our *SMR test sample* at T=7.5 K (see Fig. 6.12 (a)), we observe a similar magnetic field dependence in all field geometries, but a significantly decreased $\mathrm{MR}_{\mathrm{max}}\approx$3.5 % ($R_{B=7\,\mathrm{T}}\approx$868 kΩ) in oop at 7 T. This could be either caused by the non-existing FMI GdN layer in our AlN/TaN/AlN thin film, or due to the lower superconducting transition temperature in the AlN/TaN/AlN trilayer. For higher measurement temperatures T, there are no minima in MR visible in stark contrast to the observations in the *SMR test sample* (see Fig. 6.12 (d)-(f)) as well as in the *SMR reference sample* (see Fig. 6.14 (e)-(f)). Thus, we can conclude that the weak localization (WL) signature in our TaN thin film is due to the FMI GdN layer.

Consequently, we assume predominant weak anti-localization (WAL) effects in TaN, which we have also proposed for the multilayers GdN/TaN (see Fig. 6.12 (a)) as well as GdN/AlN/TaN (see Fig. 6.14 (a)-(c)) at low T, throughout the entire T-regime for the trilayer sample. Moreover, the sharp outer bendings of the FDMR curves recorded close to the superconducting (SC) temperature $T_{\mathrm{SC,TaN}}\approx$5 K (see Fig. 6.11 (a)-(b)) further indicate WAL transport signatures in the TaN layer (see *A. H. Al-Tawhid et al.* [90]). We simulated our FDMR measurement curves, recorded in the entire T-range 7.5 K$<T<$20 K, by intserting iteratively suitable parameters L_ϕ, L_{SO} and F in Eq. (33) (see Tab. A.11). The results of the simulation are shown in Fig. 6.16 (a)-(f) as colored lines. Here, we observe the simulation curves (light blue line for $\mathbf{h}\|\mathbf{n}$, grey line for $\mathbf{h}\|\mathbf{j}$, magenta line for $\mathbf{h}\|\mathbf{t}$) agree well with our FDMR data, which also indicates weak anti-localization (WAL) transport phenomena in the TaN layer of our AlN/TaN/AlN heterostructure.

As a last step, we plot the phase coherence length L_ϕ and the spin-orbit length L_{SO} as a function of the temperature T (see Fig. 6.17).

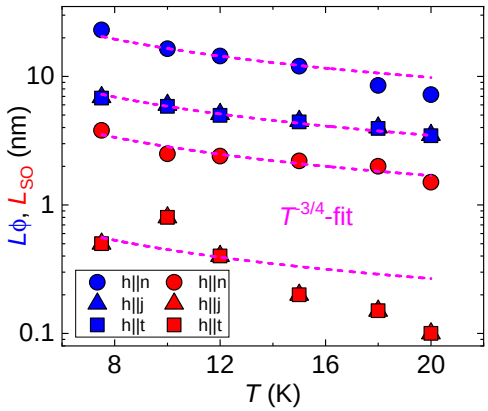

Fig. 6.17: Electron wave phase coherence length L_ϕ and spin-orbit length L_{SO}, used to model the FDMR curves by supposing WAL transport (see Eq. (33)) in TaN, as a function of the temperature T as well as the corresponding $T^{-3/4}$-fits (dashed magenta lines): L_ϕ and L_{SO} decreases with increasing T in all field geometries and their maximum values are visible in the low-temperature area.

In Fig. 6.17, we observe a decrease in phase coherence length L_ϕ (see blue data points) as well as a decrease spin-orbit length L_{SO} (see red data points) with increasing T is visible in all field geometries ($\mathbf{h}\|\mathbf{n}$, $\mathbf{h}\|\mathbf{j}$, $\mathbf{h}\|\mathbf{t}$). Furthermore, we fit our data with a $T^{-3/4}$-function (see dashed magenta lines), which is comparable to the results in the work of *M. Lv et al.* [32] and *E. M. Likovich et al.* [31]. The T-dependence of L_ϕ and L_{SO} is theoretical described by *P. A. Lee et al.* [37] and *B. L. Altshuler et al.* [38] and originates from electron-electron collisions in a disordered three-dimensional system [32]. In our work, due to the increasing L_ϕ and L_{SO} for low temperatures T, we assume stronger weak anti-localization (WAL) transport phenomena in TaN close to its superconducting (SC) temperature $T_{\mathrm{SC,TaN}}\approx 5\,\mathrm{K}$. In comparison to the work of *X. Zhang et al.* [98], we observe in Fig. 4(b) [98] of their manuscript a comparable evolution of L_ϕ and L_{SO} at a decreasing temperature T, which they associated with WAL effects in their WTe_2 thin film.

While we can model the observed FDMR effects in our samples by electron interference effects, the question arises how the superconducting transition affect our MR measurements, even at temperature above the critical transition temperature $T_{\mathrm{SC,TaN}}$. In our samples we can assume that the TaN layer consists of a polycrystalline structure with many grains residing in the Hall bar volume. A distribution of the superconducting transition temperature for these grains is to be expected and the observation of a zero-resistance state is thus related to a superconducting percolation path in the Hall bar. Thus even above the superconducting transition temperature determined from $R(T)$ measurements, we find superconducting grains, which will influence the current flow in the Hall bar and thus the measured longitudinal voltage. Upon the application of an external magnetic field, superconductivity in these grains is suppressed and the measured resistance in the Hall bar changes. At higher temperatures we need to also account for superconducting fluctuations, but the argumentation remains

the same. By introducing the FMI layer in the multilayerstructure the stray field mainly caused by magnetic domain walls and exchange field (for a direct GdN/TaN) interface will also influence the superconducting grains and thus may lead to a richer magnetoresistance signature. A similar discussion has been used for ferromagnet/superconductor/ferromagnet trilayer structures in (see work of *D. Stamopoulos et al.* [99]). This raises the interesting question if the size of the superconducting grains/grains with superconducting fluctuations is related to the extracted phase coherence length L_ϕ we use in the WL/WAL simulations.

6.2.7 Angle-dependent magnetoresistance (ADMR) of GdN/TaN heterostructures

In this section, we investigate the *angle-dependent magnetoresistance* (ADMR) of our GdN/TaN multilayer heterostructures. Figure 6.18 (a)-(l) and 6.19 (a)-(l) show the ADMR of our *SMR test sample* GdN/TaN (see Fig. 6.4), *SMR reference sample* GdN/AlN/TaN (see Fig. 6.7) and our AlN/TaN/AlN trilayer heterostructure (see Fig. 6.10) by performing magnetotransport measurements (see section 4.3.2) in the three different rotation planes in-plane (ip), out-of-plane $\perp$ **j** (oopj) and out-of-plane $\perp$ **t** (oopt) (see Fig. 4.4 (a)-(c)) and at different fixed temperatures T.

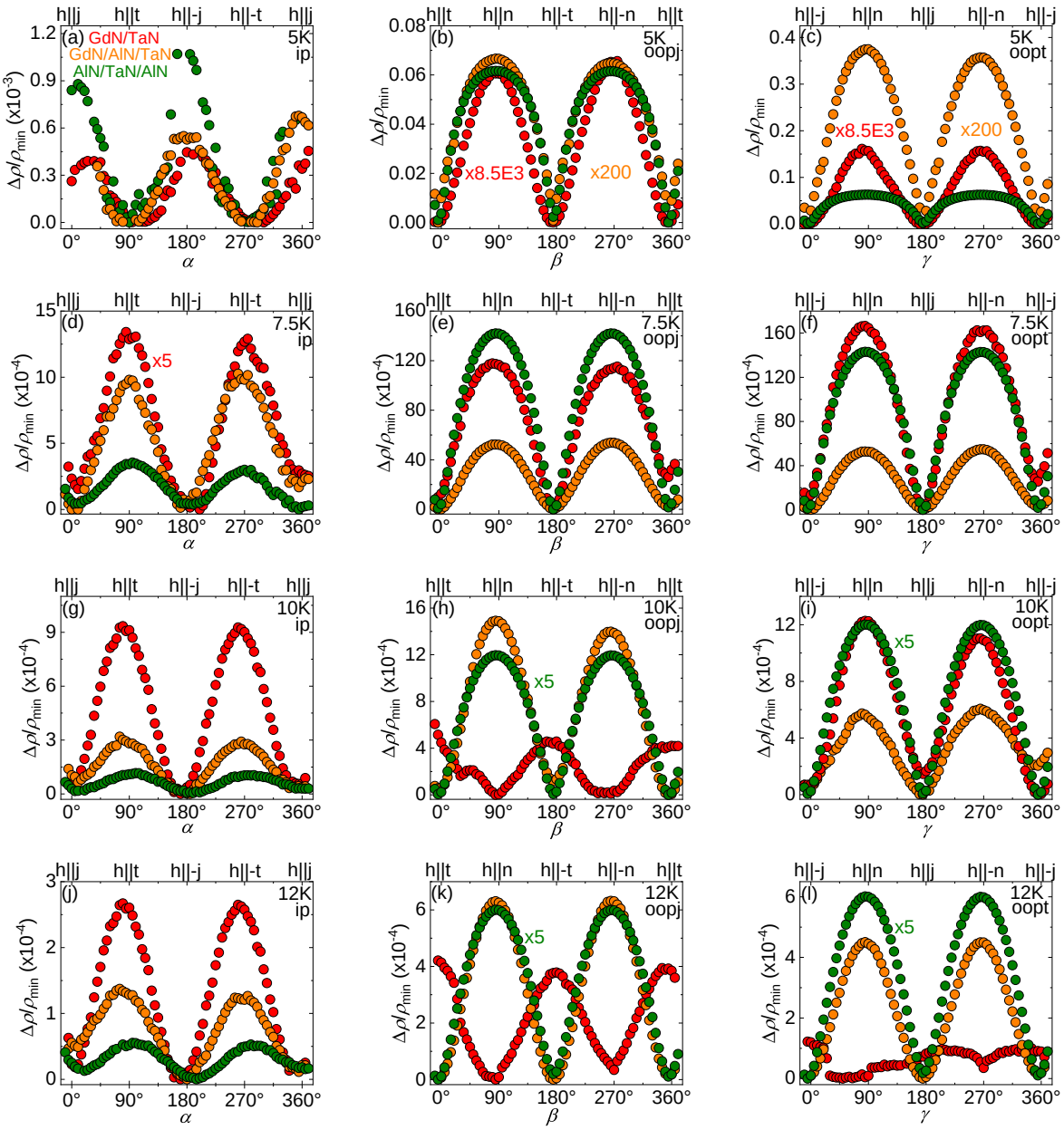

Fig. 6.18: Results of the angle-dependent magnetoresistance (ADMR) measurements of our multilayer heterostructures GdN/TaN (red data points), GdN/AlN/TaN (orange data points) and AlN/TaN/AlN (green data points) for temperatures in the range $5\,\mathrm{K} \leq T \leq 12\,\mathrm{K}$ at an applied external magnetic field $\mu_0 H_{\mathrm{ext}} = 7\,\mathrm{T}$: (a) The normalized longitudinal magnetoresistance $\Delta\rho/\rho_{\mathrm{min}}$ of the three samples shows an approximately $\cos^2(\alpha)$-behavior in the in-plane (ip) rotation plane at 5 K and in (b)-(c), we find a $\sin^2(\beta,\gamma)$-dependence in the two oop (oopj and oopt) field geometries for all multilayer thin films at $T = 5\,\mathrm{K}$. (d)-(f) The $\Delta\rho/\rho_{\mathrm{min}}(\alpha,\beta,\gamma)$-curves show a $\sin^2$-signature for all samples in the three rotation planes at $T = 7.5\,\mathrm{K}$. For higher temperatures $T = 10\,\mathrm{K}$ (g) and 12 K (j), a $\sin^2$-signature for all samples is visible in the ip geometry. In the oopj geometry, we observe a phase shift for the GdN/TaN multilayer thin film and $\Delta\rho/\rho_{\mathrm{min}}(\beta)$ shows a $\cos^2$-dependence at $T = 10\,\mathrm{K}$ (h) and 12 K (k), whereas in the ip geometry, the magnetoresistance shows a $\sin^2$-dependence at these temperatures. (i) The $\Delta\rho/\rho_{\mathrm{min}}(\gamma)$-curves of the three samples, recorded in the oopt rotation plane at $T = 10\,\mathrm{K}$, scale with a $\sin^2(\gamma)$ at $T = 10\,\mathrm{K}$. (l) At $T = 12\,\mathrm{K}$, there is no clear angle-dependence visible for the GdN/TaN sample in the oopt field geometry, whereas the normalized resistivity of the two other samples show a $\sin^2(\gamma)$-dependence. Furthermore, it should be noted that some datasets were multiplied by scaling factors to plot the ADMR curves of all three multilayer heterostructures in one graph.

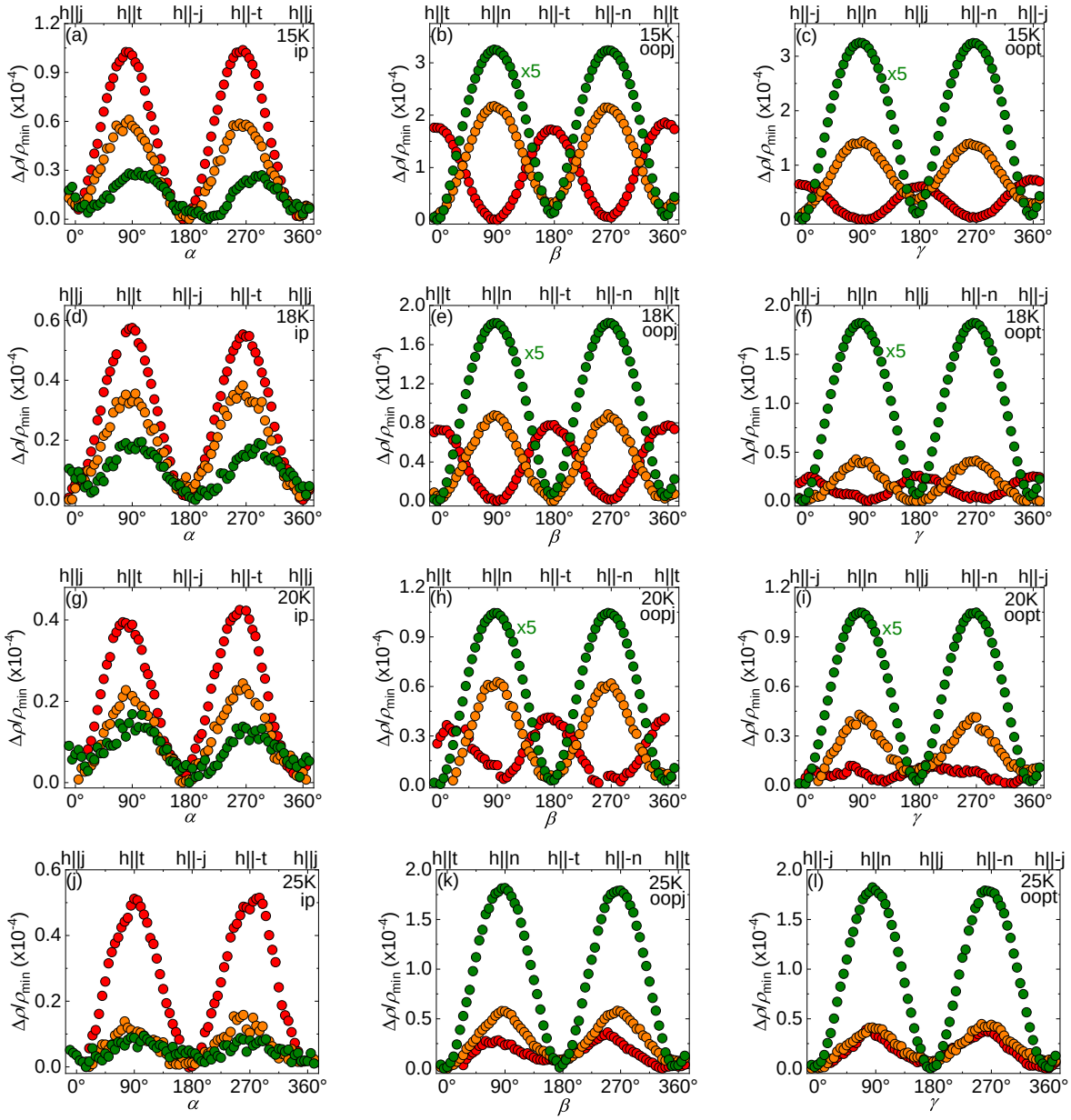

Fig. 6.19: Results of the angle-dependent magnetoresistance (ADMR) measurements of our multilayer heterostructures GdN/TaN (red data points), GdN/AlN/TaN (orange data points) and AlN/TaN/AlN (green data points) in the T-region 15 K$\leq T\leq$25 K at an applied external magnetic field $\mu_0 H_{\text{ext}}$=7 T: (a), (d), (g) The normalized longitudinal magnetoresistance $\Delta\rho/\rho_{\text{min}}$ of the three samples shows a $\sin^2(\alpha)$-dependence in the in-plane (ip) rotation plane. In the oopj field geometry, $\Delta\rho/\rho_{\text{min}}(\beta)$ still shows a $\cos^2$-dependence at T=15 K (b) 18 K (e) and 20 K (h) for our GdN/TaN multilayer thin film, whereas the normalized resistivity of the two other samples still exhibit a $\sin^2$-dependence at these temperatures. The same qualitative angular dependence of the $\Delta\rho/\rho_{\text{min}}(\gamma)$-curves of the three samples, is visible in the oopt geometry measured at T=15 K (c) and 18 K (f). (i) T=20 K, we find no significant angle-dependence for GdN/TaN measured in the oopt field geometry, whereas the normalized resistivity of the two other samples exhibit a $\sin^2(\gamma)$-dependence. (j) At T=25 K, $\Delta\rho/\rho_{\text{min}}(\alpha,\beta,\gamma)$ of the three samples show a $\sin^2$-dependence in the three different rotation planes ip, oopj and oopt.

Figure 6.18 (a)-(l) and 6.19 (a)-(l) illustrates the longitudinal magnetoresistance $\text{MR}(\phi)=[\rho_{\text{long}}(\phi)/\rho_{\text{long}}(\phi=90°)]-1=\Delta\rho/\rho_{\text{min}}$ depending on the rotation angles $\phi=\alpha$, β, γ of our multilayer heterostructure thin films (GdN/TaN see red filled circles, GdN/AlN/TaN

see orange filled circles and AlN/TaN/TaN see green filled circles) measured in the field geometries in-plane (ip), out-of-plane $\perp$ **j** (oopj) and out-of-plane $\perp$ **t** (oopt) at an applied external magnetic field $\mu_0 H_{\text{ext}}$=7 T and different fixed temperatures T. Figure 6.18 (a) shows a weak $\cos^2(\alpha)$-dependence for $\Delta\rho/\rho_{\text{min}}$ of the three different samples measured in the in-plane (ip) rotation plane at T=5 K, which is situated within the range of the superconducting (SC) transition temperature $T_{\text{SC,TaN}}\approx$5 K of TaN for all three samples. Consequently, we observe for our GdN/TaN- and GdN/AlN/TaN-sample a very low electrical resistance of $R\approx$10 mΩ and for our AlN/TaN/AlN trilayer system, a larger resistance $R\approx$15 Ω is visible. In both out-of-plane measurement geometries (oopj, see Fig. 6.18 (b) and oopt, see Fig. 6.18 (c)), the normalized resistivity $\Delta\rho/\rho_{\text{min}}$ of the three multilayer samples scales with a $\sin^2(\beta,\gamma)$-dependence and we observe for our *SMR test sample* (GdN/TaN) still a low electrical resistance of $R\approx$200 mΩ and for our *SMR reference sample* (GdN/AlN/TaN) as well as our AlN/TaN/AlN trilayer thin film there are significant higher values of $R\approx$800 Ω visible. These values are higher than for the in-plane rotation due to the breakdown of superconductivity in TaN in an oop magnetic field of 7 T.

In Figure 6.18 (d), we find a $\sin^2(\alpha)$-dependence for $\Delta\rho/\rho_{\text{min}}$ of our three multilayer thin films measured in the in-plane (ip) field geometry at T=7.5 K and we observe the significantly enhanced elctrical resistances $R_{\text{GdN/TaN}}\approx$2.4 k$\Omega$, $R_{\text{GdN/AlN/TaN}}\approx$1.8 k$\Omega$ and $R_{\text{AlN/TaN/AlN}}\approx$0.86 k$\Omega$. In the oop field geometries (oopj, see Fig. 6.18 (e) and oopt, see Fig. 6.18 (f)), remaining superconducting phases of TaN break down at 90° (**h**$\|$**n**) and $\Delta\rho/\rho_{\text{min}}$ scales with a $\sin^2(\beta,\gamma)$. Hence, we here observe almost equal resistances R in oop compared to the values measured in the in-plane (ip) field geometry (see Fig. 6.18 (d)). In the T-regime 10 K$\leq T\leq$20 K (see Fig. 6.18 (g) and (j) and Fig. 6.19 (a), (d) and (g)), the ADMR curves of the three multilayer samples recorded in the ip rotation plane show a $\sin^2(\alpha)$ signature, which originates from the quadratic contribution of the MR (see Fig. 6.12, 6.14 and 6.16), and we observe the slight enhanced electrical resistances $R_{\text{GdN/TaN}}\approx$2.7 k$\Omega$, $R_{\text{GdN/AlN/TaN}}\approx$1.9 k$\Omega$ and $R_{\text{AlN/TaN/AlN}}\approx$0.87 k$\Omega$ compared to the values recorded at T=7.5 K.

Moreover, there is a change in angle-dependence visible in the oopj geometry (see Fig. 6.18 (h) and (k) and Fig. 6.19 (b), (e) and (h)) for our GdN/TaN heterostructure and the ADMR curves scale with a $\cos^2(\beta)$-dependence in the T-range 10 K$\leq T\leq$20 K. In contrast, the ADMR curves of our multilayer thin films GdN/AlN/TaN and AlN/TaN/AlN still scale with $\sin^2(\beta)$. We assume the change in angle-dependence of the ADMR in the oopj-geometry $\text{ADMR}_{\text{oopj}}=\text{MR}_{\mathbf{h}\|\mathbf{n}}-\text{MR}_{\mathbf{h}\|\mathbf{t}}$ originates from switching from the weak anti-localization (WAL) to the weak-localization (WL) transport phenomena in the TaN layer of the GdN/TaN bilayer (see Sec. 6.2.4). Due to the non-existing GdN/TaN interface, the ADMR curves of the samples GdN/AlN/TaN and AlN/TaN/AlN shows a $\sin^2(\beta)$-dependence in the oopj geometry in the temperature range 10 K$\leq T\leq$20 K (see Fig. 6.18 (h) and (k) and Fig. 6.19 (b), (e) and (h)). However, the transition from WAL to WL is also visible in the FDMR-data recorded for the GdN/AlN/TaN sample (see Sec. 6.2.5), such that a more detailed discussion is required, which is presented in chapter 7. In the oopt field geometry, we observe a $\sin^2(\gamma)$-dependence for the ADMR curves of

the three multilayer samples recorded at T=10 K (see Fig. 6.18 (i)). For T = 12 K, there is no significant angle-dependence visible for our GdN/TaN multilayer heterostructure (see Fig. 6.18 (l)), however the ADMR curves of the two other samples show only a $\sin^2(\gamma)$ shape in the T-regime 12 K$\leq T\leq$20 K (see Fig. 6.18 (l) and Fig. 6.19 (c), (f) and (i)). We also observe a change in angle-dependence in the ADMR in the oopt geometry $\mathrm{ADMR_{oopt}}=\mathrm{MR_{\mathbf{h}\|\mathbf{n}}}-\mathrm{MR_{\mathbf{h}\|\mathbf{j}}}$ for our GdN/TaN multilayer (see Fig. 6.19 (c) and (f)) and the ADMR curves of our GdN/TaN multilayer sample measured in the T-range 15 K$\leq T\leq$18 K again scale with a $\cos^2(\gamma)$. As discussed for the oopj measurements, we associate this with a change in the field-dependence for the longitudinal MR in this regime, which can be describe as a transition from WAL to WL in the TaN thin film interfaced with GdN (see Sec. 6.2.4). For T=20 K, the $\cos^2(\gamma)$-dependence vanishes (see red data points in Fig. 6.19 (i)) and no significant angle-dependence is visible for the ADMR data of our GdN/TaN multilayer. Finally, we observe a $\sin^2(\alpha,\beta,\gamma)$ signature of the ADMR curves of our three multilayer samples measured in the rotation planes ip, oopj and oopt (see Fig. 6.19 (j)-(l)) at T=25 K, which is close to the ferromagnetic (FM) Curie temperature $T_{\mathrm{C,GdN}}\approx$30 K of GdN. We assume, that GdN only exhibits a weak magnetic moment above $T>$30 K and the WL effect in TaN disappears at even higher temperatures T.

6.2.8 Study for the ADMR amplitude of the GdN/TaN heterostructures as a function of temperature T

As a next step, we investigate the amplitude of the ADMR effect of our three multilayer heterostructures GdN/TaN, GdN/AlN/TaN and AlN/TaN/AlN in the temperature range 7.5 K$\leq T\leq$50 K. To this end, we extract the relative ADMR amplitude from our ADMR measurement results, which is exemplary illustrated in Fig. 6.20.

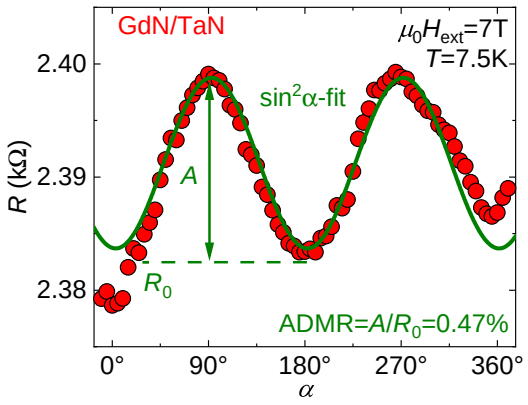

Fig. 6.20: ADMR measurement results of our GdN/TaN multilayer thin film, measured in the in-plane (ip) rotation plane at μ_0H_{ext}=7 T and T=7.5 K, to demonstrate exemplary the extraction method of the ADMR amplitude by performing a $\sin^2$-fit (green line).

Figure 6.20 shows the method to determine the ADMR amplitude of our GdN/TaN multilayer thin film measured in the in-plane (ip) rotation plane at μ_0H_{ext}=7 T and T=7.5 K. Here, we fit our ADMR data with a $\sin^2(\alpha)$-function, which allows an angular offset and is 180° periodic, and afterwards we use the fit parameters A (amplitude of the $\sin^2$-fit) and R_0

(resistance R at the minimum of the $\sin^2$-function) to calculate the ADMR amplitude with the following formula

$$\text{ADMR} = \frac{A}{R_0}. \tag{37}$$

In Figure 6.21 (a)-(i), we plot the extracted ADMR amplitude of our multilayer heterostructures GdN/TaN, GdN/AlN/TaN and AlN/TaN/AlN, measured in the three field geometries in-plane (ip), out-of-plane $\perp$ **j** (oopj) and out-of-plane $\perp$ **t** (oopt), as a function of the measurement temperature T .

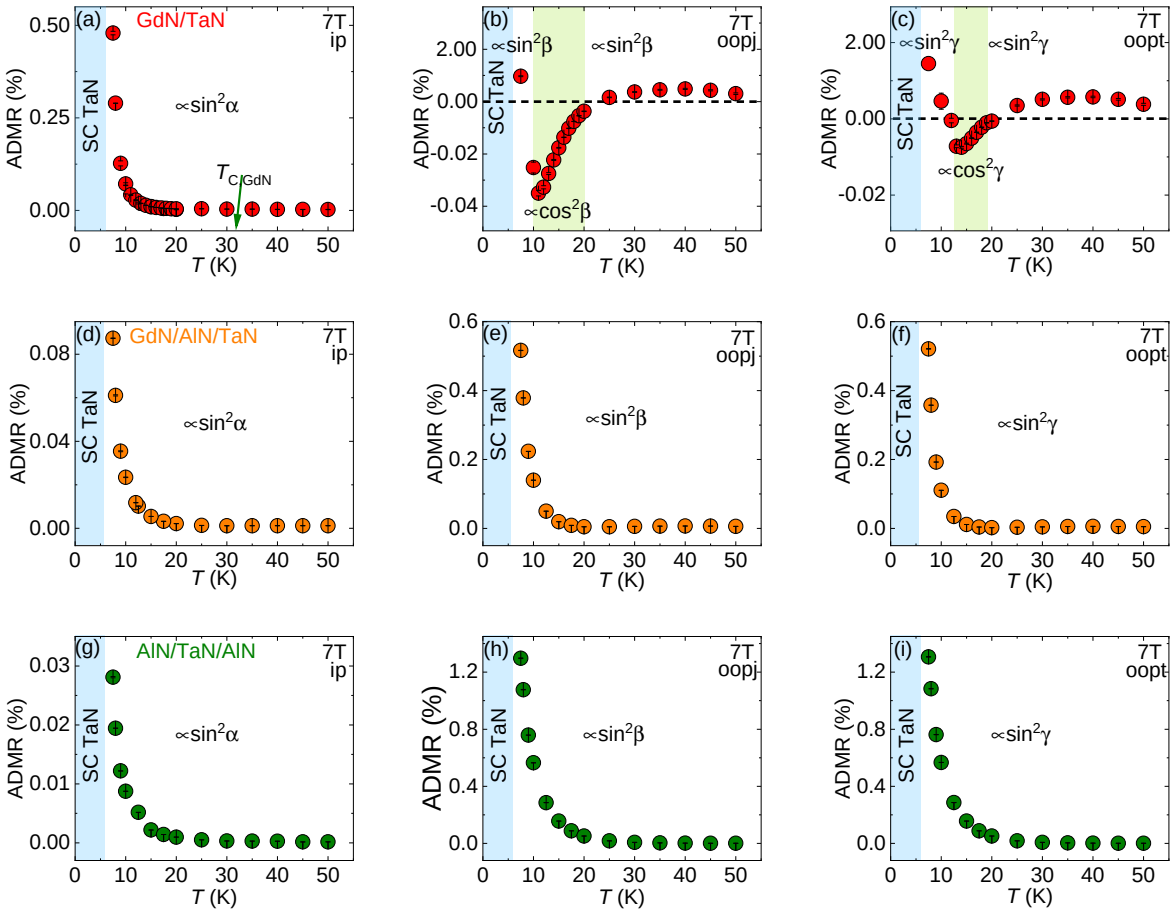

Fig. 6.21: ADMR amplitude, extracted from the angle-dependent magnetoresistance (ADMR) measurement results of our multilayer heterostructures GdN/TaN (red data points), GdN/AlN/TaN (orange data points) and AlN/TaN/AlN (green data points), in the entire measured T-range 7.5 K$\leq T\leq$50 K at an applied external magnetic field $\mu_0 H_{\text{ext}}$=7 T: (a) In the in-plane (ip) field geometry, the ADMR amplitude of our GdN/TaN multilayer heterostructure shows an almost exponential increase, which corresponds to the $\sin^2$-signature of our $\Delta\rho/\rho_{\text{min}}(\alpha)$-plots, towards low temperatures and there is a maximum value of ADMR$\approx$0.47% at T=7.5 K. (b)-(c) The ADMR(T)-curves of GdN/TaN, recorded in the two out-of-plane (oopj, oopt) field geometries, shows a significantly increased maximum ADMR amplitude at T=7.5 K and a negative dip in the T-area 10 K$\leq T\leq$20 K (oopj) and 13 K$\leq T\leq$19 K (oopt) and the ADMR amplitude changes sign, which corresponds to the change in angle-dependence ($\sin^2(\beta,\gamma) \rightarrow \cos^2(\beta,\gamma)$ and $\cos^2(\beta,\gamma) \rightarrow \sin^2(\beta,\gamma)$) in the $\Delta\rho/\rho_{\text{min}}(\beta,\gamma)$-plots. (d)-(i) The ADMR amplitude of our two reference samples GdN/AlN/TaN and AlN/TaN/AlN increases with decreasing temperatures T in the three field geometries ip, oopj, oopt. Again, a maximum ADMR amplitude is visible at T=7.5 K. The T-dependent evolution of the ADMR amplitude of our GdN/AlN/TaN and AlN/TaN/AlN sample are equivalent to the $\sin^2$-dependence of our $\Delta\rho/\rho_{\text{min}}(\alpha, \beta,\gamma)$-plots measured in all rotation planes.

Figure 6.21 (a)-(i) shows the results of the ADMR measurements of our three multilayer samples GdN/TaN (red data points), GdN/AlN/TaN (orange data points) and AlN/TaN/AlN (green data points) in the entire T-range 7.5 K$\leq T\leq$50 K at an applied external magnetic field $\mu_0 H_{\text{ext}}$=7 T. In Fig 6.21 (a), we observe an almost exponential increase of the ADMR amplitude with decreasing temperature T of our *SMR test sample* GdN/TaN and there is a maximum ADMR amplitude of ≈0.47 % at T=7.5 K. Furthermore, the signature of the ip ADMR-(T) curve corresponds to the $\sin^2(\alpha)$-dependence of our $\Delta\rho/\rho_{\text{min}}(\alpha)$-plots (see red data points in Fig. 6.18 (d), (g) and (j) and Fig. 6.19 (a), (d), (g) and (j)) throughout the entire T-range 7.5 K$\leq T\leq$50 K. The results of the ADMR measurements in the both out-of-plane field geometries (oopj and oopt), are shown in 6.21 (b)-(c). Here, we observe a noticeable increased maximum ADMR amplitude of ≈0.97 % (oopj) and ≈1.45 % (oopt) at T=7.5 K as well as negative values for the ADMR in the T-ranges 10 K$\leq T\leq$20 K (oopj) and 13 K$\leq T\leq$19 K (oopt) in the rotation planes oopj (see Fig 6.21 (b)) and oopt (see Fig 6.21 (c)). In these two temperature ranges, the ADMR amplitude changes sign, wich corresponds to a change in the angle-dependence from $\sin^2(\beta,\gamma) \rightarrow \cos^2(\beta,\gamma)$ observed in the $\Delta\rho/\rho_{\text{min}}(\beta,\gamma)$-plots (see Fig. 6.18 (h), (k) and Fig. 6.19 (b), (c), (e), (f), (h)). Moreover, we observe a low ADMR amplitude in oopt at T=12 K and 20 K, which originates from the weak angle-dependence of $\Delta\rho/\rho_{\text{min}}(\gamma)$ at these temperatures T (see Fig. 6.18 (i) and 6.19 (i)). For higher T, we observe again a positive ADMR amplitude, which saturates close to the zero line and shows a slight cusp feature, in the T-range 25 K$\leq T\leq$50 K in both oop field geometries (see Fig 6.19 (b) Fig 6.19 (c)). The positive magnitude of the ADMR amplitude in $T\geq$25 K corresponds to the second change in angle-dependence ($\cos^2(\beta,\gamma) \rightarrow \sin^2(\beta,\gamma)$) observed in our $\Delta\rho/\rho_{\text{min}}(\beta,\gamma)$-plots (see Fig. 6.19 (k), (l)). Finally, for 25 K$\leq T\leq$50 K, we find only a $\sin^2(\beta,\gamma)$-dependency, which decreases with an increasing temperature T, for the ADMR amplitude.

In Figure 6.21 (d)-(i), we plot the extracted ADMR amplitude of our *SMR reference sample* GdN/AlN/TaN (see orange data points) as well as our AlN/TaN/AlN heterostructure (see green data points) as a function of the temperature T. Here, we observe for both samples an approximately exponential increase of the ADMR amplitude, extracted from the three rotation measurements in-plane (ip), out-of-plane $\perp$ **j** (oopj) and out-of-plane $\perp$ **t** (oopt), towards low temperatures and there is a maximum ADMR amplitude of ≈0.087% (GdN/AlN/TaN) and ≈0.028% (AlN/TaN/AlN) at T=7.5 K, which is close to the superconducting (SC) transition temperature $T_{\text{SC,TaN}}$≈5.5 K of TaN. The temperature-dependent evolution of the ADMR amplitude of the two reference samples in all three field geometries corresponds to the $\sin^2(\alpha,\beta,\gamma))$ signature of our $\Delta\rho/\rho_{\text{min}}(\alpha,\beta,\gamma)$-plots (see Fig. 6.18 (d)-(l) and Fig. 6.19 (a)-(l)). Furthermore, the maximum ADMR amplitudes at T=7.5 K, extracted from the two oop field rotation measurement results (see Fig. 6.21 (e)-(f) and (h)-(i)), are significantly larger as compared to the values from the in-plane (ip) measurements of our two samples. In comparison to the maximum ADMR amplitude ≈0.47 % of our *SMR test sample* with the GdN/TaN interface (measured in ip at T=7.5 K), we observe singifcantly lower amplitudes for our two reference samples, without a direct GdN/TaN interface measured in the ip field geometry. Moreover, no negative values for the ADMR amplitude manifests in oopj and oopt geometry and therefore no negative ADMR

amplitude is visible. Consequently, there are no phase changes ($\sin^2(\beta,\gamma) \rightarrow \cos^2(\beta,\gamma)$) and ($\cos^2(\beta,\gamma) \rightarrow \sin^2(\beta,\gamma)$) visible in the $\Delta\rho/\rho_{\mathrm{min}}(\beta,\gamma)$-plots (see Fig. 6.18 (d)-(l) and Fig. 6.19 (a)-(l)) of our two reference samples GdN/AlN/TaN and AlN/TaN/AlN. We associate the unchanged $\sin^2(\beta,\gamma)$-dependence in these samples to the role of the direct GdN/TaN interface for the magnetoresistance in our *SMR reference sample* (GdN/AlN/TaN) and the missing FMI GdN layer in our AlN/TaN/AlN trilayer heterostructure.

To investigate the origin of our ADMR measurement results as well as to further analyze the evolution of the $\Delta\rho/\rho_{\min}(\alpha,\beta,\gamma)$-plots (see Fig. 6.18 (a)-(l) and Fig. 6.19 (a)-(l)), we perform a comparison of the ADMR data (see Fig.6.21 (a)-(i)) with our field-dependent magnetoresistance (FDMR) measurement results of our three multilayer heterostructures (see Sec. 6.2.4, 6.2.5, 6.2.6). For this purpose, we generate MR(T)-plots, which are shown in Figure 6.22 (a)-(i), in the three rotation field geometries in-plane (ip), out-of-plane $\perp$ **j** (oopj) and out-of-plane $\perp$ **t** (oopt).

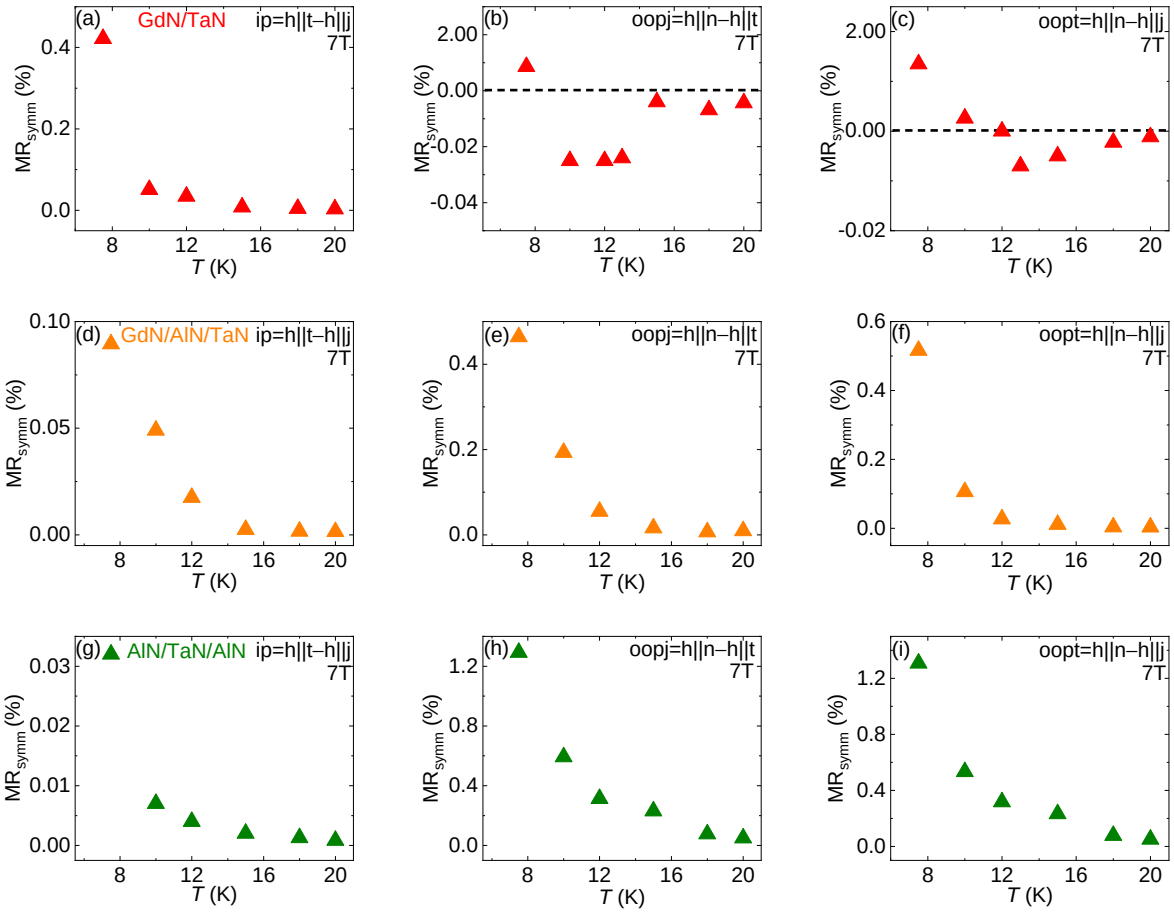

Fig. 6.22: MR amplitude, extracted from the field-dependent magnetoresistance (FDMR) data measured in the field geometries oop (**h**$\|$**n**) and ip (**h**$\|$**j** and **h**$\|$**t**) in the T-region 7.5 K$\leq T\leq$20 K and at $\mu_0 H_{\text{ext}}$=7 K, as a function of the temperature T of our multilayer heterostructures GdN/TaN (red data points), GdN/AlN/TaN (orange data points) and AlN/TaN/AlN (green data points). The MR(T)-curves are converted into the field rotation geometries in-plane (ip=**h**$\|$**t**$-$**h**$\|$**j**), out-of-plane $\perp$ **j** (oopj=**h**$\|$**n**$-$**h**$\|$**t**) and out-of-plane $\perp$ **t** (oopt=**h**$\|$**n**$-$**h**$\|$**j**): (a) In the in-plane (ip) field geometry, the MR amplitude of our GdN/TaN multilayer heterostructure shows an almost exponential increase, which is in agreement to the signature of our ADMR(T)-curves in Fig. 6.21 (a), with decreasing T and there is a maximum value of MR$\approx$0.42% visible at T=7.5 K. (b)-(c) The MR(T)-curves of GdN/TaN, converted into the two out-of-plane (oopj, oopt) field geometries, show also a noticeable increased maximum MR at T=7.5 K and a negative dip in the T-area 10 K$\leq T\leq$20 K (oopj) and 13 K$\leq T\leq$19 K (oopt), which is equivalent to the T-dependent evolution of our ADMR-curves in Fig. 6.21 (b)-(c). (d)-(i) The MR amplitudes of our two reference samples GdN/AlN/TaN and AlN/TaN/AlN increase with decreasing T in the three field geometries ip, oopj, oopt and there is also a maximum MR amplitude visible at T=7.5 K. The signatures of the MR(T)-curves of our GdN/AlN/TaN and AlN/TaN/AlN thin films are similar to the ADMR(T)-curves measured in the three rotation planes ip, oopj and oopt in Fig. 6.21 (d)-(i).

Figure 6.22 (a)-(i) shows the symmetrized longitudinal magnetoresistance MR, extracted from the FDMR measurement results (see Sec. 6.2.4, 6.2.5, 6.2.6), of our three multilayer samples as a function of T. Here, we calculate the MR in the three different rotation field geometries in-plane (ip), out-of-plane $\perp$ **j** (oopj) and out-of-plane $\perp$ **t** (oopt) by comparing and substracting the FDMR data, measured in the three different field geometries oop ($\mathbf{h}\|\mathbf{n}$) and ip ($\mathbf{h}\|\mathbf{j}$ and $\mathbf{h}\|\mathbf{t}$), at an applied external magnetic field $\mu_0 H_{\text{ext}}$=7 T. Therefore, the MR data in the in-plane (ip) rotation plane are given by

$$\text{MR}_{\text{ip}} = \text{MR}_{\mathbf{h}\|\mathbf{t}} – \text{MR}_{\mathbf{h}\|\mathbf{j}} \tag{38}$$

and the MR in the two out-of-plane (oop) geometries are defined by

$$\text{MR}_{\text{oopj}} = \text{MR}_{\mathbf{h}\|\mathbf{n}} – \text{MR}_{\mathbf{h}\|\mathbf{t}}, \tag{39}$$

and

$$\text{MR}_{\text{oopt}} = \text{MR}_{\mathbf{h}\|\mathbf{n}} – \text{MR}_{\mathbf{h}\|\mathbf{j}}. \tag{40}$$

In Figure 6.22 (a)-(i), we observe for our multilayer samples GdN/TaN (red triangles), GdN/AlN/TaN (orange triangles) and AlN/TaN/AlN (green triangles) a similar T-dependent evolution for MR compared to our ADMR(T)-plots (see Fig.6.21 (a)-(i)), which indicates the correspondence of our FDMR- and ADMR-measurement results. Moreover, the extracted MR values agree quantitatively well for both measurement methods.

As a next step, we further analyze the origin of the negative MR-dip, which corresponds to a change in the apparent angle-dependence ($\sin^2(\beta,\gamma) \rightarrow \cos^2(\beta,\gamma)$) in the $\Delta\rho/\rho_{\mathrm{min}}(\beta,\gamma)$-curves (see Fig. 6.18 (h) and Fig. 6.19 (c)), of our ADMR(T)- (see Fig. 6.21 (b)-(c)) and MR(T)-curves (see Fig. 6.22 (b)-(c)) in oopj and oopt geometry. To this end, we investigate the MR(H)-curves, recorded in our FDMR measurements (see Sec. 6.2.4), of our GdN/TaN multilayer heterostructure in the T-region 10 K$\leq T\leq$20 K at 0 T$\leq\mu_0 H_{\mathrm{ext}}\leq$7 T (see Figure 6.23 (a)-(f)).

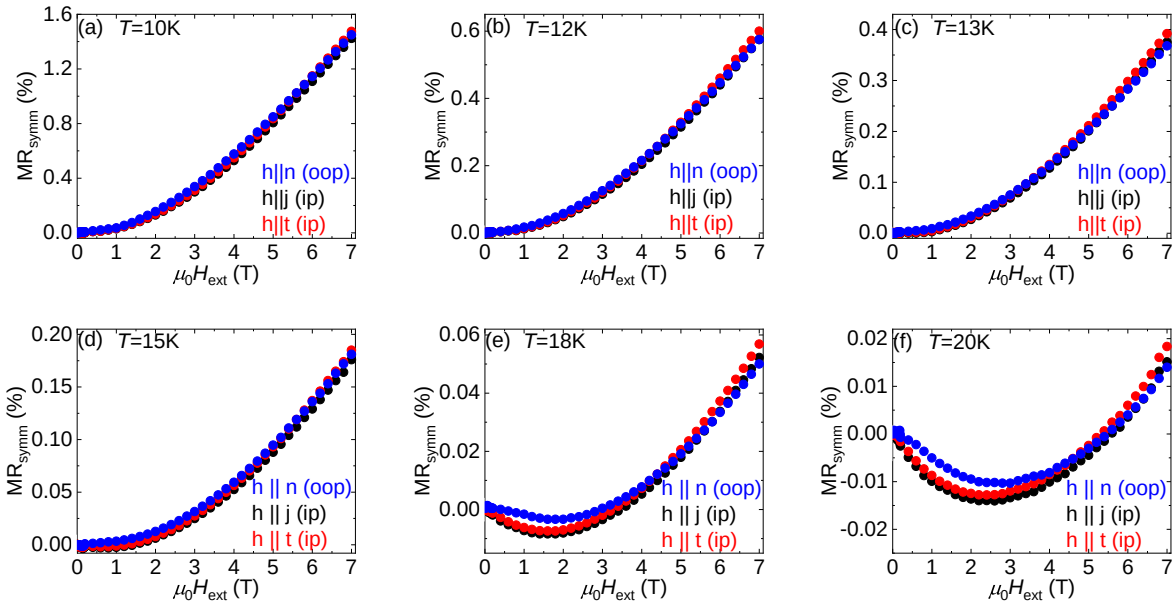

Fig. 6.23: Results of the field-dependent magnetoresistance (FDMR) measurements in the field geometries oop ($\mathbf{h}\|\mathbf{n}$) and ip ($\mathbf{h}\|\mathbf{j}$ and $\mathbf{h}\|\mathbf{t}$) to determine the symmetrized MR amplitude in the rotation geometries in-plane (ip=$\mathbf{h}\|\mathbf{t}-\mathbf{h}\|\mathbf{j}$), out-of-plane $\perp$ **j** (oopj=$\mathbf{h}\|\mathbf{n}-\mathbf{h}\|\mathbf{t}$) and out-of-plane $\perp$ **t** (oopt=$\mathbf{h}\|\mathbf{n}-\mathbf{h}\|\mathbf{j}$) in the T-range 10 K$\leq T\leq$20 K at $\mu_0 H_{\mathrm{ext}}$=7 T. (a)-(f) In 10 K$\leq T\leq$20 K we observe for the symmetrized magnetoresistance at 7 T, $\mathrm{MR}_{\mathbf{h}\|\mathbf{n}}<\mathrm{MR}_{\mathbf{h}\|\mathbf{t}}$, which generates the negative dip in the oopj ADMR(T)- and MR(T)-curves by using Eq. (39). (a) In addition, there is the relationship $\mathrm{MR}_{\mathbf{h}\|\mathbf{n}}>\mathrm{MR}_{\mathbf{h}\|\mathbf{j}}$ visible at T=10 K and 7 T, which corresponds to a positive MR in oopt by using Eq. (40). (c)-(e) In the T-range 13 K$\leq T\leq$18 K and at 7 T, we observe $\mathrm{MR}_{\mathbf{h}\|\mathbf{n}}<\mathrm{MR}_{\mathbf{h}\|\mathbf{j}}$ and we also obtain a negative dip in the oopt ADMR(T)- and MR(T)-curves by using Eq. (40). In (a) and (f) we observe, $\mathrm{MR}_{\mathbf{h}\|\mathbf{n}}\approx\mathrm{MR}_{\mathbf{h}\|\mathbf{j}}$ and therefore no clear contribution to the MR in oopt is visible in the ADMR(T)- and MR(T)-plots at T=12 K and 20 K at 7 T.

Figure 6.23 (a)-(f) shows the MR(H)-curves of our GdN/TaN multilayer sample. To verify the origin of the negative MR-dip in our ADMR(T)- and MR(T)-curves as well as the change in angle-dependence in our $\Delta\rho/\rho_{\mathrm{min}}(\beta,\gamma)$-plots, we analyze the maximum MR of the MR(H)-curves, recorded in the three different field geometries oop ($\mathbf{h}\|\mathbf{n}$) and ip ($\mathbf{h}\|\mathbf{j}$, $\mathbf{h}\|\mathbf{t}$), at the maximum external magnetic field $\mu_0 H_{\mathrm{ext}}$=7 T. Here, we observe in the entire T-area 10 K$\leq T\leq$20 K at 7 T the relationship $\mathrm{MR}_{\mathbf{h}\|\mathbf{n}}<\mathrm{MR}_{\mathbf{h}\|\mathbf{t}}$, which produces the negative dip in the ADMR(T)- and MR(T)-curves by using Eq. (39) as well as the observed $\cos^2$-signature of the $\Delta\rho/\rho_{\mathrm{min}}(\beta)$-curves in the oopj geometry. Furthermore, we observe at 10 K and 7 T the realtionship $\mathrm{MR}_{\mathbf{h}\|\mathbf{n}}>\mathrm{MR}_{\mathbf{h}\|\mathbf{j}}$, which corresponds to a positive contribution in the ADMR(T)- and MR(T)-curves using Eq. (40) and $\Delta\rho/\rho_{\mathrm{min}}(\gamma)$ scales with a $\sin^2$-dependence in the oopt geometry. In the intermediate T-range 13 K$\leq T\leq$18 K, we observe $\mathrm{MR}_{\mathbf{h}\|\mathbf{n}}<\mathrm{MR}_{\mathbf{h}\|\mathbf{j}}$ in oopt,

which also generates a negative dip in the ADMR(T)- and MR(T)-curves by using Eq. (40). Therefore, we observe also a $\cos^2$-dependence of the $\Delta\rho/\rho_{\min}(\gamma)$-curves in the oopt field geometry. Moreover, at T=12 K and 20 K, we find $\mathrm{MR}_{\mathbf{h}\|\mathbf{n}}\approx\mathrm{MR}_{\mathbf{h}\|\mathbf{j}}$ at 7 T and therefore no significant angle-dependence is visible in our $\Delta\rho/\rho_{\min}(\gamma)$-plot in oopt, which corresponds to an almost zero contribution in the MR in that field direction. Due to the results of the MR(H)-curve analysis (see Table 6.5), we verified the agreement of our *field-dependent magnetoresistance* (FDMR)- and *angle-dependent magnetoresistance* (ADMR)-measurement data at 10 K$\leq T\leq$20 K and 7 T.

T [K]	FDMR(@7 T)	$\mathrm{MR}_{\mathrm{oopj}}$	ADMR	FDMR(@7 T)	$\mathrm{MR}_{\mathrm{oopt}}$	ADMR
10	$\mathbf{h}\|\mathbf{n}<\mathbf{h}\|\mathbf{t}$	<0	$\propto\cos^2(\beta)$	$\mathbf{h}\|\mathbf{n}>\mathbf{h}\|\mathbf{j}$	>0	$\propto\sin^2(\gamma)$
12	$\mathbf{h}\|\mathbf{n}<\mathbf{h}\|\mathbf{t}$	<0	$\propto\cos^2(\beta)$	$\mathbf{h}\|\mathbf{n}\approx\mathbf{h}\|\mathbf{j}$	≈0	≈0
13	$\mathbf{h}\|\mathbf{n}<\mathbf{h}\|\mathbf{t}$	<0	$\propto\cos^2(\beta)$	$\mathbf{h}\|\mathbf{n}<\mathbf{h}\|\mathbf{j}$	<0	$\propto\cos^2(\gamma)$
15	$\mathbf{h}\|\mathbf{n}<\mathbf{h}\|\mathbf{t}$	<0	$\propto\cos^2(\beta)$	$\mathbf{h}\|\mathbf{n}<\mathbf{h}\|\mathbf{j}$	<0	$\propto\cos^2(\gamma)$
18	$\mathbf{h}\|\mathbf{n}<\mathbf{h}\|\mathbf{t}$	<0	$\propto\cos^2(\beta)$	$\mathbf{h}\|\mathbf{n}<\mathbf{h}\|\mathbf{j}$	<0	$\propto\cos^2(\gamma)$
20	$\mathbf{h}\|\mathbf{n}<\mathbf{h}\|\mathbf{t}$	<0	$\propto\cos^2(\beta)$	$\mathbf{h}\|\mathbf{n}\approx\mathbf{h}\|\mathbf{j}$	≈0	≈0

Tab. 6.5: Comparison of the FDMR- and ADMR measurement results at 10 K$\leq T\leq$20 K and H_{ext}=7 T.

6.2.9 Magnetic field dependence of the ADMR amplitude

In the last section of this chapter, we further investigate the *angle dependent magnetoresistance* (ADMR) measurement results of our *SMR test sample* GdN/TaN at T=12 K and 20 K (see Fig 6.24).

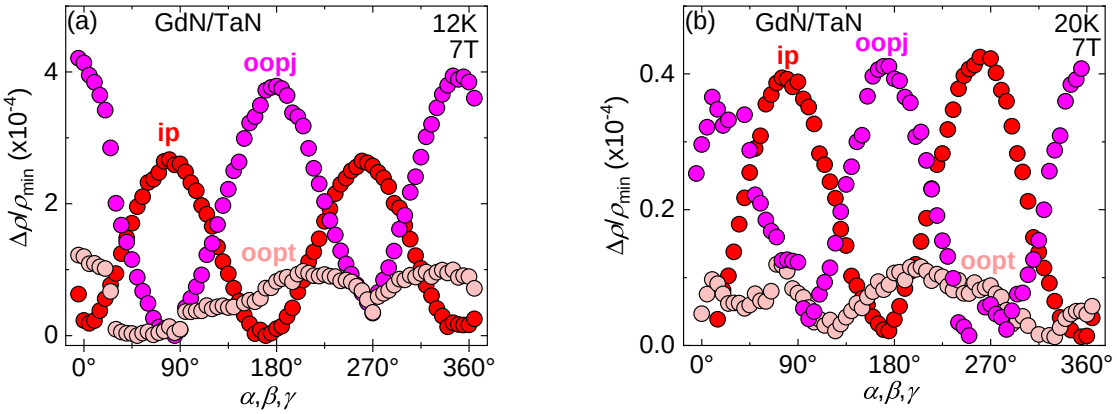

Fig. 6.24: ADMR measurement results for our GdN/TaN multilayer heterostructure at T=12 K and 20 K and $\mu_0 H_{ext}$=7 T: The normalized longitudinal resistivity $\Delta\rho/\rho_{min}$ depending on the three different rotation angles α, β, γ shows a different evolution in the three field geometries in-plane (ip) $\rightarrow$ $\Delta\rho/\rho_{min} \propto \sin^2(\alpha)$, out-of-plane $\perp$ **j** (oopj) $\rightarrow$ $\Delta\rho/\rho_{min} \propto \cos^2(\beta)$ and out-of-plane $\perp$ **t** (oopt) $\rightarrow$ no clear angle-dependence is visible for $\Delta\rho/\rho_{min}(\gamma)$.

Figure 6.24 (a)-(b) illustrates the ADMR data of our GdN/TaN multilayer heterostructure measured at an applied external magnetic field H_{ext}=7 T and different fixed temperatures T. Here, we observe for our $\Delta\rho/\rho_{min}(\alpha,\beta,\gamma)$-curves, recorded at T=12 K and 20 K, various signatures in the three different rotation geometries, where $\Delta\rho/\rho_{min}(\alpha)$ scales with a $\sin^2$ in the in-plane (ip) geometry, $\Delta\rho/\rho_{min}(\beta)$ shows a $\cos^2$-signature in out-of-plane $\perp$ **j** (oopj) and for $\Delta\rho/\rho_{min}(\gamma)$ is no clear angle-dependence visible in out-of-plane $\perp$ **t** (oopt). To investigate the origin of the various evolution of the $\Delta\rho/\rho_{min}(\alpha,\beta,\gamma)$-curves in the three different field geometries ip, oopj and oopt, we perform as a next step ADMR measurements with varying external magnetic fields $\mu_0 H_{ext}$ at T=12 K and 20 K.

To verify the critical magnetic field H_c, at which the phase change ($\sin^2(\beta,\gamma) \rightarrow \cos^2(\beta,\gamma)$) takes place in the oopj and oopt geometry, we perform ADMR-measurements under varying external magnetic fields $\mu_0 H_{ext}$ at T=12 K and 20 K. Figure 6.25 (a)-(b) shows the results of the magnetic field-dependent ADMR measurements (in 0.5 T-steps) of our GdN/TaN multilayer thin film at T=12 K and 20 K

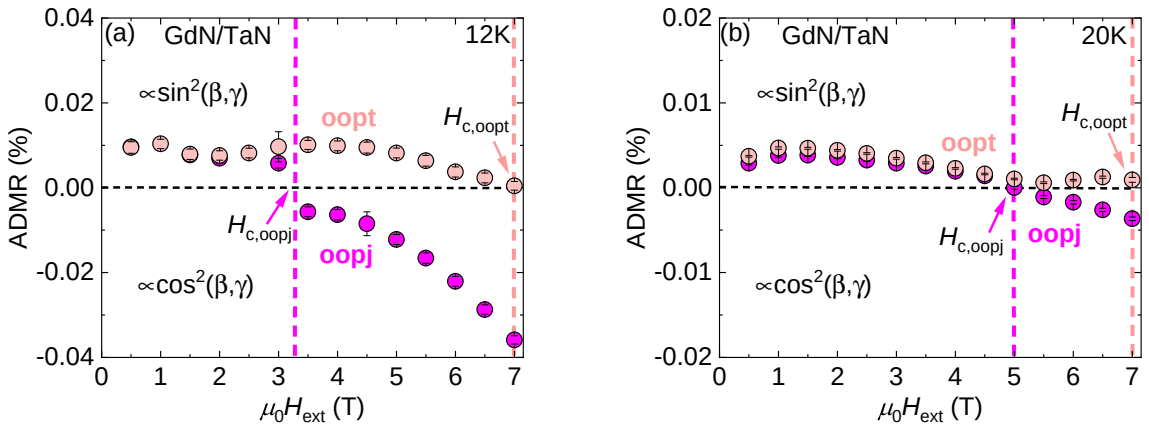

Fig. 6.25: Results of the ADMR measurements under varying external magnetic fields $\mu_0 H_{ext}$ of our GdN/TaN multilayer thin film at T=12 K and 20 K: In the oopj field geometry in (a) and (b), the ADMR amplitude decreases with an increasing $\mu_0 H_{ext}$ and there is a transition from a positive to a negative ADMR amplitude visible at the critical magnetic fields $H_{c,12\,K} \approx 3.25$ T and $H_{c,20\,K} \approx 5$ T. In the oopt field geometry in (a) and (b), the ADMR amplitude also decreases with an increasing $\mu_0 H_{ext}$ and there is no clear transition from ADMR>0 to ADMR<0 visible. Furthermore, we observe an almost zero ADMR amplitude at $\mu_0 H_{ext}$=7 T for T=12 K and 20 K in the oopt field geometry.

Figure 6.25 (a)-(b), illustrates the ADMR amplitude as a function of the external magnetic field H_{ext} of our *SMR test sample* GdN/TaN measured in oopj and oopt at T=12 K and 20 K. Here, we observe in both field geometries a magnetic field dependence of the ADMR(H)-curves. Furthermore, we observe for the 12 K- and 20 K-measurement in oopj (see Fig. 6.25 (a)-(b)) a positive ADMR amplitude in the field-range 0.5 T$\leq\mu_0 H_{ext}\leq$3 T (at 12 K) and 0.5 T$\leq\mu_0 H_{ext}\leq$4.5 T (at 20 K) as well as a negative ADMR amplitude is visible in the field-range 3.5 T$\leq\mu_0 H_{ext}\leq$7 T (at 12 K) and 5.5 T$\leq\mu_0 H_{ext}\leq$7 T (at 20 K). Therefore, we obtain the critical magnetic fields $H_{c,12\,K} \approx 3.25$ T and $H_{c,20\,K} \approx 5$ T for the transition from ADMR>0 to ADMR<0 in oopj. At this magnetic fields H_c, we find the change in angle-dependence ($\sin^2(\beta) \rightarrow \cos^2(\beta)$) in oopj, which corresponds to the $\cos^2$-dependence of the $\Delta\rho/\rho_{min}(\beta)$-curve at 12 K / 20 K and 7 T (see Fig. 6.24 (a)-(b)). In addition, the minimum values $ADMR_{min,12\,K} \approx -0.038\%$ and $ADMR_{min,20\,K} \approx -0.0048\%$ are comparable with the results of our ADMR(T)-measurements (see. Fig. 6.21 (b)) in oopj at 12 K / 20 K and 7 T. In the oopt field geometry, we only oberseve a positive ADMR amplitude for the 12 K- and 20 K-measurement. Moreover, the ADMR amplitude slightly decreases with increasing $\mu_0 H_{ext}$ and reaches a minum value close to zero at 7 T. This result is in agreement with the ADMR(T)-data points measured in oopt at 12 K / 20 K and 7 T (see. Fig. 6.21 (c)) and corresponds to complicated angle-dependence of our $\Delta\rho/\rho_{min}(\gamma)$-plots recorded at these temperatures in the oopt field geometry (see Fig. 6.24 (a)-(b)).

Finally, we also verify the comparison of the field-dependent magnetoresistance (FDMR) measurement results (see Fig. 6.26 (c)-(d)) with the ADMR(H)-plots, recorded in oopj and oopt (see Fig. 6.25 (a)-(b)) of our GdN/TaN multilayer heterostructure at T=12 K and 20 K. To this end, we produce MR(H)-plots, which are shown in Figure 6.26 (a)-(b), in the field rotation geometries out-of-plane $\perp$ **j** (oopj) and out-of-plane $\perp$ **t** (oopt).

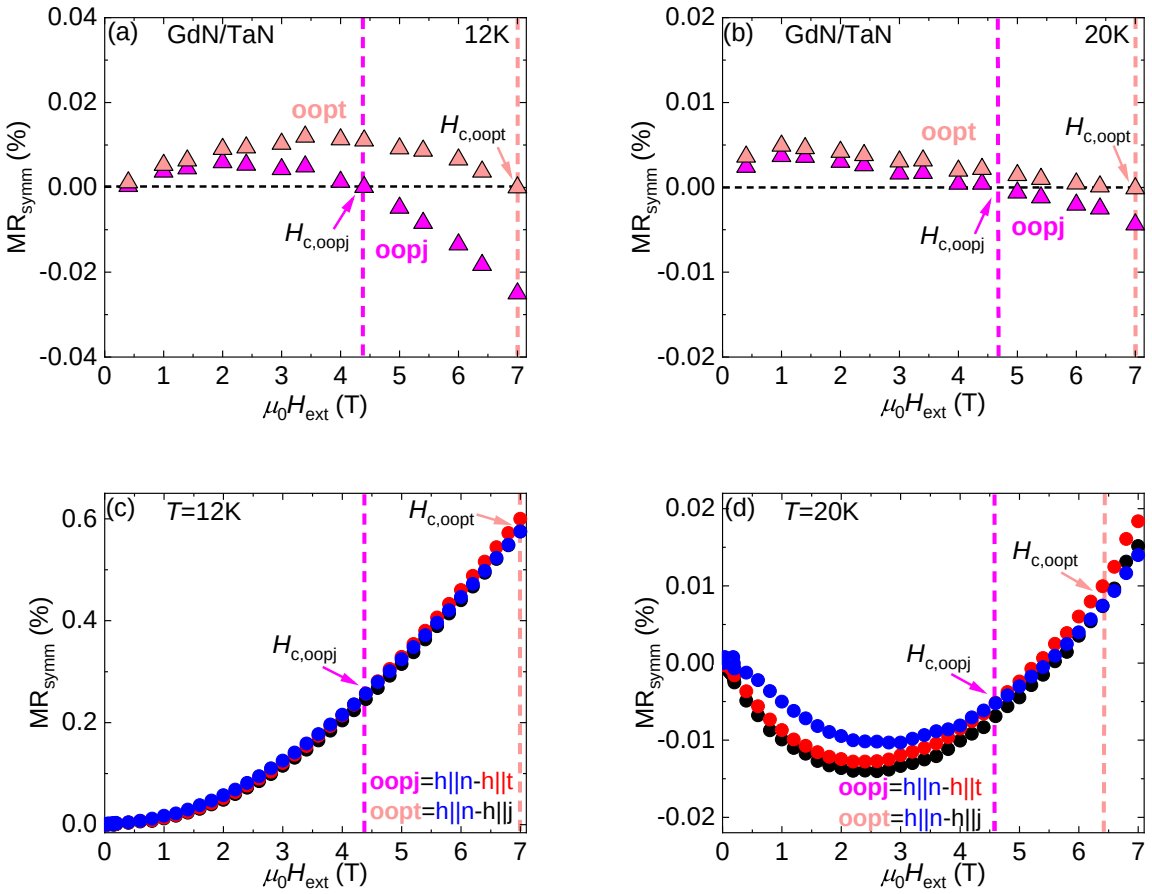

Fig. 6.26: MR amplitude, extracted from the field-dependent magnetoresistance (FDMR) data measured in the field geometries oop (**h**$\|$**n**) and ip (**h**$\|$**j** and **h**$\|$**t**) in the H-area 0.5 T$\leq\mu_0 H_{ext}\leq$7 T and at T=12 K / 20 K as a function of the applied external magnetic field $\mu_0 H_{ext}$ of our multilayer heterostructure GdN/TaN. The MR(H)-curves in (a) and (b) are converted into the field rotation geometries out-of-plane $\perp$ **j** (oopj=**h**$\|$**n**$-$**h**$\|$**t**) and out-of-plane $\perp$ **t** (oopt=**h**$\|$**n**$-$**h**$\|$**j**): In the oopj field geometry in (a) and (b), the MR amplitude decreases with an increasing $\mu_0 H_{ext}$ and there is a transition from a positive to a negative MR amplitude visible at the critical magnetic fields $H_{c,12\,K}\approx$4.45 T and $H_{c,20\,K}\approx$4.55 T. In the oopt field geometry in (a) and (b), the MR amplitude also decreases with an increasing $\mu_0 H_{ext}$ and there is no clear transition from MR>0 to MR<0 is visible. Furthermore, we observe an almost zero MR amplitude at $\mu_0 H_{ext}$=7 T for T=12 K and 20 K. (c)-(d) Illustration of the extraction method of the critical fields $H_{c,oopj}$ and $H_{c,oopt}$ from our MR(H)-plots by highlighting the intersection between the MR(H)-curves **h**$\|$**n** (blue curve) and **h**$\|$**t** (red curve) for oopj and **h**$\|$**n** (blue curve) and **h**$\|$**j** (black curve) for oopt.

Figure 6.26 (a)-(b) shows the symmetrized longitudinal magnetoresistance MR, extracted from the FDMR measurement results (see Fig. 6.12 (c) and (f)), of our GdN/TaN multilayer sample as a function of the external magnetic field $\mu_0 H_{ext}$ at T=12 K and 20 K. Here, we determine MR for the two different rotation field geometries out-of-plane $\perp$ **j** (oopj) and

out-of-plane $\perp$ **t** (oopt) by calculating and substracting the FDMR data, measured in the three different field geometries oop (**h**$\|$**n**) and ip (**h**$\|$**j** and **h**$\|$**t**) at T=12 K and 20 K (see Eq. (39), (40)). We observe in our MR(H)-plots the critical magnetic fields $H_{\mathrm{c,12\,K}}\approx$4.45 T, $H_{\mathrm{c,20\,K}}\approx$4.55 T in oopj and almost zero fields in oopt, which are comparable to the values determined in our ADMR(H)-plots (see Fig. 6.25 (a)-(b)). The extraction method of the critical magnetic fields at T=12 K and 20 K are shown in Fig. 6.25 (d)-(e). Here, we determine the intersection point of the MR(H)-curves recorded in the field geometries **h**$\|$**n** (see blue curve) and **h**$\|$**t** (see red curve) to extract $H_{\mathrm{c,oopj}}$ in the oopj field geometry at $\Delta\mathrm{MR}_{\mathrm{oopj}}\approx$0. Furthermore, we determine $H_{\mathrm{c,oopt}}$ in the oopt field direction by forming the intersection of the MR(H)-curves measured in **h**$\|$**n** (see blue curve) and **h**$\|$**j** (see black curve) at $\Delta\mathrm{MR}_{\mathrm{oopt}}\approx$0. Finally, we observe for our multilayer sample GdN/TaN a similar H-dependent evolution for MR in oopj and oopt (see Fig. 6.26 (a)-(b)) compared to our ADMR(H)-plots (see Fig. 6.25 (a)-(b)), which suggests the comparability of our FDMR- and ADMR-data recorded at T=12 K and 20 K. In the following chapter 7, we study the FDMR- and ADMR-measurement results of our *SMR test sample* GdN/TaN with respect o the investigation of a potential spin Hall magnetoresistance (SMR) effect in the FMI (GdN)/SC (TaN) interface of our multilayer heterostructure.

7 Spin Hall magnetoresistance (SMR) analysis

In the last experimental chapter of this master´s thesis, we analyze the *field-dependent magnetoresistance* (FDMR)- and *angle-dependent magnetoresistance* (ADMR)-measurement results of our *SMR test sample* GdN/TaN in terms of the manifestation of a potential spin Hall magnetoresistance (SMR) in the FMI (GdN)/SC (TaN) interface. To this end, we further examine and compare our FDMR- and ADMR-data recorded at T=12 K and $\mu_0 H_{\text{ext}}$=7 T, at which we have observed a different angular dependence for our $\Delta\rho/\rho_{\text{min}}(\alpha,\beta,\gamma)$-curves in the three different field geometries in-plane (ip) $\rightarrow \Delta\rho/\rho_{\text{min}} \propto \sin^2(\alpha)$, out-of-plane $\perp$ **j** (oopj) $\rightarrow \Delta\rho/\rho_{\text{min}} \propto \cos^2(\beta)$ and out-of-plane $\perp$ **t** (oopt) $\rightarrow$ no significant angle-dependence for $\Delta\rho/\rho_{\text{min}}(\gamma)$ (see Fig. 6.24 (a)). Figure 7.1 (a)-(d) shows the FDMR-data of our *SMR test sample* GdN/TaN and the *SMR reference sample* GdN/AlN/TaN as well as the AlN/TaN/AlN trilayer heterostructure recorded at T=12 K.

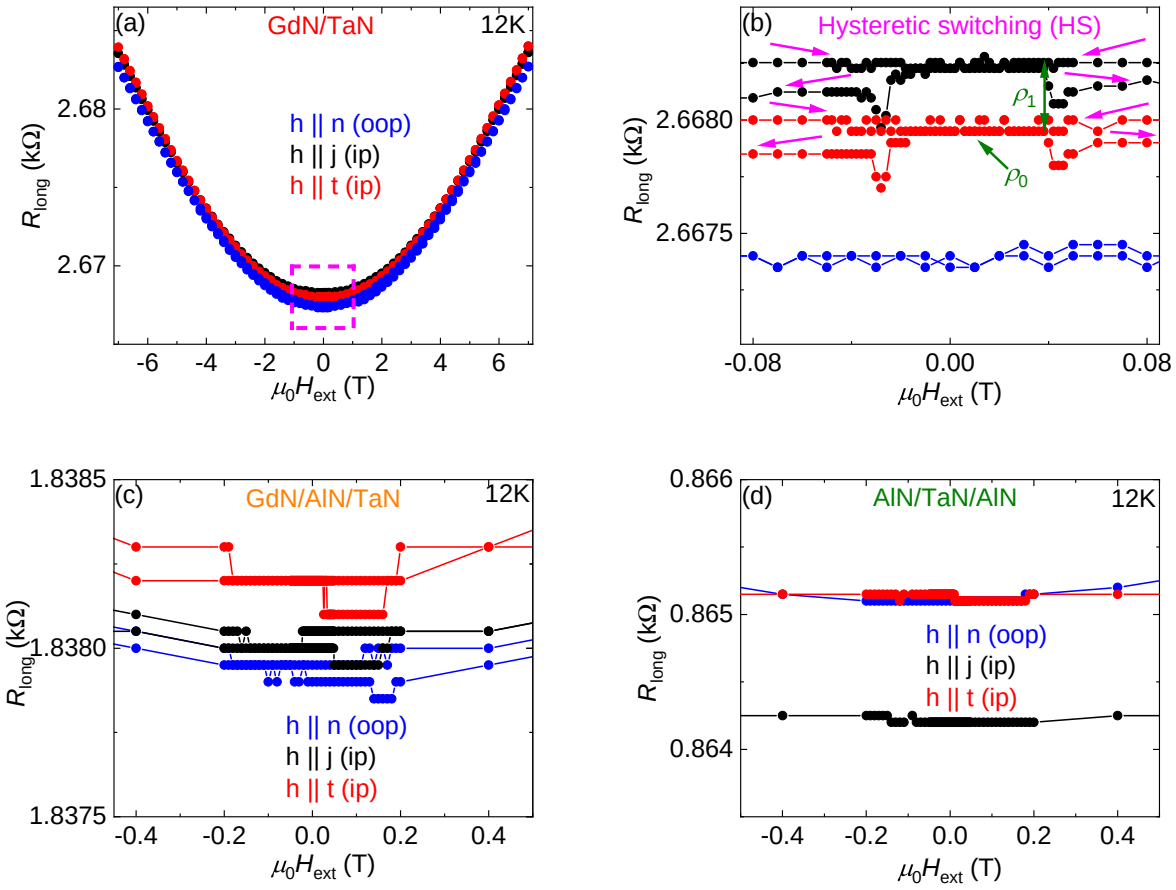

Fig. 7.1: Results of the field-dependent magnetoresistance (FDMR) measurements in the three different field geometries oop (**h**$\|$**n**), ip (**h**$\|$**j** and **h**$\|$**t**) at T=12 K: (a) Symmetrized longitudinal magnetoresistance R_{long} depending on an applied external magnetic field $\mu_0 H_{\text{ext}}$ (-7 T to +7 T) of the *SMR test sample* GdN/TaN: Here, we observe for $R_{\text{long}}(H)$ an almost parabolic behavior in all field geometries. (b) Zoomed-in view of panel (a) in the field-range -0.08 T$\leq\mu_0 H_{\text{ext}}\leq$0.08 T to highlight the difference in R_{long} for the three field geometries. We observe $R_{\text{long},\mathbf{h}\|\mathbf{j}} > R_{\text{long},\mathbf{h}\|\mathbf{t}}$ as well as a hysteretic switching (HS) of R_{long} in these both geometries. In addition, we illustrate the extraction method for the contributions ρ_0 and ρ_1 (see Eq. (41)), which we use to calculate the real part G_{r} (see Eq. (48)) of the complex spin mixing conductance $G_{\uparrow\downarrow}$ (see Eq. (43)). (c)-(d) Zoomed-in view of the $R_{\text{long}}(H)$-curves of the two reference samples shows no clear HS of R_{long}.

Figure 7.1 (a) shows the symmetrized longitudinal magnetoresistance R_{long}, extracted from the FDMR-measurements results (see Sec. 6.2.4) of our GdN/TaN multilayer heterostructure in the three different field geometries oop ($\mathbf{h}\|\mathbf{n}$), ip ($\mathbf{h}\|\mathbf{j}$ and $\mathbf{h}\|\mathbf{t}$), depending on the external magnetic field $\mu_0 H_{\text{ext}}$ (-7 T to +7 T) at a fixed temperature T=12 K. Here, we observe in all field geometries a parabolic behavior of the field-dependent longitudinal magnetoresistance R_{long}. This result suggests an ordinary magnetoresistance (OMR) in the TaN layer (see work of *P. Rosenberger et al.* [16]), which corresponds to a maximum ADMR$\approx 30 \times 10^{-4}$ for $\mathbf{h}\|\mathbf{n}$ as well as a $\propto\sin^2(\beta,\gamma)$-dependence in the oopj and oopt ADMR-measurements of our GdN/AlN/TaN and AlN/TaN/AlN heterostructures (see Fig. 6.18 (k)-(l)). In contrast, our GdN/TaN heterostructure exhibits in the oppj direction a magnetoresistance of ADMR$\approx$0 for $\mathbf{h}\|\mathbf{n}$ as well as a maximum ADMR$\approx 5 \times 10^{-4}$ for $\mathbf{h}\|\mathbf{t}$, which corresponds to a $\propto\cos^2(\beta)$-signature. In the oopt field geometry, no clear symmetric angle-dependence is visible (see Fig. 6.18 (k)-(l)). In the ip rotation geometry, we observe for all three samples a maximum ADMR in the 10^{-4}-range and there is a $\propto\sin^2(\alpha)$-dependence, induced by the superconducting (SC) TaN, visible in the ADMR-measurement results at T=12 K (see Fig. 6.18 (j)). From the SMR theory (see Sec. 2.3), we would expect in our FDMR-measurement results a larger longitudinal magnetoresistance R_{long} in the $\mathbf{h}\|\mathbf{j}$ field geometry than in the $\mathbf{h}\|\mathbf{t}$ geometry. In addition, the longitudinal magnetoresistivity ρ_{long} is defined by [16]

$$\rho_{\text{long}} = \rho_0 + \rho_1(1 - m_{\text{t}}^2), \tag{41}$$

where m_{t} represents the projection of the magnetization orientation $\mathbf{m}$ in the $\mathbf{t}$-direction (see work of *Y.-T. Chen et al.* [29]) of our Hall-bar patterned GdN thin film in the $\mathbf{n}$, $\mathbf{j}$, $\mathbf{t}$ coordinate system (see Fig. 4.3). In Figure 7.1 (a), we observe in all field geometries parabolic-like $R_{\text{long}}(H)$-curves, which are similar in shape and very close to each other with no clear discrepancy in their resistances visible. To look for small differences between the resistance values in the three different geometries, we plot in Fig. 7.1 (b) a zoomed-in view of the $R_{\text{long}}(H)$-curves of Fig. 7.1 (a) in the field-area -0.08 T$\leq\mu_0 H_{\text{ext}}\leq$0.08 T at T=12 K. Here, we observe a *hysteretic switching* in the FMI (GdN)/SC (TaN) bilayer in our $R_{\text{long}}(H)$-curves recorded in the two in-plane (ip) field geometries $\mathbf{h}\|\mathbf{j}$ and $\mathbf{h}\|\mathbf{t}$. In both cases R_{long} reduces abruptly and hysteretically at approximate +/- 4 mT. These magnetic field values are comparable to the coercive magnetic field of the GdN layer (see Fig. 6.5 (b)), which could be an indication for a potential SMR effect. Furthermore, we observe a larger longitudinal magnetoresistance R_{long} for $\mathbf{h}\|\mathbf{j}$ than for $\mathbf{h}\|\mathbf{t}$, which could be a further indication for a SMR effect in the in-plane (ip) field geometry (see work of *P. Rosenberger et al.* [16]). To verify if the hysteretic switching only occurs in our GdN/TaN sample, we also plot in Fig. 7.1 (c)-(d) a zoomed-in view of the $R_{\text{long}}(H)$-curves of our reference samples GdN/AlN/TaN and AlN/TaN/AlN at T=12 K. Here, we observe in the H-region -0.4 T$\leq\mu_0 H_{\text{ext}}\leq$0.4 T no hysteretic switching, which suggests the hysteretic switching effect originates from the GdN/TaN interface in the *SMR test sample*.

To further investigate a SMR effect in our GdN/TaN sample, we plot in Fig. 7.2 the anti-symmetrized transversal magnetoresistance R_{trans} (see Eq. (26)), extracted from the FDMR-measurements results (see Sec. 6.2.4) recorded in the out-of-plane (oop) field ($\mathbf{h}\|\mathbf{n}$), as a function of the external magnetic field $\mu_0 H_{\mathrm{ext}}$ (-7 T to +7 T) at T=12 K.

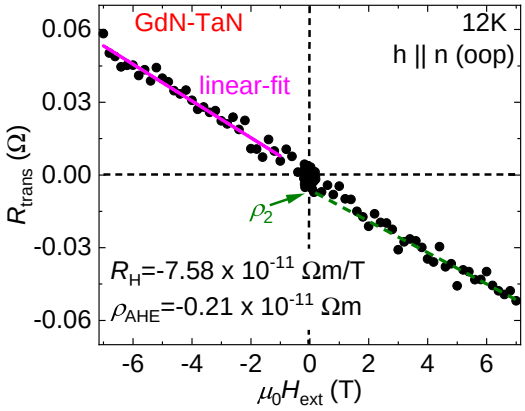

Fig. 7.2: Results for the field-dependent magnetoresistance (FDMR) measurements in the out-of-plane (oop) ($\mathbf{h}\|\mathbf{n}$) field geometry at T=12 K: (a) Anitsymmetrized transversal magnetoresistance R_{trans} depending on an applied external magnetic field $\mu_0 H_{\mathrm{ext}}$ (-7 T to +7 T) of the *SMR test sample* GdN/TaN: Here, we observe for $R_{\mathrm{trans}}(H)$ an almost linear behavior (green dashed line) in $\mathbf{h}\|\mathbf{n}$ at high fields. By performing a linear-fit to R_{trans} (magenta line), we extract from the slope the ordinary Hall constant $R_{\mathrm{H}}\approx -7.58 \times 10^{-11}\,\Omega$m/T as well as from the y-axis intercept the value $\rho_{\mathrm{AHE}}\approx -0.21 \times 10^{-11}\,\Omega$m, which represents the anomalous Hall effect (AHE) contribution to the MR. Furthermore, we illustrate the extraction method of the contribution ρ_2 rom this y-axis intercept (see Eq. (42)), which we use to calculate the imaginary part G_{i} (see Eq. (49)) of the complex spin mixing conductance $G_{\uparrow\downarrow}$ (see Eq. (43)).

Figure 7.2 shows a linear behavior of $R_{\mathrm{trans}}(H)$ with a negative slope in the transverse magnetoresistance R_{trans}, which we associate with an ordinary Hall effect (OHE) in the TaN thin film of our multilayer heterostructure. Furthermore, in the small field-area 0 T$\leq\mu_0 H_{\mathrm{ext}}\leq$0.5 T is a slightly deviation of the linear dependence visible (see green dashed line), which could be an indication for an anomalous Hall effect (AHE) in R_{trans} caused by the SMR in our GdN/TaN interface. We determine the ordinary Hall coefficient $R_{\mathrm{H}}\approx -7.58 \times 10^{-11}\,\Omega$m/T as well as the AHE contribution $\rho_{\mathrm{AHE}}\approx -0.21 \times 10^{-11}\,\Omega$m by performing a linear-fit (see magenta line) of our data as shown in Fig. 7.2. The magnitudes of R_{H} and ρ_{AHE} of our GdN/TaN sample are comparable to the results of SMR investigations in a EuO/W-bilayer (see work of *P. Rosenberger et al.* [16]) and a YIG/Pt-interface (see work of *M. Althammer et al.* [15]). As a next step, we perform a quantitative study of a potential SMR effect in our GdN/TaN interface by analyzing the FDMR-measurement results in the T-region 8 K$\leq T\leq$15 K, where we assume a dominating weak-localization (WL) transport in TaN (see Sec. 6.2.4). To this end, we extract from our $R_{\mathrm{long}}(H)$-curves recorded for $\mathbf{h}\|\mathbf{j}$ (m_{t}=0) and $\mathbf{h}\|\mathbf{t}$ (m_{t}=1) (see Eq. (41)) the resistivity ρ_0 and ρ_1 as shown in Fig. 7.1 (b). Furthermore, we determine ρ_2 in the $R_{\mathrm{trans}}(H)$-plot as illustrated in Fig. 7.2, where the transversal magnetoresistivity ρ_{trans} is defined by [16]

$$\rho_{\mathrm{trans}} = \rho_2 m_{\mathrm{n}} + R_{\mathrm{H}}\mu_0 H_{\mathrm{n}} + \rho_3 m_{\mathrm{j}} m_{\mathrm{t}}, \tag{42}$$

where m_{n}, m_{j}, m_{t} represents the magnetization orientation $\mathbf{m}$ in the $\mathbf{n}$-, $\mathbf{j}$-, $\mathbf{t}$-direction, R_{H} defines the ordinary Hall constant and $\mu_0 H_{\mathrm{n}}$ represents the applied external magnetic field along $\mathbf{n}$ (see work of *Y.-T. Chen et al.* [29]). Moreover, Eq. (42) represents the function we use to determine R_{H} and ρ_{AHE} from the $R_{\mathrm{trans}}(H)$-plot in the oop field direction $\mathbf{h}\|\mathbf{n}$ (m_{j}, m_{t}=0) (see Fig. 7.2) by performing a linear fit. In Figure 7.3, we plot the resistivity relations ρ_1/ρ_0 and ρ_2/ρ_0, which we attribute to the SMR effect (see work of *P. Rosenberger et al.* [16]), as a function of the temperature T.

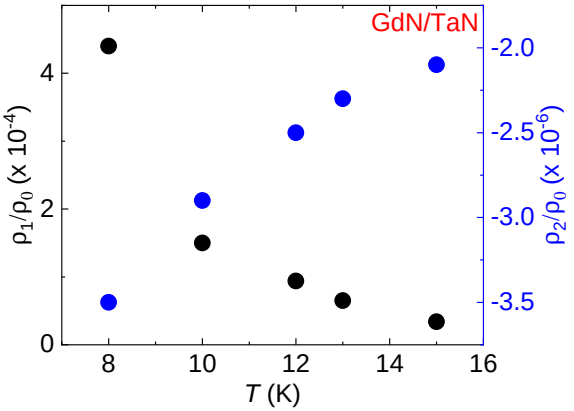

Fig. 7.3: Extracted SMR contributions ρ_1/ρ_0 and ρ_2/ρ_0 as a function of the temperature T. We observe for both contributions an increasing absolute value with decreasing T and a slight saturation is visible at high T. Furthermore, we observe $\rho_1/\rho_0 > \rho_2/\rho_0$ throughout the investigated T-range 8 K$\leq T \leq$15 K for our *SMR test sample* GdN/TaN indicating $G_{\mathrm{r}} > G_{\mathrm{i}}$.

Figure 7.3 illustrates the SMR contributions ρ_1/ρ_0 and ρ_2/ρ_0, extracted from the $R_{\mathrm{long}}(H)$-(see Fig. 7.1 (b)) and the $R_{\mathrm{trans}}(H)$ (see Fig. 7.2) exemplary at T=12 K, depending on the measured temperature T. Here, we observe for both SMR contributions an increasing absolute value with a decreasing T and a slight saturation at high T towards to the ferromagnetic Curie temperature $T_{\mathrm{C}} \approx 25$ K of GdN. The T-dependent evolution of ρ_1/ρ_0 and ρ_2/ρ_0 are comparble to the results published in the work of *P. Rosenberger et al.* [16]. Furthermore, the absolute value of ρ_1/ρ_0 is much larger than ρ_2/ρ_0 in the entire investigated T-range 8 K$\leq T \leq$15 K. To further analyze these results, we introduce the so-called *complex spin mixing conductance* $G_{\uparrow\downarrow}$, which controlles the spin current transfer across the GdN/TaN interface, definded by [29]

$$G_{\uparrow\downarrow} = G_{\mathrm{r}} + iG_{\mathrm{i}}, \tag{43}$$

where G_{r} defines the real- and G_{i} the imaginary-part of $G_{\uparrow\downarrow}$. In the work of *Y.-T. Chen et al.* [29], we find for ρ_1/ρ_0 and ρ_2/ρ_0 the following expression

$$\frac{\rho_1}{\rho_0} = \frac{\theta_{\mathrm{SH}}^2}{t_{\mathrm{NM}}} \lambda_{\mathrm{sf}} \mathrm{Re}\left[\frac{2\rho_{\mathrm{NM}} \lambda_{\mathrm{sf}} G_{\uparrow\downarrow} \tanh^2\left(\frac{t_{\mathrm{NM}}}{2\lambda_{\mathrm{sf}}}\right)}{1 + 2\rho_{\mathrm{NM}} \lambda_{\mathrm{sf}} G_{\uparrow\downarrow} \coth\left(\frac{t_{\mathrm{NM}}}{\lambda_{\mathrm{sf}}}\right)} \right] \tag{44}$$

and

$$\frac{\rho_2}{\rho_0} = -\frac{\theta_{\mathrm{SH}}^2}{t_{\mathrm{NM}}} \lambda_{\mathrm{sf}} \mathrm{Im}\left[\frac{2\rho_{\mathrm{NM}} \lambda_{\mathrm{sf}} G_{\uparrow\downarrow} \tanh^2\left(\frac{t_{\mathrm{NM}}}{2\lambda_{\mathrm{sf}}}\right)}{1 + 2\rho_{\mathrm{NM}} \lambda_{\mathrm{sf}} G_{\uparrow\downarrow} \coth\left(\frac{t_{\mathrm{NM}}}{\lambda_{\mathrm{sf}}}\right)} \right], \tag{45}$$

where θ_{SH} defines the spin Hall angle (SHA) and λ_{sf} the spin diffusion length, whereas ρ_{NM} represent the resistivity and t_{NM} the layer thickness of the normal metal (NM). In Eqs. (44) and (45), we observe ρ_1/ρ_0 is dominated by G_r and ρ_2/ρ_0 is modulated by G_i. Therefore, with the result $\rho_1/\rho_0 >> \rho_2/\rho_0$ (see Fig 7.3), which correpsonds to $G_r = \mathrm{Re}G_{\uparrow\downarrow} >> G_i = \mathrm{Im}G_{\uparrow\downarrow}$ (taken from *Y.-T. Chen et al.* [29]), we obtain for the calculation of ρ_1/ρ_0 and ρ_2/ρ_0 the approximated formulae [29]

$$\frac{\rho_1}{\rho_0} \approx \theta_{SH}^2 \frac{\lambda_{sf}}{t_{NM}} \left[\frac{2\rho_{NM}\lambda_{sf}G_r \tanh^2\left(\frac{t_{NM}}{2\lambda_{sf}}\right)}{1 + 2\rho_{NM}\lambda_{sf}G_r \coth\left(\frac{t_{NM}}{\lambda_{sf}}\right)} \right] \tag{46}$$

and [29]

$$\frac{\rho_2}{\rho_0} \approx \theta_{SH}^2 \frac{\lambda_{sf}}{t_{NM}} \left[\frac{2\lambda_{sf}\rho_{NM}G_i \tanh^2\left(\frac{t_{NM}}{2\lambda_{sf}}\right)}{\left(1 + 2\rho_{NM}\lambda_{sf}G_r \coth\left(\frac{t_{NM}}{\lambda_{sf}}\right)\right)^2} \right]. \tag{47}$$

Afterwards, we make the assumption $G_r\lambda_{sf}\rho_0 << 1$ and $G_i\lambda_{sf}\rho_0 << 1$ and we obtain the expression

$$G_r \approx \frac{\rho_1}{\rho_0} \left[\frac{\theta_{SHsf}^2}{t_{NM}} \lambda_{sf}^2 2\rho_0 \tanh^2\left(\frac{t_{NM}}{2\lambda_{sf}}\right) \right]^{-1} \tag{48}$$

and

$$G_i \approx \frac{\rho_2}{\rho_0} \left[-\frac{\theta_{SHsf}^2}{t_{NM}} \lambda_{sf}^2 2\rho_0 \tanh^2\left(\frac{t_{NM}}{2\lambda_{sf}}\right) \right]^{-1}. \tag{49}$$

Finally, we calculate G_r and G_i by using Eqs. (48) and (49) and t_{TaN}=10 nm as well as the spin Hall angle $\theta_{SH,TaN}$=0.034 and the spin diffusion length $\lambda_{sf,TaN}$=8 nm for TaN published in the work of *P. W. Swatek et al.* [28]. Furthermore, ρ_0 is defined by $\rho_{0,long} = R_{0,long} \cdot \frac{w_{HB} \cdot d_{TaN}}{l_{HB}}$ (see Eq. (22)). Figure 7.4 shows the calculated real- G_r and imaginary-contribution G_i of the complex spin mixing conductance $G_{\uparrow\downarrow}$ of our GdN/TaN interface depending on the temperature T.

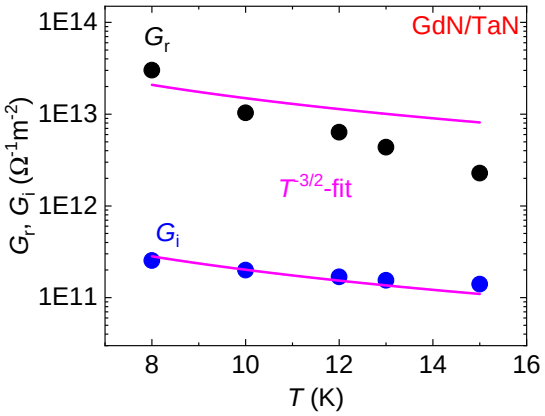

Fig. 7.4: Extracted contributions G_r and G_i of the complex spin mixing contuctance $G_{\uparrow\downarrow}$ as a function of the temperature T. We observe a monotonically decreasing behavior of G_r and G_i with an increasing T as well as a $T^{-3/2}$-dependence (magenta line represents the fits) is visible. Furthermore, we observe $G_r >> G_i$ throughout the investigated T-range 8 K$\leq T \leq$15 K for our *SMR test sample* GdN/TaN.

Figure 7.4 shows the extracted contributions G_r and G_i depending on the temperature T. Here, we observe for both values a monotonous decreasing behavior with an increasing temperature and the corresponding $T^{-3/2}$-fit (magenta line). In the work of *P. Rosenberger et al.* [16], a comparable T-dependent evolution of G_r and G_i is observed, which they associate with thermal fluctuations in the magnetic lattice of the magnetically ordered insulator (MOI). Moreover, they find in their experiments $G_\mathrm{i}>>G_\mathrm{r}$, which is in contrast to the results of our calculations. In our work, we observe $G_\mathrm{r}>>G_\mathrm{i}$ in the entire T-region $10\,\mathrm{K}\leq T\leq 15\,\mathrm{K}$, which is comparable to the results of the SMR studies in a YIG/Pt-interface published in the work of *M. Althammer et al.* [15], *X.-P. Zhang, et al.* [100] and *S. Meyer, et al.* [101]. For T=12 K, we extract the values G_r=$6.35\times10^{12}\,\Omega^{-1}\mathrm{m}^{-2}$ and G_i=$1.69\times10^{11}\,\Omega^{-1}\mathrm{m}^{-2}$, which are smaller by a factor of 10 compared to the values in *M. Althammer et al.* [15]. Afterwards, we calculate $G_\mathrm{i}/G_\mathrm{r}$=0.03, which is in agreement with the theoretical value $G_\mathrm{i}/G_\mathrm{r}\approx1/20$ computed for a YIG/Ag-bilayer in the work of *X. Jia et al.* [102].

As a last step, we calculate the mean free path l from the FDMR-measurement results, recorded in the out-of-plane (oop) field ($\mathbf{h}\|\mathbf{n}$) at T=12 K, of our our GdN/TaN sample (see Fig. 7.2). To this end, we introduce the so-called *Drude model* [41], which describes the magnetoresistance and the Hall effect in a one-band model, to calculate the scattering time τ from the Hall coefficient R_H

$$R_\mathrm{H}=\frac{e\tau}{m}\rho_0=\frac{1}{ne} \tag{50}$$

with

$$\tau=\frac{m}{ne^2\rho_0}, \tag{51}$$

where m, n, e, ρ_0=$\rho_{0,\mathrm{long}}$=$R_{0,\mathrm{long}}\cdot\frac{w_\mathrm{HB}\cdot d_\mathrm{TaN}}{l_\mathrm{HB}}$ (see Eq. (22)) defines the electron mass, electron density, electron charge, longitudinal electrical resistivity at the zero field and the layer thickness d_TaN=10 nm of TaN. We determine the electron density n of TaN at T=12 K exemplary by the calculation of

$$n=\frac{1}{eR_\mathrm{H}}=\frac{1}{e\cdot7.58\times10^{-11}\,\mathrm{m^3/C}}\overset{(12\,\mathrm{K})}{=}8.23\times10^{28}\,\mathrm{m^{-3}}, \tag{52}$$

which is the expected value of n for metals. Next, we use the Fermi velocity v_F, extracted from the Fermi energy E_F, and the scattering time τ to calculate the mean free path l of the electrons in the TaN layer of our GdN/TaN interface at T=12 K.

$$E_\mathrm{F}=\frac{\hbar^2{k_\mathrm{F}}^2}{2m}=\frac{\hbar^2}{2m}\left(3\pi^2n\right)^{2/3}\overset{(12\,\mathrm{K})}{=}6.91\,\mathrm{eV} \tag{53}$$

$$v_\mathrm{F}=\frac{\hbar k_\mathrm{F}}{m}=\sqrt{\frac{2E_\mathrm{F}}{m}}\overset{(12\,\mathrm{K})}{=}1.56\times10^{6}\,\mathrm{m/s} \tag{54}$$

$$l=v_\mathrm{F}\cdot\tau\overset{(12\,\mathrm{K})}{=}0.194\,\mathrm{nm} \tag{55}$$

Finally, we calculate the Fermi velocity v_F, the scattering time time τ and the mean free path l from the FDMR-measurement results in the T-area 7.5 K$\leq T \leq$20 K by using the Eqs. (54), (51), (55). In Figure 7.5, we plot the extracted values l, τ, v_F depending on the temperature T.

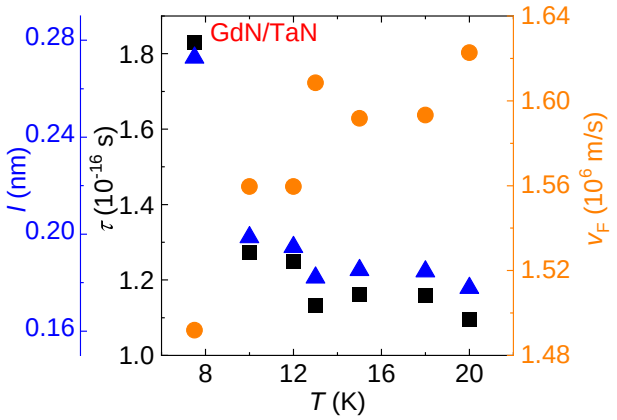

Fig. 7.5: Calculated mean free path l and scattering time τ as well as the Fermi velocity v_F as a function of the temperature T. We observe a decreasing behavior of l, τ and an increased v_F with increasing T. Furthermore, the magnitudes of these values suggest a limited electrical conductance and therefore a high amount of scattering processes in the TaN layer of our *SMR test sample* GdN/TaN.

Figure 7.5 illustrates the calculated mean free path l and scattering time τ as well as the Fermi velocity v_F as a function of the temperature T. Here, we observe, that an increasing temperature T corresponds to a decrease of l and τ as well as an increase v_F and a slight saturation of the values is visible at high T. Due to the high longitudinal electrical resistivity $R_{0,\text{long}}$ of our Hall-bar patterned GdN/TaN multilayer heterostructure, we obtain a low electrical conductivity σ. Therefore, we calculate with the relationship $\sigma \propto \text{const}\cdot\frac{l}{v_F}=\text{const}\cdot\tau$ a low mean free path l of the electrons in our TaN thin film, which suggests that our TaN contains impurities and thus scattering processes, due to the short scattering time τ, exist. It is interesting to compare the determined mean free path l to the phase coherence length L_ϕ determined in Fig. 6.13. We find a much larger phase coherence length L_ϕ (over an order of magnitude) as compared to the mean free path l, which is in agreement with the diffusive transport picture used to describe WL/WAL phenomena. Table 7.1 lists the calculated electron density n, Fermi velocity v_F, mean free path l and scattering time τ as well as the Hall constant R_H and the longitudinal electrical resistivity $R_{0,\text{long}}$ extracted from the FDMR-measurement results in the out-of-plane (oop) field ($\mathbf{h}\|\mathbf{n}$) in the T-range 7.5 K$\leq T \leq$20 K.

T [K]	$\lvert R_{\mathrm{H}}\rvert$ [$10^{-11}\,\mathrm{m}^3/\mathrm{C}$]	$R_{0,\mathrm{long}}$ [Ω]	n [$10^{28}\,\mathrm{m}^{-3}$]	v_{F} [$10^{6}\,\mathrm{m/s}$]	τ [$10^{-16}\,\mathrm{s}$]	l [nm]
7.5	8.66	2080	7.22	1.49	1.83	0.273
10	7.58	2613	8.24	1.56	1.27	0.198
12	7.58	2667	8.24	1.56	1.25	0.195
13	6.91	2681	9.04	1.61	1.13	0.182
15	7.13	2692	8.76	1.59	1.16	0.185
18	7.11	2695	8.79	1.59	1.16	0.185
20	6.73	2697	9.29	1.62	1.09	0.178

Tab. 7.1: Hall constant R_{H}, longitudinal electrical resistivity $R_{0,\mathrm{long}}$, calculated electron density n, Fermi velocity v_{F}, scattering time τ and mean free path l of our *SMR test sample* GdN/TaN extracted from the FDMR-measurement results in the out-of-plane (oop) field ($\mathbf{h}\|\mathbf{n}$) in the T-range $7.5\,\mathrm{K}\leq T\leq 20\,\mathrm{K}$.

8 Summary

In the first experimental chapter of this master´s thesis, we have fabricated high-quality ferromagnetic insulating (FMI) gadolinium nitride (GdN) thin films (see Sec. 3.3) for magnetotransport experiments by using the reactive direct current (DC) magnetron sputtering process (see Sec. 3.1). Due to the oxophilicity [12] of GdN, we have deposited GdN thin films (d=60 nm) between a protective top and bottom buffer layer of tantalum nitride (TaN) (d=20 nm) on a $(6 \times 10 \times 0.55)\,\mathrm{mm}^3$ silicon (Si) substrate with a thermally oxidized SiO_2 (d=1 μm) top layer. In individual deposition series, we have sequentially optimized the growth parameters, such as the N_2/Ar gas mixture ratio [%], the deposition rate R [Å/s] controlled by the sputtering power P_{depo} [W], and the growth temperature T_{depo} [°C] (see chapter 5), for the deposition of our GdN thin films in the cathode sputtering system SUPERBOWL (see Sec. 3.2). Furthermore, for the growth of the TaN top und bottom buffer layer, we have used the growth recipe for normally conducting (NC) TaN (N_2/Ar=10 %, T_{depo}=500 °C, P_{depo}=30 W, $p_{\mathrm{depo}}=5 \times 10^{-3}$ mbar), which was developed in my bachelor´s thesis [18] and remained unchanged in each growth series of GdN. Thus, we have developed an ideal deposition recipe for the growth of FMI GdN thin films with resepect to their static magnetic properties, such as the saturation magnetization $\mu_0 M_{\mathrm{s}}$ and the coercive field $\mu_0 H_{\mathrm{c}}$, and the ferromagnetic Curie temperature T_{C}, which we have extracted with various methods (see Sec. 5.1.1) from our SQUID magnetometry measurement results (see Sec. 4.4). Finally, we have performed XRD scans (see Sec. 3.5.1) to investigate the crystalline quality as well as to calculate the lattice constant a_{lattice} (see Sec. 5.1.3) of our GdN thin films grown at the optimized deposition parameters on a Si/SiO_2 substrate.

As a first step, we have optimized the N_2/Ar gas flow ratio of our GdN thin films, fabricated at a growth temperature of T_{depo}=500 °C as well as a sputtering pressure of $p_{\mathrm{depo}}=5 \times 10^{-3}$ mbar (see Sec. 5.2). In three separate growth series, at the different sputtering powers P_{depo}=15 W, 45 W and 75 W, we have investigated the impact of varied N_2/Ar gas flow ratios on the magnetic parameters $\mu_0 M_{\mathrm{s}}$, $\mu_0 H_{\mathrm{c}}$ and T_{C}. Here, we observed for the growth of a FM GdN thin film fabricated at N_2/Ar=40 %, T_{depo}=500 °C and P_{depo}=45 W a maximum saturation magnetization $\mu_0 M_{\mathrm{s}}$=2.21 T, a low coercive field $\mu_0 H_{\mathrm{c}}$=6.4 mT, a high Curie temperature $T_{\mathrm{C,S}}$=27.16 K and a low lattice constant a_{lattice} =5.03 Å (see red star in Fig. 5.9 (a)-(b)), which was exracted from the crystalline reflection at $2\theta \approx 31\,^\circ$ originating from GdN in the [111]-direction. Afterwards, we have compared our extracted values with those published in the work of *K. Senapati et al.* [54] and we conclude that only GdN thin films ($T_{\mathrm{C,S,max}}$=32.24 K, $a_{\mathrm{lattice,max}}$ =5.075 Å) with FM ordering mechanism and no dual-phase GdN samples with an exchange bias effect and thus AFM behavior (see Sec. 3.3) have been grown in our N_2/Ar gas flow ratio variation series.

Next, we have optimized the growth temperature T_{depo} by using the FM GdN sample optimized in the N_2/Ar gas flow ratio series with the deposition parameters T_{depo}=500 °C, N_2/Ar=40 % and P_{depo}=45 W as a starting point (see Sec. 5.3). Here, we have optimized the deposition temperature T_{depo} in the T-range 20 °C$\leq T_{\mathrm{depo}} \leq$800 °C at a defined N_2/Ar gas flow ratio of 40% and a fixed sputtering power of P_{depo}=45 W. For the growth of a FM

GdN thin film prepared at T_{depo}=500 °C, N_2/Ar=40 % and P_{depo}=45 W, we have observed a maximum saturation magnetization $\mu_0 M_{\mathrm{s}}$=2.21 T, a low coercive field $\mu_0 H_{\mathrm{c}}$=6.4 mT, a high Curie temperature $T_{\mathrm{C,S}}$=27.16 K and a low lattice constant a_{lattice}=5.03 Å (see orange star in Fig. 5.14 (a)-(b)). Due to the comparison with the results published in the work of *K. Senapati et al.* [54], we also assume the sole growth of ferromagnetic (FM) GdN thin films ($T_{\mathrm{C,S,max}}$=41.21 K, $a_{\mathrm{lattice,max}}$ =5.14 Å) in our deposition temperature T_{depo} variation series. In summary, we have developed in our growth optimization series an ideal deposition recipe, which is listed in Table 8.1, of FM GdN thin films.

Growth recipe of FM GdN				
Growth parameters	N_2/Ar [%]	T_{depo} [°C]	P_{depo} [W]	p_{depo} [mbar]
	40	500	45	5×10^{-3}
Magnetic properties	$\mu_0 M_{\mathrm{s}}$ [T]	$\mu_0 H_{\mathrm{c}}$ [mT]	$T_{\mathrm{C,t}}$ [K]	$T_{\mathrm{C,S}}$ [K]
	2.21	6.41	23.04	27.16

Tab. 8.1: Growth parameters and magnetic properties of a FM GdN thin film with a layer thickness of 60 nm fabricated on a thermally oxidized Si substrate.

Finally, we have analyzed the optimized growth recipe and the resulting magnetic properties of FM GdN thin films (d=60 nm) for its reproducibility on Si/SiO_2- as well as on crystalline sapphire (Al_2O_3)-substrates (see Sec. 5.5). Here, we have observed similar values for the magnetic paramteres $\mu_0 M_{\mathrm{s}}$, $\mu_0 H_{\mathrm{c}}$, T_{C} and the lattice constant $a_{\mathrm{lattice,GdN}}$ for the reproduced GdN thin film on Si/SiO_2 compared to the reference sample grown on Si/SiO_2 (see Tab. 5.3 and 5.4). For the reproduced GdN thin film on Al_2O_3, we have observed a slightly reduced $\mu_0 M_{\mathrm{s}}$ and enhanced $\mu_0 H_{\mathrm{c}}$ as well as a clearly increased T_{C} and a greatly improved crystalline growth on sapphire was visible (see Tab. 5.3 and 5.4). Due to the good static magnetic properties $\mu_0 M_{\mathrm{s}}$ and $\mu_0 H_{\mathrm{c}}$ and the low Curie temperature T_{C} as well as a reasonable crystalline quality of GdN on Si/SiO_2, we have fabricated our GdN/TaN multilayer heterostructures, which we have used for our magnetotransport measurements, with the optimized growth recipe for a FM GdN thin film on a thermally oxidized Si substrate (see Tab. 8.1).

In the second main part of this master´s thesis, we have investigated the magnetotransport properties of several GdN/TaN multilayer heterostructures (see chapter 6). To this end, we first have verified the magnetic and insulating properties of a ferromagnetic insulating (FMI) AlN/GdN/AlN trilayer thin film (see Sec. 6.1) fabricated by using the the optimized growth recipe for a FM GdN thin film (see Tab. 8.1). Here, we have observed an electrical resistance of $R \approx 10^9\,\Omega$ in the T-range 200 K$\leq T \leq$300 K by performing an electrical transport measurement (see Sec. 4.1) using Van-de-Pauw method (see Sec. 4.2). The growth recipe as well as the magnetic properties, recorded from the SQUID magnetometry experiments of this AlN/GdN/AlN heterostructure (see Fig. 6.1), are shown in Table 6.1.

As a next step, we have used the optimized growth recipe of our FMI GdN thin film (see Tab. 6.1) to manufacture several multilayer heterostructures for our magnetotransport measurements (see Sec. 6.2). Here, we have prepared three different multilayer samples, which we have patterned into Hall-bar structures (see Sec. 3.4), to investigate a possible spin Hall magnetoresistance (SMR) effect at the GdN/TaN interface (see Sec. 2.3). To this end, we have fa-

bricated a so-called *SMR test sample* with the stack sequence AlN/GdN/TaN/AlN (see Fig. 6.4), a *SMR reference sample* AlN/GdN/AlN/TaN/AlN (see Fig. 6.7) and a AlN/TaN/AlN trilayer heterostructure (see Fig. 6.10). Before we carried out our magnetotransport measurements, we have first determined the resistive properties of our multilayer samples by performing electrical transport measurements. Here, we have observed a maximum electrical resistance $R{\approx}2.8\,\mathrm{k\Omega}$ for our *SMR test sample* with the GdN/TaN interface (see Sec. 6.2.1). Furthermore, we have obtained a maximum electrical resistance of $R{\approx}1.78\,\mathrm{k\Omega}$ for our reference sample GdN/AlN/TaN (see Sec. 6.2.2) and a maximum resistance $R{\approx}0.85\,\mathrm{k\Omega}$ for our AlN/TaN/AlN sample (see Sec. 6.2.3). Moreover, we have observed for all three main samples a superconducting (SC) transition temperature at $T_{\mathrm{SC}}{\approx}5.5\,\mathrm{K}$, which we have associated with the nitrogen (N) instability of GdN and consequently a N-diffusion from GdN to TaN, belonging to the so-called SC δ-TaN/c-TaN with a cubic crystall structure [28]. The growth recipes of the three multilayer samples as well as their magnetic properties are listed in Tabs. 6.2, 6.3 and 6.4.

To investigate the magnetotransport properties with regard to the study of a potential SMR effect in the GdN/TaN interface, we have performed *field-dependent magnetoresistance* (FDMR) (see Sec. 4.3.1) and *angle-dependent magnetoresistance* (ADMR) measurements (see Sec. 4.3.2) of our three multilayer heterostructures. In the FDMR experiments, we have measured the symmetrized longitudinal magnetoresistance MR as a function of an applied external magnetic field $\mu_0 H_{\mathrm{ext}}$ (-7 T to +7 T) at various fixed temperatures T=(7.5, 10, 12, 15, 18, 20) K in the three different field geometries oop ($\mathbf{h}\|\mathbf{n}$) and ip ($\mathbf{h}\|\mathbf{j}$ and $\mathbf{h}\|\mathbf{t}$). Here, we have observed for all three multilayer samples, that an increasing temperature T corresponds to a decreasing MR. For our *SMR test sample* GdN/TaN (see Sec. 6.2.4) we have observed an almost linear behavior of the MR in oop ($\mathbf{h}\|\mathbf{n}$), whereas the FDMR curves recorded in ip ($\mathbf{h}\|\mathbf{j}$ and $\mathbf{h}\|\mathbf{t}$) showed a parabolic signature at 7.5 K (see Fig. 6.12 (a)). In the T-region $10\,\mathrm{K}{\leq}T{\leq}15\,\mathrm{K}$, we have observed a parabolic behavior of the MR in all field geometries and at T=15 K the manifestation of a slight dip below the zero line of $\mathrm{MR}_{\mathrm{symm}}$ was visible, which increased with increasing T and reaching a maximum dip at 20 K (see Fig. 6.12 (b)-(f)). Moreover, we have modeled the FDMR data recorded at T=7.5 K with Eq. (33), which describes magnetotransport in the presence of weak anti-localization (WAL) effect. The data measured in the T-range $10\,\mathrm{K}{\leq}T{\leq}20\,\mathrm{K}$ were modeled with Eq. (34), which describes the weak localization (WL) tranport effect in TaN (see colored lines in Fig. 6.12 (a)-(f)). In the FDMR data recorded for our *SMR reference sample* GdN/AlN/TaN (see Sec. 6.2.5), we have observed an almost parabolic behavior of the MR and a slight cusp-shape outwards of the FDMR curves were visible in the T-range $7.5\,\mathrm{K}{\leq}T{\leq}12\,\mathrm{K}$ in all field geometries (see Fig. 6.14 (a)-(c)). At T=15 K the generation of a slight dip below the zero line was visible, which increased with increasing T and reached a maximum at 20 K (see Fig. 6.14 (d)-(f)). In comparison to the negative dip of our GdN/TaN multilayer sample, the negative contribution of the MR was significantly smaller for our reference sample GdN/AlN/TaN potentially due to the interrupted GdN/TaN interface. Afterwards, we have simulated our FDMR curves by assuming weak anti-localization (WAL) (T=7.5−12 K) and weak localization (WL) (T=15−20 K) transport in TaN (see colored lines in Fig. 6.14 (a)-(f)). Finally, we have analyzed the FDMR data recorded for our AlN/TaN/AlN trilayer heterostructure

(see Sec. 6.2.6). Here, we have observed an outer curvature of the FDMR curves recorded in the T-range 7.5 K$\leq T\leq$12 K in the out-of-plane (oop) ($\mathbf{h}\|\mathbf{n}$) direction (see Fig. 6.16 (a)-(c)), which decreased with an increasing temperature T and an almost parabolic behavior for MR was visible in the oop field geometry for $T\geq$15 K (see Fig. 6.16 (d)-(f)). Furthermore, the parabolic FDMR curves measured in the both in-plane (ip) ($\mathbf{h}\|\mathbf{j}$ and $\mathbf{h}\|\mathbf{t}$) geometries were similar in shape throughout the entire T-range (see Fig. 6.16 (a)-(f)). For this multilayer sample, we have simulated our FDMR-curves by assuming only weak anti-localization (WAL) (T=7.5−20 K) transport in the TaN layer of our trilayer heterostructure (see colored lines in Fig. 6.16 (a)-(f)).

As a next step, we have analyzed the results of the *angle-dependent magnetoresistance* (ADMR) measurement results (see Sec. 6.2.7) of our three multilayer heterostructures performed in the three different rotation planes in-plane (ip), out-of-plane $\perp$ **j** (oopj) and out-of-plane $\perp$ **t** (oopt) (see Fig. 4.4 (a)-(c)) in the T-range 5 K$\leq T\leq$25 K. For T=5 K, we have observed the expected $\cos^2(\alpha)$-dependence for the normalized longitudinal resistivity $\Delta\rho/\rho_{\mathrm{min}}$ of the three samples in the ip direction (see Fig. 6.18 (a)) as well as a $\sin^2(\beta,\gamma)$-signature in the oopj and oopt field geometry (see Fig. 6.18 (c)-(b)). For T=7.5 K, we have observed a phase change ($\cos^2(\alpha) \rightarrow \sin^2(\alpha)$) in the ip rotation plane originating from the superconducting (SC) phase of TaN (see Fig. 6.18 (d)). However in the oopj and oopt field geometry, $\Delta\rho/\rho_{\mathrm{min}}$ still showed a $\sin^2(\beta,\gamma)$-dependence for all samples (see Fig. 6.18 (e)-(f)). In the oopj field geometry, we have observed a phase shift ($\sin^2(\beta) \rightarrow \cos^2(\beta)$) for our GdN/TaN multilayer thin film and $\Delta\rho/\rho_{\mathrm{min}}(\beta)$ showed a $\cos^2$-dependence at T=10−20 K (see red data points in Fig. 6.18 (h),(k) and in Fig. 6.19 (b),(e),(h)), whereas in the ip geometry (see red data points in Fig. 6.18 (g),(j) and in Fig. 6.19 (a),(d),(g)) the magnetoresistance shows a $\sin^2(\alpha)$-dependence. In the oopt rotation plane for GdN/TaN, we have observed a $\sin^2$-signature for $\Delta\rho/\rho_{\mathrm{min}}(\gamma)$ recorded at T=10 K (see red data points in Fig. 6.18 (i)) and T=15 K and 18 K (see red data points in Fig. 6.19 (c) and (f)), whereas for the intermediate temperature T=12 K (see red data points in Fig. 6.18 (l)) as well as at T=20 K (see red data points in Fig. 6.19 (i)) no clear angle-dependence was visible for $\Delta\rho/\rho_{\mathrm{min}}(\gamma)$. At T=25 K, we have observed a $\sin^2$-dependence for $\Delta\rho/\rho_{\mathrm{min}}(\alpha,\beta,\gamma)$ of our *SMR test sample* GdN/TaN in the three different rotation planes ip, oopj and oopt (see red data points in Fig. 6.19 (j),(k),(l)). Therefore, we have associated the phase change of the ADMR in the oopj and oopt geometry $\mathrm{ADMR_{oopj,t}}=\mathrm{MR}_{\mathbf{h}\|\mathbf{n}}-\mathrm{MR}_{\mathbf{h}\|\mathbf{t,j}}$ with the switching from the weak anti-localization (WAL) to the weak-localization (WL) transport phenomena, which we have observed in our FDMR measurement results (see Sec. 6.2.4), in the TaN layer of the GdN/TaN interface. In contrast, we have observed a sole $\sin^2$-dependence of $\Delta\rho/\rho_{\mathrm{min}}(\alpha,\beta,\gamma)$ for our two reference samples GdN/AlN/TaN and AlN/TaN/AlN in all field geometries in the T-range 7.5 K$\leq T\leq$25 K (see orange and green data points in Fig. 6.18 (a)-(l) and in in Fig. 6.19 (a)-(l)). Consequently, we have observed no phase change for the $\Delta\rho/\rho_{\mathrm{min}}(\beta,\gamma)$-curves recorded in the oopj and oopt geometry and we attribute the transition from WAL to WL transport in the GdN/TaN sample to its direct FMI/NM-interface.

Furthermore, we have investigated the ADMR amplitude, extracted with the method illustrated in Fig. 6.20, of our multilayer heterostructures in the three different field geometries in the entire measured T-range 7.5 K$\leq T\leq$50 K at an applied external magnetic field $\mu_0 H_{\text{ext}}$=7 T (see Sec. 6.2.8). Here, we have observed for the in-plane (ip) ADMR amplitude of our GdN/TaN multilayer heterostructure an almost exponential increase, which corresponded to the sole $\sin^2$-signature of our $\Delta\rho/\rho_{\text{min}}(\alpha)$-plots, for low temperatures and there was a maximum value of ADMR$\approx$0.47% visible at T=7.5 K (see Fig. 6.21 (a)). The ADMR(T)-curves of GdN/TaN, recorded in the two out-of-plane (oopj, oopt) field geometries, showed a negative dip in the T-area 10 K$\leq T\leq$20 K (oopj) and 13 K$\leq T\leq$19 K (oopt) and the ADMR amplitude changed sign (see Fig. 6.21 (b)-(c)), which corresponded to the phase shifts ($\sin^2(\beta,\gamma) \rightarrow \cos^2(\beta,\gamma)$ and $\cos^2(\beta,\gamma) \rightarrow \sin^2(\beta,\gamma)$) in the $\Delta\rho/\rho_{\text{min}}(\beta,\gamma)$-plots. For the ADMR amplitude of our two reference samples GdN/AlN/TaN and AlN/TaN/AlN, we have observed an increase with decreasing temperatures T in the three field geometries ip, oopj, oopt and a maximum ADMR amplitude was visible at T=7.5 K (see Fig. 6.21 (d)-(i)). Additionally, the T-dependent evolution of the ADMR amplitude of our GdN/AlN/TaN and AlN/TaN/AlN sample corresponded to the $\sin^2$-dependence of our $\Delta\rho/\rho_{\text{min}}(\alpha,\ \beta,\gamma)$-plots measured in all rotation planes. Finally, we have converted the MR(T)-curves, measured in the three different field geometries oop ($\mathbf{h}\|\mathbf{n}$) and ip ($\mathbf{h}\|\mathbf{j}$ and $\mathbf{h}\|\mathbf{t}$) (see Fig. 6.23 (a)-(f)), into the field rotation geometries in-plane (ip=$\mathbf{h}\|\mathbf{t}-\mathbf{h}\|\mathbf{j}$), out-of-plane $\perp \mathbf{j}$ (oopj=$\mathbf{h}\|\mathbf{n}-\mathbf{h}\|\mathbf{t}$) and out-of-plane $\perp \mathbf{t}$ (oopt=$\mathbf{h}\|\mathbf{n}-\mathbf{h}\|\mathbf{j}$) by using Eqs. (38), (39), (40). In the MR(T)-plots, we have observed for our multilayer samples GdN/TaN (red triangles), GdN/AlN/TaN (orange triangles) and AlN/TaN/AlN (green triangles) (see Fig. 6.22 (a)-(i)) a similar T-dependent evolution for MR compared to our ADMR(T)-plots (see Fig. 6.21 (a)-(i)), which indicated the correspondence between our FDMR- and ADMR-measurement results (see Tab. 6.5).

To further investigate the ADMR measurement results of our *SMR test sample* GdN/TaN at T=12 K and 20 K, we have analyzed the magnetic field dependence of the ADMR amplitude (see Sec. 6.2.9). To this end, we have verified the critical magnetic field H_{c}, at which the phase change ($\sin^2(\beta,\gamma) \rightarrow \cos^2(\beta,\gamma)$) happened in the oopj and oopt geometry. In the oopj ADMR(H)-plots (-7 T to +7 T), we have observed a transition from a positive to a negative ADMR amplitude at the critical magnetic fields $H_{\text{c,12 K}}\approx$3.25 T and $H_{\text{c,20 K}}\approx$5 T (see Fig. 6.25 (a)-(b)), which we have associated with the phase change ($\sin^2(\beta) \rightarrow \cos^2(\beta)$) in oopj and corresponded to the $\cos^2$-dependence of the $\Delta\rho/\rho_{\text{min}}(\beta)$-curve at 12 K / 20 K and 7 T (see Fig. 6.24 (a)-(b)). However, in the oopt field geometry, we only have oberseved a positive ADMR amplitude for the 12 K- and 20 K-measurement and the ADMR amplitude reached a minum value close to zero at 7 T (see Fig. 6.25 (a)-(b)). This result was in agreement with the ADMR(T)-data points measured in oopt at 12 K / 20 K and 7 T (see. Fig. 6.21 (c)) and corresponded to the non-trivial angle-dependence of our $\Delta\rho/\rho_{\text{min}}(\gamma)$-plots recorded at these temperatures in the oopt field geometry (see Fig. 6.24 (a)-(b)). Afterwards, we compared the FDMR measurement results (see Fig. 6.26 (c)-(d)) with the ADMR(H)-plots, recorded in oopj and oopt (see Fig. 6.25 (a)-(b)) of our GdN/TaN multilayer heterostructure at T=12 K and 20 K. To this end, we have plotted MR(H)-curves, in the two field rotation geometries out-of-plane $\perp \mathbf{j}$ (oopj) and out-of-plane $\perp \mathbf{t}$ (oopt) (see Fig. 6.26 (a)-(b)) by using Eq. (39), (40). Here, we have observed for or our GdN/TaN multilayer sample a similar H-dependent

evolution for MR in oopj and oopt (see Fig.6.25 (a)-(b)) compared to our ADMR(H)-plots, which confirmed the comparability of our FDMR- and ADMR-data recorded at T=12 K and 20 K. In summary, the observed sign changes of the ADMR amplitudes as well as the phase shifts in the $\Delta\rho/\rho_{\min}(\beta,\gamma)$-plots, recorded in oopj and oopt, depend on the temperature T- and the magnetic field H.

In the last chapter of this master´s thesis, we have analyzed the FDMR- and ADMR-measurement results of our *SMR test sample* with respect of the manifestation of a potential spin Hall magnetoresistance (SMR) effect in the GdN/TaN interface (see chapter 7). For this purpose, we have further studied our FDMR- and ADMR-data, recorded at T=12 K and $\mu_0 H_{\text{ext}}$=7 T. Here, we have observed different evolutions for our $\Delta\rho/\rho_{\min}(\alpha,\beta,\gamma)$-curves recorded in the three different field geometries: in-plane (ip) $\rightarrow \Delta\rho/\rho_{\min}\propto\sin^2(\alpha)$, out-of-plane $\perp$ **j** (oopj) $\rightarrow \Delta\rho/\rho_{\min}\propto\cos^2(\beta)$ and out-of-plane $\perp$ **t** (oopt) $\rightarrow$ no significant angle-dependence for $\Delta\rho/\rho_{\min}(\gamma)$ (see Fig. 6.24 (a)). As a first step, we have examined the FDMR-data of our *SMR test sample* GdN/TaN and the *SMR reference sample* GdN/AlN/TaN as well as the AlN/TaN/AlN trilayer heterostructure in the H-range -0.08 T$\leq\mu_0 H_{\text{ext}}\leq$0.08 T at T=12 K (see Fig. 7.1 (b)-(d)). Here, we have assumed an ordinary magnetoresistance (OMR) in the TaN layer [16] due to the parabolic behavior of the field-dependent longitudinal magnetoresistance R_{long} (see Fig. 7.1 (a)). Furthermore, a so-called *hysteretic switching* (HS) manifests in our $R_{\text{long}}(H)$-curves, recorded in the two in-plane (ip) field geometries **h**$\|$**j** and **h**$\|$**t**. In addition, we find $R_{\text{long},\mathbf{h}\|\mathbf{j}}>R_{\text{long},\mathbf{h}\|\mathbf{t}}$ in Fig. 7.1 (b). These two effects are indicative for an in-plane (ip) SMR effect in the GdN/TaN interface [16]. Moreover, we did not observe the hysteretic switching in our reference samples GdN/AlN/TaN and AlN/TaN/AlN at T=12 K (see Fig. 7.1 (c)-(d)), which suggests, that the hysteretic switching effect originates from the GdN/TaN bilayer. As a next step, we have determined the ordinary Hall constant $R_{\text{H}}\approx-7.58\times10^{-11}\,\Omega$m/T as well as the anomalous Hall effect (AHE) contribution $\rho_{\text{AHE}}\approx-0.21\times10^{-11}\,\Omega$m to the MR effect from the anitsymmetrized transversal magnetoresistance R_{trans} as a function of the applied external magnetic field $\mu_0 H_{\text{ext}}$ (-7 T to +7 T) by performing a linear fit to R_{trans} (see Fig. 7.2). Afterwards, we have compared the magnitudes of the extracted values R_{H} and ρ_{AHE} of our *SMR test sample* GdN/TaN with literature values and we have found a compatibility with the results of SMR-effect investigations in a EuO/W-bilayer [16] and in a YIG/Pt-interface [15]. Finally, we have calcualted the real- G_{r} and the imaginary-part G_{i} of the *complex spin mixing conductance* $G_{\uparrow\downarrow}$, which represents a useful tool for the analyzation of the spin current transfer across the GdN/TaN interface, by using Eqs. (48) and (49). In Fig. 7.4, we have plotted the extracted contributions G_{r} and G_{i} as a function of the temperature T. Here, we have observed for both values a monotonous decreasing behavior, which showed the expected $T^{-3/2}$-signature, with an increasing temperature. Moreover, we have observed $G_{\text{r}}>>G_{\text{i}}$ in the entire T-range 8 K$\leq T\leq$15 K, which was comparable to the results of the SMR studies in a YIG/Pt-interface published in [15],[100],[101]. Additionally, we have extracted the values $G_{\text{r}}=6.35\times10^{12}\,\Omega^{-1}\text{m}^{-2}$ and $G_{\text{i}}=1.69\times10^{11}\,\Omega^{-1}\text{m}^{-2}$ for T=12 K and thus we have calculated $G_{\text{i}}/G_{\text{r}}$=0.03, which was in agreement with the theoretical value $G_{\text{i}}/G_{\text{r}}\approx1/20$ computed for a YIG/Ag-bilayer [102].

9 Outlook

> 'So eine Arbeit ist eigentlich nie fertig, man muss sie für fertig erklären,
> wenn man nach Zeit und Umständen das Mögliche getan hat.'
> *J. W. von Goethe*

In this master´s theis, we have developed an ideal growth recipe for the fabrication of ferromagnetic insulating (FMI) gadolinium nitride (GdN) thin films, deposited between a superconducting (SC) tantalum nitride (TaN) top and bottom layer, to perform magneto-transport experiments. To this end, we have prepared several multilayer heterostructures to investigate a spin Hall magnetoresistance (SMR) effect in a GdN/TaN interface. In the analysis of the FDMR- and the ADMR-measurement results of our *SMR test sample* AlN/GdN/TaN/AlN, we have extracted the relationships ρ_1/ρ_0 and ρ_2/ρ_0 (see Fig. 7.3), which represent the longitudinal and transversal SMR amplitude in the in-plane (ip) field direction, and we have observed a similar T-depending evolution of the two values compared to the results published in [16]. Furthermore, we have calculated the real- G_r and the imaginary-part G_i of $G_{\uparrow\downarrow}$ for our GdN/TaN multilayer sample and obtained $G_\mathrm{r}>>G_\mathrm{i}$ throughout the T-range $10\,\mathrm{K}\leq T\leq 15\,\mathrm{K}$. In Fig. 7.4, we have observed a similar T-dependent evolution of G_r and G_i compared to the results of a SMR study in a YIG/Pt-interface [15],[100],[101]. Due to the experimentally determined vaules $\rho_{1,2}/\rho_0$ and $G_\mathrm{r,i}$, which are comparable with the already mentioned literature values, we assume a SMR effect could exist in the GdN/TaN interface.

To investigate a potential SMR effect in our GdN/TaN multilayer heterostructure even more intensively, it would be interesting to fabricate further *SMR test samples* with a various TaN layer thicknesses t_TaN. As Eq. (11) shows, the longitudinal SMR amplitude ρ_1/ρ_0 depends on the real-part G_r of the complex spin mixing conductance, the layer thickness t_TaN, the spin Hall angle $\theta_\mathrm{SH,TaN}$ and the spin diffusion length $\lambda_\mathrm{sf,TaN}$ of TaN. In a growth series varying the TaN layer thickness (e.g. $0.1\,\mathrm{nm}\leq t_\mathrm{TaN}\leq 0.5\,\mathrm{nm}$ in 0.1 nm-steps and $0.5\,\mathrm{nm}\leq t_\mathrm{TaN}\leq 20\,\mathrm{nm}$ in 5 nm-steps) at various fixed measurement temperatures T, we could extract the SMR amplitude of our GdN/TaN samples of a function of the various layer thickness t_TaN. In the next step, we would be able to fit our data with Eq. (11) by inserting suitable values of G_r [15],[101]. This method allow us to determine the maximum SMR amplitude at ideal TaN layer tickness $t_\mathrm{TaN}\approx 2\lambda_\mathrm{sf,TaN}$ (see Eq. (11)) as well as to extract the T-dependent spin Hall angle $\theta_\mathrm{SH,TaN}$ and the spin diffusion length $\lambda_\mathrm{sf,TaN}$ of our TaN layer [15],[101]. Finally, we could determine the temperature dependent spin Hall conductivity $\sigma_\mathrm{spin}(T)$ by using the relationship [101]

$$\theta_\mathrm{SH} = \frac{\sigma_\mathrm{spin}}{\sigma}, \tag{56}$$

where σ defines in our experiments the longitudinal conductivity of our GdN/TaN sample at the zero field

$$\sigma_0 = \frac{1}{\rho_0} = \frac{l_\mathrm{HB}}{R_\mathrm{0,long}\cdot w_\mathrm{HB}\cdot d_\mathrm{TaN}}. \tag{57}$$

Figure 9.1 shows the spin Hall conductivity σ_{spin}, extracted from the T-dependent magnetotransport measurements of our GdN(60 nm)/TaN(10 nm) multilayer sample as a function of the temperature T.

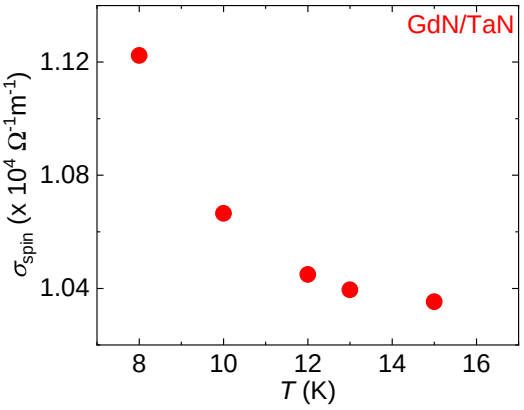

Fig. 9.1: Calculated spin Hall conductivity σ_{spin} of our *SMR test sample* GdN/TaN as a function of the temperature T. We observe a sharp increasing behavior of σ_{spin} towards to low temperatures T.

Figure 9.1 shows a sharp increasing behavior of the spin Hall conductivity σ_{spin} towards to low temperatures T. In comparison to the results of *S. Meyer, et al.* [101], we find in their publication a spin Hall conductivity of $\sigma_{\text{spin}} \approx 3 \times 10^5\,\Omega^{-1}\text{m}^{-1}$ at T=10 K for t_{Pt}=3 nm$\approx 2\lambda_{\text{sf,Pt}}$ and $\theta_{\text{SH,Pt}}$=0.075 (see Fig. 4 (a)-(d) in [101]). The clearly higher spin Hall conductivity σ_{spin} of their YIG/Pt-interface [101], compared to the resistance $R \approx 2.6\,\text{k}\Omega$ of our GdN/TaN(10 nm) sample measured at T=10 K, originates from the signficantly lower resistivity $\rho \approx 2.5 \times 10^{-7}\,\Omega\text{m} \rightarrow R \approx 187\,\Omega$ of their sample recorded at T=10 K and t_{Pt}=10 nm (see Fig. 3 (a) in [101]). Moreover we observe in the work of [101], an increasing T is corresponding to an increasing σ_{spin} in the T-range 10 K$\leq T \leq$100 K and a slight decrease of $\sigma_{\text{spin}}(T)$ is only visible in the T-region 10 K$\leq T \leq$20 K (see Fig. 4 (d) in [101]).

As already mentioned, the YIG/Pt bilayer is a well known heterostructure giving rise to a SMR effect with Pt being a well-established material for the generation of spin currents via the SHE. For this reason, it could be interesting to fabricate both YIG/TaN- and GdN/Pt-heterostructures to further investigate the origin of the non-trivial sign-changes in the ADMR amplitude and the generation of the negative dip in the ADMR(T)-curves (see Fig. 6.21 (b)-(c)) as well as the associated phase-shifts ($\sin^2(\beta,\gamma) \rightarrow \cos^2(\beta,\gamma)$ and $\cos^2(\beta,\gamma) \rightarrow \sin^2(\beta,\gamma)$) (see red data points in Fig. 6.18 and 6.19) observed in the T-ranges 10 K$\leq T \leq$20 K (oopj) and 13 K$\leq T \leq$19 K (oopt) in the ADMR experimments of our GdN/TaN sample. Here, we have assumed the transition from weak anti-localization (WAL) transport phenomena (at T=7.5 K) (see Fig. 6.12 (a)) to weak localization (WL) transport effects (T=10 K$-$20 K) (see Fig. 6.12 (b)-(f)) in the TaN layer as well as its superconducting (SC) phase could be responsible for the extraordinary effects observed in the ADMR experiments of our *SMR test sample* GdN/TaN. In addition, the coexistence of superconductivity (SC) and weak anti-localization is a complex research field, which deals with the investigation of topologically non-trivial systems as well as the development of

novel materials and devices for quantum computing (see *A. H. Al-Tawhid et al.* [90] and *G. Xu et al.* [91]). Therefore, it would be interesting to perform further magnetotransport experiments with our GdN (FMI)/TaN (SC) sample in the low temperature T-regime and thus get access to the research area of unconventional superconducting transport properties.

Another opportunity the investigation of spin currents is the so-called *spin-pumping* technique. Here, the magnetization $\mathbf{M}$ in the FMI-layer of FM/NM-heterostructures is excited to resonance via an external microwave driving field in the GHz-regime (see work of *M. Weiler et al.* [103]). Due to the injection of spin currents into the adjacent NM layer, an enhanced magnetization damping of the magnetization dynamics can be detected [103]. Moreover, spin-pumping into a superconductor (SC) is also a broad active scientific field with regard to study the dynamic spin transport properties of superconducting thin films. Some recent studies have shown that FMI/SC-bilayers are interesting hybrid structures for the investigation of spin currents in SC thin films (see work of *Yaroslav V. Turkin* et al. [104] and *M. Inoue et al.* [105]). In FMI/SC hybrid structures, many interesting spin-dependent effects have been observed, such as a large magnetoresistance effect in spin valves consisting of a FMI/SC/FMI multilayer structure [106],[107] as well as extremely long spin lifetimes [108] and a large spin Hall effect [109] for the quasiparticles of superconductors [17]. The knowledge gained from the discovery of such physical effects can be used for the development of novel SC spin dynamic-based devices deployed in the technology sector for quantum computation [17],[104]). In the work of *Y. Yao et al.* [17], they used the SC/FMI/SC hybrid structure with the stack sequence niobium nitride (NbN) (SC)/GdN(FMI)/NbN(SC) for their spin-pumping experiments via ferromagnetic resonance (FMR) measurements.

To test the dynamic magnetic properties of our GdN thin films, we have also fabricated a SC/FMI/SC junction consisting of NbN/GdN/NbN (see Tab. 9.1) by using the optimized growth recipe for FMI GdN thin films (see Tab. 8.1) as well as the deposition recipe for SC NbN thin films (20 nm) with a SC transition temperature $T_{\mathrm{SC,NbN}} \approx 12\,\mathrm{K}$ developed in the bachelor´s thesis by *M. Reichert* [50] and performed broadband ferromagnetic resonance (bbFMR) measurements in the *CHAOS* cryostat. Here, we have observed in the out-of-plane (oop) field direction at $T = 20\,\mathrm{K}$ a weak FMR mode, which originates from the magnetization dynamics in GdN (see Fig. 9.2). Hence, further FMR experiments on GdN in both ip- and oop-geometry are required to fully characterize the magnetization dynamics parameters of pure GdN and GdN/NM-heterostructures.

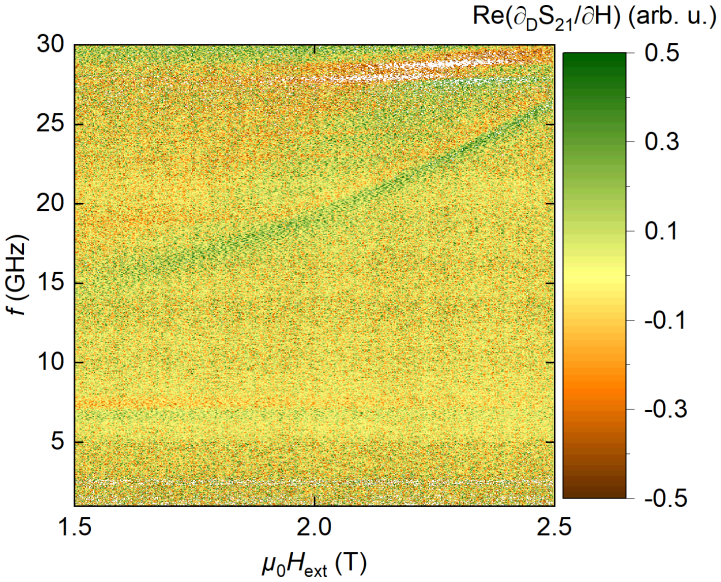

Fig. 9.2: Results of the bbFMR measurement of the NbN/GdN/NbN trilayer heterostructure in the field-range 1.5 T$\leq\mu_0 H_{\mathrm{ext}}\leq$2.5 T at T=20 K: A weak mode, originating from GdN, in the f-range 15 GHz$\leq f\leq$27 GHz is visible.

Growth recipe of a NbN/GdN/NbN heterostructure				
Stack sequence	N_2/Ar [%]	T_{depo} [°C]	P_{depo} [W]	p_{depo} [mbar]
NbN (20nm)	10.5	400	120	5×10^{-3}
GdN (60nm)	40	500	45	5×10^{-3}
NbN (20nm)	10.5	400	120	5×10^{-3}
Magnetic properties	$\mu_0 M_{\mathrm{s}}$ [T]	$\mu_0 H_{\mathrm{c}}$ [mT]	$T_{\mathrm{C,t}}$ [K]	$T_{\mathrm{C,S}}$ [K]
	1.52	1.01	27.16	27.16

Tab. 9.1: Growth parameters and magnetic properties of a NbN (SC)/GdN (FMI)/NbN (SC) heterostructure with a superconducting (SC) transition temperature $T_{\mathrm{SC,NbN}}$=12.24 K.

A Appendix

A.1 Tables of the N_2/Ar- and $P_{\mathbf{depo}}$-variation series in the SUPERBOWL

Sample	N_2/Ar [%]	P_{depo} [W]	T_{depo} [°C]	p_{depo} [mbar]
GdN-12	5	15	500	5.0×10^{-3}
GdN-13	10	15	500	5.0×10^{-3}
GdN-26	12.5	15	500	5.0×10^{-3}
GdN-14	15	15	500	5.0×10^{-3}
GdN-15	20	15	500	5.0×10^{-3}
GdN-16	25	15	500	5.0×10^{-3}
GdN-01	10	45	500	5.0×10^{-3}
GdN-02	20	45	500	5.0×10^{-3}
GdN-03	30	45	500	5.0×10^{-3}
GdN-27	40	45	500	5.0×10^{-3}
GdN-06	60	45	500	5.0×10^{-3}
GdN-07	70	45	500	5.0×10^{-3}
GdN-23	20	75	500	5.0×10^{-3}
GdN-24	25	75	500	5.0×10^{-3}
GdN-25	30	75	500	5.0×10^{-3}
GdN-31	50	75	500	5.0×10^{-3}
GdN-34	80	75	500	5.0×10^{-3}
GdN-36	100	75	500	5.0×10^{-3}

Tab. A.1: Growth parameters of the GdN thin films optimized in the N_2/Ar- and P_{depo}-variation series in the SB.

Sample	$\mu_0 M_{\mathrm{s}}$ [T]	$\mu_0 H_{\mathrm{c}}$ [mT]	$T_{\mathrm{C,t}}$ [K]	$T_{\mathrm{C,S}}$ [K]	ΔT_{C} [K]
GdN-12	2.34	64.57	-	-	-
GdN-13	2.44	46.49	-	-	-
GdN-26	2.25	33.71	-	-	-
GdN-14	2.42	26.86	-	-	-
GdN-15	2.35	13.28	-	-	-
GdN-16	2.31	9.32	-	-	-
GdN-01	1.84	85.28	14.73	32.24	17.51
GdN-02	1.91	46.44	15.23	28.12	12.89
GdN-03	2.04	12.51	17.87	29.14	11.27
GdN-27	2.21	6.41	23.04	27.16	4.12
GdN-06	1.95	6.22	19.24	24.37	4.95
GdN-07	2.04	5.94	17.56	24.14	6.85
GdN-23	1.96	60.01	15.04	27.16	12.12
GdN-24	2.01	36.43	16.63	29.13	12.51
GdN-25	2.11	16.99	18.61	28.13	9.52
GdN-31	2.02	6.86	22.56	23.12	0.56
GdN-34	2.01	5.97	18.79	22.28	3.59
GdN-36	2.01	6.39	19.73	21.13	1.41

Tab. A.2: Magnetic properties of the GdN thin films optimized in the N_2/Ar- and P_{depo}-variation series in the SB.

A.2 Tables of the $T_{\mathbf{depo}}$-variation series in the SUPERBOWL

Sample	N_2/Ar [%]	P_{depo} [W]	T_{depo} [°C]	p_{depo} [mbar]
GdN-47	40	45	20	5.0×10^{-3}
GdN-38	40	45	100	5.0×10^{-3}
GdN-39	40	45	200	5.0×10^{-3}
GdN-40	40	45	300	5.0×10^{-3}
GdN-41	40	45	400	5.0×10^{-3}
GdN-27	40	45	500	5.0×10^{-3}
GdN-42	40	45	600	5.0×10^{-3}
GdN-43	40	45	700	5.0×10^{-3}
GdN-44	40	45	800	5.0×10^{-3}

Tab. A.3: Growth parameters of the GdN thin films optimized in the T_{depo}-variation series in the SB.

Sample	$\mu_0 M_{\mathrm{s}}$ [T]	$\mu_0 H_{\mathrm{c}}$ [mT]	$T_{\mathrm{C,t}}$ [K]	$T_{\mathrm{C,S}}$ [K]	ΔT_{C} [K]
GdN-47	1.78	4.56	13.41	14.34	0.93
GdN-38	1.82	2.01	11.21	12.14	1.02
GdN-39	1.92	4.10	14.07	15.36	1.29
GdN-40	2.01	5.93	16.32	18.11	1.79
GdN-41	2.04	5.59	17.56	19.46	1.91
GdN-27	2.21	6.41	23.04	27.16	4.12
GdN-42	2.11	22.02	24.42	36.16	11.74
GdN-43	2.08	66.87	17.71	41.21	23.51
GdN-44	1.99	74.67	11.63	36.07	24.44

Tab. A.4: Magnetic properties of the GdN thin films optimized in the T_{depo}-variation series in the SB.

A.3 Table of the N_2/Ar-variation series in the SUPERBOWL (ftf-config.)

Sample	N_2/Ar [%]	P_{depo} [W]	T_{depo} [°C]	p_{depo} [mbar]
GdN-72	10	45	500	5.0×10^{-3}
GdN-71	40	45	500	5.0×10^{-3}
GdN-73	70	45	500	5.0×10^{-3}
GdN-76	100	45	500	5.0×10^{-3}
Sample	$\mu_0 M_s$ [T]	$\mu_0 H_c$ [mT]	$T_{C,t}$ [K]	$T_{C,S}$ [K]
GdN-72	1.76	55.01	19.18	61.12
GdN-71	1.89	7.98	29.44	32.12
GdN-73	1.71	8.61	26.44	29.16
GdN-76	1.76	7.06	23.94	26.13

Tab. A.5: Growth parameters and magnetic properties of the GdN thin films optimized in the N_2/Ar -variation series in the SB (ftf-config.).

A.4 Table of the P_{depo}-variation series in the SUPERBOWL (ftf-config.)

Sample	N_2/Ar [%]	P_{depo} [W]	T_{depo} [°C]	p_{depo} [mbar]
GdN-74	40	15	500	5.0×10^{-3}
GdN-71	40	45	500	5.0×10^{-3}
GdN-75	40	75	500	5.0×10^{-3}
Sample	$\mu_0 M_s$ [T]	$\mu_0 H_c$ [mT]	$T_{C,t}$ [K]	$T_{C,S}$ [K]
GdN-74	1.66	6.31	21.81	27.16
GdN-71	1.89	7.98	29.44	32.12
GdN-75	2.17	16.01	24.81	32.14

Tab. A.6: Growth parameters and magnetic properties of the GdN thin films optimized in the P_{depo}-variation series in the SB (ftf-config.).

A.5 Table of parameters for simulating FDMR-data, recorded for AlN/GdN/TaN/AlN, with WAL model

T=7.5 K			
Field geometry	L_ϕ [nm]	L_{SO} [nm]	F [$\times 10^{-6}$]
h$\|\|$**n**	14.5	3.0	1000
h$\|\|$**j**	9.5	0.5	0.1
h$\|\|$**t**	8.5	0.5	0.1

Tab. A.7: Parameters L_ϕ, L_{SO} and F used for simulating FDMR data, measured at T=7.5 K, with WAL model (see Eq. (33)).

A.6 Table of parameters for simulating FDMR-data, recorded for AlN/GdN/TaN/AlN, with WL model

T=10 K		
Field geometry	L_ϕ [nm]	β [$\times 10^{-6}$]
h$\|\|$**n**	1.0	16.0
h$\|\|$**j**	8.0	16.0
h$\|\|$**t**	10.0	16.0
T=12 K		
Field geometry	L_ϕ [nm]	β [$\times 10^{-6}$]
h$\|\|$**n**	5.0	16.0
h$\|\|$**j**	15.0	16.0
h$\|\|$**t**	12.0	16.0
T=15 K		
Field geometry	L_ϕ [nm]	β [$\times 10^{-6}$]
h$\|\|$**n**	12.0	16.0
h$\|\|$**j**	28.0	16.0
h$\|\|$**t**	24.0	16.0
T=18 K		
Field geometry	L_ϕ [nm]	β [$\times 10^{-6}$]
h$\|\|$**n**	23.0	16.0
h$\|\|$**j**	33.0	16.0
h$\|\|$**t**	30.0	16.0
T=20 K		
Field geometry	L_ϕ [nm]	β [$\times 10^{-6}$]
h$\|\|$**n**	28.2	16.0
h$\|\|$**j**	35.0	16.0
h$\|\|$**t**	37.0	16.0

Tab. A.8: Parameters L_ϕ and β used for simulating FDMR data, measured in the T-range 10 K$<T<$20 K, with WL model (see Eq. (34)).

A.7 Table of parameters for simulating FDMR-data, recorded for AlN/GdN/AlN/TaN/AlN, with WAL model

T=7.5 K			
Field geometry	L_ϕ [nm]	L_{SO} [nm]	F [$\times 10^{-6}$]
h$\|$**n**	10.0	4.0	100
h$\|$**j**	6.0	4.0	100
h$\|$**t**	5.8	3.8	100
T=10 K			
Field geometry	L_ϕ [nm]	L_{SO} [nm]	F [$\times 10^{-6}$]
h$\|$**n**	1.1	5.74	100
h$\|$**j**	3.2	2.0	0.1
h$\|$**t**	5.0	1.0	0.1
T=12 K			
Field geometry	L_ϕ [nm]	L_{SO} [nm]	F [$\times 10^{-6}$]
h$\|$**n**	3.1	5.0	100
h$\|$**j**	5.0	0.5	0.1
h$\|$**t**	8.1	0.5	0.1

Tab. A.9: Parameters L_ϕ, L_{SO} and F used for simulating FDMR data, measured in the T-range 7.5 K$<T<$12 K, with WAL model (see Eq. (33)).

A.8 Table of parameters for simulating FDMR-data, recorded for AlN/GdN/AlN/TaN/AlN, with WL model

T=15 K		
Field geometry	L_ϕ [nm]	β [$\times 10^{-6}$]
h$\|$**n**	5.00	16.0
h$\|$**j**	8.0	16.0
h$\|$**t**	12.0	16.0
T=18 K		
Field geometry	L_ϕ [nm]	β [$\times 10^{-6}$]
h$\|$**n**	10.0	16.0
h$\|$**j**	21.0	16.0
h$\|$**t**	25.0	16.0
T=20 K		
Field geometry	L_ϕ [nm]	β [$\times 10^{-6}$]
h$\|$**n**	10.0	16.0
h$\|$**j**	20.0	16.0
h$\|$**t**	25.0	16.0

Tab. A.10: Parameters L_ϕ and β used for simulating FDMR data, measured in the T-range 15 K$<T<$20 K, with WL model (see Eq. (34)).

A.9 Table of parameters for simulating FDMR-data, recorded for AlN/TaN/AlN, with WAL model

T=7.5 K			
Field geometry	L_ϕ [nm]	L_{SO} [nm]	F [$\times 10^{-6}$]
h$\|$**n**	23.0	3.8	1.0
h$\|$**j**	6.9	0.5	0.1
h$\|$**t**	6.78	0.5	0.1
T=10 K			
Field geometry	L_ϕ [nm]	L_{SO} [nm]	F [$\times 10^{-6}$]
h$\|$**n**	16.4	2.5	1.0
h$\|$**j**	6.0	0.8	0.1
h$\|$**t**	5.85	0.8	0.1
T=12 K			
Field geometry	L_ϕ [nm]	L_{SO} [nm]	F [$\times 10^{-6}$]
h$\|$**n**	14.4	2.4	1.0
h$\|$**j**	5.1	0.4	0.1
h$\|$**t**	4.98	0.4	0.1
T=15 K			
Field geometry	L_ϕ [nm]	L_{SO} [nm]	F [$\times 10^{-6}$]
h$\|$**n**	12.0	2.2	1.0
h$\|$**j**	4.50	0.2	0.1
h$\|$**t**	4.42	0.2	0.1
T=18 K			
Field geometry	L_ϕ [nm]	L_{SO} [nm]	F [$\times 10^{-6}$]
h$\|$**n**	8.5	2.0	1.0
h$\|$**j**	4.0	0.15	0.1
h$\|$**t**	3.93	0.15	0.1
T=20 K			
Field geometry	L_ϕ [nm]	L_{SO} [nm]	F [$\times 10^{-6}$]
h$\|$**n**	7.20	1.5	1.0
h$\|$**j**	3.50	0.1	0.1
h$\|$**t**	3.45	0.1	0.1

Tab. A.11: Parameters L_ϕ, L_{SO} and F used for simulating FDMR data, measured in the T-range 7.5 K$<T<$12 K, with WAL model (see Eq. (33)).

Bibliography

[1] Fang, Z., Williams, P., Odedra, R., Jeon, H. & Potter, R. Gadolinium nitride films deposited using a PEALD based process. *Journal Of Crystal Growth* **338**, 111-117 (2012), URL.

[2] Azeem, M. Optical Properties of Rare Earth Nitrides. PhD-thesis, Victoria University of Wellington (2013), URL.

[3] Ozatay, O., Hauet, T., Braganca, P., Wan, L., Mather, P., Schneider, M. & Thiele, J. Spin-based data storage. *Comprehensive Nanoscience And Nanotechnology* **1-5**, 67-122 (2019), URL.

[4] Jena, D., Page, R., Casamento, J., Dang, P., Singhal, J., Zhang, Z., Wright, J., Khalsa, G., Cho, Y. & Xing, H. The new nitrides: Layered, ferroelectric, magnetic, metallic and superconducting nitrides to boost the GaN photonics and electronics eco-system. *Japanese Journal Of Applied Physics* **58** (2019), URL.

[5] Dietl, T. Why Ferromagnetic Semiconductors?. *Acta Physica Polonica A* **100**, 139-151 (2001), URL.

[6] Ohno, Y., Young, D., Beschoten, B., Matsukura, F. & Ohno, H. Electrical spin injection in a ferromagnetic semiconductor heterostructure. **402**, 790–792 (1999), URL.

[7] Goel, S., Khang, N., Osada, Y., Anh, L., Hai, P. & Tanaka, M. Room-temperature spin injection from a ferromagnetic semiconductor. *Scientific Reports* **13**, 1-9 (2023), URL.

[8] Awschalom, D. D., Loss, D., Samarth, N. Semiconductor Spintronics and Quantum Computation. *Springer Science and Business Media, NanoScience and Technology (NANO)* (2013), URL.

[9] Cwik, S., Beer, S., Hoffmann, S., Krasnopolski, M., Rogalla, D., Becker, H., Peeters, D., Ney, A. & Devi, A. Integrating AlN with GdN Thin Films in an in Situ CVD Process: Influence on the Oxidation and Crystallinity of GdN. *ACS Applied Materials And Interfaces* **9**, 27036-27044 (2017), URL.

[10] Natali, F., Plank, N., Galipaud, J., Ruck, B., Trodahl, H., Semond, F., Sorieul, S. & Hirsch, L. Epitaxial growth of GdN on silicon substrate using an AlN buffer layer. *Journal Of Crystal Growth* **312**, 3583-3587 (2010), URL.

[11] Granville, S., Ruck, B., Budde, F., Koo, A., Pringle, D., Kuchler, F., Preston, A., Housden, D., Lund, N., Bittar, A., Williams, G. & Trodahl, H. Semiconducting ground state of GdN thin films. *Physical Review B - Condensed Matter And Materials Physics* **73**, 1-5 (2006), URL.

[12] Vidyasagar, R., Kitayama, S., Yoshitomi, H., Kita, T., Sakurai, T. & Ohta, H. Study on spin-splitting phenomena in the band structure of GdN. *Applied Physics Letters* **100** (2012), URL.

[13] Dhar, S., Pérez, L., Brandt, O., Trampert, A., Ploog, K., Keller, J. & Beschoten, B. Gd-doped GaN: A very dilute ferromagnetic semiconductor with a Curie temperature above 300 K. *Physical Review B - Condensed Matter And Materials Physics* **72**, 1-9 (2005), URL.

[14] Brataas, A., Wees, B., Klein, O., Loubens, G. & Viret, M. Spin insulatronics. *Physics Reports* **885**, 1-27 (2020), URL.

[15] Althammer, M., Meyer, S., Nakayama, H., Schreier, M., Altmannshofer, S., Weiler, M., Huebl, H., Geprägs, S., Opel, M., Gross, R., Meier, D., Klewe, C., Kuschel, T., Schmalhorst, J., Reiss, G., Shen, L., Gupta, A., Chen, Y., Bauer, G., Saitoh, E. & Goennenwein, S. Quantitative study of the spin Hall magnetoresistance in ferromagnetic insulator/normal metal hybrids. *Physical Review B - Condensed Matter And Materials Physics* **87**, 1-15 (2013), URL.

[16] Rosenberger, P., Opel, M., Geprägs, S., Huebl, H., Gross, R., Müller, M. & Althammer, M. Quantifying the spin mixing conductance of EuO/W heterostructures by spin Hall magnetoresistance experiments. *Applied Physics Letters* **118** (2021), URL.

[17] Yao, Y., Song, Q., Takamura, Y., Cascales, J., Yuan, W., Ma, Y., Yun, Y., Xie, X., Moodera, J. & Han, W. Probe of spin dynamics in superconducting NbN thin films via spin pumping. *Physical Review B* **97**, 224414 (2018), URL.

[18] Hoepfl, R. *Wachstumsoptimierung supraleitender Tantalnitrid (TaN) -Dünnfilme für fortgeschrittene Spinelektronik*. Bachelorthesis, Technische Universität München, Walther-Meissner-Institut für Tieftemperaturforschung Garching (2020), URL.

[19] Czeschka, F. D. *Spin Currents in Metallic Nanostructures*. PhD-thesis, Technische Universität München, Walther-Meissner-Institut für Tieftemperaturforschung Garching (2011), URL.

[20] Wimmer, T. *Spin Transport in Magnetic Nanostructures*. Masterthesis, Technische Universität München, Walther-Meissner-Institut für Tieftemperaturforschung Garching (2016), URL.

[21] Hirsch, J. Spin Hall Effect. *Physical Review Letters* **83**, 1834-1837 (1999), URL.

[22] Saitoh, E., Ueda, M., Miyajima, H. & Tatara, G. Conversion of spin current into charge current at room temperature: Inverse spin-Hall effect. *Applied Physics Letters* **88** (2006), URL.

[23] Berry, M. V. Quantal Phase Factors Accompanying Adiabatic Changes. *Proceedings of the Royal Society of London. A. Mathematical and Physical Sciences* **392**, 45-57 (1984), URL.

[24] Smit, J. The spontaneous hall effect in ferromagnetics I. *Physica* **21**, 877-887 (1955), URL.

[25] Smit, J. The spontaneous hall effect in ferromagnetics II. *Physica* **24**, 39-51 (1958), URL.

[26] Berger, L. Side-jump mechanism for the hall effect of ferromagnets. *Physical Review B* **2**, 4559-4566 (1970), URL.

[27] Schwenke, P. *Vertical $Pt/Y_3Fe_5O_{12}/Pt$ Heterostructures for Magnon Mediated Magnetoresistance Measurements.* Masterthesis, Technische Universität München, Walther-Meissner-Institut für Tieftemperaturforschung Garching (2021), URL.

[28] Swatek, P., Hang, X., Fan, Y., Jiang, W., Yun, H., Lyu, D., Zhang, D., Peterson, T., Sahu, P., Benally, O., Cresswell, Z., Liu, J., Pahari, R., Kukla, D., Low, T., Mkhoyan, K. & Wang, J. Room temperature spin-orbit torque efficiency in sputtered low-temperature superconductor δ-TaN. *Physical Review Materials* **6**, 07420 (2022), URL.

[29] Chen, Y., Takahashi, S., Nakayama, H., Althammer, M., Goennenwein, S., Saitoh, E. & Bauer, G. Theory of spin Hall magnetoresistance. *Physical Review B - Condensed Matter And Materials Physics* **87** (2013), URL.

[30] Ferdigg, R. *Spin Current Physics in Uniaxial Antiferromagnetic Cr_2O_3/Pt Bilayers.* Masterthesis, Technische Universität München, Walther-Meissner-Institut für Tieftemperaturforschung Garching (2020), URL.

[31] Likovich, E., Russell, K., Petersen, E. & Narayanamurti, V. Weak localization and mobility in ZnO nanostructures. *Physical Review B - Condensed Matter And Materials Physics* **80**, 1-7 (2009), URL.

[32] Lv, M., Wang, H., Xu, Y., Yu, G., Zhang, H., Lin, T., Hu, G., Dai, N. & Chu, J. Long phase coherence length and anisotropic magnetoresistance in MgZnO thin film. *Journal Of Applied Physics* **117** (2015), URL.

[33] Stefanowicz, W., Adhikari, R., Andrearczyk, T., Faina, B., Sawicki, M., Majewski, J., Dietl, T. & Bonanni, A. Experimental determination of Rashba spin-orbit coupling in wurtzite n -GaN:Si. *Physical Review B - Condensed Matter And Materials Physics* **89**, 2-6 (2014), URL.

[34] Wei, P., Katmis, F., Assaf, B., Steinberg, H., Jarillo-Herrero, P., Heiman, D. & Moodera, J. Exchange-coupling-induced symmetry breaking in topological insulators. *Physical Review Letters* **110**, 1-5 (2013), URL.

[35] Yang, Q., Dolev, M., Zhang, L., Zhao, J., Fried, A., Schemm, E., Liu, M., Palevski, A., Marshall, A., Risbud, S. & Kapitulnik, A. Emerging weak localization effects on a topological insulator-insulating ferromagnet (Bi_2Se_3-EuS) interface. *Physical Review B - Condensed Matter And Materials Physics* **88**, 3-6 (2013), URL.

[36] Kandala, A., Richardella, A., Rench, D., Zhang, D., Flanagan, T. & Samarth, N. Growth and characterization of hybrid insulating ferromagnet-topological insulator heterostructure devices. *Applied Physics Letters* **103** (2013), URL.

[37] Lee, P. & Ramakrishnan, T. V. Disordered Electronic Systems. *Review of Modern Physics* **57**, 287-337 (1985), URL.

[38] Altshuler, B. L. & Aronov, A. G. CHAPTER 1 - Electron–Electron Interaction In Disordered Conductors. *Electron–Electron Interactions In Disordered Systems* **10** 1-153 (1985), URL.

[39] Altshuler, B. L., Khmel'nitzkii, D., Larkin, A. I., Lee, P. A. Magnetoresistance and Hall effect in a disordered two-dimensional electron gas. *Physical Review B* **22**, 5142-5153 (1980), URL.

[40] Lu, H-Z. & Shen, S-Q. Weak localization and weak anti-localization in topological insulators. *Optics & Photonics - NanoScience + Engineering*. (2014), URL.

[41] Drude, P. Zur Elektronentheorie der Metalle. *Annalen Der Physik* **306**, 566-613 (1900), URL.

[42] Datta, S. Electronic Transport in Mesoscopic Systems. *Cambridge Studies in Semiconductor Physics and Microelectronic Engineering*, Cambridge: Cambridge University (1995), URL.

[43] Spavieri, G. & Mansuripur, M. Origin of the spin-orbit interaction. *Physica Scripta* **90** (2015), URL.

[44] Hikami, S., Larkin, A. & Nagaoka, Y. Spin-Orbit Interaction and Magnetoresistance in the Two Dimensional Random System. *Progress Of Theoretical Physics* **63**, 707-710 (1980), URL.

[45] Poole, D., Pepper, M. & Hughes, A. Spin-orbit coupling and weak localisation in the 2D inversion layer of indium phosphide. *Journal Of Physics C: Solid State Physics* **15** (1982), URL.

[46] Bergman, G. Influence of spin-orbit coupling on weak localization. *Physical Review Letters* **48**, 1046-1049 (1982), URL.

[47] Newton, P., Mansell, R., Holmes, S., Myronov, M. & Barnes, C. Weak localization and weak antilocalization in doped germanium epilayers. *Applied Physics Letters* **110**, 0-5 (2017), URL.

[48] Harada, T., Bredol, P., Inoue, H., Ito, S., Mannhart, J. & Tsukazaki, A. Determination of the phase coherence length of $PdCoO_2$ nanostructures by conductance fluctuation analysis. *Physical Review B* **103**, 2-7 (2021), URL.

[49] Anders, A. Tutorial: Reactive high power impulse magnetron sputtering (R-HiPIMS). *Journal Of Applied Physics* **121** (2017), URL.

[50] Reichert, M. *Hochwertige supraleitende Dünnfilme für fortgeschrittene Spinelektronik*. Bachelorthesis, Technische Universität München, Walther-Meissner-Institut für Tieftemperaturforschung Garching (2018).

[51] Faltermeier, A. *Optimierung supraleitender Schichten aus Niob, Niobnitrid und Niobtitannitrid für den Einsatz in Mikrowellenresonatoren*. Masterthesis, Technische Universität München, Walther-Meissner-Institut für Tieftemperaturforschung Garching (2019), URL.

[52] Mueller, M. *Superconductor / Ferromagnet Heterostructures for Superconducting Spintronics*. Masterthesis, Technische Universität München, Walther-Meissner-Institut für Tieftemperaturforschung Garching (2019).

[53] Graham, C. Magnetic behavior of gadolinium near the curie point. *Journal Of Applied Physics* **36**, 1135-1136 (1965), URL.

[54] Senapati, K., Fix, T., Vickers, M., Blamire, M. & Barber, Z. Structural evolution and competing magnetic orders in polycrystalline GdN films. *Physical Review B - Condensed Matter And Materials Physics* **83**, 1-8 (2011), URL.

[55] Khazen, K., Von Bardeleben, H., Cantin, J., Bittar, A., Granville, S., Trodahl, H. & Ruck, B. Ferromagnetic resonance study of GdN thin films with bulk and extended lattice constants. *Physical Review B - Condensed Matter And Materials Physics* **74**, 1-7 (2006), URL.

[56] Shaib, A., Natali, F., Chan, J., Ullstad, F., Holmes-Hewett, W., Miller, J., Ruck, B. & Trodahl, H. Coexisting structural phases in the catalytically driven growth of rock salt GdN. *Materials Research Express* **7** (2020), URL.

[57] Mi, W., Guo, Z., Duan, X., Zhang, X. & Bai, H. Large negative magnetoresistance in reactive sputtered polycrystalline GdN_x films. *Applied Physics Letters* **102** (2013), URL.

[58] Xiao, J. & Chien, L. Proximity effects in superconductor/insulating-ferromagnet nbn/gdn multilayers. *Physical Review Letters* **76**, 1727-1730 (1996), URL.

[59] Leuenberger, F., Parge, A., Felsch, W., Fauth, K. & Hessler, M. GdN thin films: Bulk and local electronic and magnetic properties. *Physical Review B - Condensed Matter And Materials Physics* **72**, 1-8 (2005), URL.

[60] Senapati, K., Fix, T., Vickers, M., Blamire, M. & Barber, Z. Magnetic exchange hardening in polycrystalline GdN thin films. *Journal Of Physics Condensed Matter* **22** (2010), URL.

[61] Cockcroft, J. K., Barnes, P., *Advanced Certificate in Powder Diffraction on the Web, Calculating the Intensity of Diffraction Using the Structure Factor Equation* , School of Crystallography, Birkbeck College, University of London (1997-2004), URL.

[62] Leuenberger, F. *Elemental resolved magnetism of Gadoliniumnitride layers and GdN/Fe multilayers* . PhD-thesis, Mathematisch-Naturwissenschaftliche Fakultät der Georg-August-Universität zu Göttingen (2004), URL.

[63] Kasuya, T. A Theory of Metallic Ferro- and Antiferromagnetism on Zener's Model. *Progress Of Theoretical Physics* **16**, 45-57 (1956), URL.

[64] Ruderman, M. & Kittel, C. Indirect exchange coupling of nuclear magnetic moments by conduction electrons. *Physical Review* **96**, 99-102 (1954), URL.

[65] Yosida, K. Magnetic properties of Cu-Mn alloys. *Physical Review* **106**, 893-898 (1957), URL.

[66] Methfessel, S. *Zeitschrift für Angewandte Physik* **18**, 414 (1965).

[67] Mitra, C. & Lambrecht, W. Magnetic exchange interactions in the gadolinium pnictides from first principles. *Physical Review B - Condensed Matter And Materials Physics* **78**, 1-8 (2008), URL.

[68] Kaplan, T. & Lyons, D. Theory of indirect exchange interactions in rare-earth metals. *Physical Review* **129**, 2072-2086 (1963), URL.

[69] Heisenberg, W. Zur Theorie des Ferromagnetismus. *Zeitschrift Für Physik* **49**, 619-636 (1928), URL.

[70] Borisov, V., Kvashnin, Y., Ntallis, N., Thonig, D., Thunström, P., Pereiro, M., Bergman, A., Sjöqvist, E., Delin, A., Nordström, L. & Eriksson, O. Heisenberg and anisotropic exchange interactions in magnetic materials with correlated electronic structure and significant spin-orbit coupling. *Physical Review B* **103**, 1-18 (2021), URL.

[71] Oxford Instruments, Plasma Technology. *Ion Beam Etching & Milling (IBE)* (2023), URL.

[72] Bunaciu, A., Udriştioiu, E. & Aboul-Enein, H. X-Ray Diffraction: Instrumentation and Applications. *Critical Reviews In Analytical Chemistry* **45**, 289-299 (2015), URL.

[73] Bragg, W. & Bragg, W. The reflection of X-rays by crystals. *Proceedings Of The Royal Society Of London. Series A, Containing Papers Of A Mathematical And Physical Character* **88**, 428-438 (1913), URL.

[74] Glazer, A. The first paper by W.L. Bragg-what and when?. *Crystallography Reviews* **19**, 117-124 (2013), URL.

[75] Van der Pauw, L. J. A method of measuring the resistivity and Hall coefficient on lamellae of arbitrary shape. *Philips Technical Review* **20**, 220-224 (1958), URL.

[76] Czeschka, F. D. *Strukturelle, elektrische und magnetische Eigenschaften dünner Sr_2CrReO_6-Schichten für die Spinelektronik.* Diplomathesis, Technische Universität München, Walther-Meissner-Institut für Tieftemperaturforschung Garching (2007), URL.

[77] Pranav, S. SQUID Magnetometer - A Study. *Indian Association for the Cultivation of Science, Jadavpur, Kolkata, 700032, India* (2021), URL.

[78] McElfresh, Q. D. M. Fundamentals of Magnetism and Magnetic Measurements, Featuring Quantum Design's magnetic property measurement System. *Quantum Design* (1994), URL.

[79] Schade, F. M. *Fabrication and Characterization of $Y_3Fe_5O_{12}/Pt/Y_3Fe_5O_{12}$ Trilayers for Spin Current Based Experiments.* Bachelorthesis, Technische Universität München, Walther-Meissner-Institut für Tieftemperaturforschung Garching (2013).

[80] Martínez Santiesteban, F. M., Swanson, S. D., Noll, D. C. & Anderson, D. J. Magnetic resonance compatibility of multichannel silicon microelectrode systems for neural recording and stimulation: design criteria, tests, and recommendations. *IEEE Transactions on Biomedical Engineering (TBME)* **53**, 547-558 (2006), URL.

[81] Downs, B., Swaminathan, R. & Bartelmehs, K. *American Mineralogist* **78**, 1104-1107 (1993).

[82] Hashizume, T., Saiki, A. & Terayama, K. Fabrication of Tantalum nitride thin film using the low vacuum magnetron sputtering system. *IOP Conference Series: Materials Science And Engineering* **18**, 092032 (2011), URL.

[83] Terao, N. Structure of tantalum nitrides. *Japanese Journal Of Applied Physics* **10**, 248-259 (1971), URL.

[84] Holleck, H., Smailos, E. & Thümmler, F. Zur mischphasenbildung der mononitride in den systemen U- (Y, La, Pr)-N. *Journal of Nuclear Materials* **32**, 281-289 (1969), URL.

[85] Gas, K. & Sawicki, M. A Simplified Method of the Assessment of Magnetic Anisotropy of Commonly Used Sapphire Substrates in SQUID Magnetometers. *Materials* **15** (2022), URL.

[86] Terrasanta, G., Müller, M., Sommer, T., Geprägs, S., Gross, R., Althammer, M. & Poot, M. Growth of aluminum nitride on a silicon nitride substrate for hybrid photonic circuits. *Materials For Quantum Technology* **1**, 021002 (2021), URL.

[87] Chen, Y., Shi, X., Yang, J. & Chen, Y. Growth and optical properties of gadolinium aluminum nitride thin films. *Physica Status Solidi (C) Current Topics In Solid State Physics* **9**, 1040-1042 (2012), URL.

[88] Ekstrum, C., Venkatesan, R., Kendrick, C., Einav, M., Sivaprakash, P., Mayandi, J., Arumugam, S. & Pearce, J. The Effects of Substrate Temperature on the Growth, Microstructural and Magnetic Properties of Gadolinium-Containing Films on Aluminum Nitride. *Surfaces* **5**, 321-333 (2022), URL.

[89] Balaji, S. & Debnath, R. Internal stress induced metallization of single-walled carbon nanotubes in a nanotube/glass conducting composite. *Nanotechnology* **22** (2011), URL.

[90] Al-Tawhid, A., Kanter, J., Hatefipour, M., Kumah, D., Shabani, J. & Ahadi, K. Superconductivity and Weak Anti-localization at $KTaO_3$ (111) Interfaces. *Journal Of Electronic Materials* **51**, 6305-6309 (2022), URL.

[91] Xu, G., Wang, W., Zhang, X., Du, Y., Liu, E., Wang, S., Wu, G., Liu, Z. & Zhang, X. Weak antilocalization effect and noncentrosymmetric superconductivity in a topologically nontrivial semimetal LuPdBi. *Scientific Reports* **4**, 1-7 (2014), URL.

[92] Stephen, G., Vail, O., Lu, J., Beck, W., Taylor, P. & Friedman, A. Weak Antilocalization and Anisotropic Magnetoresistance as a Probe of Surface States in Topological $Bi_2Te_xSe_{3-x}$ Thin Films. *Scientific Reports* **10**, 1-7 (2020), URL.

[93] Ghezzi, C., Magnanini, R. & Parisini, A. Negative magnetoresistance effects in metallic n -type GaSb. *Journal Of Applied Physics* **102**, 1-7 (2007), URL.

[94] Mani, R., Ghenim, L. & Choi, J. Weak localization in the narrow gap bulk semiconductors $Hg_{1-x}Cd_xTe$ and InSb. *Solid State Communications* **79**, 693-697 (1991), URL.

[95] Wang, Y., Wan, Z., Qian, Q., Liu, Y., Kang, Z., Fan, Z., Wang, P., Wang, Y., Li, C., Jia, C., Lin, Z., Guo, J., Shakir, I., Goorsky, M., Duan, X., Zhang, Y., Huang, Y. & Duan, X. Probing photoelectrical transport in lead halide perovskites with van der Waals contacts. *Nature Nanotechnology* **15**, 768-775 (2020), URL.

[96] Kawabata, A. Theory of negative magnetoresistance in three-dimensional systems. *Solid State Communications.* **34**, 431-432 (1980), URL.

[97] Kawabata, A. Theory of Negative Magnetoresistance I. Application to Heavily Doped Semiconductors. *Journal Of The Physical Society Of Japan.* **49**, 628-637 (1980), URL.

[98] Zhang, X., Woods, J., Cha, J. & Shi, X. Crossover between weak antilocalization and weak localization in few-layer WTe_2: Role of electron-electron interactions. *Physical Review B* **102**, 1-7 (2020), URL.

[99] Stamopoulos, D. & Aristomenopoulou, E. Superconducting magnetoresistance in ferromagnet/superconductor/ferromagnet trilayers. *Scientific Reports* **5**, 1-9 (2015), URL.

[100] Zhang, X., Bergeret, F. & Golovach, V. Theory of Spin Hall Magnetoresistance from a Microscopic Perspective. *Nano Letters* **19**, 6330-6337 (2019), URL.

[101] Meyer, S., Althammer, M., Geprägs, S., Opel, M., Gross, R. & Goennenwein, S. Temperature dependent spin transport properties of platinum inferred from spin Hall magnetoresistance measurements. *Applied Physics Letters* **104**, 1-5 (2014), URL.

[102] Jia, X., Liu, K., Xia, K. & Bauer, G. Spin transfer torque on magnetic insulators. *Europhysics Letters.* **96**, 0-6 (2011), URL.

[103] Weiler, M., Althammer, M., Schreier, M., Lotze, J., Pernpeintner, M., Meyer, S., Huebl, H., Gross, R., Kamra, A., Xiao, J., Chen, Y., Jiao, H., Bauer, G. & Goennenwein, S. Experimental test of the spin mixing interface conductivity concept. *Physical Review Letters* **111**, 1-5 (2013), URL.

[104] Turkin, Y. & Pugach, N. Spin dynamics in superconductor/ferromagnetic insulator hybrid structures with precessing magnetization. *Beilstein Journal Of Nanotechnology* **14**, 233-239 (2023), URL.

[105] Inoue, M., Ichioka, M. & Adachi, H. Spin pumping into superconductors: A new probe of spin dynamics in a superconducting thin film. *Physical Review B* **96**, 1-9 (2017), URL.

[106] Miao, G., Ramos, A. & Moodera, J. Infinite magnetoresistance from the spin dependent proximity effect in symmetry driven bcc-Fe/V/Fe heteroepitaxial superconducting spin valves. *Physical Review Letters* **101**, 1-4 (2008), URL.

[107] Miao, G., Yoon, K., Santos, T. & Moodera, J. Influence of spin-polarized current on superconductivity and the realization of large magnetoresistance. *Physical Review Letters* **98** (2007), URL.

[108] Yang, H., Yang, S., Takahashi, S., Maekawa, S. & Parkin, S. Extremely long quasiparticle spin lifetimes in superconducting aluminium using MgO tunnel spin injectors. *Nature Materials* **9**, 586-593 (2010), URL.

[109] Wakamura, T., Akaike, H., Omori, Y., Niimi, Y., Takahashi, S., Fujimaki, A., Maekawa, S. & Otani, Y. Quasiparticle-mediated spin Hall effect in a superconductor. *Nature Materials* **14**, 675-679 (2015), URL.

Acknowledgment

Finally, I would like to thank a few people who supported me during my master's thesis at the Walther-Meißner-Institut (WMI) and contributed to the success of this thesis.

- Prof. Dr. Rudolf Gross: For providing the topic and the opportunity to do my master´s thesis at the WMI and the exciting lectures in solid state physics.
- Dr. Matthias Althammer: For supervising my master's thesis and supporting me in all my experiments as well as the discussions of the results and corrections of my thesis.
- PhD-student M.Sc. Manuel Müller: For the supervision of my experiments, the support in the fabrication of the GdN thin films with the sputtering system SUPERBOWL as well as the SQUID magnetrometry experiments, his support in the cleanroom when creating the Hall-bar structured samples and the magnetotransport measurements of the multilayer thin films in the *MORIA*- and *CHAOS*-cryostat, his help with XRD- and AFM- measurements of the GdN thin films, his support in data analysis with Python, OriginLab and TeXstudio as well as the discussions of the results and the corrections of my thesis - thanks Manuel!
- Dr. Matthias Opel: For his help with the SQUID magnetrometry experiments and the discussions of my results.
- Dr. Stephan Geprägs: For his support with the XRD measurements and the etching process with the Argon ion milling gun (also many thanks to PhD-student M.Sc. Monika Scheufele) and the discussions of my results.
- My master student colleagues (magnetiker group): Julian Franz, Christian Mang, Maria Sigl, Johannes Weber, Franz Weidenhiller - Thanks for your support in the labs, your friendly manner and the pleasant working atmosphere!
- All employees of the Walter Meißner Institute for their support and the friendly working atmosphere - many thanks! I really enjoyed my work at the WMI!
- I would also like to thank my closest friends and spezl´n for their support and patience over the years during my studies and the many beautiful moments besides physics.
- A special thanks goes to my family, especially to my beloved parents and my brother, who have always supported me mentally as well as financially and believed in me at any time and without their unlimited support I would never have completed my physics studies.
- Finally, I would like to thank my girlfriend Johanna for her unconditional support, patience, loyalty and love.